Stability of magnetic skyrmions in ultrathin films

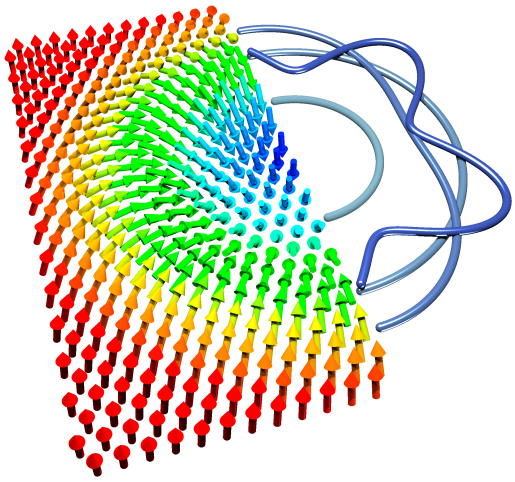

Dissertation
zur Erlangung des Doktorgrades
der Mathematisch-Naturwissenschaftlichen Fakultät
der Christian-Albrechts-Universität zu Kiel

vorgelegt von
Stephan von Malottki

Kiel, 2020

Erster Gutachter: Prof. Dr. Stefan Heinze

Zweiter Gutachter: Prof. Dr. Fabio Caruso

Dritter Gutachter: Prof. Dr. Hannes Jónsson

Datum der Disputation: 18.02.2021

Abstract

Fundamental aspects of the stability of magnetic skyrmions have been studied with atomistic spin simulations based on an extended Heisenberg model parameterised by *first-principles* calculations in the ultrathin film system Pd/Fe/Ir(111). The atomistic model contains exchange interaction beyond nearest neighbours, Dzyaloshinskii-Moriya interaction, magnetocrystalline anisotropy and the Zeeman interaction.

The minimum energy paths of skyrmion creation and annihilation are calculated with the geodesic nudged elastic band method. By comparison of the fully parameterised model with an effective nearest neighbour approximation of exchange interaction it is shown, how exchange frustration can enhance the energy barriers of metastable skyrmions and antiskyrmions, improving their stability against a collapse into the ferromagnetic state.

The prefactor in the Arrhenius-law for skyrmion collapse is calculated within transition state theory and is demonstrated to be strongly affected by external magnetic fields and system parameters. By decomposing the prefactor, localised low-energy eigenmodes of the skyrmion state are identified to be responsible for this effect.

A novel skyrmion transition mechanism is predicted by the atomistic spin simulations and confirmed by comparison to recent experimental measurements. The energy barrier and prefactor of this mechanism, coined the chimera transition mechanism, is analysed and compared to the conventional radial symmetric collapse mechanism.

For this purpose, the mode following method is introduced. It allows the analysis of low-energy eigenmodes beyond the harmonic and Goldstone mode approximation and the calculation of skyrmion and antiskyrmion lifetimes in temperature regimes and via transition mechanisms not accessible previously.

Zusammenfassung

Grundlegende Aspekte der Stabilität von magnetischen Skyrmionen werden mit atomistischen Spinsimulationen im Ultradünnschichtsystem Pd/Fe/Ir(111) auf der Basis eines erweiterten Heisenbergmodells untersucht. Das Modell wird durch *first-principles* Methoden parametrisiert und berücksichtigt die Austauschwechselwirkung über nächste Nachbarn hinaus, die Dzyaloshinskii-Moriya Wechselwirkung, die magnetokristalline Anisotropie und die Zeeman Wechselwirkung.

Die Pfade minimaler Energie zur Erzeugung und Vernichtung von Skyrmionen und Antiskyrmionen werden mithilfe der *geodesic nudged elasic band* Methode berechnet. Durch den Vergleich mit einer effektiven Nächstenachbarnäherung der Austauschwechselwirkung wird gezeigt, wie Austauschfrustration die Energiebarrieren von metastabilen Skyrmionen und Antiskyrmionen und damit ihre Stabilität gegenüber dem Kollapse in den ferromagnetischen Zustand erhöht.

Der Vorfaktor eines Arrhenius-Gesetzes für den Skyrmionkollapse wird innerhalb der *transition state theory* berechnet, was eine starke Abhängigkeit des Vorfaktors von der Magnetfeldstärke und der Wechselwirkungsparameter offenbart. Durch Zerlegung des Vorfaktors in seine Bestandteile werden lokalisierte, niederenergetische Eigenmoden des Skyrmionzustandes als Ursache für diese Effekte identifiziert.

Der Chimeraübergang, ein neuer Mechanismus zur Skyrmionvernichtung, wird mit atomistischen Spinsimulationen vorhergesagt und durch den Vergleich mit experimentellen Messungen bestätigt. Die Energiebarrieren und Vorfaktoren des Chimeraübergangs werden analysiert und mit dem konventionellen, radialsymmetrischen Kollapsemechanismus verglichen.

Für diesen Zweck wird die *mode following* Methode eingeführt. Sie erlaubt die Analyse der niederenergetischen Eigenmoden jenseits der harmonischen und Goldstonemoden Näherung, sowie die Berechnung von Skyrmionen- und Antiskyrmionenlebenszeiten in Temperaturbereichen und für Übergangsmechanismen, die zuvor nicht zugänglich waren.

List of Publications

I. S. von Malottki, B. Dupé, P. F. Bessarab, A. Delin & S. Heinze, *Enhanced skyrmion stability due to exchange frustration,* Scientific Reports **7,** 12299 (2017).

II. S. Haldar, S. von Malottki, S. Meyer, P. F. Bessarab & S. Heinze, *First-principles prediction of sub-10-nm skyrmions in Pd/Fe bilayers on Rh (111),* Physical Review B **98,** 060413 (2018).

III. M. Perini, S. Meyer, B. Dupé, S. von Malottki, A. Kubetzka, K. von Bergmann, R. Wiesendanger & S. Heinze, *Domain walls and Dzyaloshinskii-Moriya interaction in epitaxial Co/Ir (111) and Pt/Co/Ir (111),* Physical Review B **97,** 184425 (2018).

IV. U. Ritzmann, S. von Malottki, J.-V. Kim, S. Heinze, J. Sinova & B. Dupé, *Trochoidal motion and pair generation in skyrmion and antiskyrmion dynamics under spin–orbit torques,* Nature Electronics **1,** 451 (2018).

V. N. Romming, H. Pralow, A. Kubetzka, M. Hoffmann, S. von Malottki, S. Meyer, B. Dupé, R. Wiesendanger, K. von Bergmann & S. Heinze, *Competition of Dzyaloshinskii-Moriya and higher-order exchange interactions in Rh/Fe atomic bilayers on Ir (111),* Physical Review Letters **120,** 207201 (2018).

VI. A. S. Varentsova, M. N. Potkina, S. von Malottki, S. Heinze & P. F. Bessarab, *Interplay between size and stability of magnetic skyrmions,* Nanosystems: Physics, Chemistry, Mathematics **9,** 356–363 (2018).

VII. S. Meyer, M. Perini, S. von Malottki, A. Kubetzka, R. Wiesendanger, K. von Bergmann & S. Heinze, *Isolated zero field sub-10 nm skyrmions in ultrathin Co films,* Nature Communications **10,** 3823 (2019).

VIII. S. von Malottki, B. Dupé, P. F. Bessarab, A. Delin & S. Heinze, *Author Correction: Enhanced skyrmion stability due to exchange frustration,* Scientific Reports **9,** 8158 (2019).

IX. S. von Malottki, P. F. Bessarab, S. Haldar, A. Delin & S. Heinze, *Skyrmion lifetime in ultrathin films,* Physical Review B **99,** 060409 (2019).

X. S. Paul, S. Haldar, S. von Malottki & S. Heinze, *Role of higher-order exchange interactions for skyrmion stability,* Nature Communications **11,** 4756 (2020).

XI. F. Muckel, S. von Malottki, C. Holl, B. Pestka, M. Pratzer, P. F. Bessarab, S. Heinze & M. Morgenstern, *Experimental identification of two distinct skyrmion collapse mechanisms,* Nature Physics **17,** 395–402 (2021).

XII. A. S. Varentcova, S. von Malottki, M. N. Potkina, G. Kwiatkowski, S. Heinze & P. F. Bessarab, *Towards room temperature nanoscale skyrmions in ultrathin films,* NPJ Computational Materials **6,** 193 (2020).

Manuscripts in preparation:

XIII. M. A. Goerzen, S. von Malottki, P. F. Bessarab & S. Heinze, *Electric field switching of magnetic skyrmions,* in preparation (2020).

XIV. M. A. Goerzen, S. von Malottki, S. Meyer, P. F. Bessarab & S. Heinze, *Lifetime of skyrmions and antiskyrmions in the ultrathin film system Rh/Co/Ir(111),* in preparation (2020).

XV. H. Schrautzer, S. von Malottki, P. F. Bessarab & S. Heinze, *Skyrmion lifetimes in ultrathin multilayer systems,* in preparation (2020).

XVI. S. von Malottki, M. Goerzen, P. F. Bessarab & S. Heinze, *Application of the mode-following method to magnetic skyrmions in ultrathin films,* in preparation (2020).

Contents

1. Introduction

The investigation of magnetic skyrmions is a rapidly advancing field of research in nanomagnetism and spintronics [1–4]. The concept of solitons occurring as stable solutions in a non-linear field theory has originally been introduced by Tony Skyrme in high energy physics [5], but has been transferred to magnetism in the 1990s [6, 7].

In magnetic materials with conventional exchange interaction [8] and magnetocrystalline anisotropy [9], which typically favour collinear magnetic states, small magnetic whirls called skyrmions were predicted to be stabilised by the Dzyaloshinskii-Moriya interaction (DMI) [10, 11]. This chiral interaction is mediated by strong spin-orbit coupling (SOC) and occurs in materials with broken inversion symmetry [12]. Due to its symmetry, it favours chiral, non-collinear structures such as chiral domain walls [III, 13] or chiral spin spirals [14].

As a consequence of their constant winding direction, magnetic skyrmions carry a topological charge connecting them to the flourishing field of topological physics, recently awarded with a Nobel prize [15]. In a continuum model of the magnetisation, this topological charge makes the unwinding of a skyrmion impossible without breaking up the magnetic structure abruptly, similar to a twist in a ribbon [16]. While this topological protection does not, strictly speaking, apply in the discrete model of an atomistic lattice [16], magnetic states with energetically unfavourable large angles between adjacent magnetic moments still have to be overcome in order to annihilate a skyrmion [I].

The first magnetic skyrmions were observed 2009 in MnSi, a cubic B20 compound with broken inversion symmetry [17]. For small temperatures and an additionally applied magnetic field, a skyrmion lattice phase between the conical spin spiral and field-polarised phases was revealed via small angle neutron scattering (SANS). This observation initialised numerous studies of skyrmion-hosting chiral bulk materials using SANS [18] and Lorentz transmission electron microscopy (LTEM) [19].

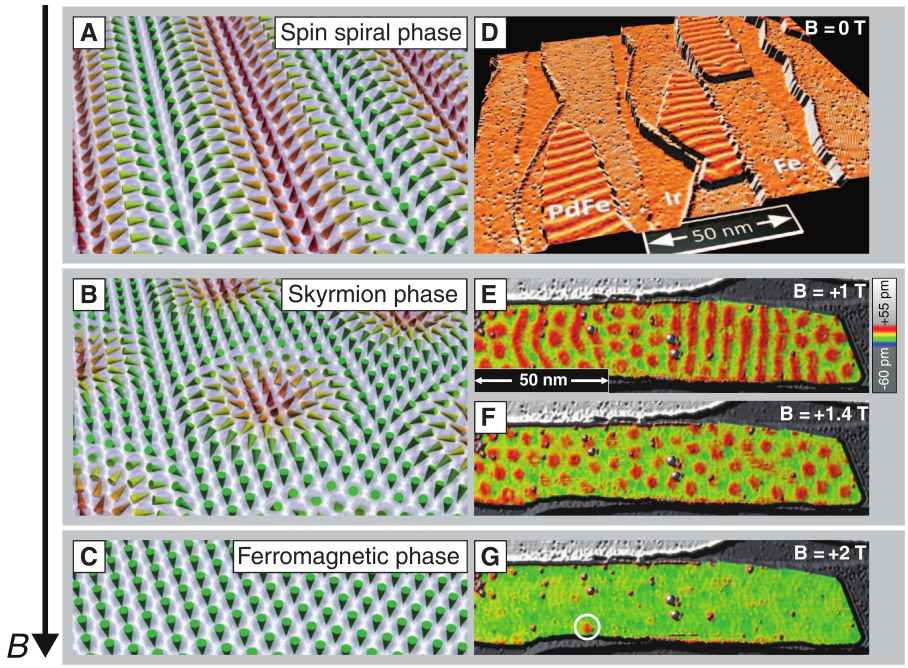

Figure 1.1 | Magnetic field dependent spin-polarised scanning tunneling microscopy (SP-STM) measurement of Pd/Fe/Ir(111). a)-c) Sketches of the magnetic structures. **d)** Overview of the sample measured by SP-STM in constant current mode without external magnetic field. **e)** SP-STM image of an Pd/Fe bilayer showing spin spirals and skyrmions coexisting with applied out-of-plane magnetic field of $B = 1$ T. **f)** Measurement of the skyrmion lattice phase. **g)** Field-polarised (ferromagnetic) phase with a remaining skyrmion highlighted by a white circle. The measurements are performed at $T = 8$ K. Figure reprinted from [20] with permission of AAAS.

In ultrathin magnetic films, skyrmions were initially observed in a monoatomic layer of Fe grown pseudomorphically on Ir(111) [21]. In combination with density functional theory (DFT) calculations, a nanoskyrmion lattice was identified as the magnetic ground state of the system. The magnetic surface structure was recorded with atomic resolution, first via spin-polarised scanning tunneling microscopy (SP-STM) [21] and later via magnetic exchange force microscopy (MExFM) [22]. The DFT calculations explained the low-temperature stability of the extremely small skyrmions of just a few atoms in size by the interplay of DMI and 4-spin interaction [21], a form of higher-order exchange interaction [23].

It has been shown, that the DMI of this system is induced by the Fe/Ir interface due to the large SOC of the heavy Ir atoms [21, 24]. By adding a Pd toplayer to the system, the exchange interaction of the Fe can be modified [24] such, that a spin

spiral ground state is formed [20]. The SP-STM measurements displayed in Fig. 1.1 show, that the spin spirals can be broken up with an external magnetic field, giving rise to a skyrmion lattice phase. For higher magnetic fields, the magnetic structure becomes field-polarised (ferromagnetic) except for single skyrmions with diameters about 6-7 nm remaining at defect locations.

The ability to tune magnetic interactions by varying the material of the magnetic film [III, 20, 25, 26], its thickness [27–29], the substrate [II, 26, 30–32], the toplayers [III, 20, 24] and the degree of intermixing [31, 33] makes ultrathin film systems promising for the understanding and optimisation of skyrmion properties. Furthermore, it has been demonstrated, that isolated skyrmions in ultrathin films can be stabilised with vanishing anisotropy [II, 34] and at zero fields [VII].

While skyrmions in ultrathin film systems have so far only been observed at low temperatures, the repetitive stacking of ultrathin films to multilayer systems, which combines the tuning capability of interfaces with the stabilisation effect of more magnetic material, has led to the discovery of room temperature skyrmions [35–38]. Moreover, antiskyrmions [39, 40], which exhibit an inverse topological charge and are part of a predicted zoo of skyrmionic structures [41, 42], as well as skyrmions in antiferromagnetic [43] and ferrimagnetic [44, 45] materials have been found.

It has been demonstrated, that skyrmions can be moved across magnetic layers with electrical currents via spin-transfer torques [35, 46–49], spin-Hall effects [48–50] and spin-orbit-torques [IV, 51, 52]. Moreover, applied currents can be used to create and annihilate skyrmions [IV, 35, 44, 47, 51–54], while reliable writing and deleting of individual skyrmions has been achieved repeatedly by applying voltages between the sample and the tip of a STM [20, 27].

Due to their versatile properties, magnetic skyrmions are seen as particular promising for future applications. Many skyrmion-based devices have been proposed [4], such as logical devices [55], magnetic reshuffler for probabilistic computing [56, 57], neural networks [58] and the racetrack-memory [49, 59–61]. In the latter, skyrmions are used as information carriers as illustrated in Fig. 1.2. Instead of moving the magnetic material itself, skyrmions in a racetrack device are moved over the magnetic surface by electrical currents, encoding information by their presence and absence below a reading head.

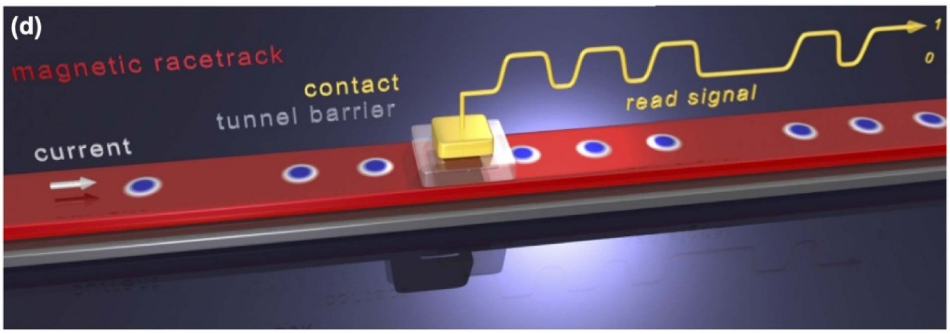

Figure 1.2 | Illustration of a skyrmion-based racetrack memory device. The ferromagnetic top-layer (red) of a stripe of an ultrathin film system carries information by the presence or absence of magnetic skyrmions (blue), which are moved over the surface by applied currents. A read/write-head (yellow) can detect magnetic skyrmions e. g. by the non-collinear magnetoresistance (NCMR) effect and write or delete them by applied electric fields and tunnel currents. Figure reprinted from [1] with permission. The figure is an adapted version of the original figure from [62]. John Wiley & Sons. ©2017 WILEY-VCH Verlag GmbH & Co. KGaA, Weinheim.

Despite the impressive progress made over the past decade, many obstacles towards skyrmion devices remain, such as the uncontrolled pinning at defects and unwanted drifts due to Hall effects, which hinder a more deterministic and efficient movement of skyrmions [1, 63]. Especially problematic is the counteracting behaviour of skyrmion size and thermal stability [VI]. While several ultrathin film systems have been found to host sub-10 nm skyrmions at low temperatures [VII, 20, 21, 34], room temperatures skyrmions with diameters ranging from 30 nm to several μm have been reported [36–39, 43, 45, 53, 54, 64].

However, skyrmion size and stability are not inseparably linked [VI], and besides the originally proposed energetic stabilisation via DMI, other effects such as exchange frustration [I, 65], higher-order exchange [X, 21] and entropic barriers [IX, 66, 67] enable for the simultaneous tuning of both properties. A thoroughly analysis of the magnetic interactions and the complex effects stabilising magnetic skyrmions is required in order to accurately describe, predict and design skyrmion properties in future materials.

Magnetic skyrmions in ultrathin film and multilayer systems are typically too complex for a consequent quantum mechanical treatment. Instead, a sophisticated multiscale approach can be applied, in which the quantum mechanical nature of the material dependent magnetic interactions and the formation of complex magnetic structures

beyond the ground state configuration are investigated separately [68, 69]. This is made possible by the separation of timescales for the dynamics of magnetic moments and the much faster dynamics of electrons [69].

The electronic structure is often calculated in the framework of DFT [70, 71], a well-established *first-principles* theory applied throughout condensed matter physics. It has been successfully applied to magnetic film systems in general [14, 29, 72, 73] and skyrmion-hosting systems in particular [VII, 1, 21, 24].

In the second part of the multiscale approach, magnetic structures of a much larger scale are investigated by using a model Hamiltonian of the magnetic interaction, parameterised by DFT-calculated energies of reference states. In the commonly applied micromagnetic model, a continuous and slowly changing magnetisation of the magnetic layers is assumed. The continuous form of the magnetisation allows for a numerical scaling in order to simulate large systems as well as for analytical solutions.

In contrast, the atomistic model describes the magnetisation as a discrete lattice of localised magnetic moments, which agrees well with the found localised moments in magnetic insulators and 3d-transition metals [69]. The atomistic model is not restricted to small angles between the moments, which is particular important for studying small skyrmionic structures [I]. Further, it naturally allows for taking exchange interactions beyond nearest neighbour into account, which includes exchange frustration effects.

Model Hamiltonians can be applied to several simulation techniques. Commonly used for the investigation of skyrmions are Monte Carlo [24, 74–78] and spin dynamics [24, 79–82] simulations. In the former case, random fluctuations of the magnetic structure are sampled and accepted on the basis of a Boltzmann-factor, while in spin dynamics, the equation of motion of magnetic moments is integrated numerically.

Both methods are applied for the energetic relaxation of magnetic structures, giving access to static properties such as size and profiles of skyrmions and the possibility to create low-temperature phase diagrams [I, 24, 74–78, 81, 82]. By modelling spin-transfer torques or applying external fields, spin dynamics simulations are a commonly used tool to study dynamical properties of skyrmions such as mobility [IV, 48, 51, 83], excitation of eigenmodes [84], dynamical creation [IV, 44, 52, 85] and defect interaction [35, 48, 83].

While Monte Carlo algorithms can be applied immediately to study the thermal stability of skyrmions, spin dynamics algorithms have to be extended with thermal fluctuations of the effective field, giving rise to Langevin-dynamics [86]. Monte Carlo simulations based on parameters fitted to experimental data suggested, that the thermal stability of skyrmions in Pd/Fe/Ir(111) is affected by entropy [77], while Langevin-dynamics simulations were successfully applied to study the dynamics of thermally induced collapses of short-lived skyrmions [86].

Both approaches are limited to conditions in which magnetic transitions are fast enough to enable sufficient statistics in a feasible simulation time [86]. One way to overcome this limitation is the development of more sophisticated algorithms, such as the parallel tempering Monte Carlo method [87, 88] or the forward-flux sampling method [89]. Another possibility is the application of purely statistical approaches such as the transition state theory (TST) [90] or Langer's theory [67].

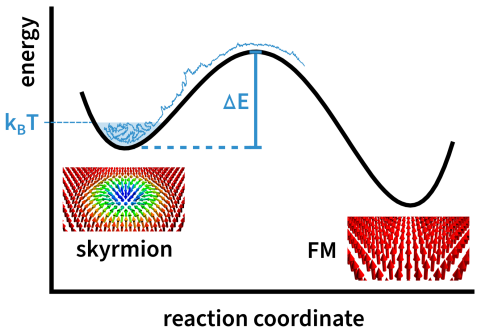

Figure 1.3 | Illustration of a thermal transition of a metastable skyrmion into the ferromagnetic state. The isolated skyrmion and the ferromagnetic (FM) state are separated by a finite energy barrier, ΔE. The system in the initial skyrmion state is thermally activated and as a rare event overcomes the energy barrier after the average time τ. Figure inspired by [91].

In the framework of these related theories, the thermal stability of metastable states is described by an Arrhenius law, yielding the mean lifetime, τ, or its inverse, the mean transition rate, ν [67, 90]:

$$\nu = \nu_0 \exp\left(-\beta \Delta E\right). \tag{1.1}$$

Here, $\beta = 1/\left(k_\mathrm{B} T\right)$ is the inverse of the thermal energy and ΔE the energy barrier of the transition, as it is illustrated in Fig. 1.3. The prefactor, ν_0, contains entropic and dynamic contributions of the transition process. In order to determine transition rates via Eq. 1.1, information about the reaction process is required.

The reaction process and the energy barrier, ΔE, is typically defined by the minimum energy path (MEP), which can be determined via the nudged elastic band (NEB)

method. With a micromagnetic model, NEB has already been applied to magnetic switching processes in the past [92, 93]. More recently, by applying the geodesic nudged elastic band (GNEB) method [94], a version of NEB optimised for atomistic magnetic lattice systems, the radial symmetric mechanism of skyrmion collapse has been discovered theoretically [94, 95].

It was commonly believed, that the transition rate of skyrmion collapse (Eq. 1.1) is exclusively dominated by the energy barrier, while the contribution of the prefactor was neglected [96]. In contrast to these believes, recent measurements of skyrmion lifetimes in the B20 system $Fe_{0.5}/Co_{0.5}/Si$ showed a decrease of skyrmion lifetimes by more than 30 orders of magnitude over a small variation of magnetic fields [66]. This large variation was attributed to the prefactor of an Arrhenius-law due to entropy effects, whose microscopic origin remained unclear at that point.

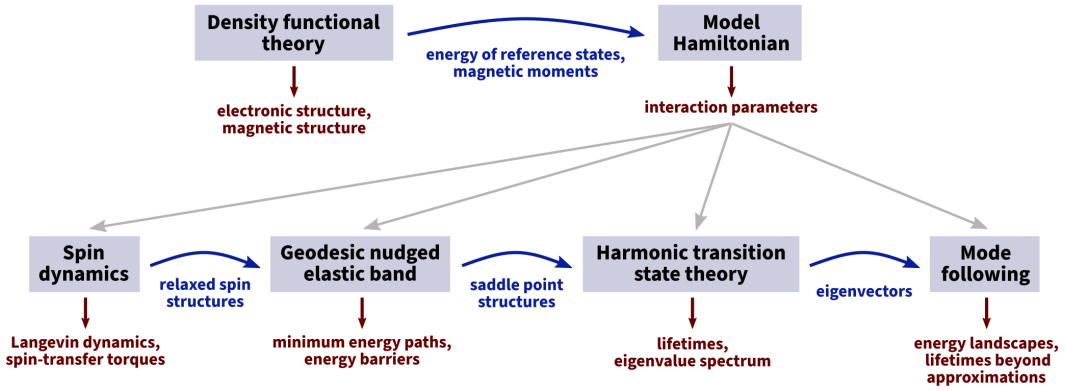

Figure 1.4 | Overview of the theoretical multiscale approach for the calculation of skyrmion lifetimes. In a first step, the electronic and magnetic structure of a system is determined by DFT calculations. The energies of reference states such as spin spirals are then fitted by the parameters of an extended Heisenberg model. The parameters determine the strength of magnetic interactions and are applied to the algorithms of atomistic spin simulations shown in the lower row. In order to determine skyrmion lifetimes, isolated skyrmions are energetically minimised via spin dynamics. Subsequently, the minimum energy path between the skyrmion and the ferromagnetic state is determined by geodesic nudged elastic band method calculations, resulting in the saddle point and energy barrier of the annihilation process. The prefactor of an Arrhenius law can be calculated via harmonic transition state theory, which requires approximations of the energy landscape along the skyrmion and saddle point states. In order to obtain more accurate energy landscapes of particular eigenmodes, the mode following method can be applied, which can improve the accuracy of the calculated lifetimes.

In this thesis, the stability of magnetic skyrmions in ultrathin films is investigated. Ultrathin film systems are well-suited for the understanding of the fundamental principles forming magnetic structures due to the clean surfaces produced by epitaxial

growth allowing for the direct comparison of theoretical results with experimental measurements [III, 21]. Subsequently, these principles can be transferred to sputtered multilayer systems in order to design competitive spintronic devices [24, 82].

The applied theoretical approach is illustrated in Fig. 1.4. It consists of an atomistic model Hamiltonian, which is parameterised by DFT calculations and applied to a combination of atomistic spin simulation algorithms. For the calculation of skyrmion lifetimes, spin dynamics simulations are used in a first step for the relaxation of magnetic structures into adjacent local energy minima. Subsequently, the minimum energy paths between different energy minima can be found by GNEB calculations, providing information about the transition mechanisms and the energy barriers between the states. Within TST, the entropic and dynamic contributions entering the prefactor of the transition can be determined. Finally, the mode following method developed in this thesis can improve the description of individual eigenmodes in order to increase the accuracy of the TST.

This theoretical approach has proven to be a capable tool to predict the magnetic properties of ultrathin film systems from *first-principles* [I, II, VII]. The results presented in this work, however, are focused on the stability of skyrmions in Pd/Fe/-Ir(111), a theoretically [I, IX, 24, 42, 78, 82, 97] and experimentally [XI, 20, 77, 81, 98] well-understood model system, allowing for the disentanglement of fundamental aspects of skyrmion stability.

For this purpose, first the extended Heisenberg model is introduced in Chap. 2, which describes the magnetic interaction of a lattice system in atomistic approximation. In Chap. 4, it is shown how the parameters of the extended Heisenberg model can be obtained by fits to DFT-calculated spin spiral dispersion curves. Magnetic structures and their properties relevant for this thesis are discussed in Chap. 3. In Chap. 5, the theoretical foundations of the atomistic simulation algorithms shown in Fig. 1.4 are introduced.

The early calculations of the MEP of skyrmion collapse relied on effective nearest neighbour approximations of the exchange interaction [86, 94, 95]. In contrast, the parameterisation of the extended Heisenberg model by DFT provides information about the exchange interaction beyond nearest neighbours and therefore takes exchange frustration effects into account. In Chap. 6, these two models of exchange interaction are compared in low-temperature phase diagrams and the properties of relaxed isolated skyrmions and antiskyrmions. A comparison of the energy barriers

for radial skyrmion collapse obtained by GNEB calculations with both models demonstrates a strong enhancement of skyrmion and antiskyrmion stability due to exchange frustration.

A systematic study of the prefactor of skyrmion collapse presented in Chap. 7 shows, that the energy barrier alone is not sufficient to predict the average lifetime of metastable skyrmions. A large entropy effect is found, changing the lifetime of skyrmions Pd/Fe/Ir(111) by more than seven orders of magnitude with varying external magnetic field and stacking-order of the Pd toplayer. The decomposition of the prefactor and the analysis of the eigenspectra of the relevant states reveals that a small number of localised skyrmion eigenmodes strongly affected by the skyrmion size and the interaction parameters is responsible for this effect.

In the course of this thesis, the chimera transition mechanism of skyrmion annihilation has been discovered in Pd/Fe/Ir(111). It has been published for the ultrathin film system Rh/Co/Ir(111) [VII] and has been reported independently in [99]. In Chap. 8, this novel mechanism is introduced and compared to the radial symmetric collapse mechanism on the example of skyrmion annihilation in Pd/Fe/Ir(111).

In literature, the mechanisms of skyrmion annihilation and creation have been studied exclusively theoretically up to this point [I, II, VII, IX, 67, 89, 90, 95, 99]. In cooperation with the experimental group of Prof. Markus Morgenstern it was possible to identify both the radial and the chimera mechanism of skyrmion collapse for the first time experimentally [XI]. The results of this study are presented in Chap. 9.

The calculation of the prefactor of some transition mechanisms such as antiskyrmion collapse or the chimera transition mechanism is challenging due to the occurrence of eigenmodes which cannot be described in the common harmonic and Goldstone mode approximations [XI, 89, 99]. In order to enable the calculation of these eigenmodes, the mode following method has been developed. It allows for a numerical determination of the entropy contribution of individual eigenmodes as well as the evaluation of the quality of the harmonic and Goldstone mode approximations. Results of its application to skyrmion transitions in Pd/Fe/Ir(111) are shown in Chap. 10. Ultimately, the thesis is concluded in Chap. 11.

2. Extended Heisenberg model

The magnetic structure of an atomic lattice emerges due to the Coulomb-interaction and the quantum mechanical nature of the electrons. In seeking a more systematic insight into the origin of these structures, however, the quantum mechanical interactions of the electrons are often mapped on, both, quantum mechanical and semi-classical model-Hamiltonians. Since no simple, single theory exists to describe the rich phenomena of magnetic materials sufficiently, a variety of different Hamiltonians is applied to the existing material systems [100]. For transition metals, often the extended Heisenberg model is considered. It consists of the Heisenberg exchange, the magnetocrystalline anisotropy and additional, system dependent terms. In this chapter, the magnetic interactions relevant for the investigations presented in this work are introduced.

2.1. Atomistic model for 3d-transition metals

Similar to classical electrodynamics, the origin of magnetic moments in solid-states lies in the angular momentum of charge carriers. Crystal lattices consist of atom cores and their orbiting electrons, yielding three sources of angular momentum: The orbital momentum of the electrons, the electronic spin and the nuclear spin [100]. With the definition of the Bohr magneton [100],

$$\begin{aligned} \mu_{\mathrm{B}} &= \frac{e\hbar}{2m_e} \\ &\approx 5.788 \cdot 10^{-5} \ \frac{eV}{T}, \end{aligned} \tag{2.1}$$

where e is the elemental charge, $\hbar$ the reduced Planck constant and m_e the electronic mass, the magnetic moment of the total electron orbital momentum $\mathbf{L}$ reads [100]

$$\mathbf{m}_{\mathrm{L}} = -\frac{\mu_{\mathrm{B}}}{\hbar}\mathbf{L}. \tag{2.2}$$

Analogously, the magnetic moment of the total electron spin $\mathbf{S}$ is given by [100]

$$\mathbf{m}_{\mathrm{S}} = -\frac{g_e\mu_{\mathrm{B}}}{\hbar}\mathbf{S}, \tag{2.3}$$

with g_e being the Landé-factor, which is defined as [100]

$$\begin{aligned} g_e &= 2\left(1 + \frac{\alpha}{2\pi} + \mathcal{O}\left(\alpha^2\right)\right) \\ &\approx 2.0023. \end{aligned} \tag{2.4}$$

Here, the appearing expansion factor α is the Sommerfeld constant. The magnetic moment caused by the total nuclear spin $\mathbf{I}$ reads [100]

$$\mathbf{m}_{\mathrm{N}} = -\frac{g_N\mu_{\mathrm{N}}}{\hbar}\mathbf{I}, \tag{2.5}$$

with g_N being the nuclear Landé factor and μ_N the nuclear magneton [100], which is defined similar to the Bohr magneton:

$$\mu_{\mathrm{N}} = \frac{e\hbar}{2m_p}. \tag{2.6}$$

Since the proton mass m_p is much larger than m_e, the nuclear magneton is smaller than the Bohr magneton with $\mu_{\mathrm{N}} \approx 10^{-3}\mu_{\mathrm{B}}$ [100]. Therefore, the magnetism of the nuclear spins, which is responsible for the hyperfine structure, can be neglected for the investigation of magnetic textures in transition metals. The remaining magnetic moments of electronic orbital momentum and electronic spin can be on the same order of magnitude and depend essentially on the electronic structure of the investigated system.

The electronic structure of isolated atoms is defined by the occupied atomic orbitals and their corresponding quantum numbers, which are described by Hund's rules and modified by spin-orbit coupling (SOC) [69]. The atom shows a net magnetic moment when the electronic structure exhibits a net angular momentum due to unpaired spins or orbital momenta [100, 101].

In condensed matter, however, predicting the electronic configuration is more complicated. The crystal field of the surrounding atoms is lifting the rotational symmetry, leading to a splitting of the atomic orbitals [100]. Furthermore, orbitals are hybridising, creating bonding and antibonding orbitals to adjacent atoms and changing the electronic structure substantially. In metals, the overlapping of the orbitals creates a band structure. Depending on the bonding partners, the coordination number and the lattice symmetry, the same element can exhibit multiple electronic configurations and magnetic properties [102].

3d-transition metals are defined by partially filled 3d sub-shells [103], which can give rise to unpaired electronic spins and strong spin magnetism. The atomic orbital moments of the typical magnetic 3d-transition metals Fe, Co and Ni, on the other hand, are often quenched due to crystal symmetry [69]. While this symmetry can be partially lifted by SOC, the orbital magnetic moments of materials based on these elements are often negligible [69]. In ultrathin film systems, the size of magnetic moments additionally depends on the material interfaces due to hybridisation effects of adjacent layers [102].

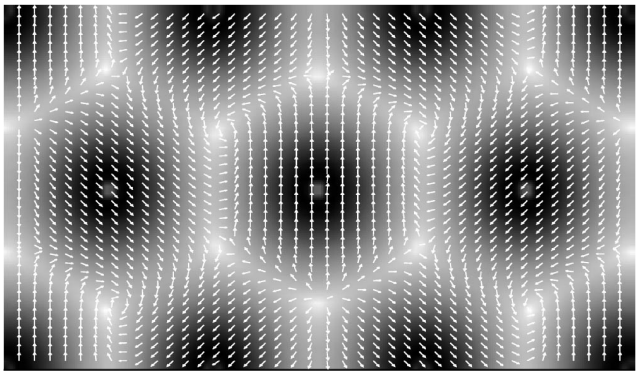

Figure 2.1 | Magnetisation density of the Néel state in an unsupported monolayer of Cr obtained by DFT. Each hexagon contains a Cr atom at its centre. High and low magnetisation densities are indicated by a dark and bright contrast, respectively, while the orientation of the local magnetisation is displayed by arrows. Figure reprinted from [73] with permission of APS physics.

While it is possible, that multiple electrons of a 3d-transition metal exhibit unpaired magnetic moments, it is common to sum up these contributions to a total magnetic moment, localised at the centre of the atom. This atomistic magnetic model is supported by density functional theory (DFT) calculations, revealing a strong concentration of the magnetic moment contributions at the atom cores [69, 73, 104].

As an example, the magnetisation density of the non-collinear Néel state in an unsupported Cr monolayer is shown in Fig. 2.1. Most of the magnetisation density of a unit cell is aligned parallel and localised near the Cr nucleus, which allows for

the atomistic approximation by integrating the local magnetisation density $\mathbf{m}(\mathbf{r})$ over the unit cell volume [69, 73, 104]:

$$\mathbf{M}_i = \int_{\mathrm{uc}} \mathbf{m}(\mathbf{r})\, \mathrm{d}\mathbf{r}. \tag{2.7}$$

The total magnetic moment at the lattice site i is denoted by the vector $\mathbf{M}_i$, but often the normalised and dimensionless vector

$$\mathbf{m}_i = \frac{\mathbf{M}_i}{\mu_i} \tag{2.8}$$

is used, which describes the orientation of the moment. The magnitude of the moment is denoted by $\mu_i = |\mathbf{M}_i|$ and typically given in units of μ_{B}. Finally, the interaction of the atomic magnetic moments can give rise to collective magnetism phenomena, such as ferromagnetism, spin spiral structures or magnetic skyrmions.

2.2. Exchange interaction

While collective magnetism has already been described as a phenomenological result of coupling between magnetic moments in 1907 by Weiss [105], the physical origin of collective magnetism remained hidden until the quantum mechanical interaction between magnetic moments was reported by Heisenberg in 1928 [8]. This Heisenberg exchange interaction is based on the direct exchange of electrons due to overlapping orbitals, which is often introduced on the example of the hydrogen molecule in the Heitler-London model [106]. By assuming an atomic lattice of N magnetic moments and pure spin magnetism, the Hamilton operator of the exchange energy reads [100, 107]

$$\hat{E}_{\mathrm{exch}}^{\mathrm{direct}} = -\sum_{\langle i,j \rangle}^{N} J_{ij} \left(\hat{s}_i \cdot \hat{s}_j \right), \tag{2.9}$$

where J_{ij} is a coupling constant describing the strength and sign of the interaction for pairs of neighbouring atoms, $\langle i, j \rangle$. Here, the operators $\hat{s}_i$ and $\hat{s}_j$ correspond to the orientation of the total spins of the atoms i and j, while the magnitudes of the spins are absorbed in the parameter J_{ij}.

In seeking a quasi-classical model to perform atomistic simulations, the spin-operators are commonly replaced by classical, $3D$ vectors, justified by the long-range coupling

of many atomic moments giving rise to a quasi-continuum of allowed quantization axes. As already mentioned, atomic magnetic moments in $3d$-metals often stem from several electrons, resulting in total magnetic moments with non-integer values of μ_B [102]. In the atomistic approximation, in which the individual contributions of the electrons are summed up to a total magnetic moment, localised at the atom core, the quasi-classical Heisenberg exchange interaction reads [100]

$$E_\mathrm{exch}^\mathrm{direct} = -\sum_{\langle i,j \rangle}^{N} J_{ij} \left(\mathbf{m}_i \cdot \mathbf{m}_j \right). \tag{2.10}$$

This form of the exchange interaction is well-suited for magnetic insulators and transition metal oxides whose net magnetic moment are carried by strongly localised $4f$- and $3d$-electrons [100, 101]. In pure $3d$-transition metals, on the other hand, the magnetic moments of the $3d$-electrons show a higher mobility, giving rise to itinerant magnetism [100]. In this case, the exchange interaction can be described in a multiband Hubbard-model, a tight binding approach considering the hopping of several magnetic electrons that contribute to the total magnetic moment of an atom [101, 108]. In Fig. 2.2, a scheme of a multiband-Hubbard model is illustrated.

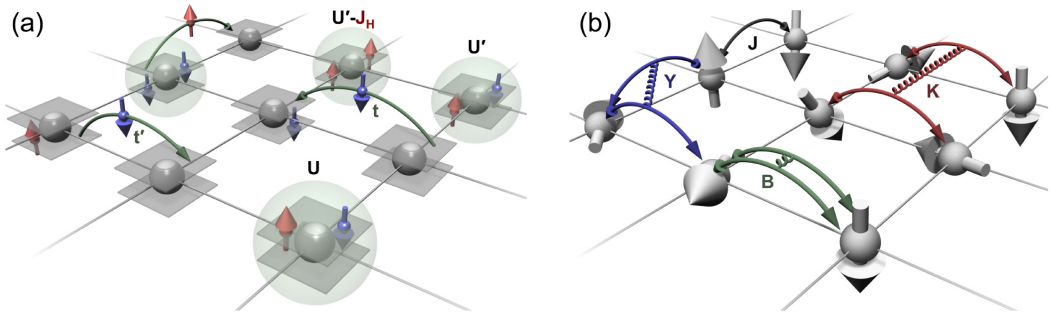

Figure 2.2 | Illustration of the multiband Hubbard model and the resulting exchange interactions in the atomistic model. a) Illustration of a two level Hubbard model, in which spin-up (red) and spin-down (blue) electrons hop between atoms (grey spheres), each with two orbitals (grey planes). The hopping parameters towards occupied and unoccupied atoms are denoted by t and t', respectively. **b)** Exchange interactions between the quasi-classical magnetic moments of the Heisenberg model (grey arrows) are denoted by coloured arrows: Direct exchange (black), biquadratic exchange (green), three-site-four-spin (blue) and four-site-four-spin (red) interaction. Figure reprinted from [108] with permission of APS physics.

In the case of half-filled bands, the mobility of electrons is limited and the Hubbard model can be expanded in orders of exchange interaction [100, 108]. The first

expansion term resembles the Heisenberg exchange interaction of Eq. 2.9, although it was originally formulated for the exchange of localised electrons. For this reason, the higher-order exchange interactions (HOI) can be interpreted as correction terms due to electron correlation effects occurring from the itinerant nature of the $3d$-electrons. While HOI terms are not considered in this work, the corresponding quasi-classical Hamiltonians can be found e. g. in [X].

Another coupling mechanism beyond the direct nearest-neighbour exchange interaction can be attributed to the RKKY interaction, named after Rudermann and Kittel, who found a form indirect coupling for nuclear spins [109] and Kasuya and Yosida, who transferred this mechanism to purely electronic magnetism [110, 111]. The model of the RKKY interaction is based on the distinction of localised electrons in the inner shells of the atom, which give rise to a net magnetic moment of the atom and valence electrons, which do not contribute to the magnetic moment of the atom [100]. While it is impossible for the magnetic electrons of adjacent atoms to couple directly, each of them can overlap with the outer shells of the their respective atoms, causing a spin-polarisation of the valence electrons. In contrast to the inner, more localised electrons, the orbitals of valence electrons of different atoms can overlap, which gives rise to a indirect coupling mechanism of the magnetic electrons, mediated by the valence electron cloud.

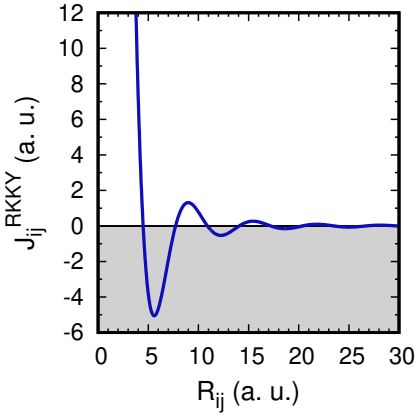

Figure 2.3 | Dependency of the RKKY interaction parameter from the inter-atomic distance. The parameter J_{ij}^{RKKY} of Eq. 2.11 is plotted over the inter-atomic distance, $\mathbf{R}_{ij}$, with $\bar{J}^2 = 1000$ and $2k_{\mathrm{F}} = 1$ in arbitrary units.

Formulated in second-order perturbation theory, the Hamilton operator of the RKKY exchange interaction reads [100]:

$$\widehat{E}_{\mathrm{RKKY}} = -\sum_{i \neq j} J_{ij}^{\mathrm{RKKY}} \left(\hat{s}_i \cdot \hat{s}_j \right) \tag{2.11}$$

The sum runs over all pairs of spins i and j in the lattice, with an exchange constant of [100]

$$J_{ij}^{\mathrm{RKKY}} = \bar{J}^2 F\left(2k_{\mathrm{F}} R_{ij}\right), \tag{2.12}$$

where k_{F} is the Fermi momentum and $\bar{J}$ is a material dependent coupling parameter. The function $F(x) = (\sin x - x\cos x)/x^4$ is oscillating with the inter-atomic distance R_{ij}, as displayed in Fig. 2.3. Due to this oscillation, some of the J_{ij} parameters can have opposite signs, leading to spin frustration effects.

Absorbing all material constants except the spin orientation into the exchange coupling parameters J_{ij} and applying the quasi-classical approximation, the RKKY interaction has a similar form to the direct Heisenberg exchange. However, due to the indirect coupling, the exchange interaction is not restricted to pairs of adjacent atoms. Formally combining the direct and indirect coupling mechanisms [107], the total exchange interaction beyond nearest neighbours reads:

$$E_{\mathrm{exch}} = -\sum_{i}^{N}\sum_{k}^{M} J_k \sum_{j}^{N_k} \left(\mathbf{m}_i \cdot \mathbf{m}_j\right). \tag{2.13}$$

On a perfect atomic lattice, the Hamiltonian is isotropic and gives rise to a shell structure of the exchange interaction, in which each shell, k, contains N_k atoms. The strength of the indirect interaction decays with $\mathbf{R}_{ij}$ at a system dependent rate. In bulk systems, this rate is $\propto x^{-3}$ [100], while it can be smaller for surface systems [112]. Due to the decay of the RKKY-interaction, only a finite number of shells has to be considered. For the hexagonal lattice, the first four shells corresponding to J_1-J_4 are illustrated in Fig. 2.4.

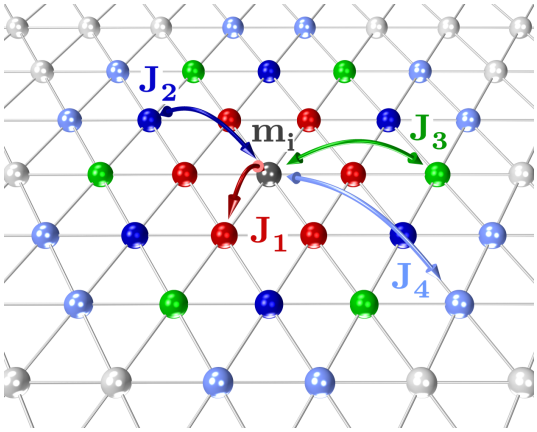

Figure 2.4 | Illustration of the shells of exchange interaction on a hexagonal lattice. Magnetic moments of the first four shells of neighbours with equal distance to the moment $\mathbf{m}_i$ are marked by the same colour. The exchange interactions of spins from these shells with the spin $\mathbf{m}_i$ are represented by the exchange parameters $J_1 - J_4$.

A positive sign of J_k leads to a parallel alignment of the magnetic moment i with the moments in the k-th shell, while a negative sign favours an antiparallel alignment. In Fig. 2.5, this is illustrated for positive (a) and negative (b) sign of the parameter of the nearest neighbour exchange interaction, J_1. Since the J_k not only decay with increasing distance of the interacting atoms but can also alternate in sign, some J_k favour a parallel and others an antiparallel alignment of magnetic moments [100]. This phenomenon is known as exchange frustration and can be partially lifted by the creation of spin spirals, the general solution of the Hamiltonian of Eq. 2.4 [104]. An example for a positive J_1 and negative J_2 is shown in Fig. 2.5 c.

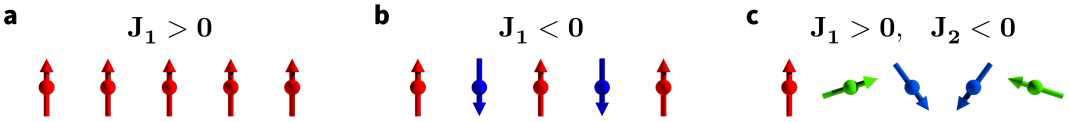

Figure 2.5 | Examples of 1D magnetic structures favoured by the exchange interaction. a) A parallel alignment energetically favoured by $J_1 > 0$. **b)** An antiparallel alignment driven by $J_1 < 0$. **c)** A spin spiral minimises the exchange frustration emerging from $J_1 > 0$ and $J_2 < 0$.

2.3. Magnetocrystalline anisotropy

The electronic structure of an atomic lattice is decisively affected by the crystal symmetry as electronic orbitals are oriented along specific crystal axes due to the emerging crystal field. While spin and real space are independent without SOC, the presence of SOC couples the orientation of the spins to the crystal symmetry.

The strength of this coupling depends crucially on the Fermi surface of the material as well as the strength of the SOC [69]. Since SOC is increasing with the charge of the atom core, heavy elements tend to yield stronger magnetocrystalline anisotropy energies (MAE) than light materials [69, 100, 101].

Ultrathin films of 3d-transition metals grown on heavy 5d-transition metals typically exhibit an uniaxial MAE symmetry with respect to the surface normal, while the energy differences of crystal axes in in-plane direction are often negligible [21, 24, 82]. This simple form of MAE can be expressed in second-order expansion, resulting

in [24, 69, 102]

$$E_{\text{ani}} = K \sum_{i}^{N} \left(\hat{\mathbf{n}} \cdot \mathbf{m}_i\right)^2 , \tag{2.14}$$

where $\hat{\mathbf{n}}$ represents the direction of the easy axis parallel to the surface normal.

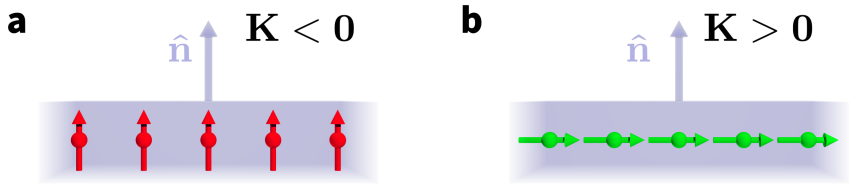

Figure 2.6 | Orientation of the surface magnetisation due to out-of-plane uniaxial anisotropy. a) A positive sign of K gives rise to an easy axis parallel to $\hat{\mathbf{n}}$, favouring the parallel and antiparallel alignment of the magnetisation with the surface normal. **b)** An easy plane arises for a negative K, yielding an orientation of the magnetisation perpendicular to $\hat{\mathbf{n}}$. Note, that the shown orientation of the magnetisation is just an example and that all orientations in the direction of the surface plane are energetically degenerate.

By convention, a negative sign of K denotes an energetically favourable orientation along the easy axis, $\hat{\mathbf{n}}$, as illustrated in Fig. 2.6 a. On the other hand, a positive value of K denotes an easy plane perpendicular to $\hat{\mathbf{n}}$, of which an example is visualised in Fig. 2.6 b. A large value of K results in a hard magnetic material, i. e. a material with a persistent orientation along a perpendicular axis, while a small value K gives rise to a soft magnetic material whose orientation can be easily manipulated.

2.4. Dzyaloshinskii-Moriya Interaction

The Dzyaloshinskii-Moriya interaction [10, 11] (DMI) between magnetic moments emerges when the inversion symmetry of a crystal is broken by nonmagnetic atoms with SOC. This is either the case in bulk magnets with non-centrosymmetric unit cells such as the B20 crystals [1, 17] or in ultrathin films, whose inversion symmetry is broken by the appearance of surfaces or interfaces [14].

By assuming a RKKY-like indirect coupling mechanism between localised magnetic moments, the orientation of the moments becomes connected to the real space arrangement of the atoms due to hopping of the conduction electrons to the nonmagnetic sites hosting strong SOC [12]. The lack of inversion symmetry lifts the isotropic

exchange of electrons, favouring one scattering sequence over another, which gives rise to the chiral character of the interaction [14].

A description of the RKKY-interaction mechanism with included SOC in first-order perturbation theory yields an energy splitting of [12, 113]

$$E_{\mathrm{DMI}} = -\sum_{i \neq j}^{N} \mathbf{D}_{ij} \cdot \left(\mathbf{m}_i \times \mathbf{m}_j \right), \tag{2.15}$$

where $\mathbf{D}_{ij}$ is the material dependent DMI vector controlling the sign and strength of the interaction. The orientation of the DMI vector is illustrated at the interface of an magnetic layer and a nonmagnetic substrate with strong SOC in Fig. 2.7.

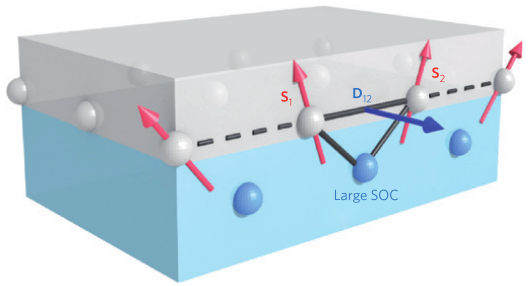

Figure 2.7 | Symmetry of the DMI vector in a magnetic surface layer placed on a substrate with strong SOC. A heavy atom of the substrate layer (blue) with strong SOC induces DMI between two magnetic surface atoms (grey) with the magnetic moments $\mathbf{s}_1$ and $\mathbf{s}_2$ (pink) above. The DMI vector $\mathbf{D}_{12}$ is oriented parallel to $(\mathbf{r}_1 \times \mathbf{r}_2)$. The vectors $\mathbf{r}_1$ and $\mathbf{r}_2$ are connecting the substrate atom with $\mathbf{s}_1$ and $\mathbf{s}_2$, respectively. Figure reprinted from [83] with permission of Springer Nature.

The DMI splitting increases with the angle between the magnetic moments with a maximum at 90°, stabilising non-collinear magnetic structures. Due to the cross product between the moments, which is illustrated in Fig. 2.8, one rotational sense is preferred over the other. The DMI vector is given due to the symmetry, leaving D_1 as parameter for the strength and chirality of the interaction. Per convention, a positive D_1 favours a right-rotating structure (Fig 2.8 a), while the opposite chirality is preferred by a negative value of D_1 (Fig. 2.8 b).

Since DMI is induced by indirect coupling of the RKKY-type, it is not limited to the interaction of nearest neighbours and similar shells of interactions can arise as described for the exchange interaction in Sec. 2.2. Moreover, higher-order DMI contributions have been proposed very recently [114–116], but are not taken into account in the extended Heisenberg model applied throughout this thesis.

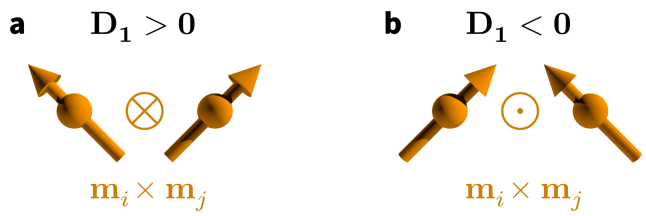

Figure 2.8 | The sign of the DMI parameter favours a particular rotational sense. The sign of D_1 controls whether the DMI vector points into or out of the paper layer. Since the alignment of the crossproduct $(\mathbf{m}_i \times \mathbf{m}_j)$ with the DMI vector is energetically favoured by Eq. 2.15, the DMI lifts the degeneracy between **(a)** and **(b)**, favouring one chirality over another. A positive value of D_1 yields an energy gain for right rotating magnetic moments **(a)**, while a negative value of D_1 favours a left rotating structure **(b)**.

2.5. Zeeman interaction

In the atomistic model, the Zeeman interaction of magnetic moments with an external magnetic field is simply described by [68, 82, 90]

$$E_{\text{Zee}} = -\sum_{i}^{N} \mu_i \left(\mathbf{B} \cdot \mathbf{m}_i\right). \tag{2.16}$$

The strength and orientation of external magnetic fields are often used as control parameter to directly manipulate magnetic textures and processes [17, 20, 77].

2.6. Dipole-dipole interaction

The classical dipole-dipole interaction between two adjacent magnetic moments is about four orders of magnitude weaker than the exchange interaction typically acting in magnetic materials [100]. However, the importance of this long-ranged interaction increases with the number of interacting magnetic moments in an atomic lattice. Especially, when they are aligned in a parallel fashion, the individual contributions add up to a decisive energy contribution which is e. g. responsible for the formation of magnetic domains in ferromagnetic materials.

In the atomistic model, the dipole-dipole-interaction straightforwardly reads [69]

$$E_{\text{dip}} = -\frac{\mu_0}{4\pi} \sum_{i \neq j}^{N} \frac{m_i m_j}{r_{ij}^3} \left[3 \left(\mathbf{m}_i \cdot \hat{\mathbf{r}}_{ij}\right) \left(\mathbf{m}_j \cdot \hat{\mathbf{r}}_{ij}\right) - \mathbf{m}_i \cdot \mathbf{m}_j\right]. \tag{2.17}$$

It increases with the size of interacting magnetic moments m_i and m_j and decays with the distance, r_{ij}, between them. μ_0 is the magnetic constant and the direction of the vector connecting both moments is given by $\hat{\mathbf{r}}_{ij}$, which links the real space positions to the orientations of the moments.

Due to the long range of the dipole-dipole interaction, its direct calculation via Eq. 2.17 is quickly computationally intensive with increasing system size. Hence, more sophisticated methods such as the fast Fourier transform are often applied in order to increase the computational efficiency of calculating this interaction [68, 95, 117, 118].

Analogously to the emergence of magnetic domains, dipole-dipole interaction can stabilise magnetic skyrmions by reducing the stray field of the ferromagnetic background [96]. In ultrathin surface films, however, the amount of magnetic material is rather small, diminishing the relevance of the dipole-dipole interaction. It has been demonstrated, that the dipole-dipole contribution to skyrmion stability in ferromagnetic monolayer systems with out-of-plane magnetisation can be modelled by a small reduction of the anisotropy constant, K, on the order of 0.1 meV/atom [95]. Therefore, no explicit dipole-dipole contribution has been considered for the atomistic simulations presented in this work.

3. Magnetic structures

Due to the collective magnetism of electrons, often described by model Hamiltonians such as the extended Heisenberg model introduced in Chap. 2, atomic magnetic moments can form a variety of magnetic structures. The emerging magnetic order is typically resilient up to the Curie temperature, a critical temperature above which the magnetic order is abolished by thermal fluctuations. In the following, magnetic structures that are important in the context of this work are presented.

3.1. Ferro- and antiferromagnetic states

An illustration of the parallel alignment of magnetic moments is displayed in Fig. 3.1 a. In the course of this work, this state is called ferromagnetic state (FM), even if it is not the groundstate but the field polarised phase. The parallel alignment is favoured by positive exchange parameters. Moreover, the moments are pointing in an energetically preferred direction, e. g. due to an uniaxial magnetocrystalline anisotropy or an external magnetic field.

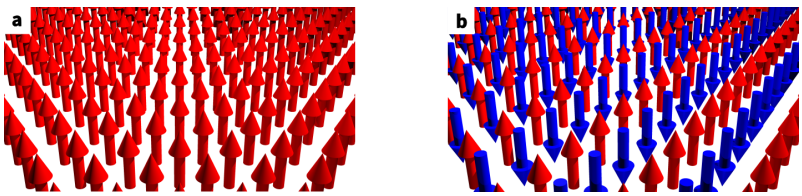

Figure 3.1 | Examples of the ferromagnetic and antiferromagnetic states. Two examples for collinear states in a hexagonal lattice are illustrated: The ferromagnetic **(a)** and the row-wise antiferromagnetic state **(b)**. Magnetic moments of both states are orientated parallel or antiparallel along the surface normal.

The antiferromagnetic (AFM) state is typically stabilised by negative exchange parameters, leading to an antiparallel alignment between adjacent magnetic moments.

In Fig. 3.1 b, an example of a row-wise antiferromagnetic configuration on a hexagonal lattice is illustrated. Both, the ferro- and antiferromagnetic states are collinear magnetic structures, whose magnetic moments are aligned parallel or antiparallel to a single axis.

3.2. Domain walls

Due to the parallel alignment of the magnetic moments, the ferromagnetic state exhibits a strong stray field. The energy costs of the dipole-dipole interaction increase with the system size, eventually giving rise to a ferromagnetic domain structure. The magnetic domains have different magnetisation directions, which minimise the stray fields, but require the formation of domain walls at the boundaries of the domains. Despite the local energy costs due to exchange interaction and magnetocrystalline anisotropy, the magnetisation of these non-collinear transition areas rotates from the orientation direction of one domain to the other. In Fig. 3.2, two types of domain walls are illustrated: In bulk and thin films, Bloch-walls are typically stabilised by the dipole-dipole interaction, while chiral Néel walls are favoured by surface Dzyaloshinskii-Moriya interaction (DMI).

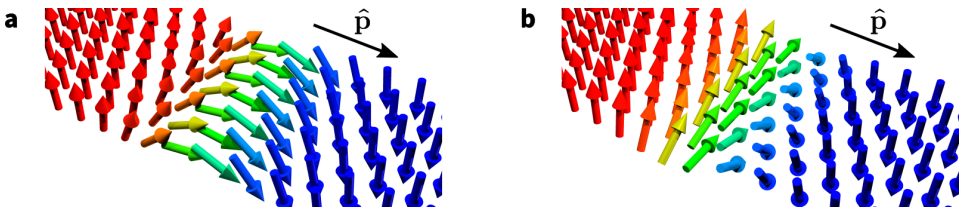

Figure 3.2 | Illustration of domain walls in ultrathin films. a) A Néel-type domain wall between two ferromagnetic domains is shown. The magnetic moments of the domain wall are oriented in the plane spanned by the propagation direction and the surface normal. **b)** A Bloch-type domain wall, whose moments are oriented perpendicular to the propagation direction.

Analytically calculated in a micromagnetic framework, the local energy costs due to the formation of a domain wall are minimised by the following theta profile [119], where theta is the angle of the magnetisation to the easy axis of the anisotropy, $\hat{\mathbf{n}}$:

$$\Theta(\mathbf{r}) = \frac{\pi}{2} + \arcsin\left[\tanh\left(\frac{(\mathbf{r}\cdot\hat{\mathbf{p}}) - r_0}{\Delta/2}\right)\right]. \tag{3.1}$$

The parameter $\hat{\mathbf{p}}$ determines the propagation direction of the DW perpendicular to $\hat{\mathbf{n}}$ and r_0 defines the distance of the central axis of the domain wall to the origin of the coordinate system. In the micromagnetic model, but expressed by atomistic exchange interaction and anisotropy parameters, the width of a domain wall in a hexagonal lattice is given by [III]

$$\Delta = a\sqrt{\frac{3J_1}{2K}}, \tag{3.2}$$

where a is the lattice constant.

3.3. Spin spirals

Non-collinear magnetic structures exhibit angles between adjacent magnetic moments different from 0° or 180°. When the relative angle between adjacent magnetic moments is constant along the spin spiral propagation direction, $\hat{\mathbf{q}}$, and zero perpendicular to it, a homogeneous spin spiral is formed.

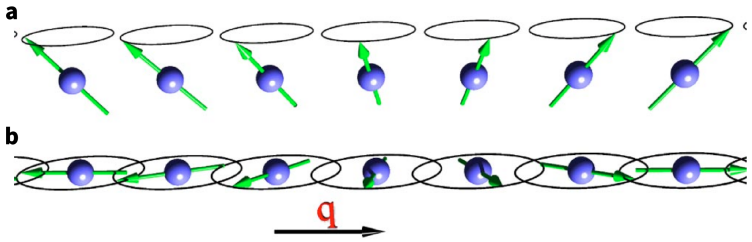

Figure 3.3 | Examples of spin spirals. The relative orientation of adjacent magnetic moments, or spins, changes by a constant angle. The rotation axis of both spirals is oriented in positive z-direction (upwards). The opening angle of the cone is set to $\theta = \pi/4$ **(a)** and $\theta = \pi/2$ **(b)**. Figure reprinted from [73] with permission of APS physics.

Spin spirals are characterised by the spin spiral vector $\mathbf{q}(\mathbf{r})$, which acts as a wave vector and, thus, determines the propagation direction, $\hat{\mathbf{q}} = \mathbf{q}(\mathbf{r})/|\mathbf{q}(\mathbf{r})|$, and the variation of the angle per distance, $|\mathbf{q}(\mathbf{r})|$. The orientation of a magnetic moment $\mathbf{m}_i(\mathbf{r}_i)$ can be calculated from its position, $\mathbf{r}_i$, via [73, 104]:

$$\mathbf{m}_i = (\cos[\mathbf{q}\cdot\mathbf{r}_i]\sin\theta,\ \sin[\mathbf{q}\cdot\mathbf{r}_i]\sin\theta,\ \cos\theta) \tag{3.3}$$

Here, the angle θ controls the opening of the cone around the rotation axis. While the rotation axis of the magnetic moments in Eq. 3.3 is oriented along the z-axis, spin spirals with a differently oriented rotation axis can be defined analogously. Examples of spin spirals with two different opening angles θ according to Eq. 3.3 are shown in Fig. 3.3.

Spin spirals have been repeatedly observed as magnetic ground states of ultrathin films [14, 20] and are of particular importance as non-collinear reference states for the determination of interaction parameters of model Hamiltonians via *first-principles* calculations [I, II, VII, 24, 32, 73]. This procedure is discussed in more detail in Chap. 4.

3.4. Magnetic Skyrmions

Magnetic skyrmions can be visualised as small, chiral whirls in the surrounding magnetisation [3]. Their chirality is typically induced by the DMI which favours non-collinear magnetic structures with a specific rotational sense. Whether the axis of rotation of the magnetic moments is oriented perpendicular or parallel to the radial direction, the corresponding skyrmions are of the Néel or Bloch type, which are illustrated in Fig. 3.4 a and b, respectively. Typically, Bloch-type skyrmions are stabilised by the dipole-dipole interaction [96] and bulk DMI [17], while Néel-type skyrmions are favoured by interfacial DMI [20, 21]. If these interactions occur together, skyrmions of a mixed-type can appear as well.

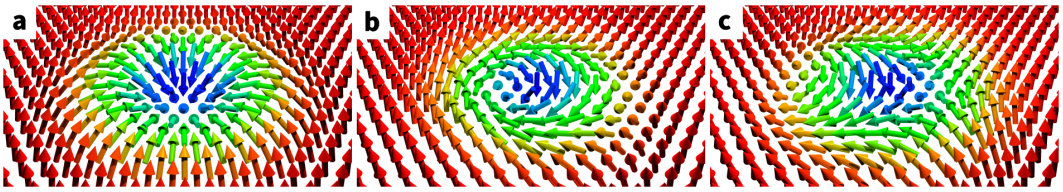

Figure 3.4 | Examples of magnetic skyrmion structures in ferromagnetic background. **a)** Néel-type skyrmion with $Q = -1$, whose magnetisation is oriented in radial direction. **b)** Bloch-type skyrmion with $Q = -1$, whose magnetisation is oriented perpendicular to the radial direction. **c)** Antiskyrmion with $Q = +1$.

3.4.1. Skyrmion profile and radius

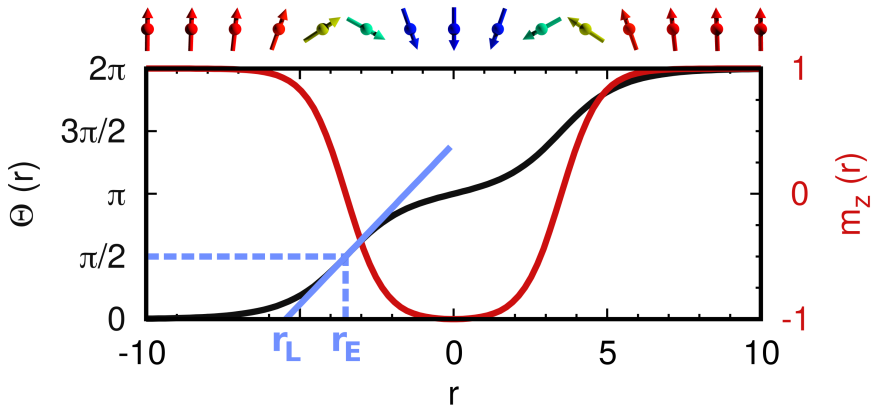

Figure 3.5 | Skyrmion profile and radius definition. The $\Theta\,(r)$-profile (black) and the z-component of the corresponding magnetisation (red) of a 1D line-cut through a skyrmion is shown over the spatial coordinate r. Above the plot, the corresponding magnetic structure of the skyrmion is displayed. The skyrmion radius as defined by the Lilley criterion, r_{L}, is constructed by the intersection of the tangent of highest slope on the $\Theta\,(r)$-profile (light blue) with the r-axis. Alternatively, the $\pi/2$ criterion of skyrmion radius often used by experimentalists, r_{E}, is illustrated by dashed lines (light blue). The $\Theta\,(r)$-profile was created via Eq. 3.4 with the parameters $\omega = 2.5$ and $c = 3.5$.

The profile of a magnetic skyrmion can be understood as a 2D superposition of two 180° domain walls of equal rotational sense [120] [119]. The adaption of the micromagnetic domain walls profile of a 360°-domain wall [120] [119] to a radial symmetric 2D structure yields the $\Theta\,(r)$ profile of a skyrmion, where Θ is the angle between the local magnetisation direction and the easy axis, $\hat{\mathbf{n}}$ [81, 119, 120]:

$$\Theta\,(r) = \pi + \arcsin\left[\tanh\left(\frac{r-c}{\omega/2}\right)\right] + \arcsin\left[\tanh\left(\frac{r+c}{\omega/2}\right)\right] \tag{3.4}$$

Here, r is a spatial coordinate in the plane whose absolute value, $|r|$, corresponds to the distance from the centre of the skyrmion, while c and ω are profile parameters.

In Fig. 3.4, a line-cut of a skyrmion profile is depicted, showing the angle $\Theta(r)$ and the out-of-plane magnetisation component $m_z\,(r) = \cos\left(\Theta\,(r)\right)$ over the spatial coordinate r. The profiles of two individual domain walls can be recognised, although they visibly overlap near the centre of the skyrmion at $r = 0$.

The parameter c can be interpreted as the distance of the two domain wall midpoints from the skyrmion centre. An increasing value of c leads to an increasingly pronounced plateau at the center of the skyrmion. The parameter ω, on the other hand, corresponds to the width of the domain walls, and controls how fast the magnetisation rotates at the skyrmion boundary.

Since the twist of the skyrmion only decays slowly into the surrounding magnetisation, a measure for the size of a skyrmion is not obvious. Analogue to the domain wall width, the Lilley definition can be applied to the skyrmion radius [121]. In this case, the radius is defined as the intersection of the spatial axis with the tangent starting from the inflection point of the profile [I, VIII, 24]. In Fig. 3.5, the tangent at the inflection point and the resulting radius, r_{L}, are displayed.

Alternatively, the skyrmion radius can be defined as the distance of the centre to the point at which the $m_z(\mathbf{r})$-component of the magnetisation equals zero or $\Theta(\mathbf{r}) = \pi/2$, respectively. This definition is commonly used to describe the radius of experimentally obtained skyrmions [VII, XI, 34, 81]. In Fig. 3.5, the radius resulting from this definition is depicted as r_{E}.

3.4.2. Topological charge

Objects with identical integer values of the topological charge are homotopic and can be transformed into each other in a continuous way [122]. In the continuous definition of the magnetisation $\mathbf{m}(\mathrm{r})$, the topological charge Q is defined in a Cartesian coordinate system as [3]

$$Q_{\mathrm{2D}} = \frac{1}{4\pi} \int \mathbf{m} \cdot \left(\frac{\partial \mathbf{m}}{\partial x} \times \frac{\partial \mathbf{m}}{\partial y} \right) \mathrm{d}x \, \mathrm{d}y, \tag{3.5}$$

where the z-axis is oriented in out-of-plane direction. Topologically trivial structures such as the FM or AFM states have a topological charge of $Q = 0$, while magnetic skyrmions in a ferromagnetic background oriented in positive z-direction have a value of $Q = -1$. Sometimes, the topological charge is also referred to as skyrmion number [21], although skyrmions with different topological charge can occur.

In the continuum model, skyrmions are topologically protected against a transition into a homotopically different structure. However, in an atomistic system, this

topological protection is lifted and transition states with large angles between adjacent magnetic moments can occur [I]. A definition of the topological charge on a discrete, 2D system has been originally provided by Berg and Lüscher for a square lattice [123]. Adapted to the hexagonal lattice, the definition reads [68]

$$Q = \frac{1}{4\pi} \sum_l A_l, \tag{3.6}$$

where A_l is the spherical segment of three adjacent magnetic moments $\mathbf{m}_i, \mathbf{m}_j$ and $\mathbf{m}_k$, which form the triangle indexed with l. See Fig. 3.6 for an illustration of the variables.

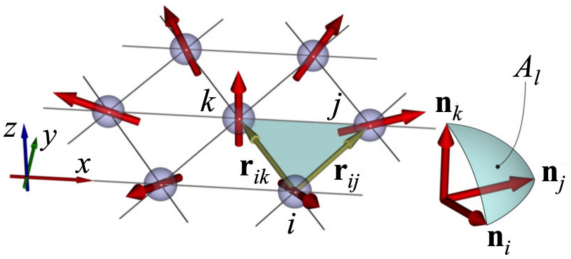

Figure 3.6 | Topological charge on a discrete lattice. The spheres represent hexagonal lattice sites, the arrows show the orientation of the magnetic moments. The moments i, j and k form the spherical segment A_l. Figure reprinted from [68] with permission of APS physics.

The value of the local topological charge density of a single segment can be calculated by [68]

$$\cos\left(\frac{A_l}{2}\right) = \frac{1 + \mathbf{m}_i \cdot \mathbf{m}_j + \mathbf{m}_j \cdot \mathbf{m}_k + \mathbf{m}_k \cdot \mathbf{m}_i}{\sqrt{2\left(1 + \mathbf{m}_i \cdot \mathbf{m}_j\right)\left(1 + \mathbf{m}_j \cdot \mathbf{m}_k\right)\left(1 + \mathbf{m}_k \cdot \mathbf{m}_i\right)}}. \tag{3.7}$$

The sign of the segment is determined by [68]

$$\operatorname{sgn}\left(A_l\right) = \operatorname{sgn}\left[\mathbf{m}_i \cdot \left(\mathbf{m}_j \times \mathbf{m}_k\right)\right]. \tag{3.8}$$

The total topological charge of the lattice is obtained by the summation over all local contributions A_l.

3.4.3. Other skyrmion structures

The Néel and Bloch skyrmions introduced in Fig. 3.4 a and b have the same $\Theta(r)$ profile, but exhibit a helicity, which controls the profile of the in-plane magnetisation. While both have the same topological charge of $Q = -1$, skyrmions with other

topological charges and with varying helicities can exist. The antiskyrmion has an opposite topological charge of $Q = +1$ and is shown in Fig. 3.4 c. In the absence of DMI, the antiskyrmion has the same $\Theta(r)$ profile as normal skyrmions. However, due to the locally changing rotation sense of the antiskyrmion structure, the presence of DMI leads to small deformations of the otherwise radial symmetric $\Theta(r)$ profile.

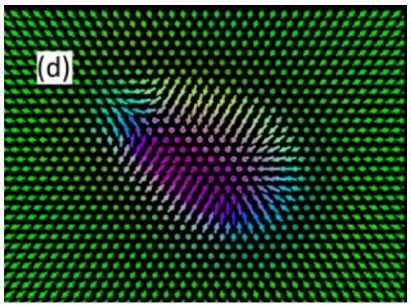

Figure 3.7 | Illustration of an chimera skyrmion. The chimera skyrmion is "two-headed": A skyrmion "head" at one side and an antiskyrmion "head" at the other side. It is topological trivial with $Q = 0$. Figure reprinted from [42] with permission of APS physics.

In addition, skyrmion structures with topological charges beyond $Q = \pm 1$, have been proposed [41, 42]. The topologically trivial chimera skyrmion with $Q = 0$ is displayed in Fig. 3.4 c. Its name is motivated by the skyrmion ”head” at one side and an antiskyrmion ”head” on the opposite site [42] and is mostly stabilised by exchange frustration [VII, XI, 99, 124] and higher order exchange interactions [X].

4. Magnetic interactions from first-principles calculations

Magnetic models as introduced in Chap. 2 are based on parameters reflecting the strength of magnetic interactions. While analytical studies of the model or the systematic variation of parameters in combination with numerical simulations can be useful to give trends and overviews of magnetic properties, e. g. the skyrmion barrier dependence on nearest neighbour interactions [VI], the investigation and prediction of real systems requires adequately determined interaction parameters.

In order to determine the parameters of magnetic interactions, the magnetic model can be fitted to the total energies of non-collinear reference states obtained from *first-principles* calculations. In general, the direct calculation of many non-collinear states such as skyrmions or domain walls is not feasible due to their non-periodic structure. Even by using density functional theory (DFT) algorithms optimised for the treatment of non-periodic structures, only extremely small skyrmions of a few lattice sites could be calculated [125].

Homogeneous spin spirals, on the other hand, offer high symmetry, which can be exploited for efficient DFT calculations of a sufficient number of non-collinear states for the fitting process of the parameters [73, 104]. In the following, a brief introduction to DFT, spin spiral dispersion curves and the fitting procedure of interaction parameters to these curves is presented for the ultrathin film systems Pd/Fe/Ir(111) and Pd/Fe/Rh(111).

4.1. Density functional theory calculations

In DFT, the quantum mechanical many body problem of electrons in an atomic lattice is reduced to a set of effective one particle Schrödinger equations [70, 71]. This

is achieved by the approximation of electron-electron interactions with exchange-correlation potentials. With this approximation, the many body problem is mapped to an effective single-electron problem, which comes with the cost of losing some information on the electron correlations, depending on the applied exchange-correlation potential [69, 101, 104, 126].

Furthermore, the energy is not minimised for the full many-electron wave-function, but with respect to the electron density $n(\mathbf{r})$. This reduces the full set of electron wave functions to a scalar function that describes the spatially resolved probability of finding an electron. With this approximations, the calculation of the electronic and magnetic structure of ultrathin film systems becomes feasible. With a chosen unit cell and exchange-correlation potential, the electronic structure can be calculated self-consistently [73, 104]. Note, that all DFT calculations shown in this work were performed by others and were done with the DFT implementation in the FLEUR code (www.flapw.de). It uses the full potential linearised augmented plane wave method to calculate the electronic structure of the system, which ranks among the most accurate implementations of DFT [73, 127, 128].

In the FLEUR code, the utilization of the system symmetry leads to a drastic reduction of the calculation effort required for the energetic minimization of the electronic structure [73, 104]. By assuming an infinite crystal, the Bloch theorem reduces the calculation from many atoms to just one unit cell. Since the electronic ground state in magnetic systems depends on the magnetic structure, the unit cell size has to cover, both, the chemical and magnetic structure. For collinear magnetism, the required unit cell size is typically on the same magnitude as the chemical unit cell. For non-collinear magnetic textures, however, the magnetic unit cell can be significantly larger, depending on the size of the magnetic structure. For this reason the direct calculation of skyrmions and other complex structures with DFT is often not feasible.

When surfaces or interfaces are considered, this problem is enhanced due to the broken symmetry in z direction, which is defined parallel to the surface or interface normal. In that direction, the Bloch theorem cannot be applied anymore and each atomic layer of material has to be taken into account separately. Therefore, a crystal surface , as e. g. Ir(111) in Pd/Fe/Ir(111), is modelled by only a small number of layers in order to reduce the computational effort [II, 24, 32, 33, 104, 114, 128]. On the other hand, the number of layers has to be sufficiently large to accurately mimic

the properties of the crystal. In practice, the convergence of the electronic structure with respect to the number of layers must be evaluated and ensured in order to describe realistic crystal substrates.

4.2. Spin spiral dispersion curves

In order to determine the interaction parameters of a magnetic model indirectly, the parameters are obtained such that they reproduce energy differences between magnetic textures calculated by DFT. For this purpose, each parameter requires at least one DFT calculated texture with a well-defined energy difference in the magnetic model. Thus, the extended Heisenberg model with interactions beyond nearest neighbours requires energies of non-collinear states which are often costly to calculate by DFT. The calculation of homogeneous spin spirals provides an elegant solution to this problem as spin spirals are non-collinear structures with symmetries allowing for an efficient computation by DFT [104].

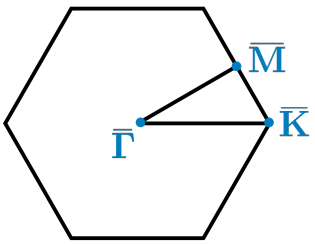

Figure 4.1 | High symmetry lines and points of the first Brillouin zone of a hexagonal lattice. The $\mathbf{q}$ vector of spin spiral dispersion curves is typically selected along the shown high symmetry lines, containing the following high symmetry points: $\mathbf{q} = \overline{\Gamma}$ corresponds to the ferromagnetic state, $\mathbf{q} = \overline{\mathrm{K}}$ to the Néel-state with 120° between adjacent spins and $\mathbf{q} = \overline{\mathrm{M}}$ to the row-wise antiferromagnetic configuration.

Each magnetic moment of a homogeneous spin spiral perceives a similar relative angle to its neighbours (see Sec. 3.3). Without spin-orbit coupling, this leads to an identical electron and magnetisation density at all lattice sites, which is known as the generalised Bloch theorem [73, 104, 128]. With this symmetry, the magnetic unit cell reduces to a single lattice site although spin spirals are non-collinear textures. This enables for systematic DFT calculations of spin spirals with varying spin spiral vector $\mathbf{q}$, yielding a spin spiral dispersion curve $E(\mathbf{q})$. Typically, the $\mathbf{q}$-vectors are chosen along high symmetry lines of the lattice [I, 24, 32, 73, 82, 104, 128]. In case of a hexagonal lattice, these lines are along $\overline{\Gamma}\overline{\mathrm{K}}$, $\overline{\Gamma}\overline{\mathrm{M}}$ and $\overline{\mathrm{M}}\overline{\mathrm{K}}$ direction, as displayed in Fig. 4.1.

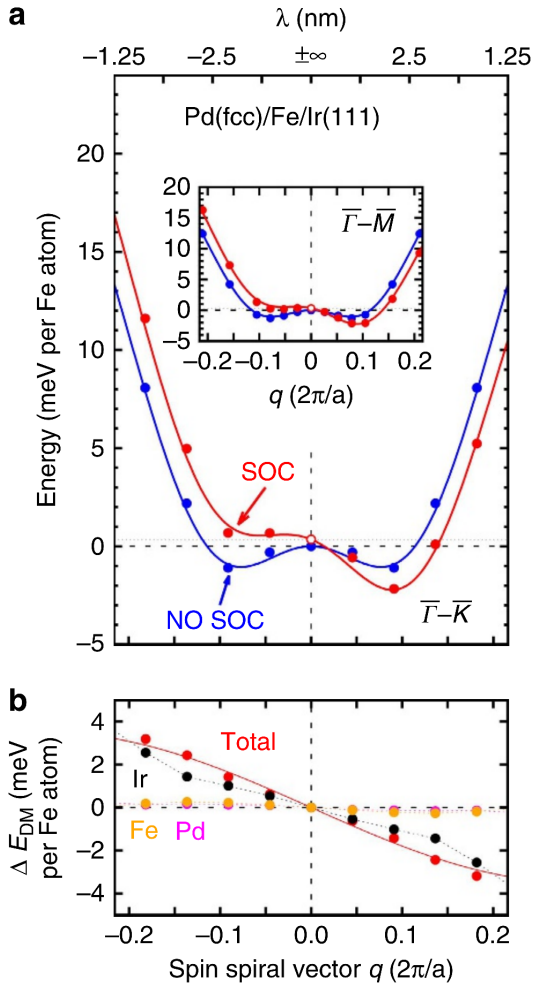

Figure 4.2 | Spin spiral dispersion curve of fcc-Pd/Fe/Ir(111) calculated with five layers of Ir. a) Spin spiral dispersion curve of fcc-Pd/Fe/Ir(111). The red and blue points show the DFT calculated energy of spin spirals as a function of $\mathbf{q}$ with and without spin-orbit coupling (SOC), respectively. The $\mathbf{q}$ vectors are chosen along the $\overline{\Gamma}\overline{\mathrm{K}}$ direction. $\overline{\Gamma}$ and $\overline{\mathrm{K}}$ correspond to the ferromagnetic (FM) and Néel state. The energies are shown relative to the FM state without SOC and the upper axis shows the corresponding wavelength of the spin spirals. The inset shows the dispersion in the $\overline{\Gamma}\overline{\mathrm{M}}$ direction. **b)** The energy contribution of SOC relative to the FM state in the $\overline{\Gamma}\overline{\mathrm{M}}$ direction of the individual Pd, Fe and top Ir layers. Figure reprinted from [24] with permission of Springer Nature.

Fig. 4.2 a shows a part of the spin spiral dispersion curve for fcc-Pd/Fe/Ir(111) calculated by Dupé *et al.* [24]. The calculations were performed within the FLEUR implementation of DFT for a PdFe bilayer on 5 layers of Ir(111) modelling the crystal. The energies of spin spirals, relative to the ferromagnetic (FM) state, are displayed for positive and negative values of q along the $\overline{\Gamma}\overline{\mathrm{K}}$ direction, while the $\overline{\Gamma}\overline{\mathrm{M}}$ direction is shown in the inset. The positive and negative values correspond to right and left rotating spin spirals, which are energetically degenerate as long as spin-orbit coupling is neglected.

In $\overline{\Gamma}\overline{\mathrm{K}}$ direction, two energy minima appear symmetrically left and right of the $\overline{\Gamma}$ point with $q \approx \pm 0.09\frac{2\pi}{a}$, where a denotes the lattice constant. The $\overline{\Gamma}\overline{\mathrm{M}}$ direction yields a similar picture with a slightly smaller q value for the minima. Since the energy minima are below the energy of the $\overline{\Gamma}$ point, spin spirals are energetically favoured in this system even without taking spin-orbit coupling into account. The minima correspond to a spin spiral wavelengths of $\lambda \approx \pm 2.4$nm.

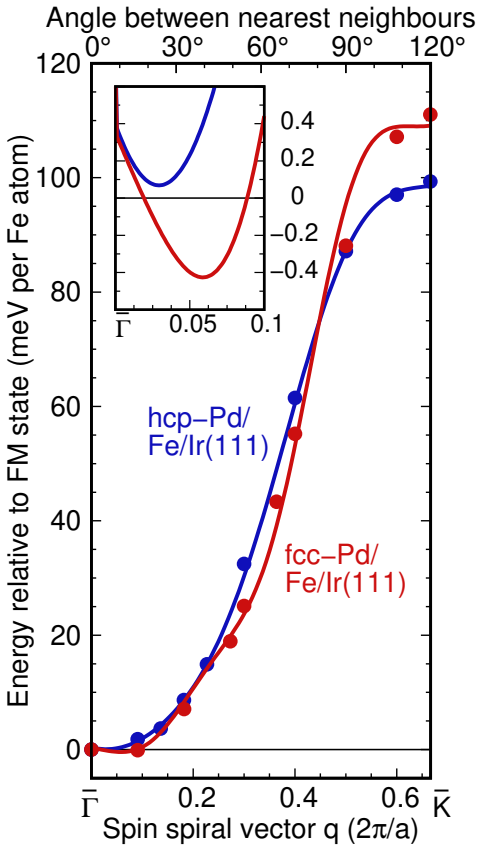

Figure 4.3 | Spin spiral dispersion curve of Pd/Fe/-Ir(111) with 13 layers of Ir. The energy of flat spin spirals relative to the FM state is shown over the spin spiral vector $\mathbf{q}$ along the high symmetry line from the $\overline{\Gamma}$ to the $\overline{\mathrm{K}}$ point. The red and blue points are calculated by DFT with 13 layers of Ir for Pd/Fe/Ir(111) with fcc and hcp stacked Pd layer, respectively. The inset shows a zoom of the area close to the $\overline{\Gamma}$-point. Fits with the extended Heisenberg model beyond nearest neighbours and including SOC are shown as sold red and blue lines, while the fits with effective nearest neighbour approximation correspond to the dotted lines. The resulting parameters are given in Tab. 4.1. Figure adapted from [I].

By taking spin-orbit coupling into account, spin space is linked to real space and magnetic moments of spin spirals perceive a varying potential depending on their lattice site [21, 24, 32, 73, 104]. Thus, the generalised Bloch theorem does not hold anymore and larger unit cells have to be used for DFT calculations, drastically increasing the computational time. For this reason, spin-orbit coupling is typically not calculated self consistently but in first order perturbation theory based on electron structures previously converged self consistently without spin-orbit coupling.

Spin-orbit coupling yields an energy shift between spin spirals and collinear states due to magnetocrystalline anisotropy [21, 24, 32]. Additionally, systems hosting Dzyaloshinskii-Moriya interaction (DMI) exhibit a spin-orbit coupling (SOC) contribution to the spin spiral dispersion curve [21, 24, 32]. Fig. 4.2 b shows the change in energy due to SOC over q value, lifting the degeneracy of the spin spiral energy minima. The minimum of the right rotating spin spiral becomes deeper (Fig. 4.2 a) while the energy of left rotating spiral rises above the energy of the $\bar{\Gamma}$ point. The decomposition of SOC into contributions per layer as shown in Fig. 4.2 b, reveals a dominating contribution of the surface Ir layer.

By increasing the number of Ir layers, Dupé *et al.* improved the modelling of the Ir(111) crystal, resulting in the dispersion curve shown in Fig. 4.3 for both, fcc and hcp stacked Pd toplayers. The overall dispersion curve is similar to the curve obtained with 9 layers of Ir, but exhibits a less pronounced spin spiral minimum for fcc-Pd/Fe/Ir(111) with an energy gain of only 0.4 meV with respect to the FM state. The hcp stacked Pd system even exhibits a FM groundstate since the local spin spiral minimum does not reach below the energy of the FM state. This demonstrates how small variations of calculation details can result in slightly different energy differences between the states, while the overall dispersion curves stay consistent.

4.3. Fitting of extended Heisenberg model parameters

Magnetic model parameters can be determined by fitting the analytical functions of the exchange energy, $E_{\mathrm{exch}}(\mathbf{q})$, and the DMI contribution, $E_{\mathrm{DMI}}(\mathbf{q})$, obtained from the extended Heisenberg model (Chap. 2), to the spin spiral dispersion with and without SOC obtained by DFT. Similar to the spin spiral dispersion curves calculated by DFT, the functions $E_{\mathrm{exch}}(\mathbf{q})$ and $E_{\mathrm{DMI}}(\mathbf{q})$ are modelled along the high symmetry lines of the Brillouin zone.

Parameters for the exchange interaction beyond nearest neighbours are fitted to the data points of the dispersion without spin-orbit coupling. When higher-order exchange interactions are considered, the parameters of both, exchange beyond nearest neighbours and higher-order interactions are entangled and require further magnetic states calculated by DFT to differentiate between them. Details are given in [X].

System	Pd fcc / Fe / Ir (111)	Pd hcp / Fe / Ir (111)	Pd fcc / Fe / Rh (111)	Pd hcp / Fe / Rh (111)
J_1	14.4046	13.6591	13.3479	12.2274
J_2	−2.4811	−0.5122	−2.6859	−1.1803
J_3	−2.6851	−2.8822	−2.8384	−2.7772
J_4	0.5206	0.0657	0.6197	0.2710
J_5	0.7376	0.5537	0.4643	0.4011
J_6	0.2776	–	−0.1011	0.0345
J_7	0.1609	–	−0.3033	−0.1428
J_8	−0.5745	–	−0.1117	−0.1022
J_9	−0.2127	–	0.0251	−0.0026
J_{10}	–	–	0.1653	0.1185
J_{11}	–	–	−0.0650	−0.0579
D_1	1.0000	1.2000	0.6244	0.8660
D_2	–	–	−0.0443	0.0184
D_3	–	–	0.0366	−0.0853
D_4	–	–	0.0038	0.0163
D_5	–	–	0.0486	0.0371
K	−0.7000	−0.4000	−0.1677	−0.3060
μ	3.0	3.0	3.2	3.13

Table 4.1 | Parameters of the extended Heisenberg model are listed for Pd/Fe/Ir(111) and Pd/Fe/Rh(111). The parameters are determined by fits to spin spiral dispersion curves calculated with DFT. Fits and DFT calculations were performed by B. Dupé for Pd/Fe/Ir(111) [I] and S. Haldar for Pd/Fe/Rh(111) [II]. The parameters for exchange interaction (J_i), DMI (D_i) and magnetocrystalline anisotropy (K) are given in $\mathrm{meV/atom}$. The magnitude of the average magnetic moment, μ, is given in units of μ_B.

The fitted function $E_\mathrm{exch}(\mathbf{q})$ is shown in Fig. 4.3 as continuous red (blue) line for fcc (hcp) stacked Pd on Fe/Ir(111). The corresponding exchange parameters J_i are listed in Tab. 4.1. As displayed in Fig. 4.4, the parameters beyond J_1 are of considerable size and exhibit alternating signs, indicating a strong exchange frustration that already manifests itself in Fig. 4.3: While the strong positive J_1 parameter favours the FM state, the alternating J_i in fcc-Pd/Fe/Ir(111) lead to a spin spiral state.

The DMI parameters are obtained by fitting $E_\mathrm{DMI}(\mathbf{q})$ to the energy difference caused by SOC as displayed in Fig. 4.2b. By convention, a positive sign corresponds to clockwise or right rotating spin spirals, while a negative sign denotes an anticlockwise rotational sense. Here, only a single DMI parameter, D_1, was fitted, as it already describes the SOC contribution sufficiently.

As a general rule of thumb, the number of considered shells of exchange interaction and DMI is selected to be just large enough to match the dispersion curves provided by DFT with the requested accuracy. Taking too many parameters into account

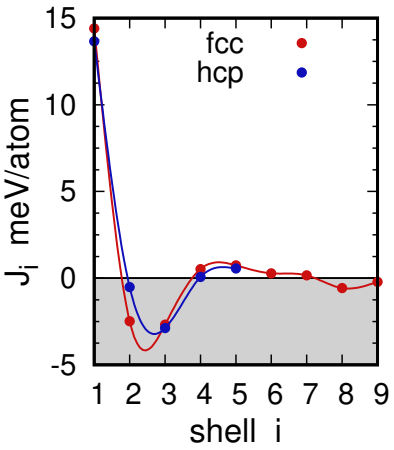

Figure 4.4 | Exchange parameters of Pd/Fe/Ir(111) per shell of neighbours. The exchange parameters of Tab. 4.1 are given in units of $\mathrm{meV/atom}$. Splines were used to create the solid lines as a guidance for the eye.

introduces unnecessary degrees of freedom to the fitting procedure. Typically, this results in up to 12 parameters for exchange interaction and up to 7 for DMI [I, II, VII, 24, 32, 82].

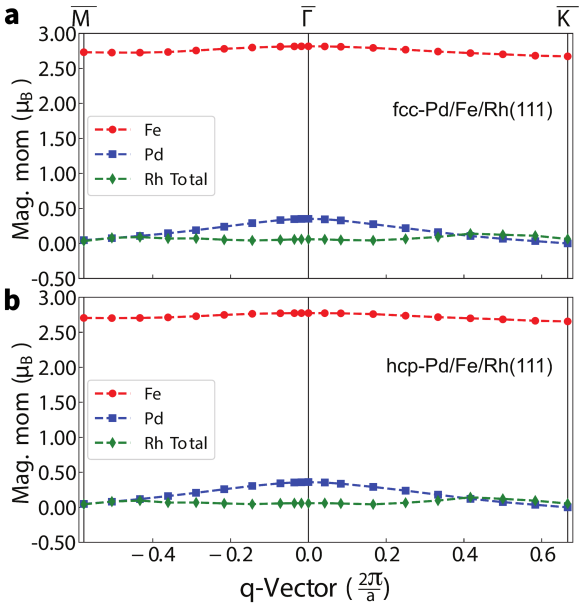

Figure 4.5 | Magnetic moments of Pd/Fe/Rh(111) over q obtained with DFT. a) The sizes of the magnetic moments in fcc-Pd/Fe/Rh(111), resolved for the Pd top layer, the Fe interlayer and the sum of all Rh layers are given in units of μ_B over the q-vector along the $\overline{\mathrm{M}}\overline{\Gamma}$ and $\overline{\Gamma}\overline{\mathrm{K}}$ high symmetry lines. **b)** Analogue to **(a)**, but for hcp-Pd/Fe/Rh(111). Figure published in [II].

The parameter of the magnetocrystalline anisotropy can be determined by self consistent DFT calculations of collinear states including spin-orbit coupling [32]. The total energy difference due to alignment of collinear states in out-of-plane and in-plane direction of the surface directly yields the uniaxial anisotropy constant K. Averaged over lattice sites, spin spirals rotating in a plane containing the easy axis of

the anisotropy receive an energy gain of $K/2$, while all magnetic moments of collinear states gain the full energy of K when aligning along the easy axis. Thus, collinear states as the $\bar{\Gamma}$ and $\overline{\mathrm{M}}$ points shift downwards in the spin spiral dispersion curve by $K/2$ with respect to the non-collinear spin spiral states [24].

Besides a good agreement of the fit with the DFT obtained dispersion curve and a good localisation of magnetic moments, the application of the extended Heisenberg model requires that the magnitude of the magnetic moments is independent of their orientation. As an example, the magnitudes of the magnetic moments of fcc-Pd/Fe/Rh(111) and hcp-Pd/Fe/Rh(111) obtained from DFT calculations along the high symmetry lines are displayed in Fig. 4.5. The magnetic moments of all shown layers are fairly constant, with only the spin-polarized Pd layer showing a considerable variation of $\Delta m \approx 0.4\mu_{\mathrm{B}}$ in both stackings. Especially the moments of the Fe layers occur to be rotationally stable, underpinning the suitability of the atomistic approximation.

5. Atomistic spin simulations

The parameterised Heisenberg model allows for the simulation of large magnetic lattice systems consisting of many thousands of atoms. A simple energetic relaxation of magnetic states is often performed by spin dynamics or Monte Carlo simulations. However, more sophisticated algorithms can provide information about properties beyond the ground state such as phase diagrams, dynamics, responses to external stimuli, and phase transitions.

The simulations presented in this work are performed with the atomistic simulation code of the group of Prof. Dr. Stefan Heinze in Kiel. Originally set up by Dr. Bertrand Dupé as a spin dynamics and Monte Carlo simulation code, it has been tested, corrected and extended by the author. The geodesic nudged elastic band (GNEB) method has been added by Dr. Pavel F. Bessarab and subsequently extended and modified by the author. The harmonic transition state theory (HTST) algorithm has been implemented by the author under supervision of Dr. Pavel Bessarab. The mode following method has been developed and implemented by the author. This chapter is dedicated to the introduction and the theoretical foundations of these methods.

5.1. Spin dynamics

In general, the numerical integration of the equation of motion of a system provides access to many interesting phenomena. Spin dynamics algorithms apply this approach to magnetic lattice systems and are based on a model Hamiltonian for the interaction of the magnetic moments and a model for the equation of motion. The latter is typically given by the Landau-Lifshitz or the Landau-Lifshitz-Gilbert equations, which are closely related and presented below. Since both variants of the equation of motion yield a coupled set of nonlinear differential equations, analytical solutions

are not feasible, except in the simplest cases. For the numerical solution of the Landau-Lifshitz equation the semi-implicit integration scheme B (SIB) of Mentink *et al.* [129] is implemented.

5.1.1. Landau-Lifshitz-Gilbert equation

The commonly used equation of motion for interacting magnetic moments of an atomic lattice has been originally introduced by Landau and Lifshitz in 1935 [130]. Quantum mechanical derivations of the Landau-Lifshitz equation can be found e. g. in [69, 131]. Following its original, classical motivation, the interactions of the extended Heisenberg model presented in Chap. 2 can be rewritten such, that they resemble the form of a classical interaction of magnetic moments with an external field, which reads $H_i = \mathbf{m}_i \cdot \mathbf{B}_i^{\text{eff}}$. The effective field, $\mathbf{B}_i^{\text{eff}}$, is created by the superposition of all magnetic interactions acting on the moment $\mathbf{m}_i$. It has the dimension of an energy and can be derived by the functional derivative of the applied model Hamiltonian [69]:

$$\mathbf{B}_i^{\text{eff}} = \frac{\delta H_i}{\delta \mathbf{m}_i}. \tag{5.1}$$

Analogue to the precessional movement of a classical magnetic moment around an external magnetic field, the magnetic moment $\mathbf{m}_i$ feels a torque created by the effective field $\mathbf{B}_i^{\text{eff}}$. The formulation of this torque is equivalent to the first term of the Landau-Lifshitz equation (LL), which reads [130]:

$$\frac{1}{\gamma}\frac{\mathrm{d}\,\mathbf{m}_i}{\mathrm{d}\,t} = -\underbrace{\left(\mathbf{m}_i \times \mathbf{B}_i^{\text{eff}}\right)}_{\text{precession}} - \underbrace{\lambda\left[\mathbf{m}_i \times \left(\mathbf{m}_i \times \mathbf{B}_i^{\text{eff}}\right)\right]}_{\text{damping}} \tag{5.2}$$

Here, γ is the gyromagnetic ratio. The first term at the right hand side is responsible for the precessional movement of $\mathbf{m}_i$. Since in this formulation the precession would last forever, Landau and Lifshitz added the second term, which describes the decay of the precession purely phenomenological. The relative size of the damping to the precession term is controlled by the parameter λ. Due to the presence of damping, the magnetic moment slowly aligns with the effective field as shown in Fig. 5.1.

In its original formulation, the damping term can lead to non-physical behaviour, in particular that the motion of the magnetic moments in strongly damped systems becomes faster instead of slowing down [132]. In order to address this issue, Gilbert

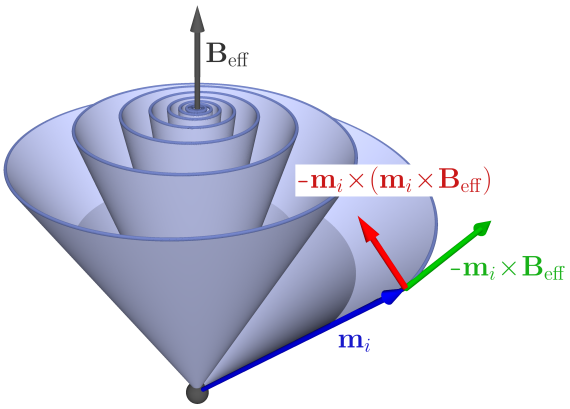

Figure 5.1 | Illustration of the damped precessional movement of a magnetic moment around a constant effective field. The trajectory of a magnetic moment, $\mathbf{m}_i$ (blue), around a constant effective field, $\mathbf{B}_i^{\text{eff}}$ (black), is obtained by solving the equation of motion given by Eq. 5.2 or Eq. 5.4 and is illustrated as a blue shaded area. The local directions of the precession term (green) and the damping term (red) are denoted by arrows.

proposed another form of the damping term, yielding the Landau-Lifshitz-Gilbert equation (LLG) [133]:

$$\frac{1}{\gamma}\frac{\mathrm{d}\,\mathbf{m}_i}{\mathrm{d}\,t} = -(\mathbf{m}_i \times \mathbf{B}_i^{\text{eff}}) + \frac{\alpha}{m_i}\left(\mathbf{m}_i \times \frac{\partial \mathbf{m}_i}{\partial t}\right). \tag{5.3}$$

The Gilbert damping also leads to a gradual alignment of the magnetic moment with the effective field as depicted in Fig. 5.1. However, with this form of the damping term, the overall speed decreases with increasing damping parameter α. Therefore, the Gilbert formulation is often the preferred form for the phenomenological damping in simulations of time-resolved dynamics [69, 132].

Eq. 5.3 can be rewritten such, that it resembles the original equation of motion in Eq. 5.2, which yields the commonly known form of the Landau-Lifshitz-Gilbert equation (LLG) [69]:

$$\frac{(1+\alpha^2)}{\gamma}\frac{\mathrm{d}\,\mathbf{m}_i}{\mathrm{d}\,t} = -\underbrace{(\mathbf{m}_i \times \mathbf{B}_i^{\text{eff}})}_{\text{precession}} - \underbrace{\alpha\,[\mathbf{m}_i \times (\mathbf{m}_i \times \mathbf{B}_i^{\text{eff}})]}_{\text{damping}} \tag{5.4}$$

In practice, both formulations in Eq. 5.2 and Eq 5.4 are equivalent up to the factor $(1+\alpha^2)$ for rescaling the time axis. In the Kieler spin dynamics code, the original LL equation (Eq. 5.2) is implemented, which can easily be rescaled to the LLG equation (Eq. 5.4) after the end of the simulation. In order to investigate Langevin dynamics or the response of applied currents, the basic formulation of the LL (Eq. 5.2) and LLG (Eq. 5.4) can be extended with terms for thermal fluctuations [69, 129, 134] and spin-transfer torques [69, 135].

Values for the damping constants λ and α can be determined experimentally [136–140] and by *first-principles* calculations [69, 141–143]. For this work, however, spin dynamics simulations were only used to energetically minimize magnetic structures. For a fast and reliable relaxation, damping parameters of $\lambda = 0.1 - 1.0$ have been applied, which are close to the damping parameter of $\alpha = 0.3$, typically assumed for Pd/Fe/Ir(111) [IV, 144].

5.1.2. Numerical integration

The effective field occurring in the Landau-Lifshitz equation depends on the lattice configuration of all interacting magnetic moments. Therefore, the equations of motion in Eq. 5.2 become a set of coupled and nonlinear differential equation. In seeking to integrate these equations and obtain the trajectory of each individual moment, several numerical integration methods are available [69, 145].

In general, these methods approximate the integration over time by a finite sum of discrete time steps, Δt^k, where $k = 1, ..., K$ and K is the number of steps. While an adaptive time step control can greatly enhance the efficiency of the simulation, all spin dynamics simulations of this work used a constant time step of $\Delta t = T/K$, where T stands for the duration of the simulation. For each time step, k, the variations, $\Delta \mathbf{m}_i^k$, of all magnetic moments, $\mathbf{m}_i^k$, are determined. At time step k, the magnetic moment of the next step, $\mathbf{m}_i^{k+1}$ is given by [145]

$$\mathbf{m}_i^{k+1} = \mathbf{m}_i^k + \Phi^k \, \Delta t. \tag{5.5}$$

The function Φ^k is the increment of the differential equation at the step k and depends on the numerical integration method. Methods with an increment $\Phi^k = \Phi^k \left(\mathbf{m}_i^k\right)$ enable for the explicit calculation of the next step, which is typically fast but susceptible to numerical instabilities [129, 145]. A particular problem for integration of the LL equation is the conservation of the length of the magnetic moment of $|\mathbf{m}_i^k| = 1$ [69, 129]. Implicit integration methods have an increment of $\Phi^k = \Phi^k \left(\mathbf{m}_i^k, \mathbf{m}_i^{k+1}\right)$ [145]. They require an analytical solution, since $\mathbf{m}_i^{k+1}$ occurs on both sides of Eq. 5.5, which makes them more elaborate than explicit formulations, but typically provides higher numerical stability.

In the Kieler code, the semi-implicit solver B (SIB) of Mentink *et al.*. is implemented, which has been designed explicitly to solve the LL equation [129]. The formulation

of the method originally contains stochastic fluctuations of the effective field for the application to Langevin dynamics simulations. Here, a reduced version is presented, since temperature effects have not been included in the spin dynamics simulations of this work. The SIB solver uses a predictor-corrector scheme, where first a predictor step is calculated, which is then used to calculate the actual next step. The predictor step of the SIB without thermal fluctuations reads [129]

$$\mathbf{P}_i^k = \mathbf{P}_i^k - \underbrace{\left[\frac{\mathbf{m}_i^k + \mathbf{P}_i^k}{2}\right]}_{\text{implicit}} \times \underbrace{\left[\mathbf{B}_k^{\text{eff},i}\left(\mathbf{m}_i^k\right) + \mathbf{m}_i^k \times \mathbf{B}_k^{\text{eff},i}\left(\mathbf{m}_i^k\right)\right]}_{\text{explicit}} \Delta t. \tag{5.6}$$

By calculating the first cross product implicitly, the equation has to be solved for the three components of $\mathbf{P}_i^k$, yielding an implicitly conserved size of the magnetic moment. The complex effective field, on the other hand, is calculated explicitly in mean-field approximation. The corrector step is defined analogue to the predictor step with [129]

$$\mathbf{m}_i^{k+1} = \mathbf{m}_i^k - \underbrace{\left[\frac{\mathbf{m}_i^k + \mathbf{m}_i^{k+1}}{2}\right]}_{\text{implicit}} \times \underbrace{\left[\mathbf{B}_k^{\text{eff,i}}\left(\widetilde{\mathbf{m}}_i^k\right) + \widetilde{\mathbf{m}}_i^k \times \mathbf{B}_k^{\text{eff,i}}\left(\widetilde{\mathbf{m}}_i^k\right)\right]}_{\text{explicit}} \Delta t, \tag{5.7}$$

where $\widetilde{\mathbf{m}}_i^k = \left(\mathbf{m}_i^k + \mathbf{P}_i^k\right)/2$ is the average of the original value $\mathbf{m}_i^k$ and the predictor step, $\mathbf{P}_i^k$.

5.2. Geodesic nudged elastic band method

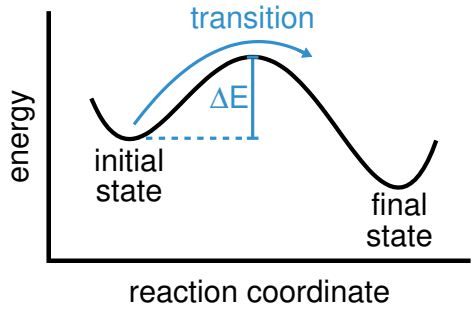

Figure 5.2 | Illustration of two local energy minima of a configuration space. The two minima, the initial state and the final state, are separated by the energy barrier, ΔE, which has to be overcome for a transition from the initial state to the final state.

Many magnetic systems exhibit more than one local energy minimum in configuration space. Each minimum corresponds to a metastable state which the system can occupy,

depending on the initial conditions. The system remains in a metastable state until it is thermally activated or exposed to external stimuli such as electric or magnetic fields. For a transition into another state and as long as quantum mechanical tunneling is neglected, the system has to overcome the energy barrier ΔE. The energy barrier separates the initial and the final state, as it is illustrated in Fig. 5.2. Information about the energy barrier and the transition process itself, which are needed in order to study the stability of metastable states, are, however, unknown *a priori*.

In principle, the transition between two metastable states can be performed over numerous trajectories in configuration space, which are called transition paths. This is illustrated in Fig. 5.3 for a system with three degrees of freedom. Naturally, the situation becomes much more complex for $3N$ dimensional lattice systems.

The position of the system on a path is given in terms of the reaction coordinate, which is a measure for the progress of the transition [146]. Along all paths, the energy increases as the magnetic moments continuously rotate from the initial to the final state, since the initial state is a local energy minimum. After the corresponding energy maximum of the path is reached, the energy drops with further increasing reaction coordinate until the system arrives at the final state.

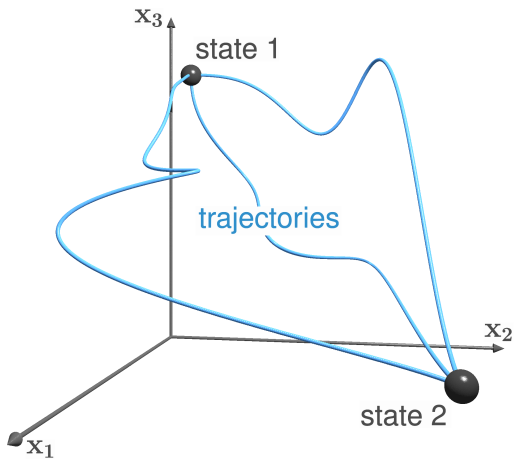

Figure 5.3 | Illustration of trajectories connecting metastable states. Two states of a 3D configuration space spanned by $\mathbf{x}_1$, $\mathbf{x}_2$ and $\mathbf{x}_3$ are shown as spheres. Examples of trajectories connecting both states in configuration space are displayed as blue lines.

A path, that locally minimises the energy in each point of the transition is called minimum energy path (MEP). The energy maximum of a MEP is a saddle point (SP), as it is an energy maximum along the path but an energy minimum with

respect to the orthogonal direction, i. e. with respect to the energy maxima of paths surrounding the MEP [147]. The energy difference of the initial state and the SP defines the energy barrier ΔE. That is, that the MEP provides the smallest ΔE available in its proximity.

If additional local energy minima occur along the path from the initial and to final state, the transition can be separated into sequenced individual transitions, each giving rise to a SP and an energy barrier between the metastable states along the path. Furthermore, for a particular transition, several MEPs with corresponding SPs can exist, each belonging to a specific transition mechanism. The knowledge of the MEP and ΔE allows first estimations of the stability of magnetic states and is the basis of further, more sophisticated investigations in the framework of transition state theory (TST), which are presented in Sec. 5.3.

In this section, it is presented how the MEP can be calculated via the geodesic nudged elastic band method (GNEB). While this method is based on the well established nudged elastic band method (NEB) method, which is used especially in chemistry for the energetic relaxation of transition paths [148, 149], only recently, in 2015, the GNEB was introduced for atomistic lattice systems by Bessarab *et al.* [94]. It will be shown, how the GNEB relaxes an initial transition path along the energy gradient into a MEP and how spring forces keep the discrete states of the path connected over the iterations. Thereby, the advantage of the GNEB over the NEB in the context of magnetic systems lies in the usage of the tangent space, a special configuration space, that takes the geodesic character of the magnetic moments with constant size into account, yielding overall better stability and convergence properties for lattice systems. The following introduction to the method is based on the original publication of Bessarab *et al.* [94].

5.2.1. Idea of the Method

For the presentation of the method, a magnetic system of N normalised magnetic moment vectors $\mathbf{m}_i$ is considered. Consistent to the definition of the extended Heisenberg model in Chap. 2, each moment is defined in 3D Euclidean space. Hence, the lattice state $\mathbf{X} = \{\mathbf{m}_1, ..., \mathbf{m}_N\}$ is defined on a $3N$ dimensional configuration space and the initial and final states of the transition are denoted as $\mathbf{X}^I = \{\mathbf{m}_1^I, ..., \mathbf{m}_N^I\}$ and $\mathbf{X}^F = \{\mathbf{m}_1^F, ..., \mathbf{m}_N^F\}$, respectively.

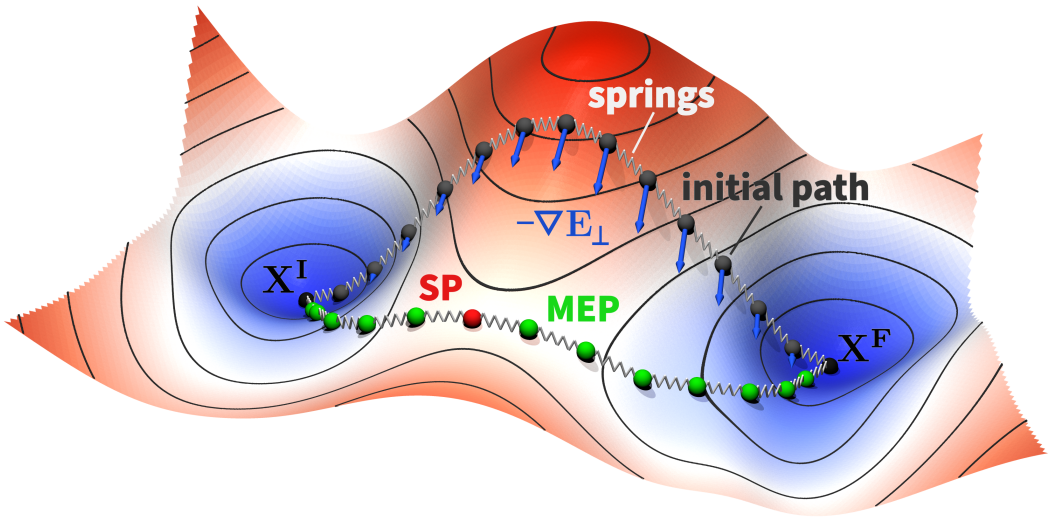

Figure 5.4 | Illustration of the NEB method on the energy surface of a 2D configuration space. The topography and the colour code denote the energy at the corresponding in-plane position. Isolines of constant energy are shown as black contours. Two local energy minima $\mathbf{X}^\mathrm{I}$ and $\mathbf{X}^\mathrm{F}$ are linked by the initial path, which consists of 15 images (dark grey spheres) connected by artificial springs (light grey). By following the negative local energy gradient, $-\nabla E_\perp^k$ (blue), at each image, the path is energetically relaxed into the minimum energy path (MEP, green) iteratively while the even distribution of images is ensured by the springs. The saddle point (red) of the MEP can be found by the climbing image method.

For the formation of a transition path Γ, both energy minima are connected by a discrete chain of M intermediate states, called images $\mathbf{I}^k$ with $k = 1, ..., M$. Each image contains a complete set of magnetic moment orientations with $\mathbf{I}^k = \{\mathbf{m}_1^k, \mathbf{m}_2^k, ..., \mathbf{m}_N^k\}$. The path reads $\Gamma = \{\mathbf{I}^1, \mathbf{I}^2, ..., \mathbf{I}^M\}$, where the first and last images are equal to the initial and final states with $\mathbf{I}^1 = \mathbf{X}^I$ and $\mathbf{I}^M = \mathbf{X}^F$.

The choice of the initial path is arbitrary and only influences the convergence behaviour of the calculation as long as only one MEP exists for the examined transition process. However, if multiple paths are available, the initial path follows the energy gradient to the next path, and the choice thus determines the result of the calculation. To find the globally lowest MEP, a more sophisticated sampling scheme of the initial paths in the configuration space is required [94], which does not yet exist for magnetic lattice systems.

In order to obtain an adequate initial path to perform a GNEB calculation, the geodesic path can be created [94]. It resembles the shortest possible rotation of each

moment $\mathbf{m}_i$ from its initial configuration $\mathbf{m}_i^1$ to its final configuration $\mathbf{m}_i^M$ and can be constructed via the Rodrigues rotation formula [69, 94, 150]:

$$\mathbf{m}_i^k = \mathbf{m}_i^1 \cos\left(\omega_i^k\right) + \left(\mathbf{R}_i \times \mathbf{m}_i^1\right) \sin\left(\omega_i^k\right) \tag{5.8}$$

The normalised axis vector $\mathbf{R}_i$ is orthogonal to the initial and final configuration of the moment $\mathbf{m}_i$ with

$$\mathbf{R}_i = \frac{\mathbf{m}_i^M \times \mathbf{m}_i^1}{|\mathbf{m}_i^M \times \mathbf{m}_i^1|}. \tag{5.9}$$

The angle ω_i^k is given as a multiple of $\Delta\omega_i = \omega_i^{M,1} / (M-1)$, where $\omega_i^{M,1}$ is the angle between $\mathbf{m}_i^M$ and $\mathbf{m}_i^1$. While the geodesic path has been proven to be practical especially for the first GNEB calculations of a system, other paths can be used as initial paths as well.

The relaxation of the selected initial path is performed iteratively by moving each image for each iteration along the negative energy gradient towards the local MEP. The procedure is illustrated in Fig. 5.4. During the following of the negative energy gradient the images are connected by artificial springs, which contract the images and form an "elastic band" that ensures a continuous distribution along the path. Additional "nudging" of the elastic band strictly decouples the direction of the energy gradient and the applied spring forces. Otherwise, the spring forces, which are of arbitrary size, would interfere with the energy gradient, leading to artificial behaviour of the relaxation process [94, 149].

The nudging is realised by applying the spring forces at each image parallel to the direction of the path, while the energy gradient is perpendicular to it. This requires the repeated estimation of the local direction of the path for each image and for each iteration since the images and thereby the path are altered every step of the simulation.

The NEB method is further adapted to lattice systems with constant moment lengths by projecting the local direction of the path and the applied forces into the tangent space of the images. In this curved subspace, the moment sizes are implicitly conserved which increases the numerical accuracy and convergence behaviour of the method now called GNEB.

5.2.2. The tangent space

When formulated in a Euclidean basis, each magnetic moment is described by three coordinates and the constraint of constant length. This way, the NEB method has to explicitly ensure the conservation of moment size during the calculation, e. g. by renomalisation, which can lead to inaccuracies and convergence problems of the method. In order to avoid these complications, the GNEB methods projects all forces onto the tangent space $\tau_{\mathbf{X}}$, a $2N$ dimensional subspace of the $3N$ dimensional configuration space which exhibits no components parallel to the moment vectors of $\mathbf{X} = \{\mathbf{m}_1, \mathbf{m}_2, ..., \mathbf{m}_N\}$, ensuring an implicit conservation of the magnetic moment size.

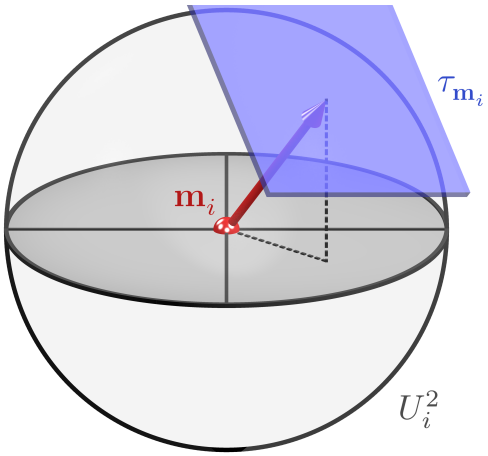

Figure 5.5 | Illustration of the tangent space of an individual magnetic moment. The moment $\mathbf{m}_i$ is pointing on the unit sphere U_i^2. The tangent space $\tau_{\mathbf{m}_i}$ is illustrated as finite, light blue plane. Note that the tangent space is not limited in the directions perpendicular to the moment.

The starting point for the calculation of the tangent space is the representation of each magnetic moment on a two dimensional unit sphere, $\widetilde{\mathbf{m}}_i \in U_i^2$. It considers information about the moment orientation, but not about its radial component which has the fixed value of unity. With this representation, a lattice state $\mathbf{X}$ can be defined on a $2N$ dimensional Riemannian manifold [94]:

$$\widetilde{\mathbf{X}} \in \mathbf{U}^{2N} = \prod_{i=1}^{N} U_i^2. \tag{5.10}$$

The tangent space $\tau_{\mathbf{m}_i}$ to a moment $\mathbf{m}_i$ is dependent on its orientation and is defined by the set of all vectors $\mathbf{A_i}$ orthogonal to it [94]:

$$\tau_{\mathbf{m}_i} = \{\mathbf{A}_i : \mathbf{A}_i \cdot \mathbf{m}_i = 0\}. \tag{5.11}$$

The tangent space of an individual magnetic moment is visualised in Fig. 5.5.

The tangent space $\tau_{\mathbf{X}}$ of a lattice state $\mathbf{X}$ can be defined as the product of the tangent spaces $\tau_{\mathbf{m}_i}$ of the individual magnetic moments $\mathbf{m}_i$ [94]:

$$\tau_{\mathbf{X}} = \prod_{i=1}^{N} \tau_{\mathbf{m}_i}. \tag{5.12}$$

The projection $\mathcal{P}_{\tau_{\mathbf{X}}}$ of an arbitrary $3N$ vector $\mathbf{A} = \{\mathbf{A}_1, \mathbf{A}_2, ..., \mathbf{A}_N\}$ in Euclidean space to the tangent space $\tau_{\mathbf{X}}$ of the lattice state $\mathbf{X}$ can be constructed by eliminating the components of each $\mathbf{A}_i$ parallel to the corresponding individual moment vector $\mathbf{m}_i$ [94]:

$$^{\tau}\mathbf{A}_i \equiv \mathcal{P}_{\tau_{\mathbf{X}}} \mathbf{A}_i = \mathbf{A}_i - (\mathbf{A}_i \cdot \mathbf{m}_i)\, \mathbf{m}_i. \tag{5.13}$$

The projected $2N$ vector $^{\tau}\mathbf{A}$ can be constructed by the individually projected components, each defined on the 2D unit sphere:

$$^{\tau}\mathbf{A} = (^{\tau}\mathbf{A}_1, ^{\tau}\mathbf{A}_2, ..., ^{\tau}\mathbf{A}_N), \tag{5.14}$$

This procedure of projecting a vector to the tangent space allows for an appropriate description of the GNEB in the following.

5.2.3. Local direction of the path

For the correct application of the GNEB forces, the local direction of the path $\hat{\mathbf{L}}^k$ has to be calculated for each individual image $\mathbf{I}^k$. The local direction $\hat{\mathbf{L}}^k$ equates the normalised tangent of the path at the image $\mathbf{I}^k$ and should not be confused with $\tau_{\mathbf{X}}$, the tangent space of the lattice state $\mathbf{X}$.

Since the path is discrete and a functional dependency of the path on the reaction coordinate is almost always unknown, the local direction $\hat{\mathbf{L}}^k$ must be determined approximately. In a simple form, this can be achieved by normalising the difference between the two neighbouring images of image $\mathbf{I}^k$ [149]:

$$\hat{\mathbf{L}}^k = \frac{\mathbf{I}^{k+1} - \mathbf{I}^{k-1}}{\left|\mathbf{I}^{k+1} - \mathbf{I}^{k-1}\right|}. \tag{5.15}$$

While its simplicity makes it fast to implement, this approach can yield local directions of the path too imprecise for a stable and fast convergence of the GNEB [149][94].

A better practice is the case dependent choice of forward and backward tangents between adjacent images, based on their energies [149]. The forward and backward tangents are defined as $\mathbf{L}_+^k = \mathbf{I}^{k+1} - \mathbf{I}^k$ and $\mathbf{L}_-^k = \mathbf{I}^k - \mathbf{I}^{k-1}$, respectively. With E^k being the energy of image $\mathbf{I}^k$, the yet unnormalised tangent is calculated as follows [94, 149]:

$$\mathbf{L}^k = \begin{cases} \mathbf{L}_+^k & \text{if } E^{k+1} > E^k > E^{k-1} \\ \mathbf{L}_-^k & \text{if } E^{k+1} < E^k < E^{k-1} \\ \mathbf{L}_+^k \Delta E_{\max} + \mathbf{L}_-^k \Delta E_{\min} & \text{if } E^{k+1} > E^{k-1} \\ \mathbf{L}_+^k \Delta E_{\min} + \mathbf{L}_-^k \Delta E_{\max} & \text{if } E^{k+1} < E^{k-1} \\ \left(\mathbf{L}_+^k + \mathbf{L}_-^k\right)/2 & \text{if } E^{k+1} = E^{k-1}, \end{cases} \tag{5.16}$$

with the energy differences

$$\begin{aligned} \Delta E_{\min} &= \min\left(|E^{k+1} - E^k|, |E^k - E^{k-1}|\right) \\ \Delta E_{\max} &= \max\left(|E^{k+1} - E^k|, |E^k - E^{k-1}|\right). \end{aligned} \tag{5.17}$$

This distinction of cases selects the forward and backward tangents when the energy of three subsequent images is monotonously increasing and decreasing, respectively. Thus, the path direction is always determined by the adjacent image closer to the SP, which improves the stability of the method against kinks appearing along the path due to the approximate nature of $\hat{\mathbf{L}}^k$ [149]. Cases 3 and 4 ensure, that the transition between cases 1 and 2 is smooth and no jumps in $\hat{\mathbf{L}}^k$ occur when a local energy extremum like the SP is passed [149].

Case 5 is introduced to fill a gap in the definition space of $\mathbf{L}^k$ that has not been addressed in [94, 149]. It ensures numerical stability when the energies of adjacent images are extremely close as it can occur for systems exhibiting Goldstone modes. This extension to the original GNEB method will be discussed in Sec. 5.2.8 in more detail.

Moving the image $\mathbf{I}^k$ a small step along $\mathbf{L}^k$ would still change the radial components of its moments because $\hat{\mathbf{L}}^k$ is not perpendicular to $\mathbf{I}^k$. The components parallel to $\mathbf{I}^k$ can be eliminated by projecting $\mathbf{L}^k$ to the tangent space $\tau_{\mathbf{I}^k}$. With simultaneous

normalisation, this results in [94]

$$ {}^{\tau}\hat{\mathbf{L}}^k = \frac{\mathcal{P}_{\tau_{\mathbf{X}}} \mathbf{L}^k}{\left| \mathcal{P}_{\tau_{\mathbf{X}}} \mathbf{L}^k \right|}. \tag{5.18} $$

This estimation of the local direction of the path enables a stable separation of force components required for GNEB computations.

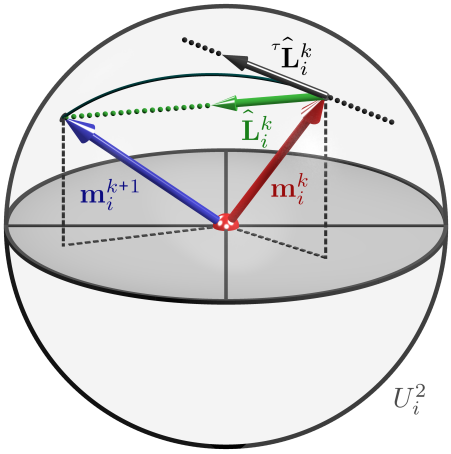

Figure 5.6 | Illustration of the projection of $\hat{\mathbf{L}}_i^k$ to the tangent space $\tau_{\mathbf{m}_i}$. The local direction of the path, $\hat{\mathbf{L}}_i^k$, connects the magnetic moment $\mathbf{m}_i$ of the image $\mathbf{I}^k$ with the moment $\mathbf{m}_{i+1}$ of the image $\mathbf{I}^{k+1}$. Projecting it on the tangent space $\tau_{\mathbf{m}_i}$ yields ${}^{\tau}\hat{\mathbf{L}}_i^k$, ensuring a geodesic movement of $\mathbf{m}_i^k$ on the unit sphere, U_i^2.

5.2.4. Spring forces

With the exception of the stationary start and end points of the path, every image is influenced by the springs of the elastic band. The spring force $\mathbf{F}_{\mathrm{s}}^k$ on image $\mathbf{I}^k$ is applied parallel to ${}^{\tau}\hat{\mathbf{L}}^k$. Therefore, it is acting in tangent space $\tau_{\mathbf{X}}$ per definition and does not require any further projection.

Sign and strength of $\mathbf{F}_{\mathrm{s}}^k$ are determined by the distances $D^{k+1,k}$ and $D^{k,k-1}$ between the image $\mathbf{I}^k$ and the two neighbouring images $\mathbf{I}^{k+1}$ and $\mathbf{I}^{k-1}$, respectively [94]:

$$ \mathbf{F}_{\mathrm{s}}^k = \kappa \left(D^{k+1,k} - D^{k,k-1} \right) {}^{\tau}\hat{\mathbf{L}}^k \tag{5.19} $$

$$ = \mathbf{F}_{\mathrm{s}}^{k,k+1} + \mathbf{F}_{\mathrm{s}}^{k,k-1}. \tag{5.20} $$

The spring constant $\kappa \geq 0$ controls the size of the springs and has the dimension of force per distance. Negative spring constants are excluded, since the springs are

supposed to pull and not push the images, which would cause convergence issues due to kinks in the transition path. If $D^{k+1,k} > D^{k,k-1}$, the forward component of the spring force, $\mathbf{F}_{\mathrm{s}}^{k,k+1}$, is larger than the backward component, $\mathbf{F}_{\mathrm{s}}^{k,k-1}$, moving the image $\mathbf{I}^k$ in positive direction of ${}^{\tau}\hat{\mathbf{L}}^k$ and vice versa.

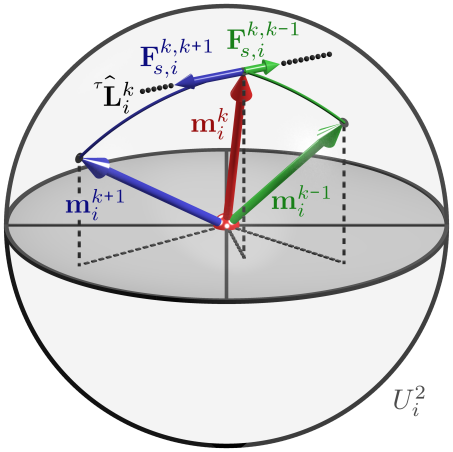

Figure 5.7 | Illustration of the spring force vectors. The forward and backward components of the spring force, $\mathbf{F}_{s,i}^{k,k+1}$ and $\mathbf{F}_{s,i}^{k,k-1}$, are oriented parallel and antiparallel to ${}^{\tau}\hat{\mathbf{L}}_i^k$, ensuring a movement of the moment in tangent space, $\tau_{\mathbf{m}_i}$. The magnetic moments, $\mathbf{m}_i^{k-1}$, $\mathbf{m}_i^k$ and $\mathbf{m}_i^{k+1}$, of three adjacent images, $k-1$, k, $k+1$, are shown as vectors on the unit sphere, U_i^2.

Since the springs are added artificially to the images as part of the method, the choice of the size of κ is arbitrary and only affects the convergence speed but not the result of the calculation. The spring constant can differ from image to image, realising a non-uniform distribution of images [94, 149]. However, for all calculations presented in this thesis, the same spring constant is applied to all images of a calculation and only varies between different calculations.

In GNEB the typical metric for the distance between images is the geodesic distance $D_{\mathrm{geo},i}^{k,l}$ [94]. It measures the length of the perimetric segment covered by an individual magnetic moment $\mathbf{m}_i$ moving between two images $\mathbf{I}^k$ and $\mathbf{I}^l$. The geodesic distance on a unit sphere can be calculated by Vincenty's formula [94, 151]:

$$D_{\mathrm{geo},i}^{k,l} = \arctan 2(|\mathbf{m}_i^k \times \mathbf{m}_i^l|, (\mathbf{m}_i^k \cdot \mathbf{m}_i^l)). \tag{5.21}$$

A definition of the function $\arctan 2$ is given in Eq. A.1. With this, the total geodesic distance between two images is given by [94]

$$D_{\mathrm{geo}}^{k,l} = \sqrt{\left(D_{\mathrm{geo},1}^{k,l}\right)^2 + \ldots + \left(D_{\mathrm{geo,N}}^{k,l}\right)^2}. \tag{5.22}$$

While $D_{\mathrm{geo}}^{k,l}$ enables for GNEB computations as presented in [94], the method is not restricted to the use of geodesic distances [148]. In some cases, the energy difference between images or a hybrid measure of energy and geodesic distance is better suited to achieve an optimal image distribution. The formulation of these metrics is presented in Sec. 5.2.7.

5.2.5. Relaxation of the path

With the ingredients presented in the previous sections, the procedure of the path relaxation can be formulated. The force $\mathbf{F}_{\mathrm{GNEB}}^{k}$ applied to the image $\mathbf{I}^{k}$ is composed out of the spring force $\mathbf{F}_{\mathrm{s}}^{k}$ and the negative energy gradient $\mathbf{F}_{\mathrm{g}}^{k} = -\nabla E^{k}$ at each iteration.

Per construction, the spring force $\mathbf{F}_{\mathrm{s}}^{k}$ is parallel to ${}^{\tau}\hat{\mathbf{L}}^{k}$, while $\mathbf{F}_{\mathrm{g}}^{k}$ can exhibit contributions in all $3N$ directions.

In order to realise the separation of spring force and energy gradient, the components of $\mathbf{F}_{\mathrm{g}}^{k}$ parallel to the local direction of the path are eliminated [94]:

$$\mathbf{F}_{\mathrm{g},\perp}^{k} = -\nabla E^{k} + \left(\nabla E^{k} \cdot {}^{\tau}\hat{\mathbf{L}}^{k}\right) {}^{\tau}\hat{\mathbf{L}}^{k} \tag{5.23}$$

Projecting the sum of both forces into the tangent space results in the GNEB force with [94]

$$\mathbf{F}_{\mathrm{GNEB}}^{k} = \mathcal{P}_{\tau_{\mathbf{x}}} \left(\mathbf{F}_{\mathrm{g},\perp}^{k} + \mathbf{F}_{\mathrm{s}}^{k}\right). \tag{5.24}$$

Due to the projection, it can be applied to image $\mathbf{I}^{k}$ to follow the inverse energy gradient in each iteration without changing the radial components of the moments.

For the displacement of $\mathbf{I}^{k}$ along $\mathbf{F}_{\mathrm{GNEB}}^{k}$ an overdamped version of the Landau-Lifshitz equation (Eq. 5.2) is used, in which the precession term is neglected. Note, that the tangent spaces, $\tau_{\mathbf{I}^{k}}$, and the local directions of the path, ${}^{\tau}\hat{\mathbf{L}}^{k}$, have to be recalculated after each step of the iteration to accurately project the forces. A GNEB calculation is considered converged, if $|\mathbf{F}_{\mathrm{GNEB}}^{k}| < F_{\mathrm{conv}}\ \forall k$, where F_{conv} is a predefined convergence criterion.

In order to give an example of a GNEB calculation, the energies of images along the transition of an isolated skyrmion into the ferromagnetic (FM) state are shown over the reaction coordinate in Fig. 5.8. In panel a, the energies of the geodesic

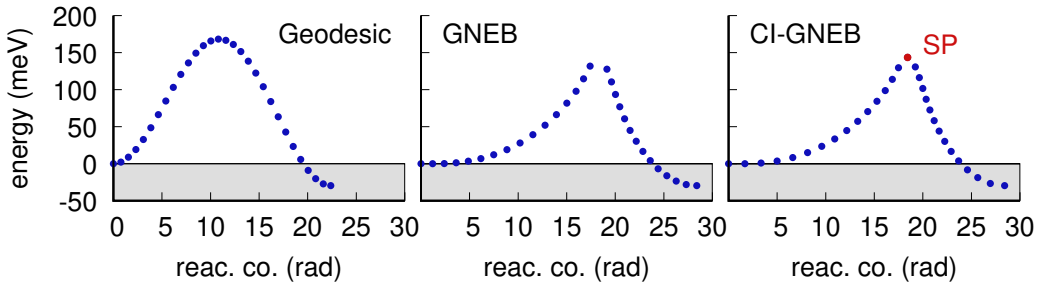

Figure 5.8 | The energies of transition path images determined with three different methods. The paths are obtained by linear interpolation **(left)**, GNEB **(centre)** and CI-GNEB **(right)**. Each path consists of 30 images and describes the transition of an isolated skyrmion into the FM state in fcc-Pd/Fe/Ir(111) with an external out-of-plane magnetic field of $B = 4\mathrm{T}$. The paths obtained by GNEB and CI-GNEB show a radial collapse mechanism. The energies are displayed relative to the energies of the initial states.

path are displayed, which consists of 30 images and serves as the initial path of the calculation. Fig. 5.8 b shows the energies of the corresponding MEP obtained by the GNEB method.

The images of the MEP already provide detailed information about the transition mechanism in form of lattice states occurring along the MEP. In this case, they show a radial collapse of the skyrmion, which is presented in detail in Sec. 6.5. However, the GNEB distributes the images such that no distinguished image is placed at the SP, which often is located between two images. The position of the SP can be approximated via interpolation, but is determined more accurately via the climbing-image GNEB method.

5.2.6. Climbing image GNEB method

The climbing image GNEB (CI-GNEB) method presented here was originally developed for the NEB method by Henkelman *et al.* [148] and later transferred to the GNEB by Bessarab *et al.* [94]. It is typically applied subsequently to a roughly converged GNEB calculation.

In CI-GNEB calculations, the image with the highest energy of the path is selected as "climbing image" $\mathbf{I}^{\mathrm{CI}}$. The same GNEB forces $\mathbf{F}^k_{\mathrm{GNEB}}$ are applied to all images but the climbing image $\mathbf{I}^{\mathrm{CI}}$. For $\mathbf{I}^{\mathrm{CI}}$, the spring force, $\mathbf{F}^k_{\mathrm{s}}$, is deactivated and replaced

by the component of the energy gradient along the path, yielding [94]:

$$\mathbf{F}^{\mathrm{CI}}_{\mathrm{GNEB}} = -\nabla E^{\mathrm{CI}} + 2\left(\nabla E^{\mathrm{CI}} \cdot {}^{\tau}\hat{\mathbf{L}}^{\mathrm{CI}}\right) {}^{\tau}\hat{\mathbf{L}}^{\mathrm{CI}}. \tag{5.25}$$

This force is applied to the climbing image, which in turn is not affected by the spring forces of adjacent images. Instead, it can follow the energy gradient upwards in the direction of ${}^{\tau}\hat{\mathbf{L}}^{\mathrm{CI}}$, while it still energetically optimises the path by following $\mathbf{F}^{k}_{\mathrm{g},\perp}$ perpendicular to ${}^{\tau}\hat{\mathbf{L}}^{\mathrm{CI}}$. By iteratively relaxing the path with the CI-GNEB method, the image $\mathbf{I}^{\mathrm{CI}}$ reaches the local energy maximum in direction of ${}^{\tau}\hat{\mathbf{L}}^{\mathrm{CI}}$ which is identical to the SP of the MEP.

In Fig. 5.8 c, the path of 5.8 b is further relaxed with the CI-GNEB. While the MEP itself is very similar to one obtained by GNEB, a distinct point at the maximum of the MEP can be seen in case of the relaxation by CI-GNEB. The accurate determination of the SP allows for the extraction of the energy barrier and a deeper insight of the transition mechanism of the MEP in general.

5.2.7. Extension to the method: Spring forces via energetic distance of the images

The evaluation of distances between images is not restricted to the difference in reaction coordinate [94, 148]. When MEPs exhibit a very steep increase or decrease in energy over only a few images, a distance metric based on the geodesic distance alone can result in an insufficient image distribution. While this primarily means a lack of information about a critical part of the MEP, it can also prevent the algorithm to find accurate estimates of the path direction, which in turn hinders convergence of the calculation. Here, the difference in energy is explored as an additional measure for the distance between images in order to address this problem.

Analogue to the geodesic distance in Eq. 5.22, the energetic distance between two images $\mathbf{I}^{k}$ and $\mathbf{I}^{l}$ reads

$$D^{k,l}_{\mathrm{en}} = \sqrt{\left(\Delta E^{k,l}_{\mathbf{m}_1}\right)^2 + ... + \left(\Delta E^{k,l}_{\mathbf{m}_N}\right)^2}, \tag{5.26}$$

where the energetic distance of an individual magnetic moment between the images $\mathbf{I}^{k}$ and $\mathbf{I}^{l}$ is given by $\Delta E^{k,l}_{\mathbf{m}_i} = E^{k}_{\mathbf{m}_i} - E^{l}_{\mathbf{m}_i}$. Applying this metric directly to Eq. 5.20

by replacing the geodesic distance, the GNEB distributes images on the energy axis evenly.

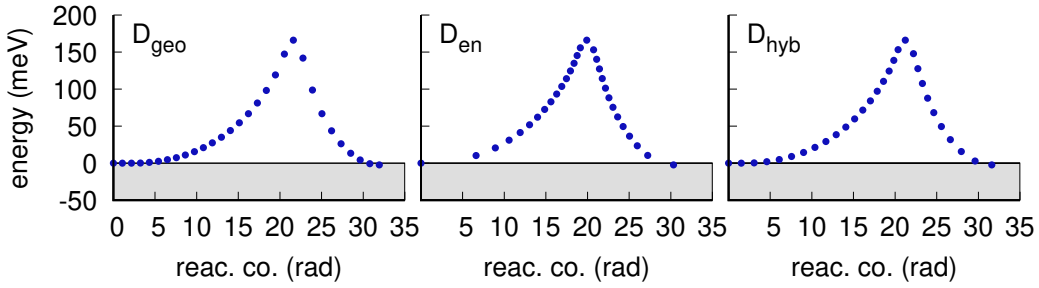

Figure 5.9 | Minimum energy paths obtained by three different measures of distance. The shown paths of the radial symmetric skyrmion collapse are calculated by CI-GNEB and spring forces using the geodesic distance D_{geo} **(left)**, energetic distance D_{en} **(centre)** and hybrid measure D_{hyb} **(right)**. The calculation was performed with 30 images and the parameters of fcc-Pd/Fe/Ir(111) at $B = 3.2\,\mathrm{T}$ and the energies are relative to the initial skyrmion state.

To give an example of the resulting image distributions, the MEPs of a radial symmetric skyrmion collapse obtained with different metrics are shown in Fig. 5.9. The geodesic distance yields images evenly distributed over the reaction coordinate while some gaps are visible on the energy axis in the vicinity of the SP. In contrast, the images of the energy metric are equally spaced on the energy axis. This results in more images placed around the SP while the energetically shallow regions at the beginning and ending of the path are sampled less frequently.

A hybrid measure, D_{hyb}, can be defined to combine the advantages of, both, the geodesic and energetic metrics. It is defined as

$$D_{\mathrm{hyb}} = \sqrt{\kappa_{\mathrm{geo}} \left(D_{\mathrm{geo}}^{k,l}\right)^2 + \kappa_{\mathrm{en}} \left(D_{\mathrm{en}}^{k,l}\right)^2}, \tag{5.27}$$

where the parameters κ_{geo} and κ_{en} control the proportion of the two individual measures.

Fig. 5.9 c shows the distribution for the same radial skyrmion collapse as before, but obtained with the hybrid metric, D_{hyb}. While not being equidistant with respect to one of the two axes anymore, the images cover the entire MEP evenly. Since the energy difference is not linear dependent on the geodesic distance, the best choice of κ_{geo} and κ_{en} is not obvious. In calculations performed for this work, both constants

are selected by hand to ensure a sufficient resolution and convergence for the studied transitions.

5.2.8. Extension to the method: Local direction of the path for images with equal energies

In the original publications of Henkelman *et al.* [149] and Bessarab *et al.* [94], the local direction of the path $\hat{\mathbf{L}}^k$ is not defined when the energies of the image $\mathbf{I}^k$ is equal to the energy of both adjacent images $\mathbf{I}^{k+1}$ and $\mathbf{I}^{k-1}$. The contributions of the forward and backward tangents are weighted with the energy differences between the images which both become zero if $E^{k+1} = E^k = E^{k-1}$. Hence, the subsequent normalisation, $\hat{\mathbf{L}}^k = \mathbf{L}^k/|\mathbf{L}^k|$, yields a division by zero causing the calculation to crash due to a "not a number" error.

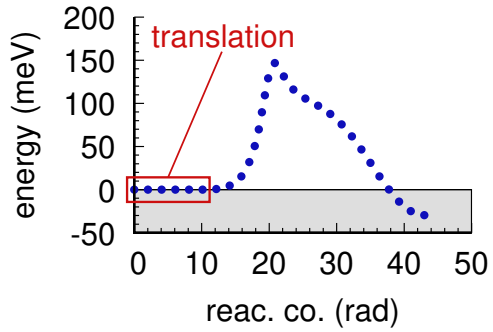

Figure 5.10 | Example of a minimum energy path with a reaction coordinate partially along a Goldstone mode. The minimum energy path of skyrmion collapse into the FM state in fcc-Pd/Fe/Ir(111) at $B = 4$ T via the the chimera mechanism is calculated via CI-GNEB. The images corresponding to a free translation of the skyrmion on the lattice are marked by a red box.

Normally, such a condition is rarely fulfilled as a finite geodesic distance between the images is typically linked to a finite difference in energy. However, when the MEP evolves partially along Goldstone modes, the energy on this part of the path is preserved and adjacent images show little to no energy differences.

As an example, the MEP of an isolated skyrmion collapsing via the chimera-type mechanism in fcc-Pd/Fe/Ir(111) is shown in Fig. 5.10. In the area of the path marked by a red box, the skyrmion translates across the lattice under almost constant energy. Hence, the condition $E^{k+1} = E^k = E^{k-1}$ can be fulfills several times during the relaxation process of this path.

In seeking to enable GNEB calculations in which the condition $E^{k+1} = E^k = E^{k-1}$ occurs to be fulfilled, case 5 of Eq. 5.16 is introduced. It simply takes the mean

value of the forward and backward tangent at $\mathbf{I}^k$ instead of weighting them with the energy differences and thus avoiding a tangent of the path with $|\mathbf{L}^k| = 0$.

While the introduction of case 5 allows for GNEB calculations of MEPs along Goldstone modes, the transition between the cases is not ensured to be steady. For example, if the forward tangent $\mathbf{L}_+^k$ is selected by case 1 in one iteration and the condition $E^{k+1} = E^k = E^{k-1}$ occurs in the next iteration, the local direction of the path suddenly jumps from $\mathbf{L}^k = \mathbf{L}_+^k$ to $\mathbf{L}^k = \left(\mathbf{L}_+^k + \mathbf{L}_-^k\right)/2$, potentially causing convergence issues.

A solution to this problem is the introduction of an envelope function $f_{\mathrm{mix}}\left(\Delta E_{\mathrm{max}}\right) = \Delta E_{\mathrm{max}}/\Delta E_{\mathrm{thr}}$. When the largest energy difference between adjacent images, ΔE_{max}, becomes smaller than a threshold parameter, ΔE_{thr}, the envelope function mixes the direction of the path calculated from Eq. 5.16 with the averaged direction $\left(\mathbf{L}_+^k + \mathbf{L}_-^k\right)/2$ to create the more stable local path direction $\mathbf{L}_{\mathrm{mix}}^k$:

$$\mathbf{L}_{\mathrm{mix}}^k = f_{\mathrm{mix}}\mathbf{L}^k + \left(1 - f_{\mathrm{mix}}\right)\left(\mathbf{L}_+^k + \mathbf{L}_-^k\right)/2. \tag{5.28}$$

Finally, the normalised local direction of the path is obtained by $\hat{\mathbf{L}}_{\mathrm{mix}}^k = \mathbf{L}_{\mathrm{mix}}^k/|\mathbf{L}_{\mathrm{mix}}^k|$.

5.3. Transition state theory

In transition state theory (TST), the evolution of a thermally activated system between two metastable states is described by the flux of states through the bottle neck of the transition, the transition state. It was developed in the 1930s [147, 152–156] for the determination of chemical reaction rates and soon became a well established method applied in numerous fields of chemistry [157, 158].

In the framework of this thesis, the TST has been implemented into the atomistic spin simulations code of the group of Prof. Dr. Stefan Heinze in seeking to describe switching rates of magnetic lattice states. The implementation has been supervised by Dr. Pavel Bessarab, who originally applied the transition state theory to atomistic spin lattice systems [93, 159, 160]. In the following, the basic ideas of TST and its application to atomistic spin lattices are presented.

Considering a $3N$ dimensional system, the configuration space is formally divided into two parts, one of which contains the initial state $\mathbf{X}^{\mathbf{I}}$ and the other the final state

$\mathbf{X^F}$. The two sections, labelled A and B, are separated by a $3N-1$ dimensional dividing surface, S, as it is illustrated in Fig. 5.11. All states of the system lying on this surface are referred to as transition state.

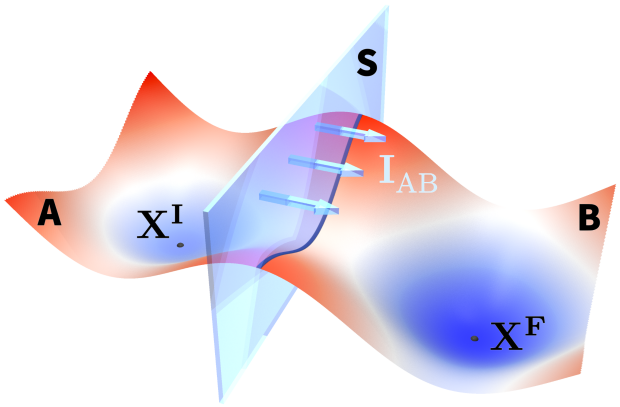

Figure 5.11 | Illustration of the flux through the dividing surface. The dividing surface (S) separates the configuration space in the two subspaces A and B, which contain the initial state, $\mathbf{X}^{\mathrm{I}}$, and the final state, $\mathbf{X}^{\mathrm{F}}$. The flux of states through the dividing surface, I_{AB}, is indicated by light blue arrows at S pointing towards B.

For a transition from A to B, the system has to cross S, which yields the flux through the dividing surface, I_{AB}. The flux is constructed from the velocity component of each state on S perpendicular to the dividing surface, weighted by the occupation probability of the respective state. In a statistical approach, the transition rate ν_{AB} is given by the ratio of the flux I_{AB} to Q_A, the probability of the system to occupy the part of phase space labelled A [161]:

$$\nu_{AB} = \frac{1}{\tau_A} = \frac{I_{AB}}{Q_A}. \tag{5.29}$$

The transition rate ν_{AB} is given in units of per second and inverse to the mean time τ that the system remains in part A of the configuration space.

In case of additional metastable states occurring along relevant trajectories from $\mathbf{X^I}$ to $\mathbf{X^F}$, the subsequent transitions have to be calculated individually. However, often one of these serial sub-transitions is the bottleneck of the total transition that defines the reaction dynamics, and therefore other sub-transitions are negligible [148].

In other cases, A and B are connected by multiple transition mechanisms simultaneously. Then again, each mechanism determines an individual transition rate ν_j and

the sum of the rates denotes the total rate [90],

$$\nu_{AB} = \sum_{j}^{R} \nu_j, \tag{5.30}$$

where R is the number of parallel transition mechanisms involved. In the following the approach of the theory of transition states is explained using the simplest example of one single transition mechanism that directly connects two metastable states.

5.3.1. The dividing surface

The construction of the dividing surface is inevitably connected to the approximation of "no recrossings", which plays an important role in TST [162]. It is assumed, that once a trajectory passes through S, it remains on the other side of the surface. This approximation is implied in Eq. 5.29, as it only takes the flux I_{AB} into account, but not the flux in opposite direction, I_{BA}.

In principle, a dividing surface can be placed anywhere in phase space, as long as it cogently assigns two parts of the phase space to the initial and final state [162]. Assuming the thermal energy of the system to be much smaller than the energy barrier of the transition, thermally activated transitions are rare events. Thus, by placing the dividing surface on top of the energy barrier, a trajectory that just crossed S is more likely to follow the energy gradient towards the final state than to move energetically uphill for a repeated crossing of S. Therefore, a properly placed dividing surface as illustrated in Fig. 5.12 supports the important condition of no recrossings in TST [162]. Typically, the dividing surface is constructed perpendicular to the isolines of the potential energy while passing through the saddle point (SP) of a minimum energy path (MEP). In this way it consists of the energetically most unfavourable states of the configuration space between $\mathbf{X}^I$ and $\mathbf{X}^F$.

Besides the minimisation of recrossings, the placement of the dividing surface on the SP of a MEP yields further advantages. The SP is a well defined point in phase space which can be determined via the CI-GNEB method presented in Sec. 5.2. The SP is also a fairly good expansion point for the harmonic approximation, as discussed in Sec. 5.3.3. Finally, such a dividing surface minimises recrossings in both transition directions and thus, can be used for the calculation of the reverse transition rate ν_{BA}.

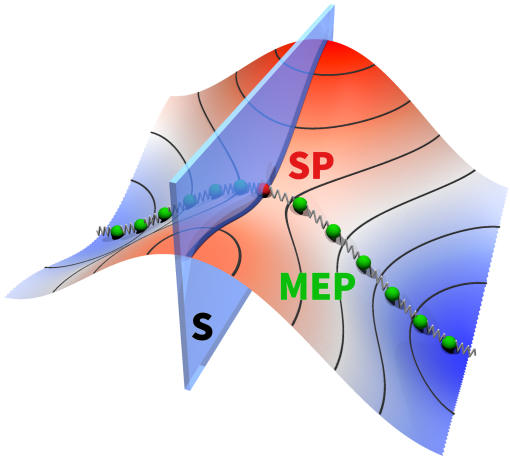

Figure 5.12 | Placement of the dividing surface. The dividing surface (S) is placed on the saddle point (SP) of the considered minimum energy path (MEP). Away from the SP, the dividing surface lies on the corresponding local maximum of the energy landscape, i. e. perpendicular to the isolines (black lines).

However, the occurrence of recrossing events cannot be prevented entirely, especially, when thermal energy becomes comparable with or higher than the energy barrier, or when the energy landscape around the SP is shallow. One option to estimate the amount of recrossing events is the performance of direct dynamical simulations as e. g. Langevin dynamics in magnetic lattice systems [160]. In this approach, the appearance of recrossing events is sampled by a large number of short-time dynamical simulations performed in the vicinity of the SP. The statistical evaluation of the recrossing dynamics yields the recrossing correction factor $\nu_{rc} \in [0, 1]$ with [93, 147]

$$\nu' = \nu_{rc}\nu. \tag{5.31}$$

It reduces the rate ν obtained by Eq. 5.29, which overestimates the transitions from A to B due to the omission of recrossing attempts returning to A after initially passing S. As a result, the recrossing corrected rate ν' is smaller than ν, which can be interpreted as an upper limit of the transition rate without recrossings.

5.3.2. Classical approximation on magnetic lattices

Since the early days of transition state theory, quantum mechanical evaluations of Eq. 5.29 were performed and discussed [147, 158, 162]. Quantum mechanical tunneling can lead to ”corner cutting” effects [162], in which the system avoids the SP of the transition by tunneling through the barrier at lower energies.

For magnetic lattice systems, however, a direct quantum mechanical calculation of the phase space is not feasible. Instead, the lattice systems of this work are described in quasi-classical approximation by applying the extended Heisenberg model introduced in Chap. 2.

Assuming a classical, canonical ensemble of lattice systems consisting of N magnetic moments in thermal equilibrium with a heat bath providing the temperature T, the occupation probability p of a lattice state $\mathbf{X} = (\mathbf{m}_1, ..., \mathbf{m}_N)$ is given by the Boltzmann distribution with [163]

$$p\left(\mathbf{X}\right) = \frac{1}{C} \mathrm{e}^{-\beta E(\mathbf{X})}. \tag{5.32}$$

Here, C is the partition function and $E\left(\mathbf{X}\right)$ the Hamiltonian of the extended Heisenberg model. This allows for the explicit formulation of Q_A with

$$Q_A = \frac{1}{C} \int_A \mathrm{e}^{-\beta E(\mathbf{X})} \mathrm{d}^N \mathbf{m}. \tag{5.33}$$

The flux of states through the dividing surface, I_{AB}, is formulated as the sum over all transition states times their velocities in the direction of B. By applying the Boltzmann distribution of the canonical ensemble analogously to Q_A, the flux reads [93, 159, 160, 162, 164]

$$I_{AB} = \frac{1}{C} \int_A \mathrm{e}^{(-\beta E(\mathbf{X}))} v_\perp\left(\mathbf{X}\right) h\left[v_\perp\left(\mathbf{X}\right)\right] \delta\left[f(\mathbf{X})\right] \mathrm{d}^N \mathbf{m}. \tag{5.34}$$

The function $f\left(\mathbf{X}\right)$ describes the dividing surface and becomes zero only when $\mathbf{X}$ lies on the surface and remains non-zero otherwise. The integral is formulated such, that it is performed over the complete subspace of A while the delta function $\delta\left[f(\mathbf{X})\right]$ ensures that only transition states contribute to the integral. The velocity of a state $\mathbf{X}$ perpendicular to the dividing surface is given by $v_\perp\left(\mathbf{X}\right)$. The Heaviside step function $h\left[v_\perp\left(\mathbf{X}\right)\right]$ realises the approximation of no recrossings, as it becomes unity only for positive velocities in the direction of B and remains zero otherwise.

The classical approximation of the system presented here enables for the explicit formulations of Q_A and I_{AB}, but a direct analytical solution of Eq. 5.33 and Eq. 5.34 still remains challenging due to the non-collinear nature of the extended Heisenberg Hamiltonian, $E\left(\mathbf{X}\right)$.

5.3.3. Harmonic approximation

In seeking an analytical solution for the integrals in Eq. 5.33 and 5.34, a multidimensional Taylor expansion of the energy landscape is performed for, both, the energy landscape of A as well as the energy landscape on the dividing surface. The initial state serves as expansion point for A, since it is the local energy minimum and, thus, states in its vicinity have the highest occupation probability. For the dividing surface the energy is expanded around the SP, which is the local energy minimum of the transition states and therefore has the most relevant reactive states in its vicinity.

Starting with the initial state, the first derivative of the energy to excitations of the system vanishes for all coordinates as the initial state is a local energy minimum. Thus, the second order term of the Taylor expansion is decisive, resulting in the harmonic approximation of the energy:

$$E^I(\mathbf{X}) \approx E_0^{\mathrm{I}} + \frac{1}{2}\sum_{i=1}^{3N}\sum_{j=1}^{3N}\left(m_i - m_i^{\mathrm{I}}\right)\left(m_j - m_j^{\mathrm{I}}\right)\left[\frac{\partial^2 E(\mathbf{X})}{\partial m_i \partial m_j}\right]_{\mathbf{X}=\mathbf{X}^{\mathrm{I}}}. \tag{5.35}$$

Due to the coupling between the individual magnetic moments, most summands of the second order terms depend on multiple coordinates, which makes them difficult to process analytically in the following.

The second order summands can be decoupled by changing to a diagonalised basis. For this reason, first, the Hessian matrix in $3N$ coordinates is constructed by

$$\mathcal{H}_{ij}^{3N} = \frac{\partial^2 E(\mathbf{X})}{\partial m_i \partial m_j}. \tag{5.36}$$

Hence, the $3N$ Hessian has the following form [XII]:

$$\mathcal{H}^{3N} = \begin{pmatrix} \frac{\partial^2 E(\mathbf{X})}{\partial m_{1,x}\partial m_{1,x}} & \frac{\partial^2 E(\mathbf{X})}{\partial m_{1,x}\partial m_{1,y}} & \cdots & \frac{\partial^2 E(\mathbf{X})}{\partial m_{1,x}\partial m_{N,z}} \\ \frac{\partial^2 E(\mathbf{X})}{\partial m_{1,y}\partial m_{1,x}} & \frac{\partial^2 E(\mathbf{X})}{\partial m_{1,y}\partial m_{1,y}} & \cdots & \frac{\partial^2 E(\mathbf{X})}{\partial m_{2,x}\partial m_{N,z}} \\ \vdots & \vdots & \ddots & \vdots \\ \frac{\partial^2 E(\mathbf{X})}{\partial m_{N,z}\partial m_{1,x}} & \frac{\partial^2 E(\mathbf{X})}{\partial m_{N,z}\partial m_{1,y}} & \cdots & \frac{\partial^2 E(\mathbf{X})}{\partial m_{N,z}\partial m_{N,z}} \end{pmatrix} \tag{5.37}$$

Note, that this matrix is a banded matrix as long as the dipole-dipole interaction is neglected and that the width of the diagonal band is determined by the number of interacting lattice shells.

The derivatives of the energy in Eq. 5.36 and 5.37 can be performed analytically, which allows for the implementation of an algorithm that calculates $\mathcal{H}_{ij}^{3N}$ from the Hamiltonian of the system and the magnetic moment configurations $\mathbf{X}$ of the expansion point. However, the constraint of $|\mathbf{m}_i| = 1$ is not yet fulfilled in the Eq. 5.35, 5.36 and 5.37. It can be considered by subtracting the Lagrange multiplier $\lambda_i = \mathbf{m}_i \cdot \mathbf{B}_i^{\text{eff}}$, sometimes called shape operator [XII, 165], from the diagonal elements of the matrix:

$$\widetilde{\mathcal{H}}^{3N} = \mathcal{H}^{3N} + \mathcal{I}^{3N}\lambda_i. \tag{5.38}$$

Here, $\mathcal{I}^{3N}$ is the $3N \times 3N$ unity matrix and $\mathbf{B}_i^{\text{eff}}$ the effective field at the lattice site i.

Subsequently, the $3N$ Hessian, $\widetilde{\mathcal{H}}^{3N}$, is projected on the tangent space of $\mathbf{X}$ (see Sec. 5.2.2), resulting in the $2N$ Hessian matrix, $\widetilde{\mathcal{H}}^{2N}$, spanned by the generalised coordinates $\widetilde{Q} = (\widetilde{q}_i, ..., \widetilde{q}_{2N})$. While $\widetilde{\mathcal{H}}^{2N}$ could be written in spherical coordinates, this approach suffers from instabilities at the poles [XII, 94, 165]. Thus, the generalised coordinates are written in Cartesian coordinates defined in the tangential subspace of the Euclidean space [94], whose curvature is ensured by the Lagrange multipliers applied to the Hessian in Eq. 5.38 [XII, 94, 165].

Direct diagonalisation of $\widetilde{\mathcal{H}}^{2N}$ yields the diagonalised Hessian matrix $\mathcal{H}^{2N}$ and the basis of eigencoordinates $\mathbf{Q} = (q_1, q_2, ..., q_{2N})$, which correspond to the eigenvectors of $\mathcal{H}^{2N}$. The eigenvalues of the Hessian matrix, ϵ_i, are equivalent to the second order derivatives of the Taylor expansion, performed in the basis of eigencoordinates $\mathbf{Q}$:

$$\epsilon_i^{\text{I}} = \left[\frac{\partial^2 E(\mathbf{Q})}{\partial^2 q_i}\right]_{\mathbf{Q}=\mathbf{Q}^{\text{I}}} \tag{5.39}$$

With this, the harmonic approximation of the energy around the initial state simplifies to [93]

$$E^I(\mathbf{Q}) \approx E_0^{\text{I}} + \frac{1}{2}\sum_{i=1}^{2N} q_i^2 \epsilon_i^{\text{I}}. \tag{5.40}$$

The harmonic approximation of the energy landscape, $E(q_i)$, along the eigenvector q_i is illustrated in Fig. 5.13. The eigenvalue ϵ_i is equivalent to the curvature of the

energy landscape along q_i and the quality of the harmonic approximation depends on the form of the energy surface around $\mathbf{X}^{\mathrm{I}}$ and the thermal energy.

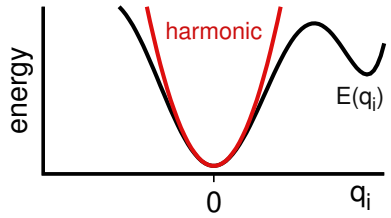

Figure 5.13 | Illustration of the harmonic approximation. At $q_i = 0$, the curvature of the energy landscape $E(q_i)$ is approximated by the parabola shape of a harmonic oscillator.

When the thermal energy is small, only states close to the expansion point are occupied and it can be assumed that the energy landscape is described sufficiently well in harmonic approximation. For increasing energies, however, the approximated parabola and the real energy landscape of the eigenmode increasingly deviate until the harmonic approximation does not hold any more.

The expansion of the SP energy can be performed analogously to the initial state, [93]

$$E^{SP}(\mathbf{Q}) \approx E_0^{\mathrm{SP}} + \frac{1}{2}\sum_{i=1}^{2N} q_i^2 \epsilon_i^{\mathrm{SP}}, \tag{5.41}$$

with the sole difference of a single eigenvalue occurring to be negative. This eigenvalue corresponds to the unstable mode, which is equivalent to the direction of the reaction coordinate at the SP and perpendicular to the dividing surface. The eigenvalues of the unstable mode is negative since $\mathbf{X}^{\mathrm{SP}}$ is a local energy maximum in the direction of the mode and, thus, exhibits a negative curvature of the energy landscape.

By convention, the eigenvalues are sorted in increasing order. This results in the first eigenvalue of the SP being negative, since it belongs to the unstable mode of the transition. In contrast, all other eigenvalues of the SP state, ϵ_i^{SP}, and all eigenvalues of the initial state, ϵ_i^{I}, are larger or equal to zero. In practice, when the first eigenvalue of the initial state occurs to be negative, the selected initial state is not a local energy minimum of A and further energetic relaxation is necessary.

Applying the harmonic approximation to Eq. 5.33, the probability Q_A reads

$$Q_A = \frac{1}{C}\int_{-\infty}^{\infty} \mathrm{e}^{-\beta\left(E_0^{\mathrm{I}} + \frac{1}{2}\sum_{i=1}^{2N} q_i^2 \epsilon_i^{\mathrm{I}}\right)} \mathrm{d}^{2N} q_i \tag{5.42}$$

Here, the limits of the integration are changed from A to infinity, which enables for an easier evaluation of the integral. This is justified if no eigenvalue is extremely close to zero as the exponent quickly converges to zero for large amplitudes of q_i. The rearrangement of the integrals yields:

$$\begin{aligned} Q_A &= \frac{\mathrm{e}^{-\beta E_0^{\mathrm{I}}}}{C} \int_{-\infty}^{\infty} \prod_{i=1}^{2N} \mathrm{e}^{-\beta \frac{1}{2} q_i^2 \epsilon_i^{\mathrm{I}}} \mathrm{d}q_i \\ &= \frac{\mathrm{e}^{-\beta E_0^{\mathrm{I}}}}{C} \prod_{i=1}^{2N} \int_{-\infty}^{\infty} \mathrm{e}^{-\beta \frac{1}{2} q_i^2 \epsilon_i^{\mathrm{I}}} \mathrm{d}q_i. \end{aligned} \tag{5.43}$$

Finally, the execution of the Gaussian integrals gives

$$Q_A = \frac{\mathrm{e}^{-\beta E_0^{\mathrm{I}}}}{C} \prod_{i=1}^{2N} \sqrt{\frac{2\pi}{\beta \epsilon_i^{\mathrm{I}}}}. \tag{5.44}$$

The probability to find the system in A depends on the inverse of the eigenvalues ϵ_i and thus the occupation probability increases with a gradually flattening energy landscape around $\mathbf{X}^{\mathrm{I}}$.

In order to calculate the flux I_{AB} from Eq. 5.34 in harmonic approximation, the Taylor expansion is applied to the formula in a first step:

$$\begin{aligned} I_{AB} &= \frac{1}{C} \int_{-\infty}^{\infty} \mathrm{e}^{-\beta\left(E_0^{\mathrm{SP}} + \frac{1}{2}\sum_{i=1}^{2N} q_i^2 \epsilon_i^{\mathrm{SP}}\right)} v_{\perp}(\mathbf{Q})\, h\left[v_{\perp}(\mathbf{Q})\right] \delta\left[f(\mathbf{Q})\right] \mathrm{d}^{2N} q_i \\ &= \frac{\mathrm{e}^{-\beta E_0^{\mathrm{SP}}}}{C} \int_{-\infty}^{\infty} \prod_{i=1}^{2N} \mathrm{e}^{-\beta \frac{1}{2} q_i^2 \epsilon_i^{\mathrm{SP}}} v_{\perp}(\mathbf{Q})\, h\left[v_{\perp}(\mathbf{Q})\right] \delta\left[f(\mathbf{Q})\right] dq_i. \end{aligned} \tag{5.45}$$

The velocity can be calculated from the equation of motion of magnetic lattice systems, the Landau-Lifshitz equation (see Eq. 5.2). In harmonic approximation, the Landau-Lifshitz equation becomes linear, allowing for an analytical solution of the velocity [XII, 93, 159, 165].

At the SP itself, velocities of all modes are zero since the first derivative vanishes. With increasing distance to the SP on the dividing surface along $q_2, ..., q_{2N}$, the energy of states increases proportionally to q_i^2, while the velocity increases linearly with q_i. The energy landscape around the SP in harmonic approximation and the resulting velocities are illustrated in Fig. 5.14. Note, that the unstable mode, q_1,

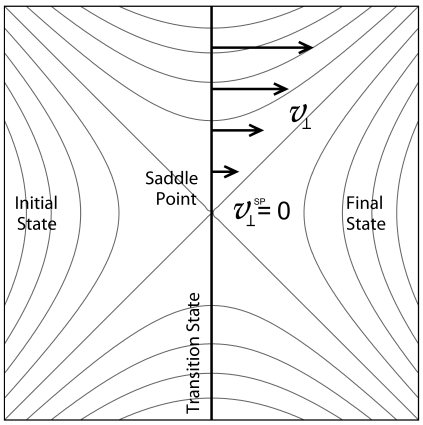

Figure 5.14 | Illustration of the velocity contributions in harmonic approximation in the direction of the final state. The isolines of the energy in harmonic approximation are shown for the example of a 2D configuration space. The mode along the transition state is stable, while the mode along the reaction coordinate is unstable. The velocity is zero on the SP and increases proportional with the distance from it. Figure is reprinted with permission from P. F. Bessarab, V. M. Uzdin, H. Jónsson, "*Potential energy surfaces and rates of spin transitions*"; in: Zeitschrift für Physikalische Chemie, **227**, Ort: DeGruyter, 2013, S. 1551, Abb. 2 [159].

evolves perpendicular to the dividing surface and therefore yields no further transition states that could contribute.

From the two terms of the Landau-Lifshitz equation, the damping term always points in the direction of the inverse energy gradient and thus towards the SP. Therefore, it does not contribute to the orthogonal velocity, $v_\perp(\mathbf{Q})$. This is an important difference between the TST and Langer's theory, which is otherwise very similar to the TST [67, 166].

The precessional term, on the other hand, contributes to $v_\perp(\mathbf{Q})$ as it lies perpendicular to the dividing surface. By applying the Gilbert formulation of the LL equation (Eq. 5.4), the transition rate becomes dependent on the Gilbert damping parameter. However, this dependence only rescales the time axis (see Sec 5.1.1) and is negligible for weak to medium couplings.

The orthogonal velocity of the state $\mathbf{Q}$ can be written in the eigenbasis of $\mathcal{H}^{2N}$ as the sum over all eigencoordinates [91, 93, 159]

$$v_\perp(\mathbf{Q}) = \gamma \sum_{i=2}^{2N} a_i q_i, \tag{5.46}$$

where a_i are the linear slopes of the velocities in the direction of q_i. This makes it possible to separate the dynamic and entropic contributions to the prefactor.

With all contributions of the unstable mode except for $q_1 = 0$ vanishing, the delta function $\delta[f(\mathbf{Q})] = 1$. The Heaviside function divides the integral in two subspaces

with negative and positive contributions of $v_\perp(\mathbf{Q})$.

$$I_{AB} = \frac{\mathrm{e}^{-\beta E_0^{\mathrm{SP}}}}{C} \int_{-\infty}^{\infty} \prod_{i=2}^{2N} \mathrm{e}^{-\beta \frac{1}{2} q_i^2 \epsilon_i^{\mathrm{SP}}} \gamma \sum_{i=2}^{2N} a_i q_i h\left[v_\perp(\mathbf{Q})\right] \mathrm{d}q_i. \tag{5.47}$$

Without further approximations, this integral can be solved analytically [91]:

$$I_{AB} = \frac{\gamma}{\sqrt{2\pi\beta}} \frac{\mathrm{e}^{-\beta E_0^{\mathrm{SP}}}}{C} \sum_{i=2}^{2N} \sqrt{\frac{a_i^2}{\epsilon_i^{\mathrm{SP}}}} \prod_{i=2}^{2N} \sqrt{\frac{2\pi}{\beta \epsilon_i^{\mathrm{SP}}}} \tag{5.48}$$

Applying the results of Eq. 5.44 and 5.48 to Eq. 5.29 yields the transition rate in harmonic approximation [91, 93]:

$$\nu_{AB} = \frac{\gamma}{2\pi} \sqrt{\sum_{j=2}^{2N} \frac{a_j^2}{\epsilon_j^{\mathrm{SP}}}} \frac{\prod_{i=1}^{2N} \sqrt{\epsilon_i^{\mathrm{I}}}}{\prod_{j=2}^{2N} \sqrt{\epsilon_j^{\mathrm{SP}}}} \mathrm{e}^{-\beta \Delta E}. \tag{5.49}$$

Here, $\Delta E = E_0^{\mathrm{SP}} - E_0^{\mathrm{I}}$ is the energy barrier of the transition. By labelling ν_0 the prefactor of the transition with

$$\nu_0 = \frac{\gamma}{2\pi} \sqrt{\sum_{j=2}^{2N} \frac{a_j^2}{\epsilon_j^{\mathrm{SP}}}} \frac{\prod_{i=1}^{2N} \sqrt{\epsilon_i^{\mathrm{I}}}}{\prod_{j=2}^{2N} \sqrt{\epsilon_j^{\mathrm{SP}}}}, \tag{5.50}$$

the formula of the transition rate appears in the form of an Arrhenius law, as it has been introduced in Eq. 1.1 [91, 93, 159]:

$$\nu_{AB} = \nu_0 \mathrm{e}^{-\beta \Delta E} \tag{5.51}$$

The derivation of Eq. 5.49 has been performed on the assumption, that all eigenvalues are larger than zero except for the first eigenvalue of the SP. This assumption is justified only, when no Goldstone modes occur in the system.

5.3.4. Goldstone approximation

Not all modes are suited for a description in harmonic approximation. If the energy landscape of a mode, $E(q_i)$, is periodic, which is the case e. g. for the translational

modes of a magnetic skyrmion, it depends on the temperature which approximation is appropriate. In Fig. 5.15, this is illustrated for different levels of thermal energy. In the case of $k_\mathrm{B}T_1$, the parabola of the harmonic approximation coincides with the energy landscape for low thermal energies. However, it strongly deviates when the thermal energy is larger than the amplitude of the oscillation, as it is the case for $k_\mathrm{B}T_2$. In the latter case, the occupation probability of the states along q_i is drastically underestimated by the harmonic approximation.

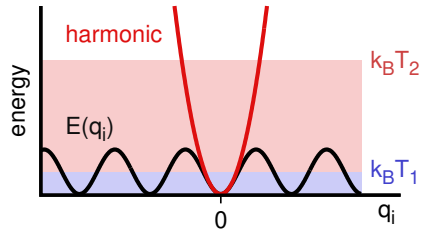

Figure 5.15 | Illustration of the harmonic approximation of a periodic energy landscape. The periodic energy landscape, $E(q_i)$ (black line), is expanded around $q_i = 0$ in harmonic approximation (red line). Examples of small and large thermal energies, $k_\mathrm{B}T_1$ and $k_\mathrm{B}T_2$, are displayed by blue and red shaded areas, respectively.

Another problem occurs when the curvature of the energy landscape is extremely flat, which corresponds to a small eigenvalue ϵ_i. In order to solve the integrals in Eq. 5.43 and Eq. 5.47, the limits of integration have been set to infinity based on the assumption, that the exponent decays quickly enough to not include states outside of A, the considered part of configuration space. When the factor $\beta\epsilon_i$ in Eq. 5.42 and 5.43 is too small, this approximation no longer holds and the integral diverges non-physically. For the case of translational skyrmion modes, this corresponds to the occupation of lattice positions that are not part of the simulation box (see Fig. 5.16).

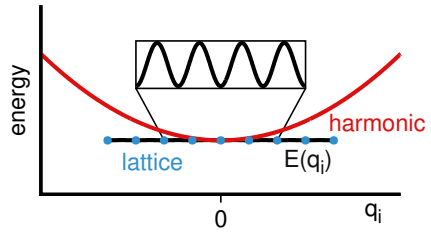

Figure 5.16 | Harmonic approximation of an extremely flat energy landscape. The periodic energy landscape, $E(q_i)$ (black line), is expanded around $q_i = 0$ in harmonic approximation (red line). The finite lattice size of the simulation box is denoted by light blue circles. In the inset, the periodic energy landscape is shown on a finer energy scale.

The Goldstone theorem predicts, that each phase transition breaking a continuous symmetry leads to a continuous low-energy excitation [167, 168]. Therefore, Goldstone

modes corresponds to symmetry operations that do not change the energy of the system [90]. However, while the energy is preserved for some symmetry operations like translations or rotations in a continuum model, they can lead to small energy variations on a discrete lattice. In general, when the amplitude of the energy landscape, ΔE_i, along the eigencoordinate, q_i, is much smaller than the thermal energy, i. e.

$$\Delta E(q_i) \ll k_\mathrm{B} T, \tag{5.52}$$

the energy landscape is better described in Goldstone than in harmonic approximation [II, 67, 90].

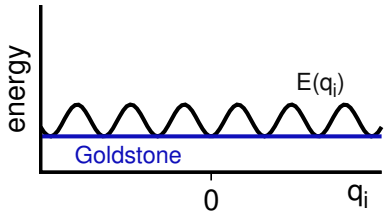

Figure 5.17 | Illustration of the Goldstone approximation. The periodic energy landscape, $E(q_i)$ (black line), is approximated by the constant energy of $E(q_i = 0)$ (blue line).

In Goldstone approximation, the energy of mode q_i is approximated to be constant (Fig. 5.17), which reads

$$E(q_i) = E(0). \tag{5.53}$$

When Eq. 5.52 is fulfilled, the influence of the small energy variation along q_i to the exponent of Eq. 5.32 is negligible and all states are occupied evenly.

Inserting the Goldstone approximation in Eq. 5.43 and 5.47, the individual integrals over q_i simplify to

$$\int_A \mathrm{d}q_i = V_i, \tag{5.54}$$

where V_i is the volume of the configuration space along q_i. This volume is also referred to as zeromode or Goldstone mode volume [90, 169, 170] and corresponds to the case of $\epsilon_i \to 0$ in Eq. 5.43 and 5.47, when the integral is performed over the correct limits of integration instead of infinity. It constitutes an upper limit for the partition function and thus for the entropy of the mode q_i, which is illustrated in Fig. 5.18.

For Goldstone modes of the transition state, the first derivative, $\frac{\partial E(q_i)}{\partial q_i}$, is always zero, and thus all of their velocity components, a_i, are vanishing. The integration over Goldstone modes can be separated from other integrals in Eq. 5.47. With

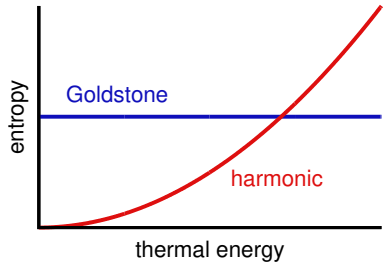

Figure 5.18 | Contribution of the eigenmode q_i to the entropy in harmonic and Goldstone approximation. The entropy contributions of an eigenmode q_i obtained with the harmonic and Goldstone mode approximations are shown as a function of the thermal energy as red and blue lines, respectively.

the convention of sorted eigenvalues in increasing order, the formula for the prefactor including a number of α and σ Goldstone modes at the initial and SP state, respectively, reads [II, 90]

$$\nu_0 = \frac{\gamma}{2\pi}\left(\frac{2\pi}{\beta}\right)^{(\alpha-\sigma)/2} \frac{V^{\mathrm{SP}}}{V^{\mathrm{I}}} \sqrt{\sum_{j=2+\sigma}^{2N} \frac{a_j^2}{\epsilon_j^{\mathrm{SP}}}} \frac{\prod_{i=1+\alpha}^{2N} \sqrt{\epsilon_i^{\mathrm{I}}}}{\prod_{j=2+\sigma}^{2N} \sqrt{\epsilon_j^{\mathrm{SP}}}}. \tag{5.55}$$

The Goldstone mode volumes of the SP and initial state, V^{SP} and V^{I}, are the products of all individual Goldstone mode volumes of the corresponding state and are set to unity if $\alpha = 0$ or $\sigma = 0$, respectively. When $\alpha \neq \sigma$, factors of $\sqrt{2\pi k_{\mathrm{B}} T}$ from the Gaussian integrals remain uncancelled and the prefactor becomes explicitly temperature dependent [II, 67, 90].

Typical candidates for a Goldstone mode approximation are translational modes that move localised magnetic structures over the atomic lattice [IX, XII, 89, 90, 120, 170]. Depending on the temperature and lattice effects, this can be the case for different magnetic skyrmions and antiskyrmions as well as the SP structures of corresponding collapse mechanisms. The Goldstone mode volume of translational modes can be determined analytically, which is briefly presented by following the derivations performed in [II] and [XII].

Assuming a continuum model, the translation of the magnetisation $\mathbf{m}(\mathbf{r})$ in the direction $\hat{\mathbf{u}}$ yields [II, XII]

$$\mathbf{m}(\mathbf{r} + \hat{\mathbf{u}}\,\mathrm{d}r) - \mathbf{m}(\mathbf{r}) = (\hat{\mathbf{u}} \cdot \nabla)\,\mathbf{m}(\mathbf{r})\,\mathrm{d}r, \tag{5.56}$$

where $\mathrm{d}r$ is the infinitesimal distance of the translation. With the eigenvector $\mathbf{q}_i(\mathbf{r})$ corresponding to the same translational mode, this infinitesimal step can be rewritten

as

$$\mathbf{m}\left(\mathbf{r}+\hat{\mathbf{u}}\,\mathrm{d}r\right)-\mathbf{m}\left(\mathbf{r}\right)=\mathbf{q}_i\left(\mathbf{r}\right)\mathrm{d}q_i. \tag{5.57}$$

Here, $\mathrm{d}q_i = P\mathrm{d}r$ is the size of the infinitesimal step formulated in the eigenbasis with the proportionality factor P. By using that $|\mathbf{q}_i| = 1$, it can be determined by comparing Eq. 5.56 and Eq. 5.57, that

$$P_i = |\left(\hat{\mathbf{u}}\cdot\nabla\right)\mathbf{m}\left(\mathbf{r}\right)|. \tag{5.58}$$

On a 2D magnetic lattice, the simultaneous integration over two perpendicular translational modes, $\mathbf{q}_i$ and $\mathbf{q}_j$, which are equivalent in continuum approximation, yields a Goldstone mode volume of [II, XII]

$$V_0^{\mathrm{tot}} = V_0 N. \tag{5.59}$$

Here,

$$V_0 = P_i^2 F \tag{5.60}$$

is the Goldstone volume per unit cell with F being the surface area of one magnetic unit cell. For skyrmion collapse, the number of unit cells, N, usually cancels out in Eq. 5.49 due to the possibility to form a SP at each unit cell of the lattice.

5.3.5. Entropy barrier

The prefactor of Eq. 5.50 is correlated to the entropy difference between the SP and initial states [IX, 67]. Analogue to Eq. 5.44, the partition function of a canonical ensemble of the initial part of the configuration space, Q^{A}, can be solved in harmonic approximation while considering α Goldstone modes [IX]:

$$Q^{\mathrm{A}} = \frac{V^{\mathrm{I}}\,\mathrm{e}^{-\beta E_0^{\mathrm{I}}}}{C}\prod_{i=1+\alpha}^{2N}\sqrt{\frac{2\pi}{\beta\epsilon_i^{\mathrm{I}}}}. \tag{5.61}$$

In contrast to Eq. 5.47, here, the velocity components of the SP modes do not play a role and the integral over the unstable mode yields the width of the transition state, ξ. With this, the partition function of the SP reads [IX]

$$Q^{\mathrm{SP}} = \frac{\xi V^{\mathrm{SP}}\mathrm{e}^{-\beta E_0^{\mathrm{SP}}}}{C}\prod_{i=2+\sigma}^{2N}\sqrt{\frac{2\pi}{\beta\epsilon_i^{\mathrm{SP}}}}, \tag{5.62}$$

where again σ is the number of Goldstone modes at the SP.

The Helmholtz free energy of both states is then given by [IX, 163]

$$F_{\mathrm{I}} = -k_{\mathrm{B}}T \ln Q^{\mathrm{A}} = E^{\mathrm{I}} - k_{\mathrm{B}}T \ln V^{\mathrm{I}} + k_{\mathrm{B}}T \ln C - k_{\mathrm{B}}T \ln \left(\prod_{i=1+\alpha}^{2N} \sqrt{\frac{2\pi}{\beta \epsilon_i^{\mathrm{I}}}} \right), \quad (5.63)$$

$$F_{\mathrm{SP}} = -k_{\mathrm{B}}T \ln Q^{\mathrm{SP}} = E^{\mathrm{SP}} - k_{\mathrm{B}}T \ln \left(\xi V^{\mathrm{SP}}\right) + k_{\mathrm{B}}T \ln C - k_{\mathrm{B}}T \ln \left(\prod_{i=2+\sigma}^{2N} \sqrt{\frac{2\pi}{\beta \epsilon_i^{\mathrm{SP}}}} \right). \quad (5.64)$$

From the Helmholtz free energy, the entropy, $S = -\frac{\partial F}{\partial T}$, can be calculated via [IX, 163]

$$S^{\mathrm{I}} = k_{\mathrm{B}} \ln V^{\mathrm{I}} - k_{\mathrm{B}} \ln C + k_{\mathrm{B}} \ln \left(\prod_{i=1+\alpha}^{2N} \sqrt{\frac{2\pi}{\beta \epsilon_i^{\mathrm{I}}}} \right) + k_{\mathrm{B}} \left(N - \frac{\alpha}{2} \right), \quad (5.65)$$

$$S^{\mathrm{SP}} = k_{\mathrm{B}} \ln \left(\xi V^{\mathrm{SP}}\right) - k_{\mathrm{B}} \ln C + k_{\mathrm{B}} \ln \left(\prod_{i=2+\sigma}^{2N} \sqrt{\frac{2\pi}{\beta \epsilon_i^{\mathrm{SP}}}} \right) + k_{\mathrm{B}} \left(N - \frac{\sigma + 1}{2} \right). \quad (5.66)$$

With the definition of the system parameter $\eta = (\alpha - \sigma - 1)/2$, the difference in entropy between both states can be determined by [IX]:

$$\frac{\Delta S}{k_{\mathrm{B}}} = \frac{S^{\mathrm{SP}} - S^{\mathrm{I}}}{k_{\mathrm{B}}} = \eta + \ln \left(\frac{\xi V^{\mathrm{SP}}}{V^{\mathrm{I}}} \right) + \ln \left(\left(\frac{2\pi}{\beta} \right)^{\eta} \frac{\prod_{i=1+\alpha}^{2N} \sqrt{\epsilon_i^{\mathrm{I}}}}{\prod_{j=2+\sigma}^{2N} \sqrt{\epsilon_j^{\mathrm{SP}}}} \right). \quad (5.67)$$

Finally, the exponent of this expression yields [IX]

$$\exp \left(\frac{\Delta S}{k_{\mathrm{B}}} \right) = \mathrm{e}^{\eta} \, \frac{\xi V^{\mathrm{SP}}}{V^{\mathrm{I}}} \left(\frac{2\pi}{\beta} \right)^{\eta} \frac{\prod_{i=1+\alpha}^{2N} \sqrt{\epsilon_i^{\mathrm{I}}}}{\prod_{j=2+\sigma}^{2N} \sqrt{\epsilon_j^{\mathrm{SP}}}}. \quad (5.68)$$

By omitting the first two factors, a reduced entropy difference can be defined by [IX]:

$$\exp \left(\frac{\Delta S'}{k_{\mathrm{B}}} \right) = \left(\frac{2\pi}{\beta} \right)^{\eta} \frac{\prod_{i=1+\alpha}^{2N} \sqrt{\epsilon_i^{\mathrm{I}}}}{\prod_{j=2+\sigma}^{2N} \sqrt{\epsilon_j^{\mathrm{SP}}}}. \quad (5.69)$$

The prefactor of Eq. 5.55 can be rewritten as

$$\nu_0 = \nu_{0_D} \nu_{0_S}, \tag{5.70}$$

where the dynamic contribution reads

$$\nu_{0_D} = \frac{\gamma}{2\pi} \sqrt{\sum_{j=2+\sigma}^{2N} \frac{a_j^2}{\epsilon_j^{\mathrm{SP}}}}, \tag{5.71}$$

and its entropic part is defined as

$$\nu_{0_S} = \left(\frac{2\pi}{\beta}\right)^{(\alpha-\sigma)/2} \frac{V^{\mathrm{SP}}}{V^{\mathrm{I}}} \frac{\prod_{i=1+\alpha}^{2N} \sqrt{\epsilon_i^{\mathrm{I}}}}{\prod_{j=2+\sigma}^{2N} \sqrt{\epsilon_j^{\mathrm{SP}}}}. \tag{5.72}$$

Inserting the entropy from Eq. 5.68 in Eq. 5.72 yields

$$\nu_{0_S} = \mathrm{e}^{-\eta} \left(\frac{2\pi}{\beta}\right)^{1/2} \exp\left(\frac{\Delta S}{k_{\mathrm{B}}}\right), \tag{5.73}$$

This form of the entropic contribution allows for a formulation of the transition rate with the difference in Helmholtz free energy between the SP and initial state, $\Delta F = \Delta E - T\Delta S$:

$$\nu_{AB} = \nu_{0_D} \frac{\mathrm{e}^{-\eta}}{\xi} \left(\frac{2\pi}{\beta}\right)^{1/2} \exp\left(-\beta \Delta F\right). \tag{5.74}$$

5.4. Mode following method

While it is often assumed that most eigenmodes are well described in either harmonic or Goldstone approximation, the quality of these approximations is unknown. In some cases, it is even unclear which of the two approximations should be applied [89]. Furthermore, the approximations cover only the extreme cases of high or low thermal energies relative to the energy landscapes local to the expansion points and thus are likely to fail for intermediate temperatures.

The problem can be illustrated on the example of the hindered oscillator models [171], which approximate the energy landscape of adsorbate movements on surfaces

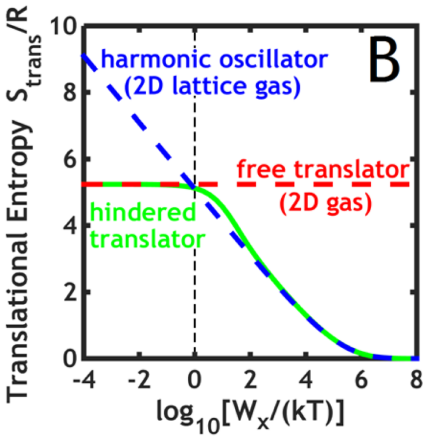

Figure 5.19 | Entropy of different approximations to the translation mode of adsorbates on surfaces. The contribution of the translation mode of ethane on Pt(111) at $T = 106$ K to the molar entropy is calculated by three different approximations of the energy landscape as a function of the logarithmic ratio of the energy barrier between adjacent lattice sites, W_x, over the thermal energy: The hindered oscillator model, in which a cosine-shaped energy landscape of the translation is assumed, the harmonic approximation and the free translator model, which corresponds to a Goldstone mode approximation of the translation. Figure reprinted from [171] with permission of ACS. Note, that further requests of permission have to be directed to the ACS.

by trigonometrical functions, allowing for the calculation of transition rates in the intermediate regime. For low temperatures, the resulting entropy of the hindered translator is close to the one of the harmonic oscillator, as it is shown in Fig. 5.19. With increasing temperature, however, the curve of the hindered translator model smoothly converges to the constant value of the Goldstone approximation, i. e. the free translator model. While the hindered oscillator models are capable of bridging the gap between the harmonic and the Goldstone mode approximation, they are based on parameterised potentials with a trigonometrical shape.

In this section, a mode following method it presented that allows for the numerical calculation of the contributions of individual eigenmodes to the transition rate without the application of any approximation but the classical approximation of magnetic moments. In this way, modes in the intermediate temperature regime can be adequately calculated and the overall quality of the harmonic and Goldstone mode approximations evaluated, paving the way for more accurate and general predictions based on TST.

5.4.1. Mathematical formalism

The goal of the mode following method is to solve the integral along a number of m eigenmodes q_p with $p = 1, ..., m$ numerically, while the rest of the modes is integrated analytically in harmonic or Goldstone mode approximation. For the following presentation of the mathematical framework of this approach, however, it is

assumed for the sake of simplicity, that only one mode is calculated by mode following and that no modes are modelled in Goldstone approximation. This formulation, however, can be generalised to treat an arbitrary amount of modes by mode following and to include a number of α and σ Goldstone modes at the respective initial and SP states, analogue to what has been presented in Sec. 5.3.4.

If the specially treated mode is an eigenmode of the initial state, the integrals are formulated in the eigenbasis of the state $\mathbf{X}^{\mathrm{I}}$,

$$Q_A = \frac{1}{C} \int \mathrm{e}^{-\beta E(\mathbf{Q})} \mathrm{d}^{2N} q_i. \tag{5.75}$$

Now, $2N-1$ eigenmodes are described in harmonic approximation, while one eigenmode remains within the exact energy notation:

$$Q_A = \underbrace{\frac{\mathrm{e}^{-\beta E_0^{\mathrm{I}}}}{C} \left(\prod_{i=1, i\neq p}^{2N} \int_{-\infty}^{\infty} \mathrm{e}^{-\beta \frac{1}{2} q_i^2 \epsilon_i^{\mathrm{I}}} \mathrm{d}q_i \right)}_{Q'_A} \underbrace{\int_{A_p} \mathrm{e}^{-\beta E(q_p)} \mathrm{d}q_p}_{\Phi_p}. \tag{5.76}$$

Here, A_p is the part of configuration space A along q_p. The dependencies of the energy can be seperated in the basis of the eigenmodes and the energy along q_p reads $E\left(q_p\right) = E\left(\mathbf{Q}\right)|_{q_i=0\,\forall i\neq p} - E_0^{\mathrm{I}}$. In order to solve the integral Φ_p numerically, it is approximated by the sum of k small, discrete steps of Δq_p^k, which yields

$$\Phi_p \approx \sum_{k}^{M_p} \mathrm{e}^{-\beta E(k\Delta q_p)} \Delta q_p^k, \tag{5.77}$$

where M_p is the number of steps necessary to sample the corresponding part of configuration space, A_p. Hence, when the contribution of q_p is determined numerically, the probability Q_A^{MF} can be calculated via

$$Q_A^{\mathrm{MF}} = Q'_A \Phi_p \tag{5.78}$$

and the prefactor, generalised to the occurance of Goldstone modes, reads

$$\nu_0 = \frac{\gamma}{2\pi} \left(2\pi k_{\mathrm{B}} T\right)^{(\alpha-\sigma+1)/2} \frac{V^{\mathrm{SP}}}{V^{\mathrm{I}}} \Phi_p \sqrt{\sum_{j=2+\sigma}^{2N} \frac{a_j^2}{\epsilon_j^{\mathrm{SP}}}} \frac{\prod_{i=1+\alpha, i\neq p}^{2N} \sqrt{\epsilon_i^{\mathrm{I}}}}{\prod_{j=2+\sigma}^{2N} \sqrt{\epsilon_j^{\mathrm{SP}}}}. \tag{5.79}$$

When mode following is applied to an eigenmode of the SP, the flux through the dividing surface, I_{AB}, has to be reformulated. In general, the occupation probability is multiplied with the velocity component perpendicular to S. Due to the linear increase of the velocity with the distance to the SP, it was possible to separate the velocity contribution from the entropic contribution in Eq. 5.48. However, with the numerical integration of the SP mode, this linear dependence is no longer given. In a first approximation, the velocity contribution of the mode, a_p, is omitted in the sum of the total perpendicular velocity:

$$v_{\perp}\left(\mathbf{Q}\right) \approx \sum_{i=1, i\neq p}^{2N} a_i q_i. \tag{5.80}$$

The separation of the numerically solved mode from the others, analogue to Eq. 5.76, yields for the flux through the dividing surface

$$I_{AB} = \underbrace{\frac{\mathrm{e}^{-\beta E_0^{\mathrm{SP}}}}{C}\left(\int_{-\infty}^{\infty}\prod_{i=2, i\neq p}^{2N}\mathrm{e}^{-\beta\frac{1}{2}q_i^2\epsilon_i^{\mathrm{SP}}}\sum_{i=2, i\neq p}^{2N}a_i q_i h\left[v_{\perp}\left(\mathbf{Q}\right)\right]\mathrm{d}q_i\right)}_{I'_{AB}}\underbrace{\int_{A_p}\mathrm{e}^{-\beta E(q_p)}\mathrm{d}q_p}_{\Phi_p}. \tag{5.81}$$

Analogue to Eq. 5.76, the integrals in harmonic approximation are solved analytically while the integral of the followed mode is determined numerically. The flux through the dividing surface with one mode obtained by mode following reads

$$I_{AB}^{\mathrm{MF}} = I'_{AB}\Phi_p, \tag{5.82}$$

which yields the prefactor of the transition, generalised to the occurrence of Goldstone modes, with

$$\nu_0 = \frac{\gamma}{2\pi}\left(2\pi k_{\mathrm{B}}T\right)^{(\alpha-\sigma-1)/2}\frac{V^{\mathrm{SP}}}{V^{\mathrm{I}}}\Phi_p^{-1}\sqrt{\sum_{j=2+\sigma, j\neq p}^{2N}\frac{a_j^2}{\epsilon_j^{\mathrm{SP}}}}\frac{\prod_{i=1+\alpha}^{2N}\sqrt{\epsilon_i^{\mathrm{I}}}}{\prod_{j=2+\sigma, j\neq p}^{2N}\sqrt{\epsilon_j^{\mathrm{SP}}}}. \tag{5.83}$$

5.4.2. Algorithm

The mode following algorithm shall follow a prescribed eigenmode of a magnetic structure for a given distance. Since the corresponding eigenvectors can change along the way, a mode tracking algorithm is required. Here, the algorithm of the mode

following implemented into the Kieler atomistic spin simulation code is presented. A flowchart of the program is displayed in Fig. 5.20.

The setup of the simulation requires information about the lattice symmetry, the magnetic structure as well as the parameters for the magnetic interactions. Especially for mode following, the width of the test interval of the mode tracker, a maximal angle, $\omega_{\max}$, used for the rotation of the magnetic structure in the direction of the followed eigenmode at each step and the number of mode following steps, M, must be specified.

The magnetic structure is defined by $3N$ coordinates distributed on N lattice sites each with a $3D$ vector, $\mathbf{m}_i$, for the atomistic magnetic moment and with $i = 1, ..., N$. Similarly, each of the $3N$-dimensional eigenvectors (EVs) of the magnetic structure contains N lattice sites, each with a $3D$ vector, $\mathbf{v}_i$. While the magnetic structure is loaded directly from an input file, the initial eigenvector of the followed mode, called "mode following vector" (MFV), can be set up in two ways. Either it is loaded from an input file as well, or the initial index of the followed mode in the spectrum is given. In the latter case, the initial MFV is determined by diagonalisation of the Hessian matrix of the magnetic structure.

Each step of the main loop starts with the diagonalisation of the Hessian matrix of the current magnetic structure. The diagonalisation is performed in the $2N$ dimensional tangent space of the system, resulting in a set of $2N$ dimensional EVs which are transferred back to the $3N$ basis of the system.

In the next step, the mode tracker has to determine, which EV of the set of newly calculated EVs is the most similar to the previous MFV, in order to follow the correct eigenmode. A flowchart of the mode tracker is shown in Fig. 5.21.

To save computing time, only a small fraction of the EVs are considered candidates for the next MFV by filtering out all EVs outside an interval around the index of the current MFV. This procedure is based on the assumption, that the index of an eigenmode in the spectrum between two steps does not change more than a few numbers. However, due to the symmetry of the energy landscape in harmonic approximation, the inverted EVs of the Hessian matrix have to be considered as candidates, too, and are therefore added to the set of considered EVs.

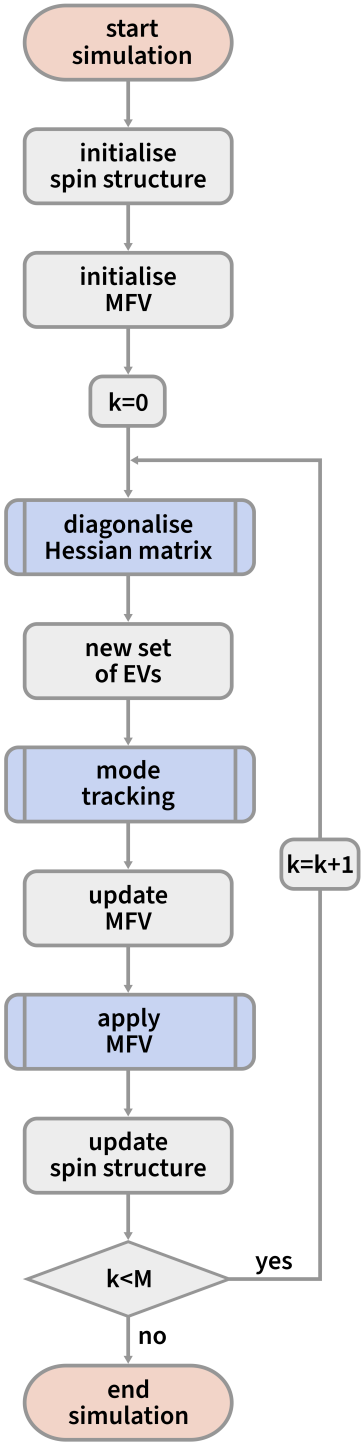

Figure 5.20 | Flowchart of the mode following algorithm. First, inputs of the lattice, magnetic structure, magnetic interactions and simulation control are loaded. The magnetic structure and the mode following vector (MFV), which is the eigenvector corresponding to the eigenmode followed in the simulation, are initialised. In the main loop, first the Hessian matrix is diagonalised, yielding a set of eigenvectors (EVs). The mode tracker determines, which of the new EVs is most similar to the previous MFV. The EV with the largest scalar product with the previous MFV is selected as MFV for the next step. By using the Rodrigues rotation formula, the magnetic structure is rotated a small step width in the direction of the MFV. Subsequently, the updated magnetic structure is used to determine the Hessian matrix of the next iteration, until the maximal number of iterations, M, is reached.

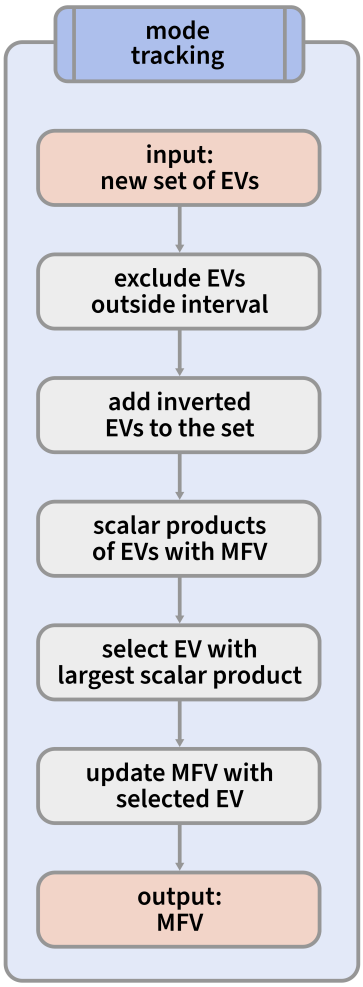

Figure 5.21 | Flowchart of the mode tracking algorithm. From the set of EVs given as an input, only the ones with an index inside a predefined interval around the index of the previous MFV are considered as candidates for the next MFV. Due to the randomised sign of the EVs, also the inverted versions of the EVs are added to the set of candidates. For each EV in the set of candidates, the scalar product with the previous MFV is evaluated. The EV with the largest scalar product is selected as next MFV. It is stored inside the mode tracker as a reference for the next iteration and is handed as output to the next routine of the mode following algorithm.

In order to determine the most similar EV to the previous MFV, the scalar product between each EV of the set of candidates with the previous MFV is evaluated. Note, that while the EVs are normed, the components, $\mathbf{v}_i$, are not, and thus, lattice sites with large corresponding $|\mathbf{v}_i|$ exhibit a larger contribution to the scalar product than site with a small vector component. Subsequently, the EV with the highest scalar product is selected as next MFV, which is applied to the magnetic structure and stored in the mode tracker as a reference for the next iteration.

In order to move the magnetic structure in the direction of the MFV, each magnetic moment, $\mathbf{m}_i$, is rotated in the direction of the corresponding vector component, $\mathbf{v}_i$. Since the $\mathbf{v}_i$ are perpendicular to $\mathbf{m}_i$ on all lattice sites, i, the updated magnetic

moments can be calculated simply by

$$\mathbf{m}_i^{k+1} = \mathbf{m}_i^k \cos(\omega) + \frac{\mathbf{v}_i^k}{|\mathbf{v}_i^k|} \sin(\omega) . \tag{5.84}$$

Here, the angle $\omega = \omega_{\max}|\mathbf{v}_i^k|/v_{\max}^k$, where $\omega_{\max}$ is an input parameter, controlling the step size, while $v_{\max}^k$ is the largest value of all $|\mathbf{v}_i^k|$ of the step k. In this way, the maximum applied rotation angle of each step is $\omega_{\max}$, which ensures a controlled mode following in steps sizes small enough for the mode tracker to determine the MFV of the next step accordingly.

6. Enhanced energy barriers due to exchange frustration

In seeking insight to the thermal stability of skyrmions in ultrathin films, geodesic nudget elastic band (GNEB) calculations of skyrmion collapse in fcc-Pd/Fe/Ir(111) and hcp-Pd/Fe/Ir(111) have been performed with the Kieler atomistic spin simulations code. At the beginning of this investigation, which is published in [I], properties of magnetic skyrmions were typically calculated with exchange interactions modelled in nearest neighbour approximation [7, 47, 77, 81, 86, 172, 173], with only a few exceptions [24, 65, 78, 82]. The effective nearest neighbour parameters of such models were often fitted to experimental data, which do not give access to shell resolved magnetic interactions [47, 77, 81].

Early theoretical studies of skyrmion collapse via GNEB [86, 94, 95, 174, 175] and Langevin dynamics [86, 174, 175] also relied on this model. This raises the question when such simplifications are justified and how skyrmion properties calculated within the nearest neighbour approximation of exchange interaction compare to skyrmions simulated with parameters for exchange interactions beyond nearest neighbours obtained from density functional theory (DFT).

To answer this question, a procedure is presented to map the full set of DFT-based interaction parameters, J_{DFT}, onto a set of effective nearest neighbour parameters, J_{eff}. In order to compare both exchange models, equilibrium properties such as skyrmion energy, profile and radius are calculated with atomistic spin dynamics simulations. Subsequently, skyrmion stability is studied by performing GNEB calculations of skyrmion annihilation processes, yielding the radial symmetric skyrmion collapse mechanism. Significant differences of the energy barriers obtained with J_{DFT} and J_{eff} are found, which are explained by a decomposition of energy contributions, revealing a stabilisation of magnetic skyrmions by exchange frustration which cannot be modelled accurately with J_{eff}.

6.1. Effective nearest neighbour exchange model

In Chap. 4, it is presented, how the parameters of the extended Heisenberg model are obtained from DFT-based spin spiral energy dispersions. By fitting of the analytical contributions of Heisenberg exchange beyond nearest neighbours, $E_{\mathrm{exch}}(\mathbf{q})$, to the dispersions of fcc-Pd/Fe/Ir(111) hcp-Pd/Fe/Ir(111), one set of J_i parameters is determined for each system, which are listed in Tab. 4.1. Including the parameters for Dzyaloshinskii-Moriya interaction (DMI) and magnetocrystalline anisotropy, the DFT-based parameter sets for Pd/Fe/Ir(111) with a fcc and hcp stacked Pd layer are referred to as J_{DFT} in the following.

In $E_{\mathrm{exch}}(\mathbf{q})$, each shell of exchange interaction has a different dependence of the spin spiral vector $\mathbf{q}$ and, thus, cannot be reproduced adequately by an effective nearest neighbour exchange parameter with the analytical form of a J_1 interaction. Therefore, by mapping the contributions of the exchange interaction beyond nearest neighbours onto J_{eff}, information is lost, and thus J_{eff} can only describe the dispersion curve locally.

Previously, Dupé *et al.* suggested a Tailor expansion around the $\bar{\Gamma}$ point to calculate J_{eff} [24]. This procedure is suited for capturing properties of slow rotating spin spirals and the ferromagnetic (FM) state and allows for a simple classification of systems [24]. In order to capture the properties of small skyrmions, here, J_{eff} is obtained differently by fitting the exchange dispersion locally around the minimum of the dispersion curve. The angle of the spin spiral minimum is used as an estimate for angles occurring in skyrmions in equilibrium configuration. In $\bar{\Gamma}\bar{\mathrm{K}}$ direction, the analytic spin spiral dispersion of the effective model reads [I]

$$E_{\mathrm{eff}}(q) = J_{\mathrm{eff}}(2\cos(q) + 4\cos(q/2)) + D_{\mathrm{eff}}(2\sin(q) + 2\sin(q/2)) + K_{\mathrm{eff}}/2. \quad (6.1)$$

Note, that the parameter of the effective exchange and the entire set of effective parameters, including D_{eff} and K_{eff}, are both labelled J_{eff} in this chapter. The function $E_{\mathrm{eff}}(q)$ is fitted to a fine grid of points sampling the analytical function $E^{\mathrm{hcp}}_{\mathrm{DFT}}(q)$ parameterised by $J^{\mathrm{hcp}}_{\mathrm{DFT}}$. For hcp Pd, the parameters for DMI and anisotropy remain $D_{\mathrm{eff}} = D_1$ and $K_{\mathrm{eff}} = K$ and the fit is performed with J_{eff} as fit parameter. The resulting function $E^{\mathrm{hcp}}_{\mathrm{eff}}(q)$ is plotted on the left side of Fig. 6.1 and agrees almost perfectly to the sampled points of $E^{\mathrm{hcp}}_{\mathrm{DFT}}(q)$.

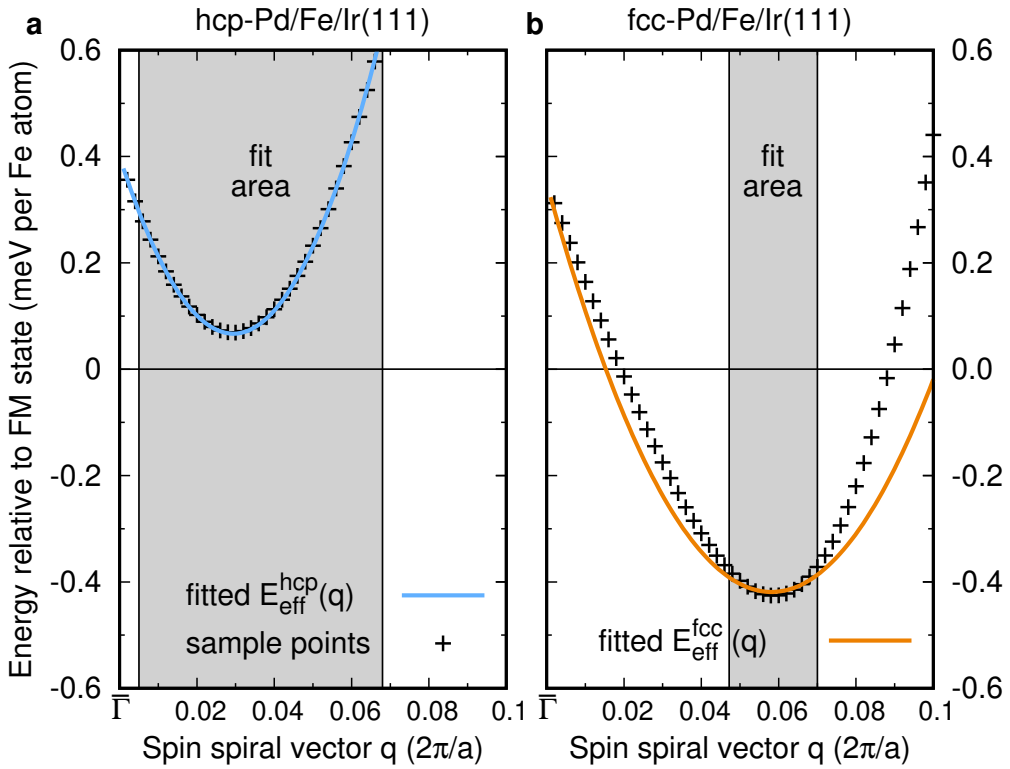

Figure 6.1 | Mapping of the exchange interaction beyond nearest neighbours onto an effective nearest neighbour exchange model. The spin spiral dispersion in $\overline{\Gamma}\overline{\mathrm{K}}$ direction is shown in the interval $q \in [0, 0.1]$ for Pd/Fe/Ir(111) with hcp (**a**) and fcc (**b**) stacked Pd. The originally obtained parameters J_{DFT} are sampled as points in order to allow a least square fit with the functions $E_{\mathrm{eff}}^{\mathrm{hcp}}$ and $E_{\mathrm{eff}}^{\mathrm{fcc}}$. For reasons of clarity only every 20th sample point is plotted. The fit interval is shown as shaded area. In the case of hcp Pd, J_{eff} was used as fit parameter, while for fcc Pd both J_{eff} and D_{eff} had to be fitted in order to match the points reasonably.

	J_{eff}	D_{eff}	K_{eff}
fcc fit	3.68	1.39	0.7
hcp fit	6.44	1.2	0.8
Ref. [81]	2.95	0.8	0.4
Ref. [77]	3.5	1.1	0.5

Table 6.1 | Effective nearest neighbour parameters of the extended Heisenberg model obtained for fcc-Pd/Fe/-Ir(111) and hcp-Pd/Fe/Ir(111). The parameters sets fcc J_{eff} and hcp J_{eff} are determined by the fits of Eq. 6.1 to the corresponding dispersions of J_{DFT} as displayed in Fig. 6.1. For reference, the interaction parameters fitted to experimental data by Romming *et al.* [81] and Hagemeister *et al.* [77] have been converted into atomistic parameters. All parameters are given in meV/atom.

The dispersion of fcc-Pd/Fe/Ir(111) already exhibits a spin spiral minimum without spin-orbit coupling (SOC) and thus cannot be reproduced by the parabola of a J_1 interaction alone. By taking, both, J_{eff} and D_{eff} into account as fit parameters and keeping $K_{\mathrm{eff}} = K$, the approximate form of $E^{\mathrm{eff}}_{\mathrm{DFT}}(q)$ can be reproduced by the fit of $E_{\mathrm{eff}}(q)$ around the minimum. As shown on the right side of Fig. 6.1, a very narrow fit interval is selected to make a compromise between curvature, depth and position of the minimum. The resulting parameters for both stackings are shown in Tab. 6.1.

With $J^{\mathrm{hcp}}_{\mathrm{eff}} = 6.44$ meV and $J^{\mathrm{fcc}}_{\mathrm{eff}} = 3.68$ meV, the effective exchange parameters are significantly smaller than the corresponding J_1 parameters of J_{DFT}, with $J^{\mathrm{hcp}}_1 = 13.66$ meV and $J^{\mathrm{fcc}}_1 = 14.40$ meV. Due to the selected fit interval, this yields a similarly shallow dispersion for small q values around the energy minimum. For larger q values, however, the curves of J_{DFT} steeply increase and yield an energy difference of ≈ 100 meV and ≈ 110 meV between the $\bar{\Gamma}$ and $\bar{\mathrm{K}}$ point for hcp and fcc Pd, respectively. For the effective model, these energy differences are much smaller with only about 50 meV and 30 meV.

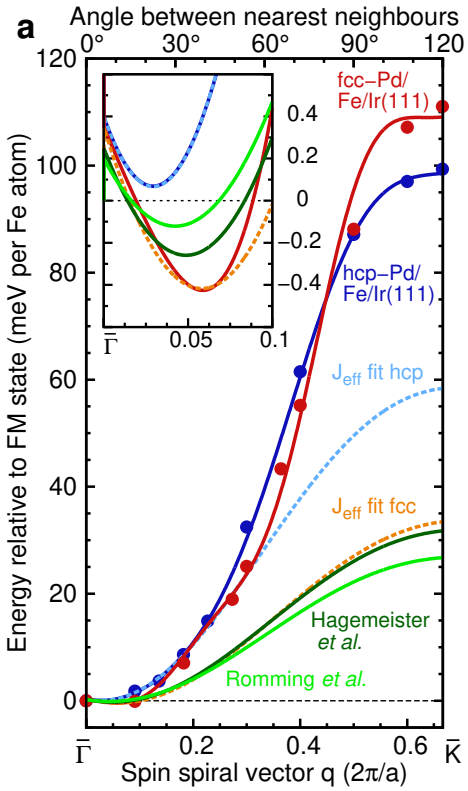

Figure 6.2 | Spin spiral dispersion curve of Pd/Fe/Ir(111). The energy of flat spin spirals relative to the FM state is shown over the value of the spin spiral vector, q, along the high symmetry line from the $\bar{\Gamma}$ to the $\bar{\mathrm{K}}$ point. The red and blue points are calculated with DFT for the fcc and hcp stacking of Pd, respectively. The inset shows a zoom of the area close to the $\bar{\Gamma}$-point. Fits of the extended Heisenberg model beyond nearest neighbours and including SOC are shown as solid red and blue lines. The corresponding parameters are listed in Tab. 4.1. The fits of the effective nearest neighbour model correspond to the dotted lines, whose parameters are shown in Tab. 6.1. For comparison, the dispersions calculated from the parameters given by Romming *et al.* [81] and Hagemeister *et al.* [77] are shown as green lines. Figure published in [I].

For comparison, the dispersion curves calculated from parameters fitted to experiments by Romming *et al.* [81] and Hagemeister *et al.* [77] are added to Fig. 6.2. The parameters are listed in Tab. 6.1. In the inset of Fig. 6.2, the experimental curves lie between the theoretical fcc and hcp curves, already indicating a good agreement between the DFT calculations and the experiment. However, dispersion curves calculated by DFT provide additional information about the whole interval of $q \in [\overline{\Gamma}, \overline{\mathrm{K}}]$, while the experiments are restricted to the realised states near the energy minimum. Hence, the experiment-based effective models do not follow the steep increase predicted by the J_{DFT} curves, but stay close to the fcc curve of J_{eff}.

6.2. Stability diagrams

With stability or zero-temperature phase diagrams, the relative energies of magnetic states over a selected control parameter are explored. Here, the applied out-of-plane magnetic field is chosen as control parameter, as it has been shown experimentally (Fig. 1.1) to efficiently tune the magnetic configuration of Pd/Fe/Ir(111). Stability diagrams are created for hcp and fcc stacked Pd on Fe/Ir(111), using both models of exchange interaction with the corresponding parameter sets J_{eff} and J_{DFT}, respectively.

Atomistic spin dynamics simulations are performed to energetically relax and compare spin spirals (SS), skyrmion lattices (SkX), isolated skyrmions (ISk) and antiskyrmions (ASk) and the ferromagnetic state (FM), examples of which are shown in Fig. 6.3.

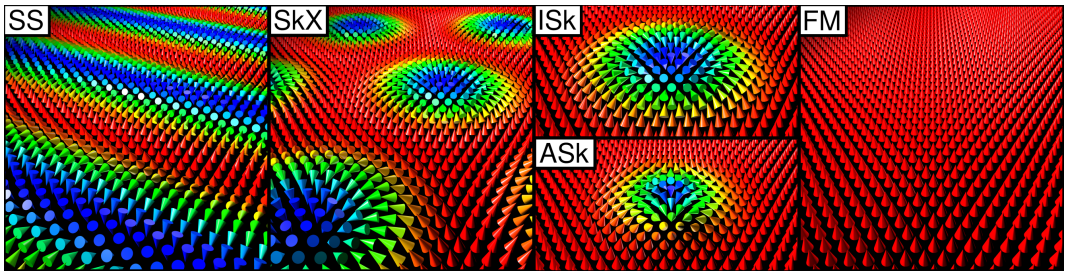

Figure 6.3 | Overview of magnetic structures relaxed by spin dynamics. Examples are shown for fcc-Pd/-Fe/Ir(111) J_{DFT} at $B = 4$ T. Presented are spin spirals (SS), a 5×5 skyrmion lattice (SkX) in a 100×100 simulation box, isolated skyrmions (ISk) and antiskyrmions (ASk) with ferromagnetic background as well as the ferromagnetic state (FM).

As initial states, homogeneous spin spirals with a q value similar to the corresponding energy minimum of the dispersion curve and skyrmion lattices with the energetically most favourable skyrmion density on a 100×100 lattice are selected. Isolated skyrmions and antiskyrmions are created in a ferromagnetic background. Details on the performed simulations can be found in App. A.1.

The resulting stability diagrams are displayed in Fig. 6.4. In case of hcp-Pd/Fe/-Ir(111), the ferromagnetic state is lowest in energy over the whole interval of 0.0-3.0 T. While the spin spiral state gains some energy by anisotropy and the Zeeman term due to inhomogeneous relaxation with increasing field, it remains unfavourable compared to the FM state. The homogeneous spin spiral lies about 0.07 meV above the FM state at zero field, which agrees well with the distance of the spin spiral minimum to the $\bar{\Gamma}$ point in Fig. 6.2. Over the whole interval, the energy of isolated skyrmions lies slightly above the FM energy with a slowly increasing energy difference between them. These results are nearly identical for J_{DFT} and J_{eff}, which resembles the very good agreement of the both dispersion curves and demonstrates, that the equilibrium energies of the SS, ISk and FM state are modelled sufficiently well by J_{eff}.

The stability diagrams of fcc-Pd/Fe/Ir(111) are qualitatively different from the hcp case and show three distinct phases for both exchange models: A spin spiral phase for low fields, a skyrmion lattice phase at intermediate fields and the ferromagnetic phase for fields above a critical field strength of $B_c \approx 3.2$ T for exchange modelled by J_{DFT} and $B_c \approx 3.6$ T for J_{eff}. Besides the slightly larger skyrmion lattice phase in case of J_{eff}, which is due to the increased strength of DMI stabilising non-collinear magnetic textures, both models yield very similar stability diagrams.

Isolated antiskyrmions appear to be metastable only with fcc J_{DFT} parameters. This agrees with [41], in which the authors observed metastable skyrmions and antiskyrmions in their atomistic spin dynamics simulations for fcc-Pd/Fe/Ir(111). In [42], similar spin dynamics simulations were performed with and without DMI, indicating a stabilisation effect due to the exchange interaction. The disappearance of antiskyrmions in Fig. 6.4 with J_{eff} indicates, that the exchange frustration is necessary for the antiskyrmions to be metastable. However, the use of spin dynamics simulations for stability investigations is very limited due to finite simulation time. When a state is unstable, it may still collapse very slowly and falsely appear as

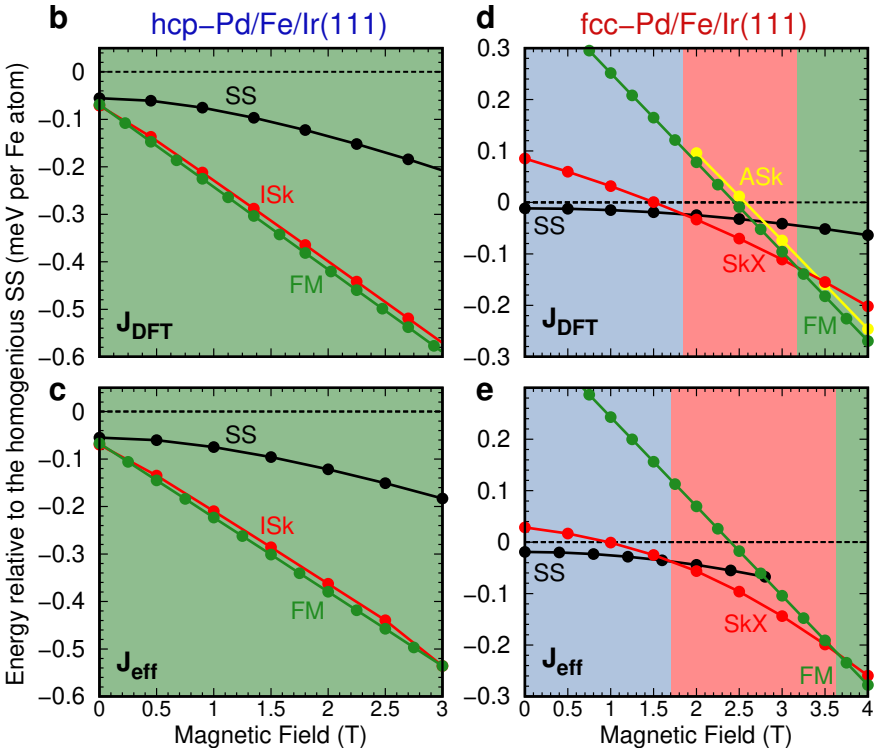

Figure 6.4 | Zero temperature stability diagrams of Pd/Fe/Ir(111). The diagrams are shown for Pd/Fe/-Ir(111) with a hcp (**b,c**) and fcc (**d,e**) stacked Pd layer, each with the corresponding parameter sets J_{DFT} (**b,d**) and J_{eff} (**c,e**). The energies of the FM state (FM, green), relaxed spin spirals (SS, black), skyrmion lattice (SkX, red), isolated skyrmion (ISk, red) and isolated antiskyrmion (ASk, yellow) are displayed relative to the energy of the homogeneous SS (dotted line). Background colours indicate the ground state of the SS (blue), SkX (red) and FM state (green). The Figure is adapted from [l], with slightly different reference energies in the case of fcc-Pd/Fe/Ir(111). The energies of the homogeneous spin spirals are increased by ≈ 0.011 meV per atom and ≈ 0.019 meV per atom for the parameter sets J_{DFT} and J_{eff}, respectively.

metastable. For which reason the frustrated hcp system does not host antiskyrmions remains unclear up to this point.

In contrast to the stability diagrams of the hcp stacked Pd, the fcc diagrams qualitatively resemble the experimentally obtained phase diagram at low temperature displayed in Fig. 1.1. The experiment, however, was performed on a hcp stacked Pd islands [176]. Additionally, the theoretically obtained fields of phase transition in case of fcc Pd are approximately twice as large as the experimental measured values. The reason for this deviation can be found in the dispersion curves of the system in Fig. 6.2. Since the energy differences between the states are on a scale of

≈ 0.1 meV/atom (Fig. 6.4), very small changes in the DFT calculations or the fitting procedures of the Heisenberg parameters can affect the resulting stability diagrams. While the overall form of the dispersion and frustration of exchange interaction are captured consistently, slight deviations can shift the spin spiral minimum above or below the $\bar{\Gamma}$ point. Therefore, small adjustments to the hcp parameters shifting the spin spiral minimum a few 0.1 meV/atom downwards results in a stability diagram similar to the experimental measurements, as it has been demonstrated in [177].

This sensitive balance between the interactions also explains deviations in critical magnetic fields between theory and experiment, since the Zeeman term is rather week compared to the exchange or DMI contributions. With an atomic magnetic moment of $3\mu_\mathrm{B}$ and in case of ferromagnetic alignment, an increase in magnetic field of $\Delta B = 1.0$ T yields an energy gain of $\Delta E_\mathrm{Zee} \approx 0.17$ meV/atom only. Considering this, the accordance between simulated stability diagrams and experimentally obtained phase diagram is remarkable.

6.3. Radii and profiles

The size of magnetic skyrmions varies with out-of-plane magnetic fields. As the parallel ferromagnetic alignment is favoured by the field, non-collinear structures such as skyrmions increasingly cost energy with increasing field strength and, thus, are shrinking in the ferromagnetic background [81].

The skyrmion radius defined in Sec. 3.4.1 is extracted from isolated skyrmions relaxed by spin dynamics simulations and displayed in Fig. 6.5 for varying magnetic field strengths. For all parameter sets, the skyrmion radii are quite similar in value, decrease monotonously with increasing field and converge to a parameter specific minimum radius. On the other end of the displayed interval, the skyrmion radii are diverging in the direction of decreasing magnetic field for all parameters. Ultimately, this leads to a stripe out transition from the skyrmion to the spin spiral phase for small magnetic fields [178].

The nearest neighbour approximation of exchange interaction and the exchange beyond nearest neighbours yield very similar skyrmion radii for hcp-Pd/Fe/Ir(111), as the data points almost perfectly coincide. For fcc Pd, the radii exhibit similar values for both parameter models with the radii of J_DFT being more rigid to the

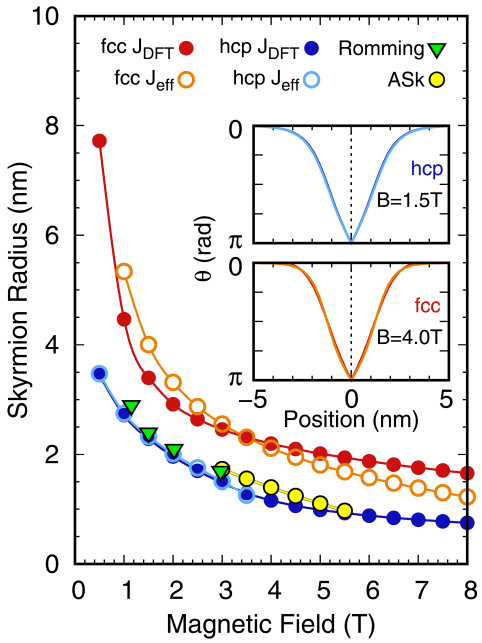

Figure 6.5 | Skyrmion and antiskyrmion radii in Pd/-Fe/Ir(111) vs. out-of-plane magnetic field strength. The radii are determined via a numerical implementation of the Lilley-criterion described in Sec. 3.4.1. Green triangles mark the radii published by Romming *et al.* [81]. As insets, skyrmion Θ-profiles are shown for the fcc and hcp stacking, each with J_{dft} and J_{eff} parameters, indicated by darker and brighter colours, respectively. Figure published in [VIII].

magnetic field than the radii of J_{eff}. The experimentally obtained radii for Pd/-Fe/Ir(111) lie close to the theoretical values of hcp-Pd/Fe/Ir(111). The radii of antiskyrmions calculated with fcc J_{DFT} parameters show the same overall trends but are smaller than their skyrmion counterparts, which is straightforwardly explained by the higher energy costs of antiskyrmions compared to skyrmions.

Line cuts through the center of the $\Theta(\mathbf{r})$ profile of a skyrmion (see Sec. 3.4.1) are shown in the inset of Fig. 6.5. The profiles have been fitted to the m_z component of the relaxed ISk spin configurations. Profiles calculated with J_{eff} and J_{DFT} are compared at magnetic fields resulting in similar skyrmion radii, i. e. $B = 1.5$ T and $B = 4.0$ T for hcp and fcc, respectively. For hcp, the two lines are nearly indistinguishable due to excellent agreement. While the fcc profiles also provide a very good agreement, the profile of J_{DFT} shows a small deviation from the micromagnetic profile due to the exchange frustration, as reported earlier in [24].

The comparison of magnetic field dependent skyrmion radii and profiles calculated with J_{eff} and J_{DFT} emphasises, that relaxed skyrmion structures of Pd/Fe/Ir(111) are well described by exchange interaction in nearest neighbour approximation. While the exchange frustration leads to small effects such as a higher rigidity against magnetic

field induced radius changes and slightly deviations in profiles, the overall equilibrium properties of skyrmions are quite similar.

6.4. Energy profiles of magnetic skyrmions

In Fig. 6.6 a, energetically relaxed skyrmions are displayed, calculated with both exchange models via spin dynamics simulations. The skyrmions were relaxed with out-of-plane fields of $B = 4$ T and $B = 1.5$ T for fcc-Pd/Fe/Ir(111) and hcp-Pd/-Fe/Ir(111), respectively. While all skyrmions are similar in size and shape, the corresponding energy density maps displayed in Fig. 6.6 b exhibit some differences. Qualitatively, all depicted skyrmions gain energy at their periphery, while the intermediate region of almost in-plane magnetic moments with large relative angles clearly exhibit energy costs.

In case of hcp-Pd/Fe/Ir(111), the two exchange models also yield quantitatively similar energy maps, which is further underpinned by the similar energy profile lines shown in Fig. 6.6 c. The magnetocrystalline anisotropy, the Zeeman and the exchange interaction contribute to the energy cost at the intermediate region, while the skyrmion is stabilised by the DMI, which favours the non-collinear alignment.

For fcc-Pd/Fe/Ir(111), however, both models yield different energy maps and profile lines despite the similar magnetic structures. While the anisotropy and the Zeeman interaction show the same behaviour as for hcp-Pd/Fe/Ir(111), the frustrated exchange interaction of the J_{DFT} model leads to an relative energy gain at the centre and the periphery of the skyrmion, while it also costs energy at the intermediate region. This is different from the skyrmion calculated with J_{eff}, where the exchange interaction only contributes to the energy costs.

The DMI contribution, on the other hand, is larger for the J_{eff} model, which can be straightforwardly explained by the higher value of the DMI parameter. It was introduced to preserve the spin spiral minimum resulting from exchange frustration. This demonstrates, that both exchange models of fcc-Pd/Fe/Ir(111) yield similar skyrmion sizes and shapes, but result in qualitatively different energy profiles of the skyrmion.

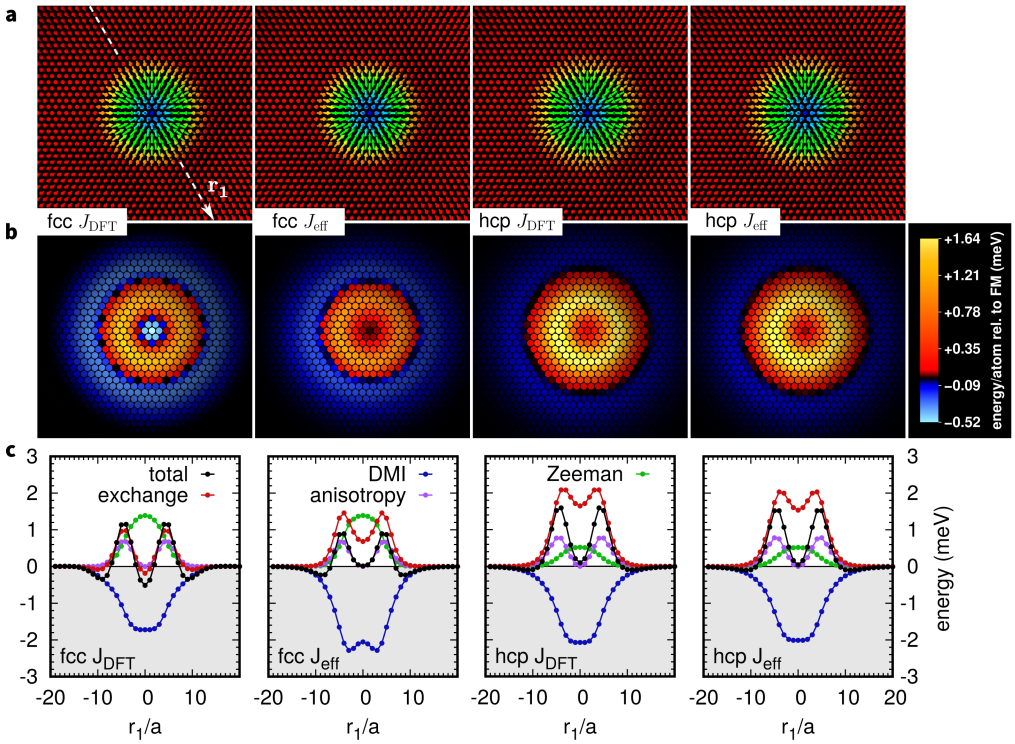

Figure 6.6 | Energy density maps and profile lines of relaxed skyrmions in fcc-Pd/Fe/Ir(111) and hcp-Pd/-Fe/Ir(111). a) The magnetic structure of skyrmions in Pd/Fe/Ir(111), calculated with spin dynamics for the fcc and hcp stacking of Pd and with the full exchange model (J_{DFT}) and the effective nearest neighbour model (J_{eff}). External fields of $B = 4$ T and $B = 1.5$ T are assumed in case of fcc-Pd/Fe/Ir(111) and hcp-Pd/Fe/Ir(111), respectively. **b)** Energy density maps of the magnetic structures shown in **(a)** with a shared colour bar for all four maps, indicating the energy difference between the relaxed skyrmion and the FM state for each lattice site. **c)** Profile lines of the decomposed energy density along the direction of $\mathbf{r}_1$ in units of the lattice constant, a, as illustrated in **(a)**.

The magnetic texture, energy density map and energy profile lines of an antiskyrmion in fcc-Pd/Fe/Ir(111) at $B = 4$ T is shown in Fig. 6.7. Only with parameters including exchange frustration (J_{DFT}), it was possible to relax metastable antiskyrmions. With the effective exchange model of fcc-Pd/Fe/Ir(111) and both parameter sets of hcp-Pd/Fe/Ir(111), the antiskyrmions disappeared during the spin dynamics simulations.

The structure of the antiskyrmion in Fig. 6.7 a has two distinct axes denoted $\mathbf{r}_1$ and $\mathbf{r}_2$. The rotational sense of magnetic moments along $\mathbf{r}_1$ is similar to the skyrmions in Fig. 6.6 a and is favoured by DMI, leading to the energy gain visible in Fig. 6.7 b

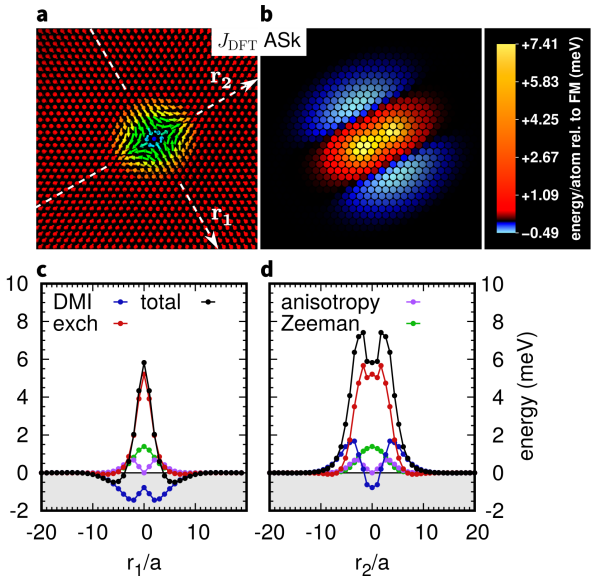

Figure 6.7 | Energy density maps and profile lines of a relaxed antiskyrmion in fcc-Pd/Fe/Ir(111). a) The magnetic structure of skyrmions in fcc-Pd/Fe/Ir(111), calculated with the full exchange model (J_{DFT}) at $B = 4$ T via spin dynamics. **b)** Energy density maps of the antiskyrmion shown in **(a)**. The colour code indicates the energy difference between the relaxed antiskyrmion and the FM state for each lattice site. **c)** Profile line of the decomposed energy density along the axis $\mathbf{r}_1$ in units of the lattice constant, a, as illustrated in **(a)**. **d)** Profile line along $\mathbf{r}_2$.

and c. In contrast, the opposite chirality along $\mathbf{r}_2$ yields the DMI energy costs (Fig. 6.7 b and d), which explains the lower stability of antiskyrmions in Pd/Fe/Ir(111) compared to skyrmions.

The exchange interaction in Fig. 6.7 c and d, on the other hand, shows a small energy gain at the periphery of the antiskyrmion in the direction of both axes. For this reason, antiskyrmions become more stable the more the spin spiral dispersion minimum of Fig. 6.2 is described by frustrated exchange interaction instead of DMI, which explains why antiskyrmions exhibit a higher stability when they are calculated with J_{DFT} instead of J_{eff}.

6.5. Radial symmetric collapse mechanism

So far only the energies of relaxed magnetic (anti)skyrmions have been discussed. In order to obtain energy barriers and transition rates of skyrmion annihilation processes, information about the transition mechanisms is required. Here, minimum energy paths between isolated (anti)skyrmion states and the ferromagnetic state are calculated with the GNEB method presented in Sec. 5.2.

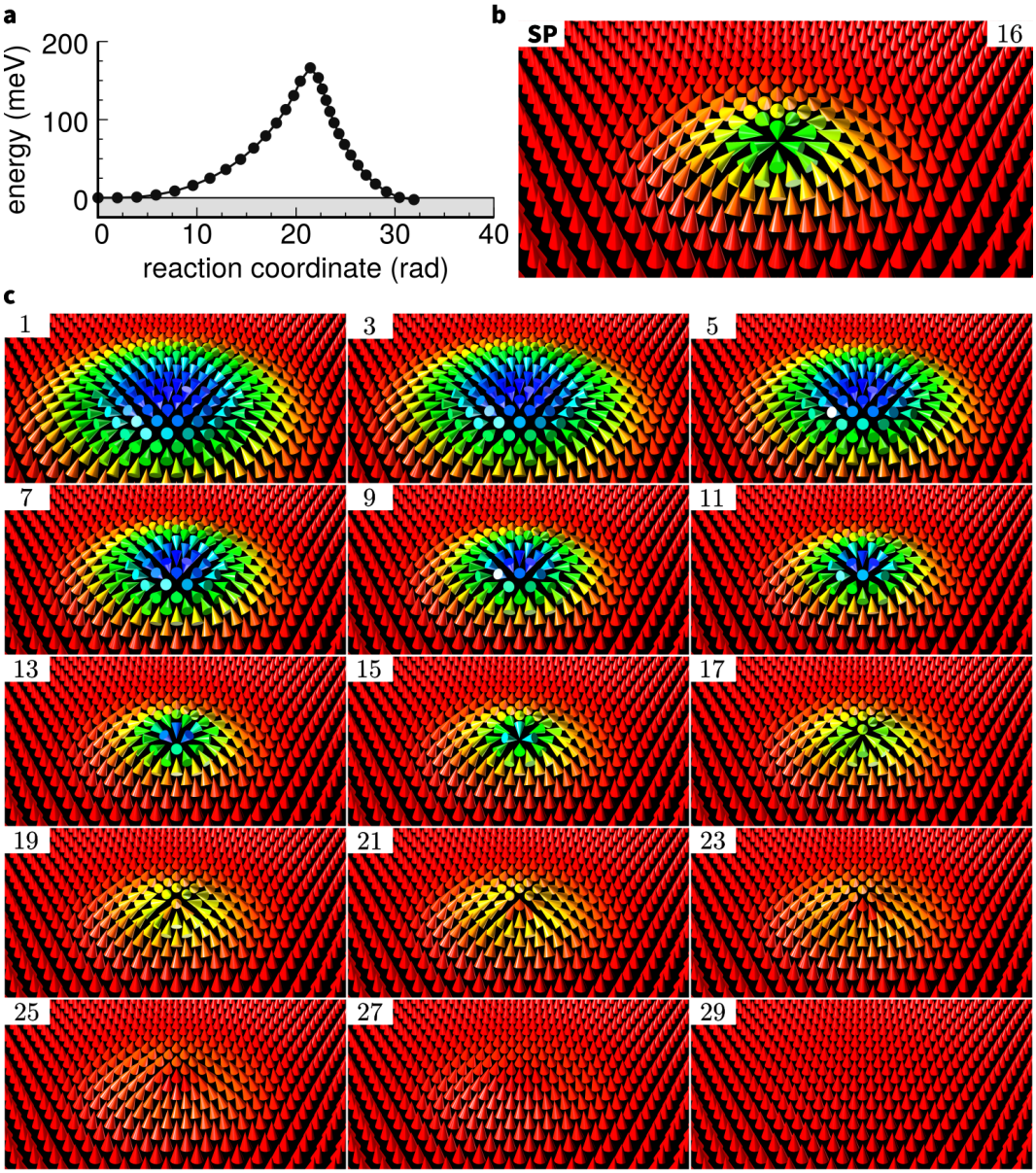

Figure 6.8 | Minimum energy path of the radial collapse mechanism in fcc-Pd/Fe/Ir(111) at $B = 3.2$ T. a) The MEP consists of 30 images and is calculated with J_{DFT} and a hybrid measure of distance applied to the spring forces. The energy of each image is displayed relative to the energy of the initial state. **b)** A section of the magnetic structure of the saddle point image. The colour code denotes the out-of-plane component of the magnetic moments. **c)** A sequence of every second image of the MEP. Indices of the corresponding images are shown in the upper left corner of each magnetic structure.

For each parameter set and with varying out-of-plane magnetic field strengths, isolated skyrmions, previously relaxed using spin dynamics, are used as initial states for the calculation. By homogeneous rotation, 30 images connecting skyrmions and the final state, i. e. the ferromagnetic state, are created to form the initial paths for the calculations.

During GNEB calculations, the initial path is relaxed into a minimum energy path (MEP), that corresponds to the transition mechanism with lowest energy costs in the local vicinity of the initial path. Subsequently, climbing image GNEB (CI-GNEB) calculations are performed in order to find the saddle point (SP) state. Initial paths of all four parameter sets of Pd/Fe/Ir(111) tend to converge into the radial symmetric collapse mechanism, which has been reported earlier based on calculations performed with nearest neighbour exchange interaction only [86, 94, 95].

With frustrated exchange interaction, however, a novel transition mechanism can occur. While this chapter focuses exclusively on the radial symmetric collapse mechanism, skyrmion annihilation via the chimera collapse mechanism is presented in detail in the Chap. 8 and 9. Furthermore, an escape mechanism for skyrmion annihilation has been predicted subsequent to the study presented here [90]. Due to periodic boundary conditions applied for all simulations presented in this work, the escape mechanism, in which skyrmions in finite systems and small magnetic fields can escape over the systems edge, can not occur.

The resulting radial symmetric skyrmion collapse mechanism is presented in Fig. 6.8 on the example of the exchange frustrated fcc-Pd/Fe/Ir(111) at $B = 3.2$ T. The qualitatively similar collapse mechanisms of the other parameter sets are shown in App. A.5. In Fig. 6.8 a, the energy of the MEP is shown over the reaction coordinate, while the magnetic structures of every second image are shown in Fig. 6.8 c. In panel b, the magnetic structure of the SP is displayed.

In the beginning, the skyrmion translates sidewards until its centre is placed between three lattice sites. Subsequently, the skyrmion starts to shrink increasing its energy. Around image 13, the three core moments of the skyrmion start to rotate upwards. The SP is reached, when the angle between these moments is almost 120°. Behind the SP, the energy decreases as the core moments continue to rotate upwards, resulting in a non-collinear ring structure of the skyrmion remnants. Ultimately, the magnetic moments of this ring align parallel to the ferromagnetic background.

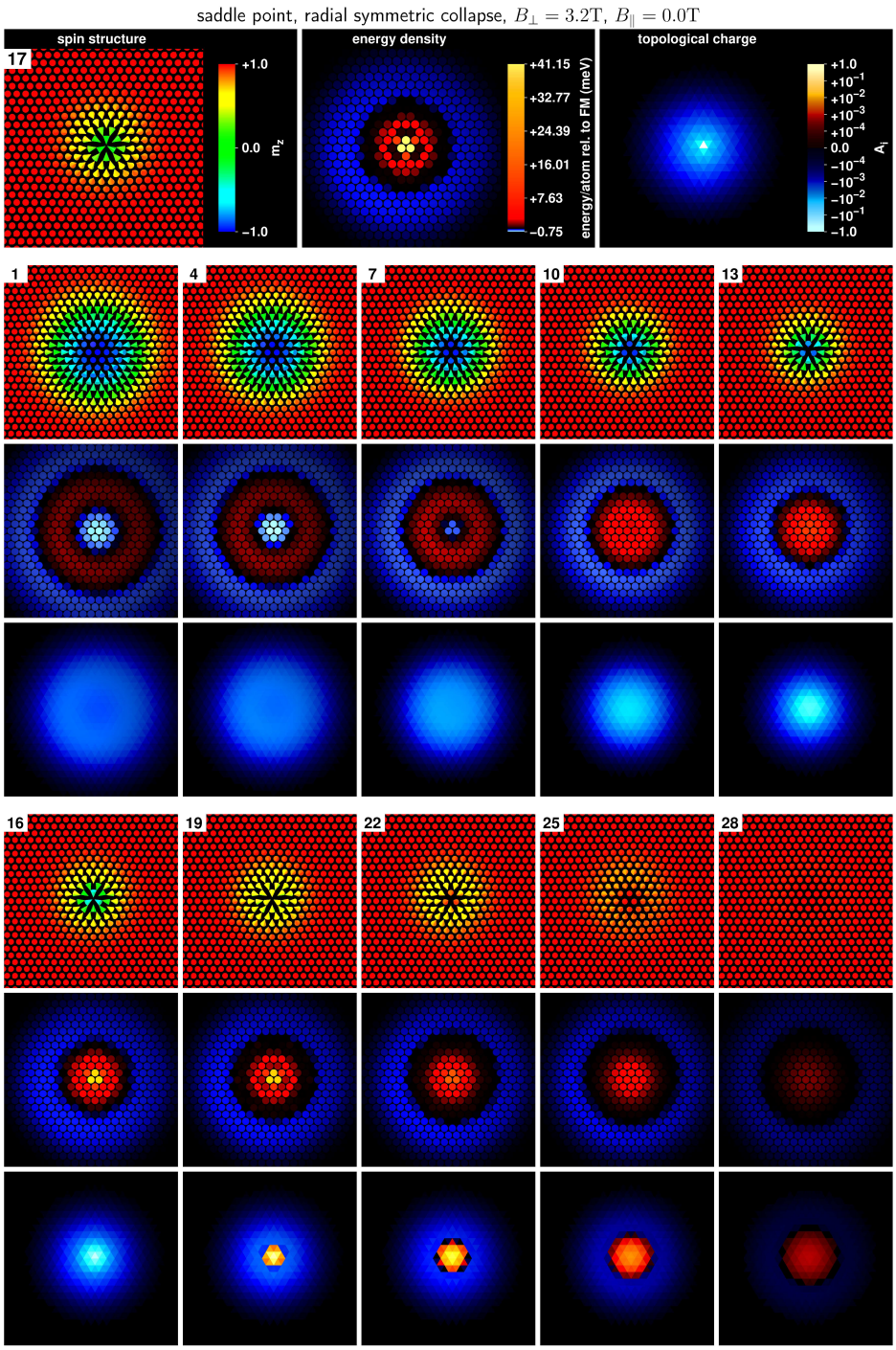

Figure 6.9 | Sequence of the radial symmetric skyrmion collapse in fcc-Pd/Fe/Ir(111) calculated with J_{DFT} parameters at $B = 3.2$ T. The magnetic structure, energy density map relative to the FM state, topological charge density map of the saddle point image and the corresponding colour codes are displayed at the top. The topological charge density is calculated per triangle of adjacent magnetic moments. Below, the same information is shown for every third image of the MEP whose indices are shown in the upper left corner. Figure published in the supplemental material of [XI].

In Fig. 6.9, the same skyrmion collapse is shown for every third image and from birds-eye perspective. Additionally, the corresponding energy density and topological charge density maps are displayed. It can be seen, that the small area of energy gain at the centre of the skyrmion becomes eliminated by the shrinking, while the topological charge becomes more compressed. The energy costs of the three core moments drastically increase as they rotate upward, condensing a significant amount of the topological charge between them. After the SP is reached, the topological charge at the centre flips sign and subsequently spreads over the inner part of the former skyrmion. The positive and negative contributions of, both, the energy density and the topological charge density increasingly decay and cancel each other out as the FM state is approached.

To understand the effect of exchange frustration in Pd/Fe/Ir(111) on the radial skyrmion collapse, the energies along the MEP and relative to the initial states are shown in Fig. 6.10 for both exchange models and for both Pd stackings. The MEPs have been calculated for skyrmions in fcc-Pd/Fe/Ir(111) and hcp-Pd/Fe/-Ir(111) with fields of $B = 4$ T and $B = 1.5$ T, respectively, and are displayed in Fig. 6.10Depending on the model of exchange interaction, the resulting MEPs of both systems show distinctly different SP energies, although the corresponding skyrmion profiles (Fig. 6.5) are very similar.

For hcp-Pd/Fe/Ir(111), the energies of the images calculated with J_{DFT} and J_{eff} remain similar for most of the path. In accordance to the earlier observation of almost indistinguishable energy density maps for relaxed skyrmions (Fig. 6.6), the energy differences between skyrmion and ferromagnetic state coincide almost perfectly for both exchange models. However, while the energy of the SP amounts ≈ 35 meV for J_{eff}, the SP energy climbs up to ≈ 55 meV for J_{DFT}.

Despite the different energies, the magnetic structures of the SP, which are displayed in the insets of Fig. 6.10 a, appear quite similar for both exchange models. This proves that the energy of the SP may depend on the exchange interaction model, although both models lead to identical energy densities of relaxed skyrmions. The impact of exchange frustration on skyrmion stability is emphasised even more by the enhancement of the energy barrier from ≈ 70 meV for J_{eff} to ≈ 145 meV for J_{DFT} in case of fcc-Pd/Fe/Ir(111) (Fig. 6.10 b).

Furthermore, the size of the SP structures is affected by the model of exchange interaction. For fcc-Pd/Fe/Ir(111), the SP obtained with the effective exchange

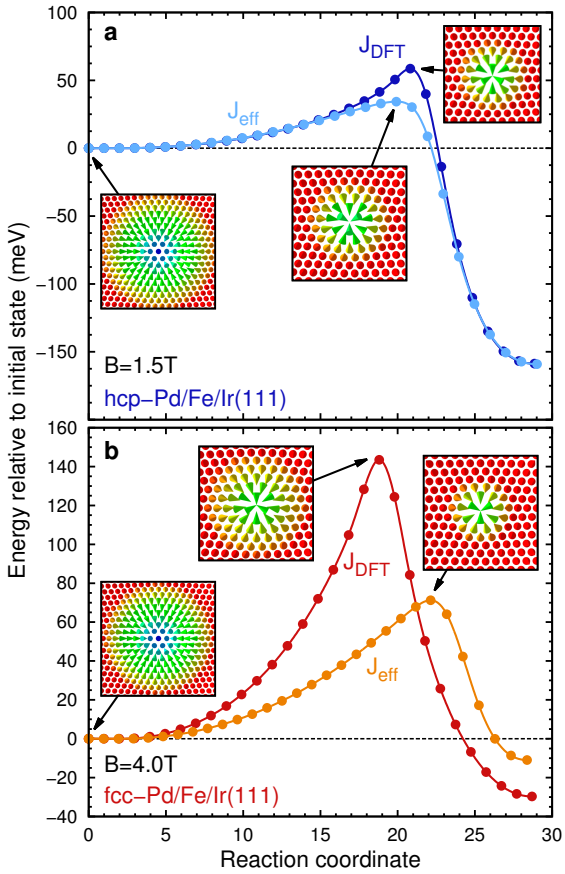

Figure 6.10 | Minimum energy paths of the radial skyrmion collapse in Pd/Fe/-Ir(111). The minimum energy paths are shown for Pd/Fe/Ir(111) with hcp (**a**) and fcc (**b**) stacked Pd. For each stacking both, the energies obtained by using the J_{dft} as well as the J_{eff} parameter sets are presented relative to the corresponding initial states. Magnetic structures of the initial state of the J_{dft} parameter set and the saddle points states of both sets are displayed. Figure published in [I].

model is smaller than its frustrated counterparts with only a few remaining non-collinear magnetic moments. The larger SP size in fcc-Pd/Fe/Ir(111) obtained with the parameter set J_{DFT} coincides with the more rigid skyrmion sizes with included exchange frustration observed in Fig. 6.5. Recently, the relation of SP size and exchange frustration has been reproduced and studied more systematically in [124].

The antiskyrmion annihilation mechanism resembles the radial skyrmion collapse but with four magnetic moments rotated almost in-plane at the SP image, which is depicted in the inset of Fig. 6.11. Similar to the SP of the skyrmion collapse in exchange frustrated fcc-Pd/Fe/Ir(111), the SP structure is quite extent due to exchange frustration. However, the energy barrier of ≈ 10 meV is much smaller than for the corresponding skyrmion with ≈ 145 meV, which can be explained by the almost negated energy contribution of the DMI to the antiskyrmion. The energy

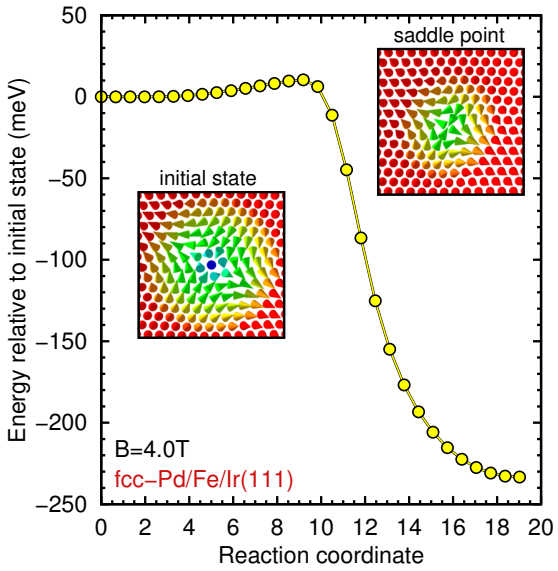

Figure 6.11 | Minimum energy paths of the radial antiskyrmion collapse in fcc-Pd/Fe/Ir(111). The energies along the path are obtained by CI-GNEB using the J_{dft} parameter set at $B = 4\,\mathrm{T}$. Magnetic structures of the initial and saddle point state are displayed as insets. Figure published in [I].

gain of the antiskyrmion collapse is quite large with ≈ -230 meV, which is about -200 meV more than for the corresponding skyrmion.

6.6. Energy contributions to the minimum energy path

In order to obtain further insight of the enhanced energy barriers due to exchange frustration, the decomposed energy contributions of the MEPs are displayed in Fig. 6.12. For both models of exchange interaction of fcc-Pd/Fe/Ir(111) and hcp-Pd/Fe/-Ir(111), the anisotropy and Zeeman contributions continuously gain energy during the collapse, effectively lowering the energy barrier. The DMI energy, favouring the non-collinear orientation of the moments, is gradually lost during the collapse, leading to the energy barriers of the MEPs.

In case of fcc-Pd/Fe/Ir(111) with considered exchange frustration (Fig. 6.12 a), however, the exchange interaction contributes an additional energy barrier clearly visible as a peak around the SP. This feature does not occur for the same collapse with effective exchange (Fig. 6.12 c), as the exchange energy monotonously decreases along the MEP, effectively lowering the energy barrier. While the DMI contribution to the barrier is larger than in Fig. 6.12 a due to the larger DMI parameter in the set

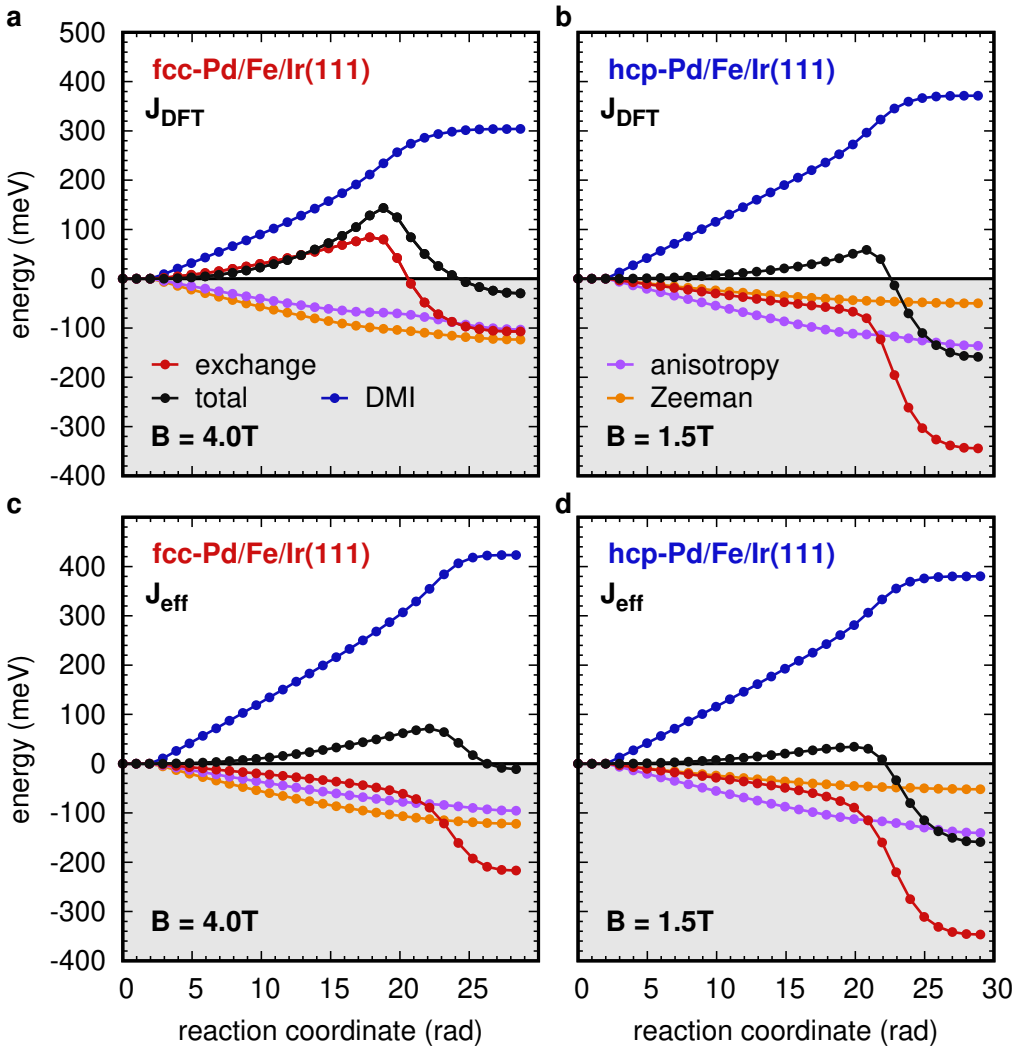

Figure 6.12 | Decomposed energy contributions along the minimum energy path of skyrmion collapse in Pd/Fe/Ir(111). a) MEP of a skyrmion collapse calculated with J_{DFT} parameters via CI-GNEB for fcc-Pd/Fe/-Ir(111) at $B = 4$ T. The energies of the images are shown relative to the initial state. **b)** Similar to **(a)**, but with J_{DFT} parameters for hcp-Pd/Fe/Ir(111) at $B = 1.5$ T. **c)** Similar to **(a)**, but with J_{eff} parameters. **d)** Similar to **(b)**, but with J_{eff} parameters. The data of this figure is published in the supplemental information of [I].

of effective parameters, the resulting energy barrier is smaller. This demonstrates, that the mapping of exchange frustration on an effective nearest neighbour exchange parameter is not sufficient in order to model skyrmion stability in frustrated ultrathin films.

For hcp-Pd/Fe/Ir(111), the exchange energy reduces the energy barrier with both models of exchange interaction. However, the curve of the frustrated exchange in 6.12 b exhibits a slightly less steep slope around the SP than the effective exchange in 6.12 d. This affects the position and energy of the SP, yielding a higher energy barrier with included exchange frustration, although this effect is much more subtle than in case of fcc-Pd/Fe/Ir(111). The decomposed MEP of the antiskyrmion collapse

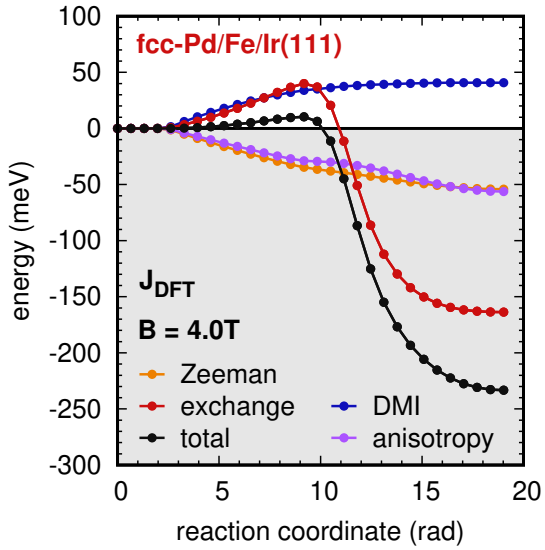

Figure 6.13 | Decomposed energy contributions along the minimum energy path of antiskyrmion collapse in Pd/Fe/Ir(111). MEP of an antiskyrmion collapse calculated with J_{DFT} parameters via CI-GNEB for fcc-Pd/Fe/Ir(111) at $B = 4$ T. The energies of the images are shown relative to the initial state. The data of this figure is published in the supplemental information of [I].

in fcc-Pd/Fe/Ir(111) with included exchange frustration is displayed in Fig. 6.13. Compared to the skyrmion collapse, the DMI contribution and thus the overall energy barrier is strongly reduced. In fact, the barrier stemming from the exchange interaction exceeds the DMI contribution at the SP.

Assuming a similar drop in exchange energy as for the skyrmion collapse with effective exchange interaction, the energy barrier of the antiskyrmion would clearly disappear with J_{eff} parameters. By additionally considering that for hcp-Pd/Fe/-Ir(111) no energy barrier was created by the exchange contribution, it becomes clear,

why antiskyrmions could only be metastabilised in fcc-Pd/Fe/Ir(111) with included exchange frustration.

6.7. Shell resolved energy contributions

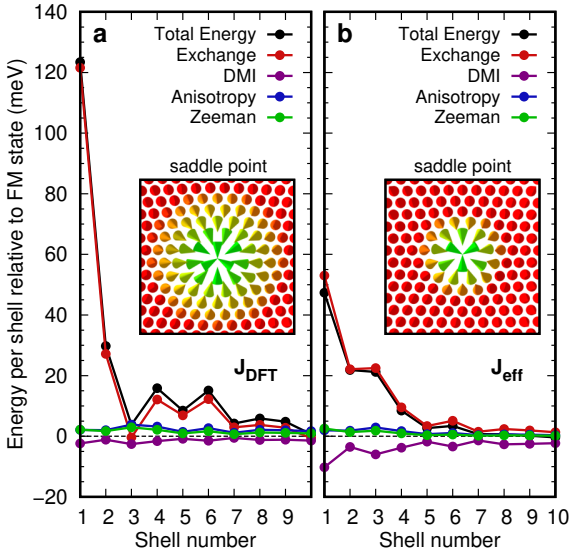

Figure 6.14 | Shell resolved energy contributions of the radial skyrmion collapse in Pd/Fe/Ir(111). The SPs and the corresponding energy decompositions of fcc-Pd/Fe/Ir(111) calculated with J_{DFT} (**a**) and J_{eff} (**b**) are shown relative to the FM state and over the lattice shells around the SP. The midpoints of the SPs are determined numerically and each magnetic moment is allocated to a shell with similar distance to the midpoint. Graphic adapted from [I] with a corrected reference energy of the Zeeman interaction in case of J_{DFT}. Therefore, the reference energy of the Zeeman energy contribution and total energy contribution decreased by about 0.07 meV.

To gain a better understanding of the origin of the different energy contributions of the two exchange models to the SPs, the energy contributions of the SP images of fcc-Pd/Fe/Ir(111) are spatially resolved and displayed in Fig. 6.14 as a function of the lattice shells around the SP centre. For both exchange models, the energy of the most inner shell is dominated by the exchange interaction, which in turn has the largest energy contribution of all shells. Since the energy contributions in Fig. 6.14 are shown relative to the FM energy, they can be compared to the spin spiral dispersion curve in Fig. 6.2.

For both SPs, the magnetic moments of the first shell have a relative angle of almost 120°, which corresponds to the $\overline{\mathrm{K}}$ point of the dispersion curve. While the dispersion curves of both exchange models agree well for small values of q, they deviate by more than a factor of 3 at $\overline{\mathrm{K}}$. This difference in energy for angles of 120° can also be found in the energy contributions of the most inner shells, which exhibit a ratio of $2-3$ between the values shown in Fig. 6.14 a and b.

This can be interpreted as a direct effect of the nearest neighbour approximation which is restricted to a local description of the spin spiral dispersion curve in the vicinity of the fitted spin spiral minimum. While small angles between magnetic moments occur in the equilibrium configuration of skyrmions, the energy of the SPs is dominated by large angles between the moments at the centre. Therefore, the stability of skyrmions and antiskyrmions cannot be described adequately by J_{eff} when the corresponding spin spiral dispersion curve deviates significantly from the actual dispersion curve of the system, i. e. when the system exhibits strong exchange frustration.

6.8. Energy barriers over magnetic field

Here, the effect of exchange frustration on skyrmion stability is studied more systematically by performing GNEB calculations of skyrmion and antiskyrmion collapses in Pd/Fe/Ir(111). The energy difference between the SP and the initial state, i. e. the relaxed skyrmion state, is extracted as energy barrier ΔE and plotted as a function of external magnetic field in Fig. 6.15. As a general trend, the energy barriers of fcc-Pd/Fe/Ir(111) and hcp-Pd/Fe/Ir(111) decline with increasing magnetic field, regardless of the applied model of exchange interaction.

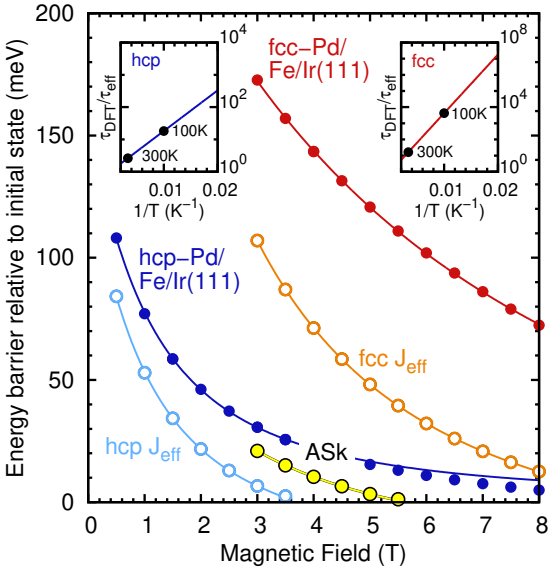

Figure 6.15 | Energy barriers over external magnetic field in Pd/Fe/Ir(111). Energy barriers of radial skyrmion collapse obtained via CI-GNEB calculations for fcc-Pd/Fe/Ir(111) and hcp-Pd/Fe/Ir(111) with both models of exchange interaction, J_{DFT} and J_{eff}, are displayed vs. out-of-plane magnetic field strength. The antiskyrmion barriers (ASk) are calculated with the J_{DFT} parameters of fcc-Pd/Fe/Ir(111). The insets show ratios of skyrmion lifetimes calculated via Eq. 5.51 with the energy barriers obtained for J_{DFT} and J_{eff}. The prefactors are assumed to be identical for both models and therefore cancel out in the ratio of lifetimes. Figure published in [I].

However, in contrast to the skyrmion radii in Fig. 6.5, the energy barriers resulting from the two exchange models are clearly distinct over the entire interval of magnetic fields for, both, fcc-Pd/Fe/Ir(111) and hcp-Pd/Fe/Ir(111). The energy barriers of hcp-Pd/Fe/Ir(111) with frustrated exchange is ≈ 25 meV larger than the barriers obtained with effective nearest neighbour exchange. At magnetic fields of more than 3.5 T, skyrmions in hcp-Pd/Fe/Ir(111) are no longer metastable when effective exchange interaction.

For fcc-Pd/Fe/Ir(111) even a difference in energy barrier of about 60 meV can be seen. However, skyrmions obtained with J_{eff} parameters remain metastable over the entire interval of magnetic fields. As already discussed, only antiskyrmions in fcc-Pd/Fe/Ir(111) with included exchange frustration exhibit an energy barrier towards the FM state. This barrier is altogether much smaller than the barrier of the skyrmion counterpart and vanishes by 5.5 T.

While it is evident, that the energy barriers of radial symmetric skyrmion collapse in Pd/Fe/Ir(111) is enhanced by exchange frustration, the Arrhenius law describing lifetimes of metastable skyrmions also depends on the prefactor of the transition, which is discussed in detail in Chap. 7. In order to estimate the resulting improvement of skyrmion lifetimes solely by the effect of exchange frustration on the energy barrier, the same prefactor for both models of exchange interaction is assumed.

Hence, the prefactors cancel each other out in the ratio of lifetimes presented in the insets of Fig. 6.15. For hcp-Pd/Fe/Ir(111), the mean lifetime increases by a factor of three at room temperature and by more than one order of magnitude at 100 K. In case of fcc-Pd/Fe/Ir(111), the lifetime at room temperature increases by ≈ 5 while it is around four orders of magnitude larger at 100 K, compared to the lifetimes of skyrmions obtained with effective exchange.

The results presented in this chapter clearly demonstrated, that skyrmion transition processes cannot be modelled adequately by an effective nearest neighbour approximation for the exchange interaction in exchange frustrated film systems. Instead, the model Hamiltonian of exchange interaction has to describe the complete spin spiral dispersion curve with reasonable precision. A good match of the model with the dispersion curve in the vicinity of the $\bar{\Gamma}$ point and the spin spiral minimum may be sufficient for the simulation of relaxed skyrmions. Larger values of q, however, are crucial for magnetic states with fast rotating moments such as the SP structures of skyrmion transition processes.

The effect of larger energy barriers due to exchange frustration appears to be rather general, as it has also been predicted for the exchange frustrated ultrathin film system Pd/Fe/Rh(111) [II]. Recently, the effect has been reproduced by micromagnetic simulations with incorporated exchange frustration [124] and by calculations considering several layers of magnetic material [23].

Moreover, recent Monte Carlo simulations of skyrmion transitions in fcc-Pd/Fe/-Ir(111) performed with the parameter sets J_{DFT} and J_{eff} yield phase diagrams showing higher temperature stability of skyrmions with included exchange frustration [97]. The temperature stability predicted with J_{DFT} in [97] is supported by measurements on skyrmion stability in Pd/Fe/Ir(111) published very recently in [98].

Furthermore, the multiscale approach presented in this thesis enabled for the prediction of metastable skyrmions in the strongly frustrated ultrathin film system Rh/Co/Ir(111), which was subsequently confirmed by spin-polarised scanning tunneling microscopy (SP-STM) measurements on this system [VII]. In this system, the stabilisation due to exchange frustration even exceeds the contribution of DMI, making Rh/Co/Ir(111) a promising candidate for hosting metastable antiskyrmions [VII, XIV].

7. Entropy-size effect on skyrmion lifetimes

In transition state theory (TST), the rate of thermally induced skyrmion annihilations is given by an Arrhenius law (Eq. 5.51) and depends on the prefactor, the energy barrier and the thermal energy. At the beginning of this study, estimations of skyrmion stability were typically based on the energy barrier and the thermal energy alone [I, VI, 95, 96, 179–182]. It was often assumed, that a magnetic state with a barrier of 50 times the thermal energy is sufficiently stable for data storage [45, 96]. This simple criterion was motivated by the exponential dependency of the transition rate on the energy barrier and the general assumption, that the prefactor is quite constant with values on the order of $\nu_0 \approx 10^9 - 10^{10}$ s^{-1}, which were found by direct Langevin dynamics simulations [78, 86].

More recently, Wild *et al.* published a highly debated experimental study [66] on skyrmion lifetimes in $Fe_{0.5}Co_{0.5}Si$, a B20 compound, in which they measured a giant variation of the prefactor of more than 30 orders of magnitude with small changes of magnetic field. The authors identified this as an enthalpy-entropy compensation effect, although the origin of this effect remained unclear.

Subsequently, a theoretical study [90] on the prefactor of skyrmion collapse carried out by Bessarab *et al.* in the framework of TST reported a prefactor of about 10^{10} s^{-1} for radial skyrmion collapse in hcp-Pd/Fe/Ir(111). It was found, that the prefactor increases by two orders of magnitude with an increasing magnetic field, while the prefactor in fcc-Pd/Fe/Ir(111) decreases from approx. 10^{14} to 10^{12} s^{-1}. These small variations of the prefactor gradually appear over an interval of about 10 T and its origins remained unexplored in this study, too.

In this chapter, a detailed study (published in Ref. [IX]) on the prefactor of radial symmetric skyrmion collapse in ultrathin films and its dependence on external magnetic fields and material parameters is presented. The prefactors and the resulting transition rates of skyrmion annihilation in Pd/Fe/Ir(111) and Pd/Fe/-

Rh(111) are calculated in TST over a large interval of magnetic fields, revealing a strong entropy-size effect that can stabilise magnetic skyrmions. This effect, which enhances skyrmion lifetimes by over seven orders of magnitude in case of hcp-Pd/-Fe/Ir(111), is traced back to a few localised, low energy skyrmion eigenmodes which are strongly affected by the skyrmion size as well as the interaction parameters of the system. These findings about the dependencies of the prefactor, which proves to be anything but constant, offer new possibilities to optimise the stability of magnetic skyrmions beyond the energy barrier.

7.1. Barriers and prefactors

The magnetic interaction parameters of the Pd/Fe bilayers on Ir(111) and Rh(111) obtained from *first-principles* calculations are listed in Tab. 4.1. For each substrate, both, the fcc and hcp stacking of the Pd layer is considered. The exchange interaction of both Pd/Fe/Rh(111) systems is comparable with the Pd/Fe/Ir(111) systems including exchange frustration effects. However, the parameters of Dzyaloshinskii-Moriya interaction (DMI) and magnetocrystalline anisotropy are much smaller due to the weaker spin-orbit coupling (SOC) induced by the lighter Rh(111) substrate compared to Ir(111).

system	B_c (T)
fcc-Pd/Fe/Ir(111)	3.20
hcp-Pd/Fe/Ir(111)	0.20
fcc-Pd/Fe/Rh(111)	2.80
hcp-Pd/Fe/Rh(111)	1.80

Table 7.1 | Critical magnetic fields for Pd/Fe/Ir(111) and Pd/Fe/Rh(111). The values of the magnetic field, B_c, shown here are estimated from the intersection of the skyrmion and FM phases in the stability diagrams in Fig. 6.4 and Fig. A.3. Subsequently, the magnetic field values of the intersections are rounded up to ensure simulations in the FM phase. The values can also be found in the supplemental material of [IX].

To obtain an overview of the magnetic structures, magnetic phase diagrams of Pd/-Fe/Ir(111) with both stackings of Pd are shown in Fig. 6.4. For fcc-Pd/Fe/Ir(111) a spin spiral ground state is found, which changes to a skyrmion lattice phase with increasing magnetic field before reaching the critical magnetic field, B_c, and becoming ferromagnetic.

While no spin spiral or skyrmion lattice phases has been observed in case of hcp-Pd/Fe/Ir(111), non-collinear domain wall structures are lower in energy than the

ferromagnetic (FM) state at zero field. In order to ensure the calculation of metastable skyrmions in a FM background, a critical magnetic field of $B_c \approx 0.2$ T has been determined. Both Pd/Fe bilayers on the Rh(111) substrate exhibit phase diagrams qualitatively similar to fcc-Pd/Fe/Ir(111) and are shown in Fig. A.3.

In order to directly compare the properties of isolated skyrmions in these systems, quantities can be plotted as a function of $B - B_c$ instead of the total value of the magnetic field. The critical magnetic field, B_c, depends in first approximation on the depth of the spin spiral dispersion and thus can be seen as an offset to the beginning of the ferromagnetic phase. By plotting over $B - B_c$, the properties of skyrmions are evaluated without this offset, allowing for comparison of the systems in the same phase. The values of B_c are determined by the intersection of the energies of the skyrmion state and the FM background. However, the values of B_c shown in Tab. 7.1 and used in the course of this chapter are rounded up to ensure that the simulations are performed in the FM phase where isolated skyrmions are metastable.

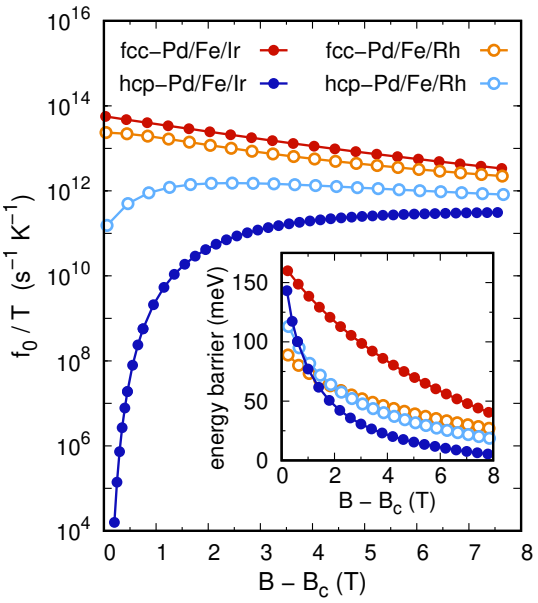

Figure 7.1 | Prefactors divided by temperature and energy barriers are shown as a function of $B - B_c$. For the four systems, Pd/Fe/Ir(111) and Pd/Fe/Rh(111) with fcc and hcp stacked Pd layer, the energy barriers, ΔE, are obtained by CI-GNEB simulations. Subsequently, the prefactors divided by temperature, here denoted as f_0/T, are determined by diagonalisation of the Hessian matrix in the framework of transition state theory. The corresponding critical fields, B_c, are listed in Tab. 7.1. Figure published in [IX].

In seeking to calculate the prefactor of the radial skyrmion annihilation in TST (see Sec. 5.3), the Hessian matrices of the initial and saddle point (SP) states are diagonalised, yielding the eigenvalues of both states sorted in increasing order. For the skyrmion state, the first two eigenmodes are corresponding to the free translation on the atomic lattice, which are therefore modelled in Goldstone mode approximation. The unequal number of Goldstone modes at the initial and SP states leads to an

uncancelled factor of $2\pi k_{\mathrm{B}}T$ giving rise to an explicit temperature dependence of the prefactor which is finally calculated via Eq. 5.55.

In Fig. 7.1, the prefactors of the four systems, divided by the temperature T, are plotted over the magnetic field relative to B_c. In logarithmic scale, an immense variation in prefactor over magnetic field becomes visible for hcp-Pd/Fe/Ir(111). Beginning with a value of about 10^4 ($\mathrm{s}^{-1}\mathrm{K}^{-1}$), the prefactor rapidly increases at first, until it slowly converges to a value of $\approx 5 \cdot 10^{11}$ ($\mathrm{s}^{-1}\mathrm{K}^{-1}$).

In contrast, both bilayers with fcc stacked Pd show values of $10^{13} - 10^{14}$ ($\mathrm{s}^{-1}\mathrm{K}^{-1}$) at $B - B_{\mathrm{c}} = 0$ T and decay almost linear on the logarithmic scale with roughly one order of magnitude over an increase in magnetic field of 8 T. The prefactor in hcp-Pd/Fe/Rh(111) shows an intermediate behaviour with an initial increase of about one order of magnitude and a subsequent slow decay over the vast part of the field interval. The values of hcp-Pd/Fe/Rh(111) are also intermediate with 10^{11} ($\mathrm{s}^{-1}\mathrm{K}^{-1}$) at the beginning and 10^{12} ($\mathrm{s}^{-1}\mathrm{K}^{-1}$) at the end of the interval.

The inset of Fig. 7.1 shows the corresponding energy barriers ΔE of the four systems over $B - B_{\mathrm{c}}$. The barriers are determined by climbing image geodesic nudged elastic band (CI-GNEB) calculations and correspond to the radial symmetric annihilation mechanism presented in Sec. 6.5. Both Pd stackings of Pd/Fe/Ir(111) exhibit similar energy barriers of ≈ 150 meV at the beginning of the ferromagnetic phase at $B - B_{\mathrm{c}} = 0$ T. However, the barriers of hcp-Pd/Fe/Ir(111) decrease much faster for small fields and thus the values of ΔE increasingly deviate between both Pd/Fe/Ir(111) systems.

The barriers of the bilayers on Rh(111) start below both Pd/Fe/Ir(111) systems with values of ≈ 90 meV and ≈ 120 meV for hcp and fcc, respectively. With increasing magnetic field, they gradually lie between fcc-Pd/Fe/Ir(111) and hcp-Pd/Fe/Ir(111) due to the rapid decrease of the barrier of hcp-Pd/Fe/Ir(111). Similar to the Pd/Fe bilayers on Ir(111), the barrier of fcc-Pd/Fe/Rh(111) shows a steeper increase than hcp-Pd/Fe/Rh(111) eventually leading to an intersection of both curves around $B - B_{\mathrm{c}} = 2$ T.

The first obvious conclusions that can be drawn from the data in Fig. 7.1 are as follows: The prefactor of skyrmion annihilation can depend heavily on the external magnetic field, even shows qualitatively different trends for different systems and is by no means constant.

7.2. Decomposition of the prefactor

The question arises as to the origin of the observed trends in the prefactor. In order to answer this, the prefactor is broken down into the individual components entering Eq. 5.55: The Goldstone mode volume V_0 of the two translational modes of the skyrmion state, the velocity factor $\sqrt{\sum_j a_j^2/\epsilon_j^{\mathrm{SP}}}$ and the difference in entropy between the initial and SP state, $\Delta S'$, that is determined by the eigenvalues of the Hessian matrices of the two states. The rest of the ingredients in Eq. 5.55 is independent of the magnetic field and, thus, cannot contribute to the drastic change in prefactor visible in Fig. 7.1.

In Fig. 7.2, the components of the prefactor as well as the skyrmion radius are displayed over $B - B_{\mathrm{c}}$. The radii of all four systems gradually decay with increasing magnetic fields. On the other end of the interval, the radii tend to diverge with decreasing fields. The divergence of skyrmion radius with decreasing magnetic field is due to the stripe out instability [178] and is determined by the system dependent interaction parameters.

The behaviour of skyrmion radii can be roughly divided into two regimes: The convergent regime with little change in the skyrmion radius and the divergent regime with asymptotic behaviour of the radius. In case of hcp-Pd/Fe/Ir(111), the transition from the divergent into the convergent regime is visible nicely, while both Pd/Fe/Rh(111) systems show the divergent behaviour only partially.

The radii of fcc-Pd/Fe/Ir(111) remain rather constant and decrease only slightly with increasing fields. The accessible interval of magnetic fields for a transition from one radius regime into another is limited by the interval in which isolated skyrmions can be metastablised in the FM background. Therefore, it can be interpreted, that the skyrmion radii of fcc-Pd/Fe/Ir(111) are already close to the convergence regime in the vicinity of $B - B_{\mathrm{c}} = 0$ T.

Analysing the inverse of the Goldstone mode volume in Fig. 7.2 a, only a slight change of values can be seen. The inverse volume of all four systems increases, with the largest increase by a factor of about two for hcp-Pd/Fe/Ir(111). Comparing Fig. 7.2 a and d, a direct connection between the Goldstone mode volume and the skyrmion radius can be seen for all four systems. This behaviour is not unexpected, since the volumes are calculated by the determination of the potential change in orientation of

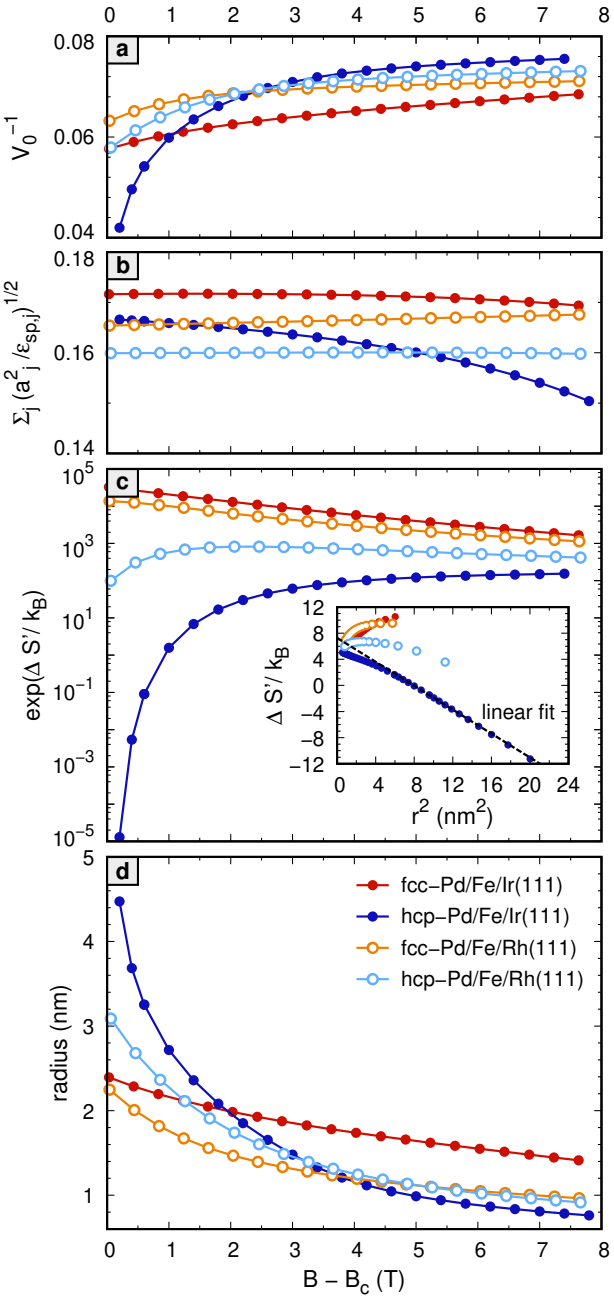

Figure 7.2 | The decomposed ingredients of the prefactor as a function of $B - B_c$. For Pd/Fe/Ir(111) and Pd/Fe/Rh(111), each with fcc and hcp stacked Pd layers, the prefactors of radial symmetric skyrmion collapse are calculated via transition state theory. The different panels show the inverse of the Goldstone mode volume **(a)**, the velocity contributions of the prefactor **(b)**, the exponent of the entropy difference between saddle point and skyrmion state **(c)** and the skyrmion radius **(d)**. In the inset of **(c)**, the entropy difference is plotted over the squared skyrmion radius. Figure published in [IX].

the magnetic moments due to skyrmion translation. Since the $\Theta(\mathbf{r})$-profile and the skyrmion radius are strongly entangled (see Sec. 3.4.1), also the Goldstone mode volume depends on the skyrmion radius. The large change in prefactor is supported by the trend of the Goldstone mode volumes, but with a maximal variation of a factor of two, the origin for the change has to lie somewhere else.

Next, the sum over the velocity components shown in Fig. 7.2 b is analysed. The sum of the components is slightly increasing for both Pd/Fe/Rh(111) systems, while it is decreasing for both systems on the Ir(111) substrate. The magnitude of variation is even smaller than for the Goldstone mode volumes, with the largest change occurring for hcp-Pd/Fe/Ir(111) by about 10%. Although at this point it remains unclear where the changes come from, it is clear that they are too small to have a noticeable impact on the trend of the prefactor.

Finally, it is the exponent of the entropy difference, calculated by Eq. 5.69 and displayed in Fig. 7.2 c, that gives rise to the huge change in prefactor seen in Fig. 7.1. For all four systems the trends of entropy are almost identical to the trends of the prefactor, whose magnetic field dependence is therefore largely defined by entropy.

The strong initial increase of the entropy difference for hcp-Pd/Fe/Ir(111) and to some extend for hcp-Pd/Fe/Rh(111), resembles the trends of the skyrmion radius. In the inset of Fig. 7.2 c, the entropy difference is plotted over the square skyrmion radius. For hcp-Pd/Fe/Ir(111), the entropy difference can be fitted linear for square radii larger than $\approx 4\text{nm}^2$. Note, that the skyrmion radius is inverse to the magnetic field strength and, thus, the linear fit is applicable in the divergent regime of small magnetic fields. Consistently, for hcp-Pd/Fe/Ir(111), the deviations from the linear fit increase for very small square radii, i. e. large magnetic fields.

The transition from asymptotic to convergent regime can also be anticipated for hcp-Pd/Fe/Rh(111), as the entropy for large square radii begins to decrease. For fcc-Pd/Fe/Rh(111), the change of trend appears slower as the skyrmion radius does not reach the divergence regime as fast as for hcp-Pd/Fe/Rh(111). In the case of fcc-Pd/Fe/Ir(111), whose skyrmion radii are more resilient to changes in the magnetic field, the entropy increases over the entire interval of magnetic fields studied. These results already give an indication of the relationship between entropy difference and skyrmion size.

7.3. Eigenvalue spectra

To shed light on the magnetic field dependence of the entropy difference between the initial and SP states, the eigenvalues of both states are studied in more detail. Considering a state with $2N-P$ degrees of freedom treated in harmonic approximation, the entropy of the state is calculated by the product of $2N-P$ eigenvalues (see Eq. 5.69). Additional P eigenmodes are treated in Goldstone mode approximation, and thus are omitted from the product and enter the entropy via the Goldstone mode volume (see Eq. 5.55). For the typical simulation box of 70×70 atoms, as it is used throughout this chapter, this results in $9800-P$ contributing eigenvalues for the initial skyrmion state and $9800-P-1$ eigenvalues for the SP state, whose first eigenmode is additionally omitted from the product as the unstable mode.

Each eigenvalue corresponds to an eigenvector, which can be characterised into three groups: Localised skyrmion or SP modes, magnon modes of the ferromagnetic background and mixed modes, a combination of both. Retransformed into the $3N$ basis of real space, an eigenvector of the Hessian matrix consists of N $3D$ vectors, one $3D$ vector for each magnetic moment of the lattice. These $3D$ vectors give the direction and magnitude of rotation for the moment along the corresponding eigenmode. Note, that the positive and negative directions of the eigenvectors are degenerate and the algorithm only returns one of them by random choice.

In Fig. 7.3, one eigenvector of each type is displayed on the example of the isolated skyrmion state in hcp-Pd/Fe/Ir(111) at $B = 0.25$ T. One can see the magnetic lattice as the diamond simulation box in black and each $3D$ vector with a non-vanishing magnitude as coloured arrow. In the left panel, the four-fold skyrmion deformation mode is localised around the central skyrmion and exhibits its typical four nodes of which two are narrowing the skyrmion while the other two are elongating it. A mixed mode can be seen in the central panel. It has non-vanishing $3D$ vectors in the ferromagnetic background as well as at the skyrmion. In the right panel, the vectors spare the area of the skyrmion and belong to a pure magnon mode.

While the analysis of all $2N$ eigenmodes is beyond practical options, the lowest 100 eigenvalues of the initial skyrmion and the SP state of hcp-Pd/Fe/Ir(111) are displayed in Fig. 7.4 a and b. The eigenvalues are plotted over the magnetic field, creating the low energy eigenvalue spectra of both states, in which each vertical line belongs to one diagonalised Hessian matrix at the given value of the magnetic

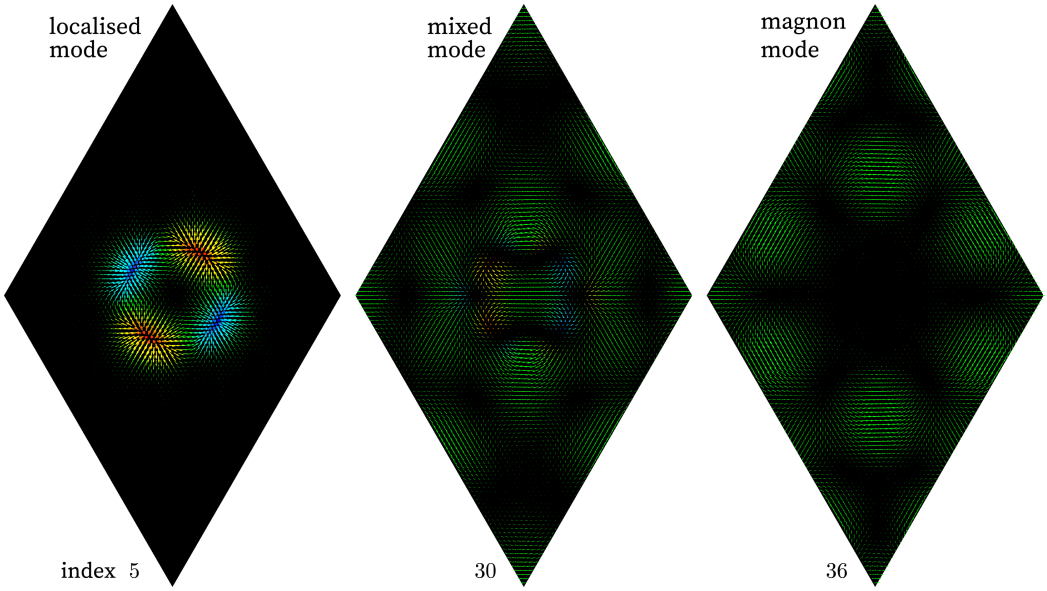

Figure 7.3 | Eigenvectors of a localised skyrmion mode, a mixed mode and a ferromagnetic mode in hcp-Pd/Fe/Ir(111) at $B = 0.25$ T. The form of the black diamond is given by the hexagonal 70×70 atomistic lattice used as simulation box. Each eigenvector consists of one $3D$ vector per magnetic moment site which are shown as arrows whose size corresponds to the norm of the $3D$ vector. The out-of-plane components are denoted by the colour code with red and blue for positive and negative out-of-plane direction, respectively, and green for an in-plane orientation of the $3D$ vector. At the bottom of each simulation box, the index of the corresponding eigenvalue spectrum is displayed.

field. The individual points create a band structure of the eigenvalues in which the dispersion of single bands is visible.

In contrast to the magnon continuum of infinite systems, magnon modes of a finite system give rise to a discrete number of bands. In combination with mixed modes, these discrete bands form several parallel bundles increasing monotonously with increasing magnetic field. In doing so, the dispersions of the mixed modes appear to be dominated by their magnon contributions as they exhibit a similar slope.

In the spectrum of the skyrmion state, in Fig. 7.4 a, several bands with larger and more variable slopes can be seen, corresponding to localized skyrmion modes. In Fig. 7.5, the eigenvectors corresponding to the first ten eigenvalues of the spectrum at $B = 0.25$ T are displayed. For the selected magnetic field, the first nine of them are skyrmion modes, of which most are two-fold degenerated. The first two modes are translational modes whose eigenvalues remain almost zero over the whole

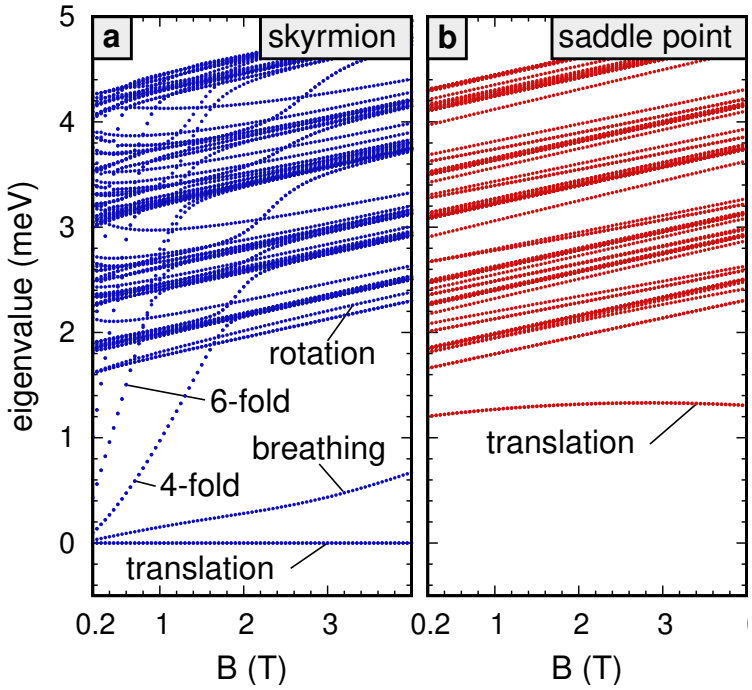

Figure 7.4 | Low energy eigenvalue spectrum of hcp-Pd/Fe/Ir(111). The lowest 100 eigenvalues are displayed for the initial skyrmion **(a)** and saddle point **(b)** states. Each column of points corresponds to one Hessian matrix that was diagonalised at the corresponding magnetic field. A few localised skyrmion and saddle point modes are labelled and the corresponding eigenvalues are displayed in Fig. 7.5 and Fig. 7.8. The eigenvalue of the unstable mode of the saddle point state is not visible as it exhibits a strongly negative value beyond the shown eigenvalue interval. Figure published in [IX].

magnetic field interval. For this reason, they enter the prefactor in Goldstone mode approximation. The eigenvalue of the breathing mode is increasing with magnetic field, but remains the lowest non-Goldstone eigenvalue in the spectrum. It is followed by the four-fold, six-fold and eight-fold deformation modes, which all are steeply increasing with magnetic field, crossing the magnon and mixed mode bundles. The tenth mode is the first mixed mode corresponding to the lowest of the parallel increasing modes of the spectrum.

The approach of steeply rising skyrmion bands to the vicinity of magnon bands occasionally leads to a hybridisation of the participating modes instead of a simple crossing. In Fig. 7.6, a part of the skyrmion eigenvalue spectrum from Fig. 7.4 is shown, in which the eigenvalues of hybridising skyrmion and magnon bands are highlighted by green and red colour, respectively. As it is shown in Fig. 7.7, the

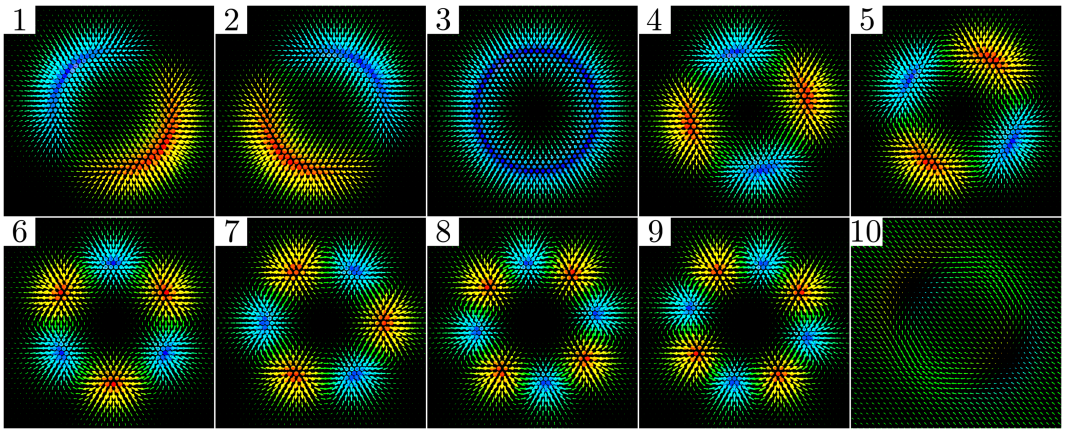

Figure 7.5 | First ten skyrmion eigenvectors for hcp-Pd/Fe/Ir(111) at $B = 0.25$ T. A zoom of the eigenvectors consisting of one $3D$ vector per lattice site is shown with the isolated skyrmion at its centre. The size of the arrows scales with the norm of the vector, while the colour code denotes the out-of-plane component with red and blue for positive and negative out-of-plane components and green for in-plane oriented vectors. The eigenvectors corresponds to the following localised skyrmion modes: **1,2**: translation; **3**: breathing; **4,5**: 4-fold deformation; **6,7**: 6-fold deformation; **8,9**: 8-fold deformation. The last shown eigenvector belongs to a mixed mode.

decisive difference between both modes is lifted during the approach as both hybridise and become mixed modes. With further increasing magnetic field, both modes finally interchange their initial characters and move apart.

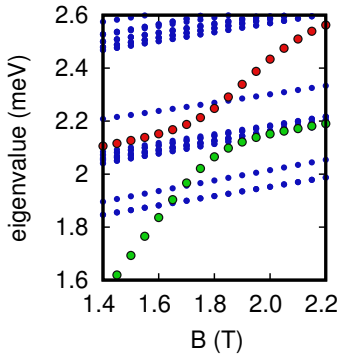

Figure 7.6 | Illustration of band hybridisation of skyrmion and magnon modes. A section of the low energy eigenvalue spectrum from Fig. 7.4 is shown with highlighted eigenvalues of a magnon mode (red) and the 4-fold skyrmion deformation mode (green). Note, that both eigenmodes are two-fold degenerated in the spectrum. The corresponding eigenvectors are shown in Fig. 7.7

In contrast to the skyrmion, the spectrum of the SP state in Fig. 7.4 b does not show many localised modes. The vast majority of bands increases parallel to the magnon bands and no hybridisations occur due to a lack of steeply increasing SP modes. The eigenvalues of the unstable mode are negative with values on the order

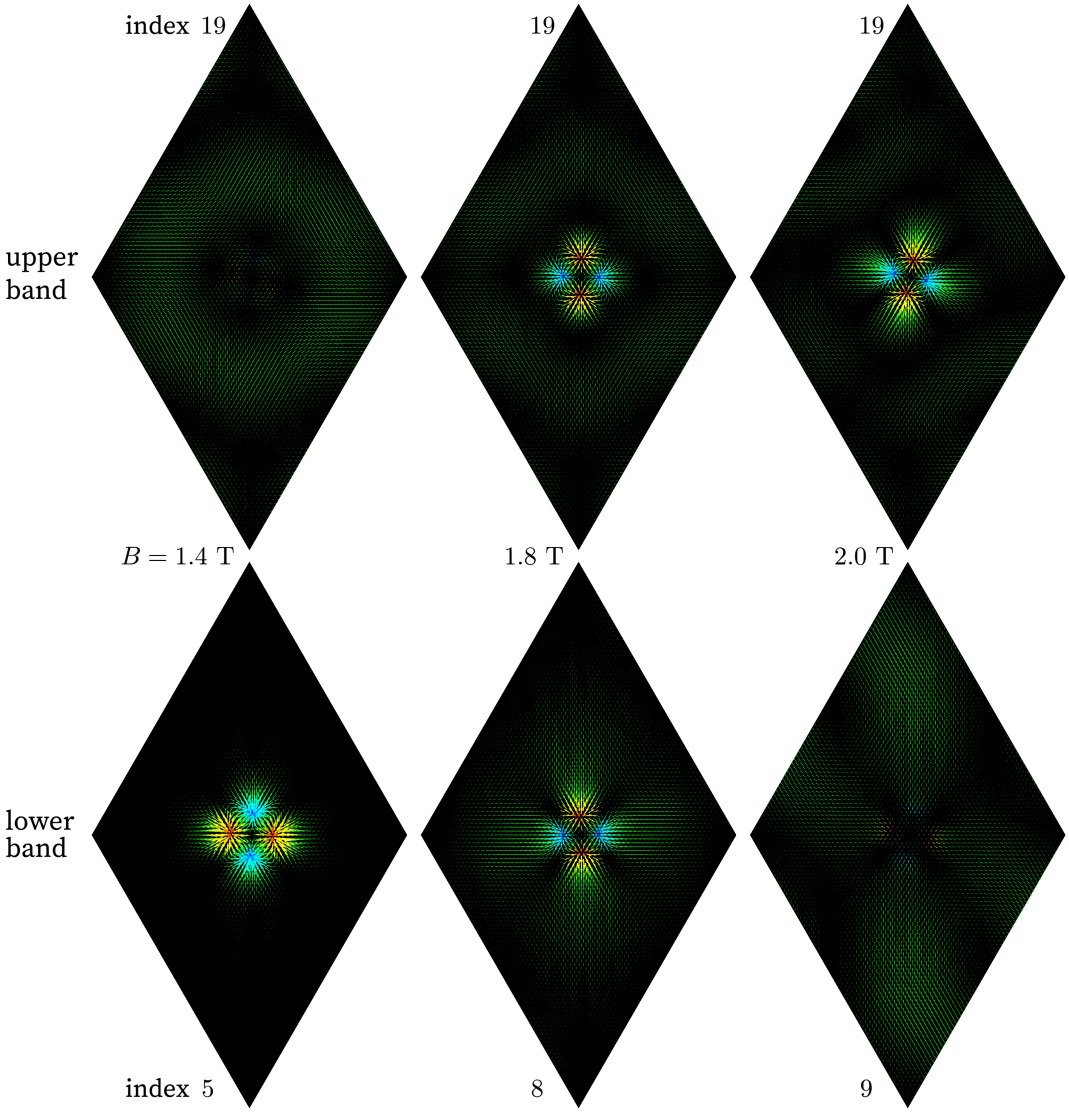

Figure 7.7 | Eigenvectors of hybridising skyrmion and magnon modes in hcp-Pd/Fe/Ir(111). The size of the $3D$ vectors, each belonging to a site of the black 70×70 atomistic lattice, scales with its norm. The out-of-plane components are denoted by the colour code with red and blue for positive and negative out-of-plane direction, respectively, and green for an in-plane orientation of the $3D$ vector. The upper and lower row of three eigenvectors correspond to the red and green bands highlighted in Fig. 7.6, respectively. The applied magnetic fields and indices of the selected eigenmodes in the spectrum are displayed next to the corners of the diamonds.

of ≈ -20 meV and are omitted in the spectrum. Its eigenvector is displayed in Fig. 7.8 and is responsible for the rotation of the three innermost moments of the SP structure along the reaction coordinate. The other two modes shown in Fig. 7.8 are denoted as translation modes in the spectrum, but do have eigenvalues unequal zero due to the smaller size of the SP structure, which in turn is more affected by lattice effects than the skyrmion state. For this reason, they enter the entropy in harmonic approximation in contrast to the translation modes of the skyrmion states.

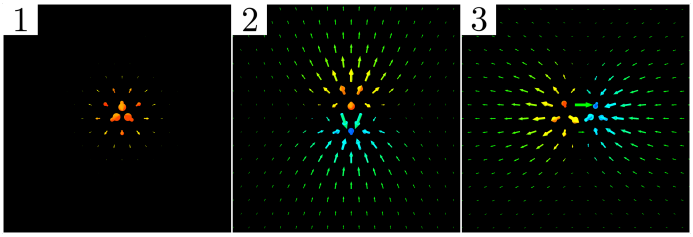

Figure 7.8 | First three saddle point eigenvectors of radial symmetric skyrmion collapse in hcp-Pd/Fe/-Ir(111) at $B = 0.25$ T. The colour code denotes the out-of-plane component. The size of the arrows scales with the norm of the vectors. Note, that the first image depicts the eigenvector of the unstable mode. The second and third eigenmodes appear as saddle point translation modes. For the sake of clarity, the cone sizes of the first mode are scaled down with respect to the other two modes.

It becomes evident from the eigenvalue spectra, that both states exhibit a majority of magnon and mixed modes with parallel increasing eigenvalues. The ratio of pairs of these eigenvalues remains constant over magnetic field and therefore magnon and mixed modes do not influence the magnetic field dependency of the entropy, which in turn, has to be dominated by localised skyrmion and SP modes.

When keeping in mind, that the product of eigenvalues is affected by the ratio and not the absolute value of a variation, it becomes clear, that variations of small eigenvalues have the largest effect on the entropy. For this reason, skyrmion modes with small eigenvalues below the magnon gap allow for a rapid change of the entropy. Indeed, the high slope of the skyrmion modes and the drastic entropy change coincide in the interval of magnetic field.

The assumption, that n skyrmion modes give rise to the field dependency of the entropy and that their slopes can be approximated to be linear with $\epsilon_i^{\mathrm{I,Sk}}(B) = a_i B$, yields

$$\frac{\Delta S'}{k_\mathrm{B}} = \ln\left(\sqrt{2\pi k_\mathrm{B} T}\, c \prod_i^n \sqrt{a_i B}\right)$$

Here, a_i are the slopes of the skyrmion modes and c is the part of the ratio of eigenvalues that is constant under magnetic field. By combining c, the slopes a_i and other constant contributions to c' the formula simplifies to [IX]

$$\begin{aligned}\frac{\Delta S'}{k_\mathrm{B}} &= c' + \sum_i^n \ln\left(\sqrt{B}\right) \\ &= c' + \frac{n}{2}\ln\left(B\right). \end{aligned} \tag{7.1}$$

In Eq. 7.1, the slope of the entropy depends linearly on the number of skyrmion modes and can be fitted to the data points obtained by simulations with n as fit parameter. Taking into account only the asymptotic region of the field, the fit yields a parameter $n = 11.3$, which is reasonable close to the manually counted number of 13 skyrmion modes in the low energy spectrum at $B = 0.2$ T. As it can be seen in Fig. 7.9, the fitted formula is in good agreement with the simulation data, which substantiates the finding of this section, that the magnetic field dependence of the entropy is dominated by the eigenvalues of the low energy skyrmion modes.

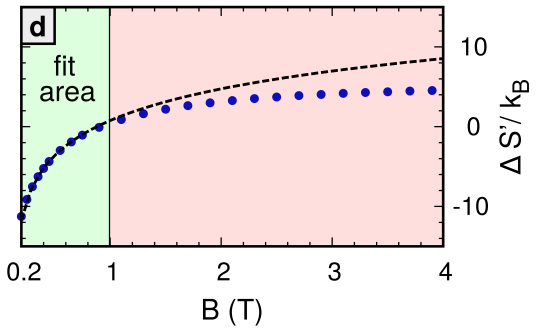

Figure 7.9 | The entropy difference over magnetic field is fitted by the number of skyrmion eigenmodes. The blue points show the entropy difference obtained by simulations for hcp-Pd/-Fe/Ir(111). The dashed line results from fitting Eq. 7.1 to the blue data points with the number of localised skyrmion modes, n, as fit parameter. The fit was performed in the denoted area, with a result of $n = 11.3$. Figure published in [IX].

7.4. Effect of skyrmion and saddle point sizes

Since localised skyrmion modes have been identified as the origin of the drastic change in entropy with magnetic fields, the entanglement of localised modes with the size of the corresponding magnetic structure will be analysed in the following.

In Sec. 7.2 it is mentioned, that the entropy follows the square skyrmion radius in the asymptotic regime, the same region of magnetic fields, in which the eigenvalues

of the skyrmion modes exhibit a steep increase. This observation can be broken down to two origins: First, the number of skyrmion deformation modes is linked to the skyrmion size. The larger the skyrmion circumference, the more deformation nodes can be placed on it and the number of low energy skyrmion modes increases.

Second, the energy cost of skyrmion deformation modes below the magnon gap decreases with skyrmion size as well. With increasing skyrmion circumference, the relative angles of adjacent magnetic moments appearing during a deformation are decreasing. Since the exchange interaction of the investigated systems is ferromagnetic and typically yields the largest energy contribution, smaller occurring angles during a deformation lower the energy costs and thus the eigenvalues of the corresponding modes. A more detailed analysis can be found in the supplement of Ref. [XII]. In the end, both effects result in more accessible states in the vicinity of the initial skyrmion state to occupy for the system.

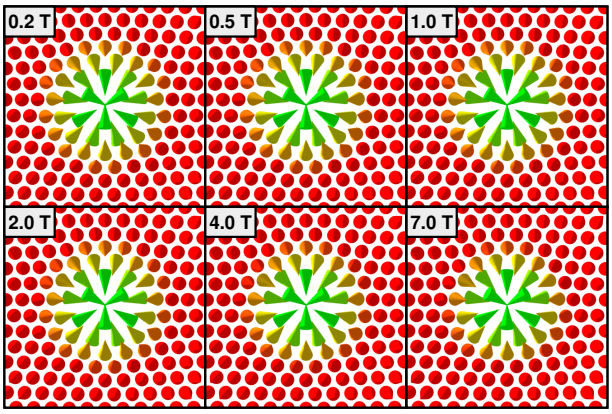

Figure 7.10 | Magnetic structures of the saddle points of skyrmion collapse in hcp-Pd/Fe/Ir(111) for different magnetic fields. The colour code indicates the out-of-plane component of the magnetisation. Figure published in the supplemental material of [IX].

The SP size, on the other hand, is more rigid under magnetic fields. Since no radius is defined for the SP structure, the SP structures obtained at different magnetic fields are shown in Fig. 7.10 instead. It can be seen, that the size of the SP is not affected by the magnetic field, which is consistent with the lack of high slope eigenvalues in the spectrum of the SP in Fig. 7.4 b. Therefore, the amount of accessible states in the vicinity of the SP does not change significantly with increasing magnetic field and thus, does not contribute to the field dependence of the entropy.

The connection of entropy and size of the magnetic structures allows for a simplified physical interpretation of the entropy effect on the transition rate: The contribution of the entropy to the prefactor is determined by the number of accessible states at

the SP, divided by the number of accessible states at the initial state. When the SP region becomes larger, the probability of reaching the transition state, which acts as a gate for the transition, increases. In contrast, when the size of the skyrmion region enhances, the system is more likely to remain in the part of phase space belonging to the initial state and the relative probability to reach the SP decreases. Therefore, the asymptotic behaviour of the skyrmion radius affects the statistical weight of the initial state, which in turn leads to the dramatic entropic stabilisation effect observed for hcp-Pd/Fe/Ir(111) at low fields.

7.5. Effect of exchange frustration

Up to now, solely exchange frustrated systems are investigated in this chapter. In order to see whether or not the observed results are due to exchange frustration, the effective nearest neighbour approximation of exchange interaction is applied to the Pd/Fe/Ir(111) systems. The model is introduced in Sec. 6.1. It applies an effective set of parameters, J_{eff}, and allows for the comparison of skyrmion properties with and without exchange frustration.

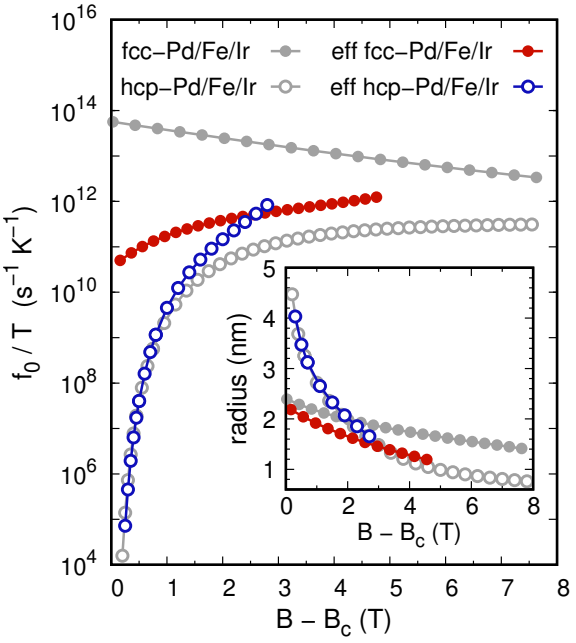

Figure 7.11 | Prefactor divided by temperature and skyrmion radius as a function of the magnetic field. For fcc-Pd/Fe/Ir(111) and hcp-Pd/Fe/Ir(111), the skyrmion radius, r, and the prefactors over temperature, f_0/T, were calculated with effective nearest neighbour parameters, J_{eff}, over $B - B_{\mathrm{c}}$. The values obtained for the same systems but with included exchange frustration are displayed in grey for reference. Figure published in the supplemental material of [IX].

In Fig. 7.11, the prefactors of skyrmion annihilation, calculated with J_{eff}, are shown for fcc-Pd/Fe/Ir(111) and hcp-Pd/Fe/Ir(111) next to the prefactors including exchange frustration. In contrast to the system with frustrated exchange, the prefactors of fcc-Pd/Fe/Ir(111) calculated with J_{eff} are increasing by more than order of magnitude with magnetic field instead of decreasing. The values are three to one order of magnitude smaller than the prefactors of the frustrated system.

One can speculate, that the larger SP structure due to exchange frustration (see the insets of Fig. 6.10) enables for more low energy SP modes and hence, yields the deviation in prefactor between both models. This is increasingly counteracted by the more rapid decrease in skyrmion size for fcc-Pd/Fe/Ir(111) without exchange frustration as displayed in the inset of Fig. 7.11, which yields the increasing prefactor for the effective nearest neighbour model.

The origin of the decreasing prefactor of the frustrated system is connected to the softening of the second and third SP modes. While these modes were originally interpreted as SP translation modes, the application of the mode following method revealed, that these modes lead to the SP of the chimera transition mechanism, which is discussed in more detail in Chap. 10.

Since the chimera transition is favoured by exchange frustration, it can be concluded that the increasing prefactor observed for fcc-Pd/Fe/Ir(111) with applied J_{eff} and hcp-Pd/Fe/Ir(111) with both exchange models appears to be the typical magnetic field dependence of the prefactor of radial skyrmion collapse. The decreasing prefactor of fcc-Pd/Fe/Rh(111) with included exchange frustration, on the other hand, can be interpreted as a frustration effect, which corresponds to the decreasing prefactor of fcc-Pd/Fe/Rh(111), which also exhibits a chimeric transition mechanism for low magnetic field strengths.

For hcp-Pd/Fe/Ir(111), the both models of exchange interaction yield quite similar prefactors in the asymptotic regime. However, the prefactor of the effective model continues to rapidly increase with increasing magnetic fields while the prefactor of the frustrated begins to saturate. The reason for this behaviour remains unclear at this point and requires further, more systematic investigations.

The data in Fig. 7.11 shows that the prefactor is not a unique function of the skyrmion size which is elaborated exhaustively in Ref. [XII] in order to enable room temperature skyrmions stabilised by the entropy-size effect. Moreover, the data

reveals that the skyrmion stabilisation due to the entropy-size effect does not stem from exchange frustration but is affected by it. This result has been reproduced very recently by two theoretical studies [23, 170], showing a complex relationship between prefactor and exchange frustration which also can be further explored to optimise skyrmion stability.

7.6. Skyrmion lifetimes

While the last sections were devoted to the detailed investigation of the prefactor, it is now combined with the energy barrier to obtain skyrmion lifetimes. In Fig. 7.12, the average lifetime, $\tau = 1/\nu$, of skyrmions in Pd/Fe/Ir(111) is evaluated from Eq. 5.51 for different temperatures and magnetic fields. Isolines of constant lifetimes are shown as a guideline for the eye, and it can be seen that skyrmion lifetimes gradually decrease with increasing magnetic fields and temperatures for both stackings of Pd.

At high magnetic fields, skyrmions in fcc-Pd/Fe/Ir(111) have a higher stability than skyrmions in hcp-Pd/Fe/Ir(111) due to their superior energy barrier. Even at $B = 11$ T it exhibits an average life time of more than one week at $T = 10$ K, while the lifetime of hcp-Pd/Fe/Ir(111) falls below the $T = 5$ K mark already for fields below $B = 5$ T.

However, when the magnetic field becomes close to the critical fields, the stability of skyrmions in hcp-Pd/Fe/Ir(111) increases rapidly. While the lifetimes show a small and steady increase with decreasing fields in case of fcc-Pd/Fe/Ir(111), the lifetimes of hcp-Pd/Fe/Ir(111) exhibit a nearly asymptotic behaviour at low fields due to the entropy-driven increase in prefactor of mean lifetimes, $\tau_0 = 1/\nu_0$.

The isolines of one week lifetime intersect with the temperature axis at approximately 40 K and 60 K for skyrmions in fcc-Pd/Fe/Ir(111) and hcp-Pd/Fe/Ir(111), respectively. While the energy barriers of hcp-Pd/Fe/Ir(111) are still smaller than the barriers of fcc-Pd/Fe/Ir(111) at low magnetic fields, the effect of the prefactor exceeds the contribution of the barrier and yields a higher stability for skyrmions in hcp-Pd/Fe/-Ir(111).

The large influence of the entropy stabilisation effect on the resulting skyrmion lifetimes can be illustrated by the example of skyrmions in both systems at $T = 100$

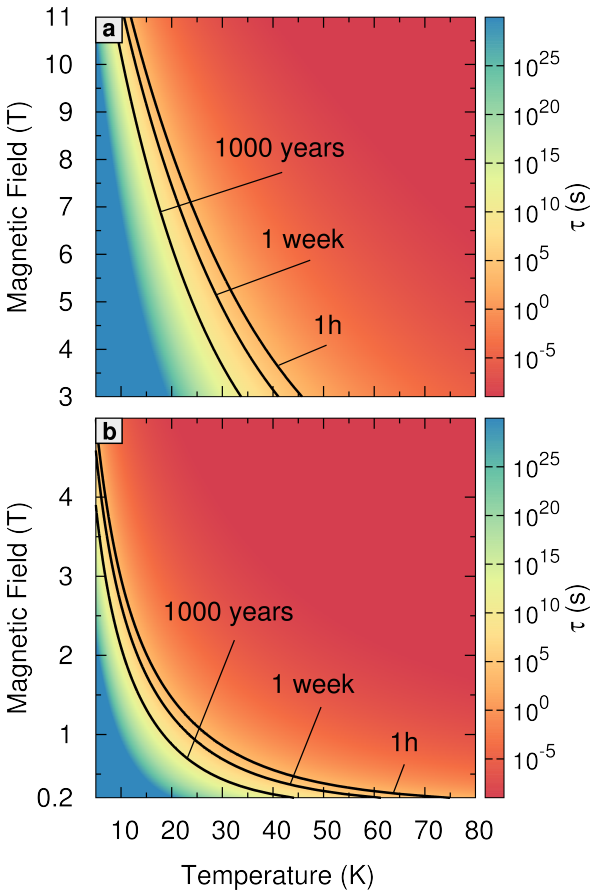

Figure 7.12 | Average skyrmion lifetimes over magnetic field and temperature. For fcc-Pd/Fe/Ir(111) **(a)** and hcp-Pd/Fe/Ir(111) **(b)**, the lifetime, τ, is displayed by a colour code. The lifetime was calculated via Eq. 5.51 with datapoints for every 0.05 T and a subsequent interpolation between the data points. Three isolines of constant skyrmion lifetime are given as a guideline for the eye. Figure published in [IX].

K and fields close above the corresponding critical fields: While skyrmions in fcc-Pd/-Fe/Ir(111) have an average lifetime of about 42 ns, skyrmions in hcp-Pd/Fe/Ir(111) already reach lifetimes of 10 s, despite the lower energy barriers of the latter. This difference of about nine orders of magnitude demonstrates that the effect of the prefactor on the lifetime of skyrmions can be decisive and must be taken into account when studying the stability of magnetic skyrmions.

The entropy-size effect discovered in this study could be accountable for the dramatic drop of 30 orders of magnitudes in skyrmion lifetimes observed by Wild *et al.* [66]. While the ultrathin films investigated in this chapter are two-dimensional, B20 compounds are three-dimensional bulk systems whose skyrmion eigenmodes should have an even stronger dependence on skyrmion size, since they exist on a skyrmion surface rather than on the circumference.

In summary, it could be shown that the prefactor of skyrmion collapse is dominated by only a few localised eigenmodes, which are strongly affected by external magnetic fields and interaction parameters. The found entropy-size effect enables for stabilisation opportunities beyond the conventional tuning of the energy barrier. Very recently, this effect has been studied systematically over a large variety of interaction parameters, demonstrating the possibility to achieve metastable sub-10 nm skyrmions at room temperature by entropy stabilisation [XII].

8. Prediction of the chimera collapse mechanism

The geodesic nudged elastic band (GNEB) method moves an initial path along the energy gradient into a near minimum energy path (MEP). The geodesic path of isolated skyrmion annihilation in fcc-Pd/Fe/Ir(111) usually relaxes to the radial symmetric collapse mechanism. However, for low magnetic fields around B_c, small disturbances of the initial path, deliberately created via random numbers in order to preclude a fixation at unfavourable but highly symmetric states, can be strong enough for the GNEB to reach another local MEP, the chimera collapse.

This novel path of skyrmion annihilation first appeared occasionally in the authors simulations at low fields in fcc-Pd/Fe/Ir(111). In the bachelor's thesis of Thaddäus Hartmann [177], we then systematically studied the chimera mechanism in hcp-Pd/Fe/Ir(111) and subsequently predicted it to play an important role for the stability of isolated skyrmions in the hexagonal ultrathin film system Rh/Co/Ir(111) [VII]. Recently, we demonstrated the appearance of this new collapse mechanism in collaboration with the experimental group of Prof. Markus Morgenstern [XI], which is discussed in more detail in the next chapter.

Independently, Desplat *et al.* found a similar mechanism on an atomistic square lattice using model parameters with exchange interactions up to the third nearest neighbour [99]. Subsequently, the mechanism was theoretically reproduced by Heil *et al.*, who performed simulations using an improved micromagnetic model that takes exchange frustration effects into account [124].

In this chapter, first the chimera collapse mechanism is presented for the example of fcc-Pd/Fe/Ir(111), followed by the magnetic field dependence of the energy barrier in comparison to the radial symmetric mechanism. Then, the contributions of the individual magnetic interactions to the energy of the chimera collapse are discussed.

Finally, the eigenvalue spectrum of the saddle point (SP) is analysed and the appearing complications for the calculation of the prefactor are elaborated.

8.1. The chimera collapse mechanism

Once the images of the chimera collapse path are obtained by chance or created manually, they can be used as initial path for further GNEB calculations. In Fig. 8.1, the resulting MEP and magnetic structures of every second image along the path are shown for skyrmion annihilation via the chimera collapse mechanism in fcc-Pd/Fe/Ir(111) at $B = 3.2$ T.

The chimera collapse begins with a sidewards translation of the skyrmion which does not affect the energy of the images (Fig. 8.1 images 1-7). This is a consequence of the selected initial path, in which the largest angles between magnetic moments are located at the centre of the skyrmion. This Bloch-like point at the SP is small in size and thus, a displacement results in additional energy costs due to lattice effects. Since the GNEB algorithm cannot move the SP image up in energy, a displacement of the Bloch-like point relative to the initial skyrmion state is performed by a sidewards translation of the skyrmion rather than a movement of the Bloch-like point itself.

The translation is followed by the out-of-plane alignment of magnetic moments at one side of the skyrmion (Fig. 8.1 images 9-15). The moments on the inside of the skyrmion boundary rotate downwards while the moments on the outside rotate upwards, creating a Bloch-like point at the SP image of the MEP (Fig. 8.1 image 17). By further rotation, the moments enter the surface plane again, but this time pointing away from the skyrmion centre, while they initially pointed inwards (Fig. 8.1 image 19). With this modifications, the skyrmion has transformed into the chimera skyrmion structure (see Sec. 3.4.3). Finally, the chimera skyrmion continuously collapses into the ferromagnetic (FM) background (Fig. 8.1 images 21-29).

For the same skyrmion collapse the magnetic structure, energy density and topological charge density are shown in Fig. 8.2 from a different perspective and for every third image. The energy density reveals the largest energy increase at the Bloch-like point during the collapse, while the skyrmion boundary remains energetically favourable (Fig. 8.2 images 9-16). Especially the three moments with angles of nearly 120° exhibit a large contribution to the energy of the SP state, similar as it has been

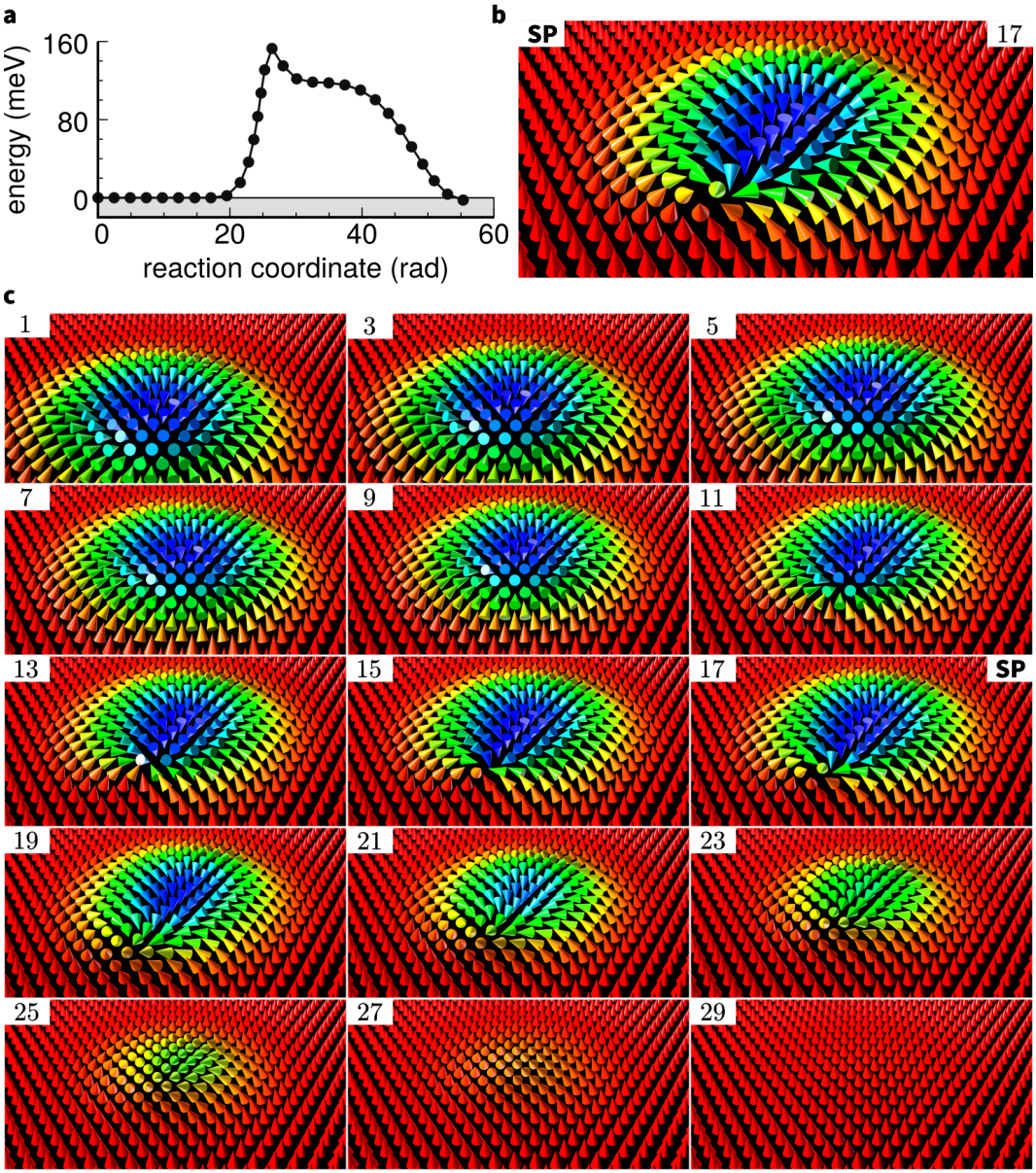

Figure 8.1 | Minimum energy path of the chimera collapse mechanism in fcc-Pd/Fe/Ir(111) at $B = 3.2$ T. **a)** The MEP consists of 30 images and is calculated with a hybrid measure of distance applied to the spring forces. The energy of each image is displayed relative to the energy of the initial state. **b)** A section of the magnetic structure of the saddle point image. The colour code denotes the out-of-plane component of the magnetic moments. **c)** A sequence of every second image of the MEP. Indices of the corresponding images are shown in the upper corner of each magnetic structure and the saddle point image is denoted by "SP".

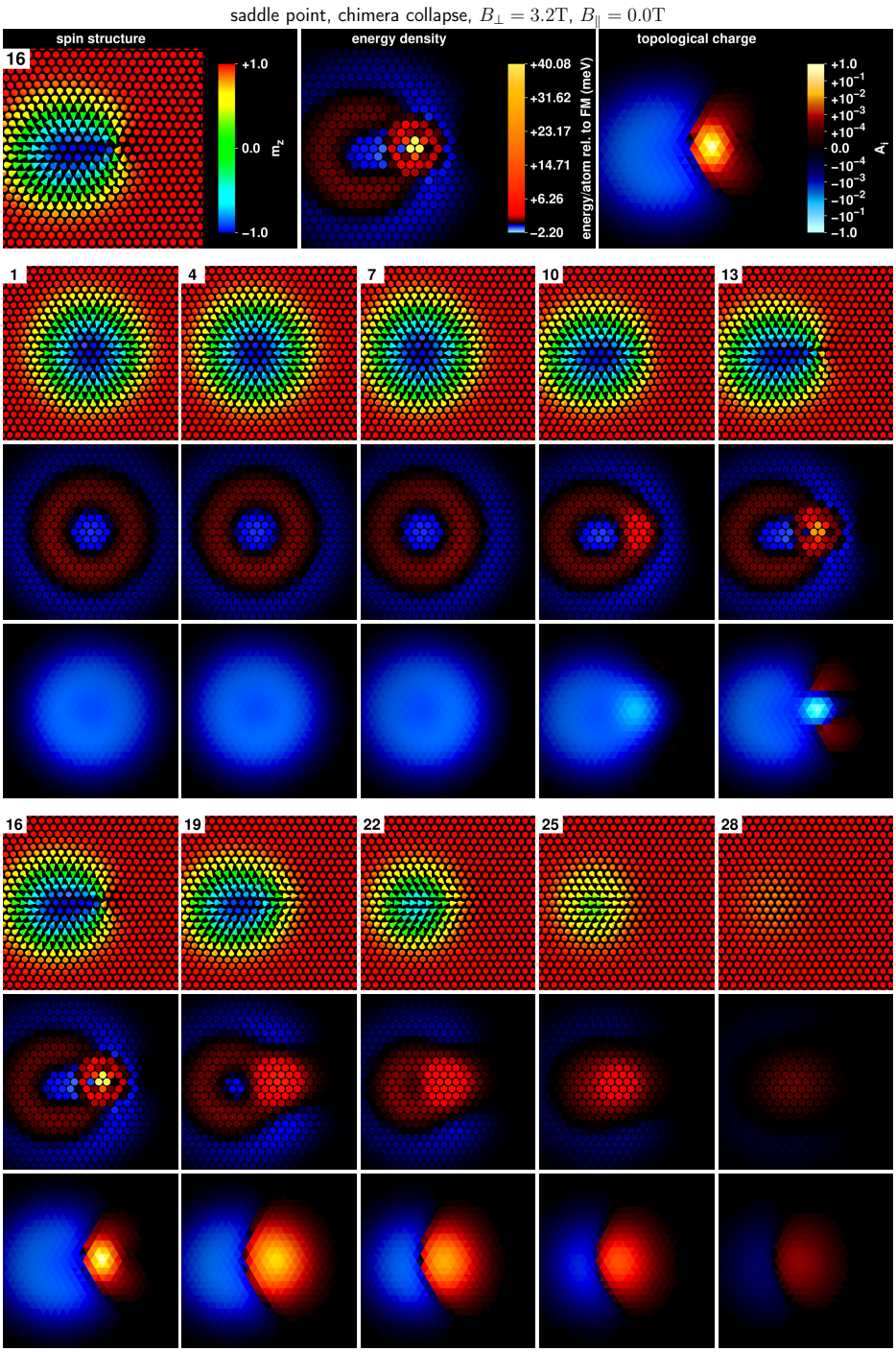

Figure 8.2 | Sequence of skyrmion collapse in fcc-Pd/Fe/Ir(111) via the chimera mechanism at $B = 3.2$ T. The magnetic structure, energy density map relative to the FM state, topological charge density map of the saddle point image and the corresponding colour codes are displayed at the top. The topological charge density is calculated per triangle of adjacent magnetic moments. Below, the same information is shown for every third image of the MEP whose indices are shown in the upper left corner.

observed for the central moments of the radial symmetric collapse in Sec. 6.5. Subsequently, the energy costs become more evenly distributed with the moments of the Bloch-like point forming the antiskyrmion edge of the chimera structure (Fig. 8.2 image 19). The areas of relative energy costs move further towards the centre and annihilate gradually with the areas of energy gain still present at the chimera skyrmion boundary (Fig. 8.2 images 22-28).

During the formation of the Bloch-like point, the topological charge density becomes more condensed around the moments with increasing angles until opposite charge density is created around them (Fig. 8.2 images 10-16). At the SP, the charge density of the Bloch-like point flips, giving rise to a concentrated area of opposite charge density that smears out over the relaxing antiskyrmion edge, creating a dipole-like charge distribution that gradually vanishes with the shrinking chimera skyrmion (Fig. 8.2 images 19-28).

8.2. Out-of-plane magnetic field dependence

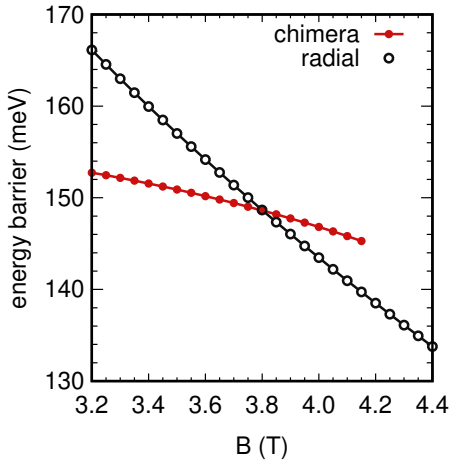

Figure 8.3 | Energy barriers of skyrmion annihilation in fcc-Pd/Fe/Ir(111) via the radial symmetric and chimera collapse mechanisms over out-of-plane magnetic field. The corresponding MEPs consist of 30 images and are calculated with CI-GNEB by successive variation of the magnetic field. The chimera transition mechanism is found to be metastable only with fields lower than $B = 4.2$ T.

In order to force the GNEB calculation to converge to a specific MEP over a range of magnetic fields, the MEP is first relaxed at a magnetic field strength at which the desired collapse mechanism is obtained easily. Subsequently, the relaxed path is used as initial path for the GNEB calculation at the next magnetic field value, relaxed again and so forth. This procedure is successful until the corresponding SP is not a local energy minimum on the dividing surface anymore and the GNEB follows the

energy gradient into another MEP. It is good practice to relax the MEPs with the GNEB method for all fields first and subsequently apply the CI-GNEB method to obtain the SPs.

With this technique the energy barriers of both the radial symmetric and chimera collapse mechanism are obtained. They are shown in Fig. 8.3 as a function of the magnetic field. While the radial symmetric collapse is metastable over the entire interval of magnetic fields, the limit of the chimera collapse mechanism is reached at around $B = 4.2$ T. For larger magnetic fields, the GNEB converges into the MEP of the radial symmetric collapse, regardless of the initial path.

The energy barriers of both annihilation mechanisms decline with magnetic field. While the chimera collapse is energetically favourable by about 15 meV at $B = 3.2$ T, the barrier of the radial collapse exhibits a steeper slope leading to an intersection of both barriers around $B = 3.8$ T. For fields larger than this, the radial symmetric collapse is preferred energetically.

8.3. Energy decomposition of the saddle point states

In order to investigate the energetic effects favouring the radial symmetric and the chimera collapse mechanism, respectively, the energy decomposition of the MEPs is shown in Fig. 8.4 at a field of $B = 3.8$ T. This field is selected as it yields similar energy barriers for both mechanisms and thus enables for a more direct comparison. Additionally, the energy density maps of the corresponding SPs are displayed in Fig. 8.5, providing spatial resolved information about the role each interaction is playing for the energy barriers.

Subsequent to the initial skyrmion translation with constant energy, both MEPs steadily increase in Dzyaloshinskii-Moriya interaction (DMI) energy (Fig. 8.4). The collinear ferromagnetic state has no DMI contribution and all energy of the DMI gained at the skyrmion state is lost during the collapse. However, as it is visible in Fig. 8.5, the majority of the chiral skyrmion structure is still present at the SP of the chimera transition, preserving a large part of the initial DMI energy. Hence, the contribution of the DMI to the energy barrier is much smaller for the chimera collapse mechanism, which is therefore an efficient way for the system to avoid large energy barriers due to DMI appearing for the radial symmetric collapse mechanism.

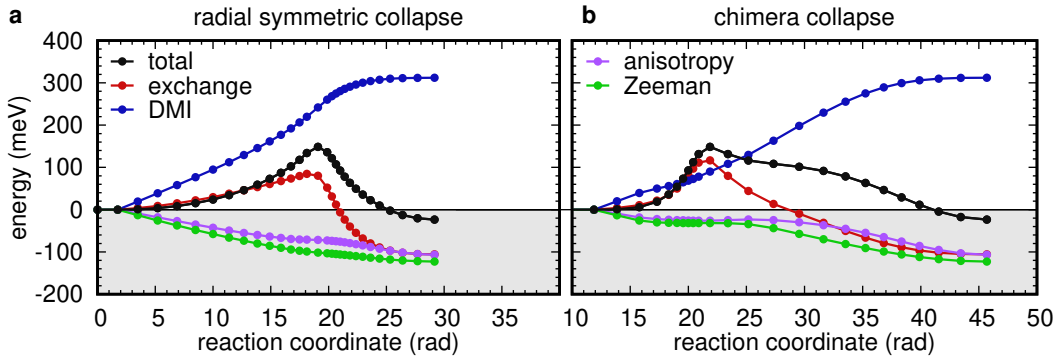

Figure 8.4 | Decomposed energy contributions along the minimum energy paths of radial (a) and chimera collapse (b). The minimum energy paths are obtained from CI-GNEB simulations of isolated skyrmion annihilation in fcc-Pd/Fe/Ir(111) at $B = 3.8$ T. A hybrid measure of the distance between images is applied to the spring forces. In order to compare both mechanisms on the same scale, the first 10 rad of the reaction coordinate of the chimera collapse are not shown. The omitted part of the reaction coordinate correspond to the translation of the skyrmion without a change in energy. The energy of the images is shown relative to the initial skyrmion state.

Simultaneously, the ferromagnetic state steadily gains energy due to the Zeeman term and the magnetocrystalline anisotropy during the collapse. On the contrary to the DMI contribution, the SP of the radial collapse benefits from its structure in form of larger energy gains in Zeeman and anisotropy energy. The chimera SP only gains a small portion of this energy and thus exhibits larger energy costs for these two interactions as visible in Fig. 8.5. Hence, the energy barrier of the radial collapse is lowered efficiently by increasing Zeeman and anisotropy terms, while the chimera SP is less affected by these interactions. The role of exchange interaction and exchange frustration is less obvious. While in Fig. 8.4, the contribution of the exchange energy to the energy barrier is larger for the chimera than for the radial SP, the chimera transition has only been observed in calculations taking frustrated exchange into account.

To disentangle the role of exchange frustration the GNEB calculations have been repeated with a varying degree of exchange frustration, realised by a mixing of J_{DFT} and J_{eff} via

$$J_{\mathrm{mix}} = x\, J_{\mathrm{DFT}} + (1 - x)\, J_{\mathrm{eff}}, \tag{8.1}$$

where $x \in [0, 1]$ defines the proportion of both parameter sets. The resulting energy barriers of both transition mechanisms are plotted in Fig. 8.6 at $B = 3.8$ T. With

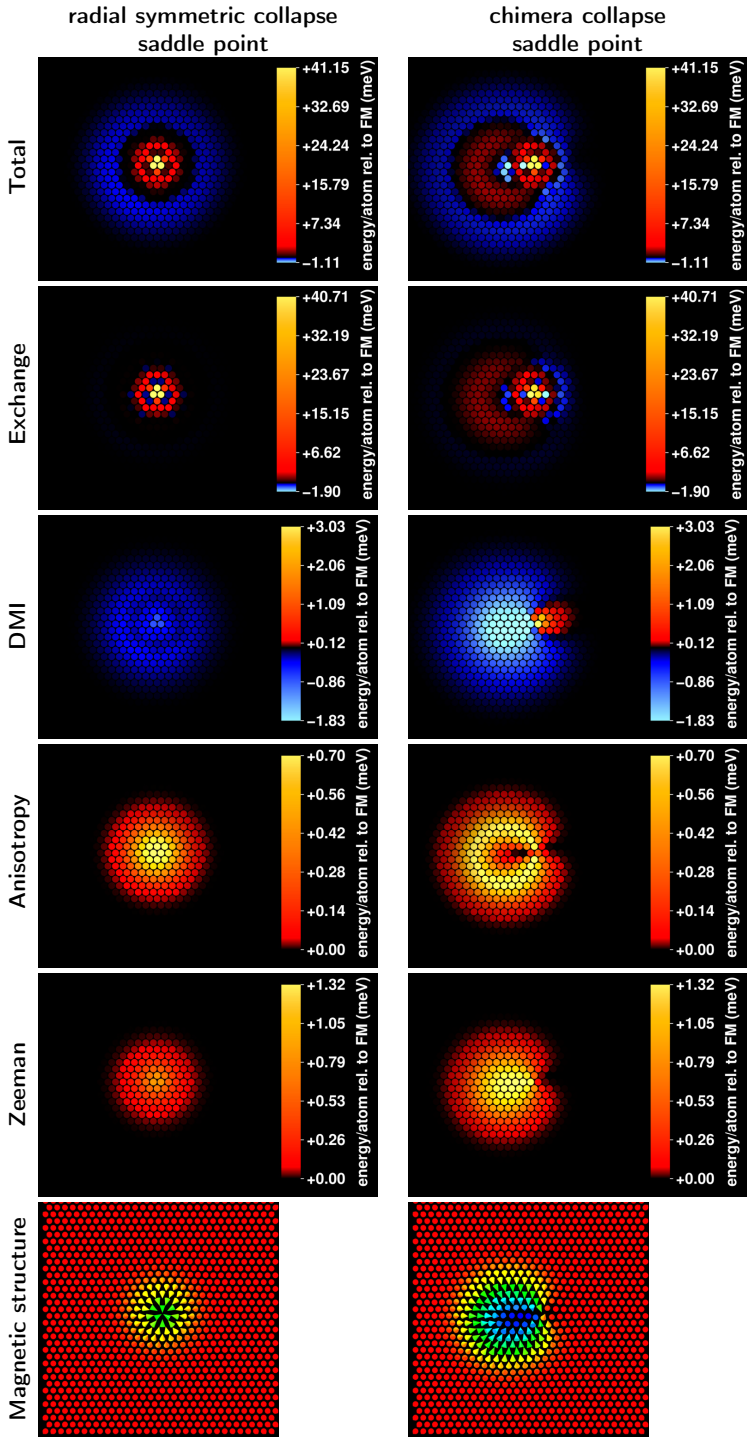

Figure 8.5 | Energy density maps of the saddle points of the radial and chimera collapse, decomposed by magnetic interaction. The saddle points are obtained by CI-GNEB simulations of isolated skyrmion annihilation in fcc-Pd/Fe/Ir(111) at $B = 3.8$ T. The colour of each point denotes the energy of the lattice site relative to the energy of ferromagnetically aligned magnetic moments. For both saddle points, the same colour codes are applied. Magnetic structures of the saddle points are shown at the bottom.

100% J_{DFT}, both energy barriers are similar in value. However, the barrier of the radial SP decreases faster with decreasing exchange frustration than the barrier of the chimera collapse.

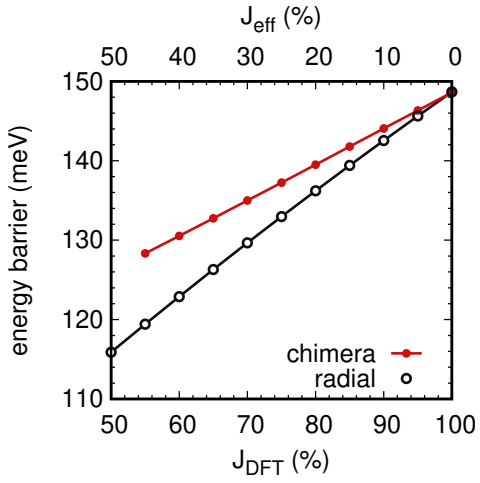

Figure 8.6 | Energy barriers of the radial symmetric and chimera skyrmion annihilation with varying degrees of exchange frustration. The degree of exchange frustration is altered by mixing the parameter set of fcc-Pd/Fe/Ir(111) including exchange frustration, J_{DFT} (see Tab. 4.1), and the effective nearest neighbour parameter set, J_{eff} (see Tab. 6.1), via Eq. 8.1. An out-of-plane magnetic field of $B = 3.8$ T is applied. The minimum energy paths are relaxed by CI-GNEB by successively changing the mixing ratio of the parameter sets. The chimera mechanism is not metastable for parameters consisting of 50% J_{DFT} or less.

This behaviour can be explained with the help of Fig. 8.7, in which the contribution of each shell of exchange interaction to the energy barrier is shown. It becomes evident, that the radial SP experiences large positive and negative contributions of all shells of exchange which lead to an overall net increase of the energy barrier with increasing exchange frustration. As expected, the contributions of all shells reduce with increasing percentage of J_{eff}. On the other hand, the energy barrier of the chimera SP is dominated by J_1 while the other shells only give rise to small modifications of the energy barrier.

Remarkably, the energy barriers of the radial and chimera mechanisms exhibit opposite trends with J_1, as the radial barrier decreases with J_1 while the chimera barrier increases. Furthermore, the radial collapse barrier is significantly enhanced due to exchange frustration while the energy of the chimera SP only slightly changes. Therefore, a skyrmion collapse via the radial mechanism becomes increasingly unfavourable with increasing exchange frustration and it can be concluded that skyrmion annihilation via the chimera mechanism plays a significant role especially in highly exchange frustrated systems. This observation agrees well with the comparison of the radial and chimera collapse for skyrmions in Rh/Co/Ir(111) [VII] and the studies presented in Ref. [99] and [124].

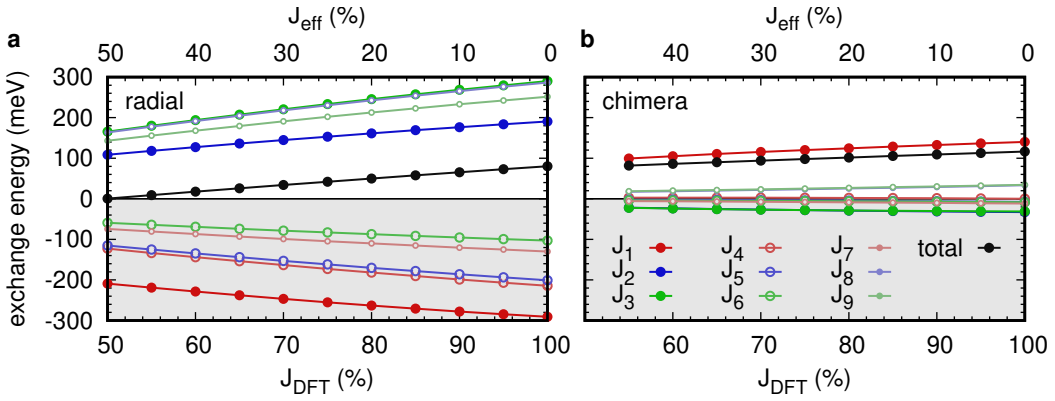

Figure 8.7 | Contributions of the exchange interaction to the energy barrier of radial (a) and chimera (b) skyrmion collapse with varying degree of exchange frustration. The minimum energy paths of skyrmion annihilation in fcc-Pd/Fe/Ir(111) are calculated via CI-GNEB with an applied out-of-plane field of $B = 3.8$ T. The degree of exchange frustration is altered by mixing the parameter set of fcc-Pd/Fe/Ir(111) including exchange frustration, J_{DFT} (see Tab. 4.1), and the effective nearest neighbour parameter set, J_{eff} (see Tab. 6.1), via Eq. 8.1. The energy of each shell of exchange interaction is displayed relative to that of ferromagnetically aligned moments.

The opposing trends can straightforwardly be explained with the different SP structures. In a simplified model, the chimera SP can be viewed as a skyrmion structure with a Bloch-like defect at its periphery, the creation of which mainly costs nearest neighbour exchange energy. This gives rise to the contribution of nearest neighbour exchange interaction to the energy barrier. Exchange frustration, on the other hand, stabilises the non-collinear rest of the skyrmion structure and thus creates an energy gain for the chimera SP, effectively lowering the energy barrier. Since most of the skyrmion structure stays intact at the SP, the energy contributions of exchange interaction beyond nearest neighbours in Fig. 8.7 remains rather constant for the chimera SP.

The contrary is found for the radial symmetric mechanism, whose SP structure consists of a strongly shrunk skyrmion and large angles between the magnetic moments at the centre. While these central moments lose energy due to the nearest neighbour exchange, most of the SP structure is more ferromagnetic than the initial skyrmion state and thus gains energy by nearest neighbour exchange interaction. Exchange frustration again stabilises the non-collinear skyrmion structure and this energy gain is almost lost at the radial SP structure, which therefore gives rise to an additional contribution to the energy barrier. Hence, the energies of the different

shells of exchange interaction relative to the initial skyrmion state fan out with increasing degree of frustration as it is observed in Fig. 8.7.

8.4. Eigenvalue spectra

In order to obtain the prefactor of the transition rates, the Hessian matrices of the initial and SP states are diagonalised. Fig. 8.8 shows the low energy eigenvalue spectrum of the initial skyrmion state and of both SP states at $B = 3.8$ T. The skyrmion state of fcc-Pd/Fe/Ir(111) exhibits only a few localised eigenmodes below the magnon bands. Similar to hcp-Pd/Fe/Ir(111), the two translational skyrmion modes appear as degenerate Goldstone modes in the spectrum with eigenvalues of zero.

As visible in Fig. 8.8, the SP of the radial collapse also shows a small number of localised low-energy modes. Note that the negative eigenvalue of the unstable mode is not shown. The second and third lowest eigenvalues of the spectrum are degenerate and, similar to the spectrum of hcp-Pd/Fe/Ir(111) shown in Sec. 7.3, they were initially interpreted as translational modes of the SP structure. However, the application of the mode following method shows, that the second and third eigenmodes lead to the SP of the chimera transition, which is discussed in more detail in Sec. 10.3.1. Since the corresponding eigenvalues are non-zero, they are treated in harmonic approximation.

The SP of the chimera transition exhibits more localised modes than the radial SP state. This can be explained by the size of the SP structure and its higher asymmetry compared to the radial SP, which allows for more low-energy deformations. The eigenvectors of the chimera SP are displayed in Fig. 8.9, of which the first corresponds to the unstable mode.

Most noteworthy, the second eigenvalue of the chimera spectrum is almost zero and cannot be treated in harmonic approximation. In Sec. 10.4.1, its eigenvector, which looks similar to a translational vector of the skyrmion state at first glance, can be assigned to a rotation of the magnetic structure around the Bloch-like point by using the mode-following method developed for this purpose.

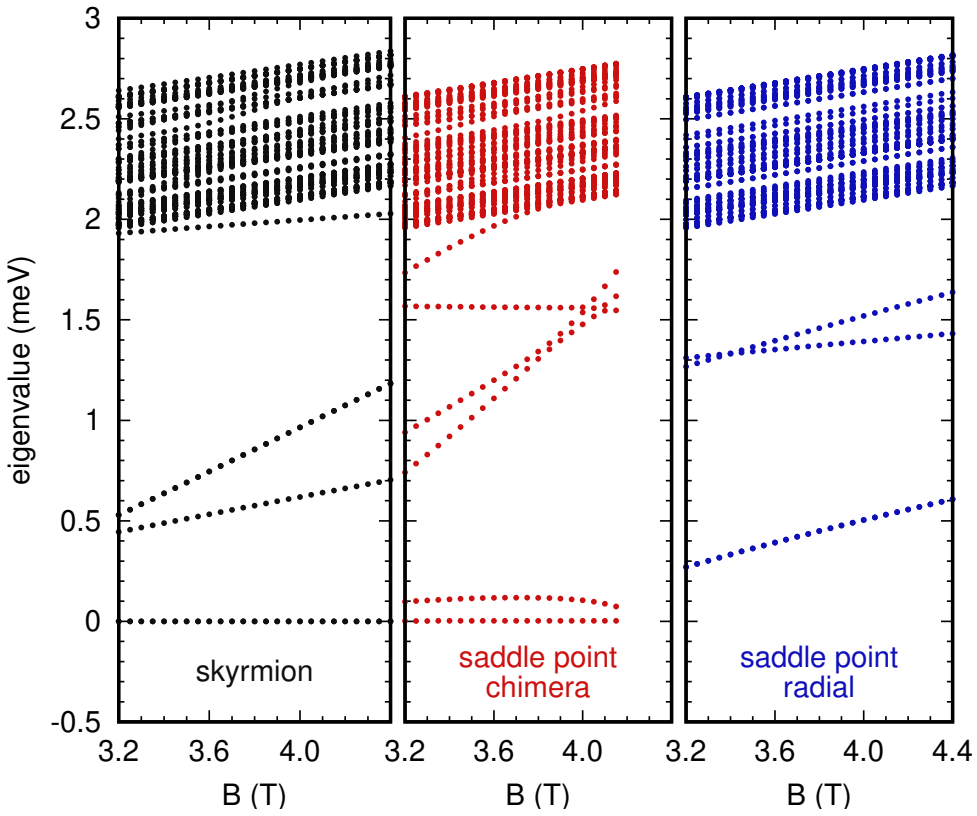

Figure 8.8 | Low-energy eigenvalue spectra over magnetic field for skyrmion annihilation in fcc-Pd/Fe/-Ir(111). The first 100 eigenvalues of the diagonalised Hessian matrices of the initial skyrmion state **(left)** and the two saddle point states of the chimera **(centre)** and radial symmetric **(right)** annihilation mechanisms. For both saddle points, the lowest eigenvalue belongs to the unstable mode and is not visible in the displayed interval. The corresponding minimum energy paths are energetically relaxed via the CI-GNEB method.

.

The rotation is physically equivalent to a rotation of the Bloch-like point on the skyrmion periphery. It corresponds to the higher probability of creating a Bloch-like point at the skyrmion periphery compared to the orchestrated collective motion of all magnetic moments required to reach the SP of the radially symmetric collapse mechanism. The large number of possible Bloch-like point positions leads to an increase of the entropy of the SP structure, already hinting that the chimera transition is statistically favoured over the radial symmetric collapse.

Up to this point, the rotation mode prohibits an adequate calculation of the prefactor, because it cannot be treated accurately in harmonic approximation and it is not

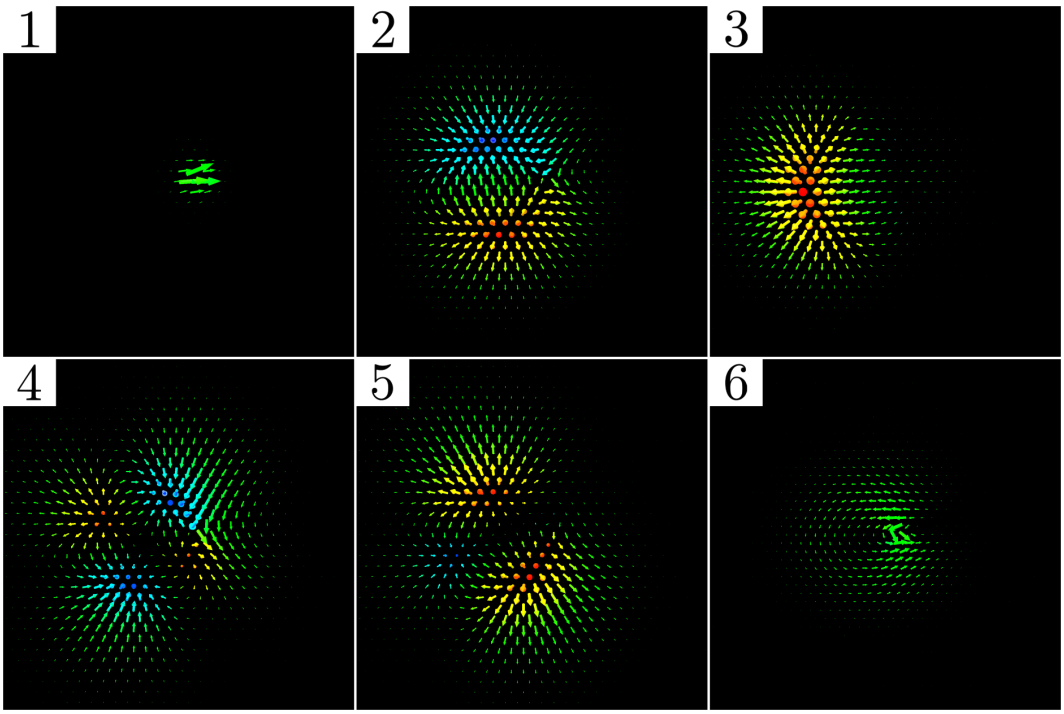

Figure 8.9 | First six eigenvectors of the saddle point of the chimera transition in fcc-Pd/Fe/Ir(111) at $B = 3.80$ T. The colour code denotes the out-of-plane component. The size of the arrows scales with the norm of the vectors. The first image depicts the eigenvector of the unstable mode. For the sake of clarity, the size of the arrows belonging to the first and the sixth mode are scaled down with respect to the other three modes.

.

known whether it behaves like a Goldstone mode. In Chap. 10, the solution of this problem by the application of the mode-following method is presented.

Although the prefactor of the chimera transition mechanism cannot be determined accurately by applying the usual approximations, the results of this chapter demonstrate, that this transition mechanism can be energetically favourable in systems with large exchange frustration. The negligible energy costs of the rotation of the Bloch-like point at the chimera SP also suggest that the chimera transition is entropically favoured over the radial symmetric collapse. It can therefore be expected that the chimera transition mechanism becomes increasingly important with increasing skyrmion size.

9. Discovery of the chimera collapse mechanism

In a recent collaboration with the group of Prof. Markus Morgenstern, it was possible for the first time to experimentally uncover mechanisms of skyrmion annihilation [XI]. In his group, Florian Muckel, Christian Holl, Benjamin Pestka and Marco Pratzer measured the rate of skyrmion annihilation and creation events thermally induced by a current flow between the scanning tunneling microscopy (STM) tip and the surface of the ultrathin film system fcc-Pd/Fe/Ir(111). With a novel STM mapping technique, the spacial resolved switching rate for different tip positions was obtained. By comparison with theoretical investigations presented in this chapter it was possible to identify, both, the radial symmetric and the chimera collapse mechanisms in the maps of the switching rates and to explain the occurring transition between both mechanisms under applied in-plane magnetic field [XI].

In the beginning of this chapter a brief introduction to the experimental setup and the performed measurements is provided. A special focus lies on the spacial resolved sub-nm maps of the transition rates, that initiated an extensive theoretical study on the skyrmion lifetimes under in-plane magnetic field in the fcc-Pd/Fe/Ir(111) system, which is the main subject of this chapter. Finally, the comparison of theoretical and experimental results does not only provide a profound inside into the skyrmion annihilation processes in fcc-Pd/Fe/Ir(111), but also demonstrates a surprisingly sound agreement between experiment and theory.

9.1. Tip induced switching events

A sketch of the experiment performed by Florian Muckel and coworkers [XI] is shown in Fig. 9.1. An antiferromagnetic Cr tip is applied close to the Pd surface in order

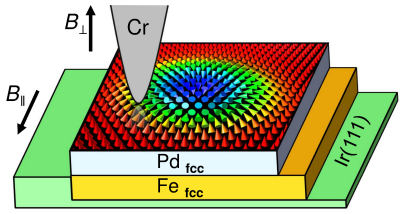

Figure 9.1 | Illustration of the experimental setup. SP-STM measurements are performed with a Cr tip on a fcc-Pd/Fe/-Ir(111) surface. Applied magnetic fields are indicated by $B_\perp$ and $B_\parallel$. A skyrmion obtained by atomistic simulations is displayed as an example of the magnetic structures of the material. Figure published in [XI].

to perform spin-polarised scanning tunneling microscopy (SP-STM) measurements [183] at a temperature of $T = 6$ K. In the following, applied external magnetic fields in out-of-plane direction are labelled $B_\perp$, while in-plane fields are denoted as $B_\parallel$.

During a scan, the differential conductance signal, dI/dV, varies with the underlying magnetic structure due to several contributing magnetoresistance effects: The non-collinear magnetoresistance (NCMR) effect emerges as electronic contrast between the collinear areas of the sample in which both spin channels are separated and the non-collinear areas that exhibit a mixing of both spin channels due to electrons hopping over adjacent lattice sites with different quantization axes. Additionally, the spin-polarised Cr atom at the apex experiences a tunneling magnetoresistance (TMR) effect, depending on the degree of spin alignment of the underlying surface atoms with the spin of the Cr atom. Finally, a small contribution of the tunneling anisotropic magnetoresistance (TAMR) effect occurs, which has been found to play a minor role for the fcc-Pd/Fe/Ir(111) system [184, 185].

While the Fe layer is known to grow on Ir(111) in fcc stacking [21], the Pd toplayer can be hcp or fcc stacked [I, 185]. A comparison of the characteristic dI/dV spectra of the skyrmion [185] and the ferromagnetic texture identifies the Pd layer of the measured island to be stacked fcc. See the supplemental material of Ref. [XI] for more details. Similar to hcp-Pd/Fe/Ir(111) (see Fig. 1.1), fcc-Pd/Fe/Ir(111) exhibits a spin spiral as ground state that evolves gradually into a skyrmion lattice phase and ultimately into the ferromagnetic state with increasing out-of-plane magnetic field. Values for the critical fields are difficult to obtain experimentally due to the metastable nature of the skyrmions and the influence of defects on their stability.

A recorded dI/dV map of an fcc-Pd island with an external field of $B_\perp = 1.5$ T is shown in Fig. 9.2 a. One can distinguish several deformed skyrmion structures in a ferromagnetic background. The topographic measurement of the same area in Fig. 9.2 d reveals many defects on the Pd/Fe island, which are most-likely responsible for the asymmetric shape of the skyrmions. In order to limit the influence of the

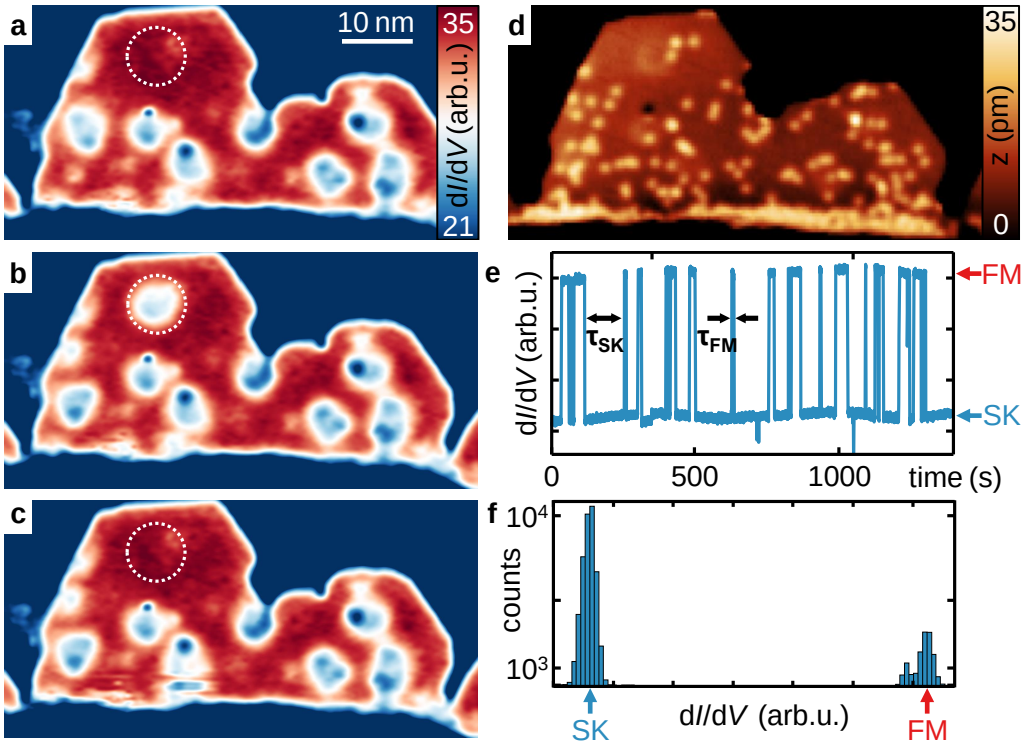

Figure 9.2 | Measurement of transition rates in fcc-Pd/Fe/Ir(111). a)-c) A sequence of recorded differential conductance maps of a fcc-Pd island of Fe/Ir(111). The creation and annihilation of a single skyrmion is visible in the area marked by a white dotted circle. **d)** The topographic image of the island measured simultaneously to **(b)**. **e)** The dI/dV signal recorded over $\Delta t = 1430$ s at the centre of the dotted circle in **(a-c)**. Two levels of dI/dV signal are labelled as ferromagnetic (FM) and skyrmion (SK) state and examples of the states individual lifetimes τ are shown. **f)** A histogram of the measured dI/dV values of **(e)** is shown and reveals distinct peaks for both states.The measurement was performed with $B_\perp = 1.5$ T, $B_\parallel = 0$ T and $T = 6$ K. Figure published in [XI].

defects, the area denoted by a white dotted circle in Fig. 9.2 a is selected for the measurements of switching rates presented in the following.

By applying a bias voltage, V, and thus, a tunnel current I, switching events are induced below the Cr tip. Although tip-induced writing and deleting of skyrmions has been demonstrated before [20, 27, 77], it is not entire understood which effect causes the transition. In the beginning, spin-transfer torque effects generated by the spin polarised current of a magnetic tip were believed to flip the magnetic moments of the underlying surface [20]. However, similar writing and deleting of skyrmions

was achieved with a nonmagnetic tip [27] that does not provide a net spin-polarised current.

Hence, two other effects are discussed to be responsible for the switching processes. One is Joule heating of the sample activating a thermal switching process of the magnetic surface structure. In the case of skyrmions on a triple layer of Fe on Ir(111), the writing and deleting processes appeared very deterministic [27], so that the more stochastic thermal transitions due to Joule heating are assumed to play only an assisting role in that system.

The magnetoelectric effect on the other hand changes the magnetic interactions due to a spin dependent shift of occupation probabilities in the electronic structure of the sample driven by the electric field emitted by the STM-tip. Therefore, energy barriers and prefactors between magnetic states can be modified reliably over the voltage applied between tip and sample, which can yield rather deterministic switching events [27, 186]. However, the strength of this effect is system dependent [186, 187] and for fcc-Pd/Fe/Ir(111), we expect to find a thermal induced switching potentially assisted by the magnetoelectric effect [XIII, 186].

In Fig. 9.2 a-c, a sequence of measurements shows the creation and deletion of the skyrmion in the dotted circle on the fcc-Pd/Fe/Ir(111) surface. Placing the tip in the centre of the circle, the presence and absence of the skyrmion can be detected in the telegraph noise displayed in Fig. 9.2 e, which allows to distinguish between two values of the dI/dV signal shown in the histogram of Fig. 9.2 f. A temporary reduction of the tunnel current allows for the recording of a dI/dV map, and hence, the identification of the two dI/dV levels as ferromagnetic and skyrmion state. By averaging over many switching events in the telegraph noise, the mean lifetime of both states can be determined, similar to what has been demonstrated by Hagemeister *et al.* in Ref. [77].

9.2. Mapping of skyrmion annihilation rates

Here, Muckel and coworkers go beyond previous measurement techniques by mapping the current induced switching rates for varying tip positions. At each point, the telegraph noise signal is recorded over a certain time interval, yielding the mean

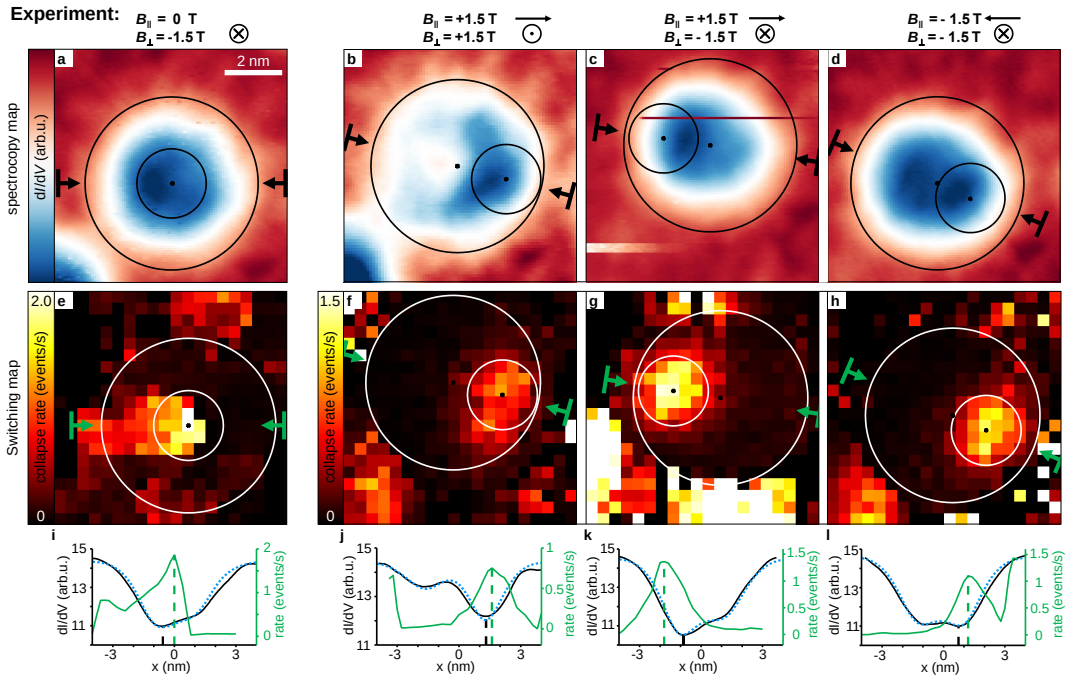

Figure 9.3 | Maps of skyrmion annihilation rates measured in fcc-Pd/Fe/Ir(111). a) The experimental dI/dV map of a skyrmion with $B_\perp = 1.5$ T, $I = 1$ nA and $V = 610$ mV. **b)-d)** For the same skyrmion, the dI/dV maps are obtained with varying directions of $B_\perp$ and the additionally applied $B_\parallel$, as labelled above the maps. The outer circles mark the skyrmion radius of $r = 3$ nm that corresponds to a mean angle between magnetic moments and the surface normal of 10°, deduced by a comparison of simulated and measured skyrmion dI/dV signals. The inner circles enclose areas of high switching intensity visible in the maps of skyrmion collapse rates of **(e-h)**. One map consists of 20×20 pixels and in each pixel, the number of switching events is measured over $\Delta t = 400$ s at $I = 600$ nA in **(e)** and $\Delta t = 150$ s at $I = 60$ nA in **(f)**, at $I = 50$ nA in **(g)** and at $I = 55$ nA in **(h)**. **i)-l)** The profile lines along the arrows of the measured dI/dV contrast in **(a-d)** are shown as black lines. The simulated dI/dV contrast of skyrmions relaxed by DFT-based spin dynamics are added as blue dotted lines. In green, the profile lines of the switching rates along the arrows in **(e-h)** are displayed. All profile lines are averaged over a 1 nm wide bar, indicated perpendicular to the direction of the arrows. The dashed vertical lines correspond to the maximum and minimum values of the green and black profile lines. Figure published in [XI].

switching rate of, both, the skyrmion and the ferromagnetic state. With this approach, sub-nm maps of the transition rate can be created.

Fig. 9.3 a shows the dI/dV signal of a skyrmion on fcc-Pd/Fe/Ir(111), visible as nearly circular, white contrast. The rather round shape of the skyrmion suggests a low influence of lattice defects. In Fig. 9.3 e, the same area is displayed where the colour code of each pixel corresponds to the local switching rate obtained by the novel mapping technique. The strong variation of the switching rate with the tip position reveals the local character of the tip activation. In contrast, the transition map of the ferromagnetic state is rather constant (see supplemental material of Ref. [XI]) since the magnetic structure exhibits equal conditions at each position except for local defect effects.

A decisive hot spot of switching events is visible in Fig. 9.3 e, denoted by the inner white circle. The centre of the circle is identical to the maximum of the line profile of the switching rates in 9.3 i, which lies almost perfectly at the centre of the skyrmion. Thus, a maximum of transitions is recorded when placing the tip over the centre of the skyrmion, indicating a radial symmetric skyrmion collapse since the core magnetic moments of the skyrmion have to be activated the most to overcome the energy barrier.

Applying an additional in-plane magnetic field, $B_{\parallel}$, to the sample leads to a more asymmetric shape of the dI/dV contrast shown in Fig. 9.3 b. The asymmetry stems from an enhancement of the in-plane region on the skyrmion side parallel to the in-plane field and a reduction in size on the opposite side, similar to a measurement published in Ref. [188]. But more importantly, the area of highest transition rates also becomes excentric under applied in-plane field as shown in Fig. 9.3 f. Again, a clear hot spot is formed, but this time it lies more than 1.5 nm off-centre at the skyrmion rim as denoted by the line profile of the switching intensity in Fig. 9.3 j.

The inversion of either the out-of-plane component or the entire direction of the magnetic field yields a corresponding inversion of the dI/dV signal shown in Fig. 9.3 c and d. This, again, denotes a rather defect free section of the Pd island and shows, that the asymmetry of the signal stems from the magnetic texture of the surface. However, the asymmetries are much less pronounced than in Fig. 9.3 b, which is attributed to a tip changing event taking place between the measurements as the data presented in Fig. 9.3 b were recorded with some temporal distance to the data of Fig. 9.3 c and d. A change in tip polarisation directly affects the

magnetic contrast. By comparison with maps of simulated magnetoresistance effects shown in the supplement of Ref. [XI], such a change of the STM-tip can result in the observed difference in contrast. Moreover, the eccentricity of the hot spot in the map of transition rates occurs consistently when the magnetic field is reversed and the question arises to the origin of this phenomenon.

9.3. Identification of skyrmion collapse mechanisms

In seeking an explanation for the observed dependency of the map of transition rates on the in-plane field, geodesic nudged elastic band (GNEB) calculations of the skyrmion annihilation process are performed. For this task, the extended Heisenberg parameters, presented in Sec. 4.3 and obtained from first-principle calculations of fcc-Pd/Fe/Ir(111), are well suited. As shown in Fig. 6.4 d, the stability diagram simulated with these parameters exhibits similar magnetic phases as the experiment. Due to small inaccuracies of the density functional theory (DFT) calculations (see Sec. 6.2), however, the corresponding critical field of about $B_c \approx 3.2$ T is larger than that of the experiment. For this reason, a theoretical study of isolated skyrmion collapse in a ferromagnetic background is not feasible with the experimentally applied $B_\perp = 1.5$ T as the theoretical system exhibits a spin spiral phase at that field strength.

Instead, we chose the adaption of the skyrmion size to the experiment as a criterion in order to select a suitable out-of-plane magnetic field for the simulations, since it is known that the size of skyrmions has a decisive influence on their stability [I, VI, IX, XII]. It is found that a field of $B_\perp = 3.2$ T in the simulation yields skyrmions with a size similar to that in the experiment.

In Fig. 9.4 a and b, simulated skyrmions without and with in-plane magnetic field are displayed. The panels c and d in Fig. 9.4 show the corresponding dI/dV contrasts obtained from the magnetic structures by Florian Muckel. While the magnetic structures of both skyrmions resemble each other, the simulated dI/dV contrasts reveals an asymmetry due to the in-plane field similar to that observed in the experiment. As it can be seen on the dI/dV line profiles in Fig. 9.3 i and j, the simulated skyrmion contrasts agree well with the measured ones. Therefore, the following GNEB calculations are performed with 3.2 T out-of-plane field while the in-plane field values of the simulations are the same as in the experiment.

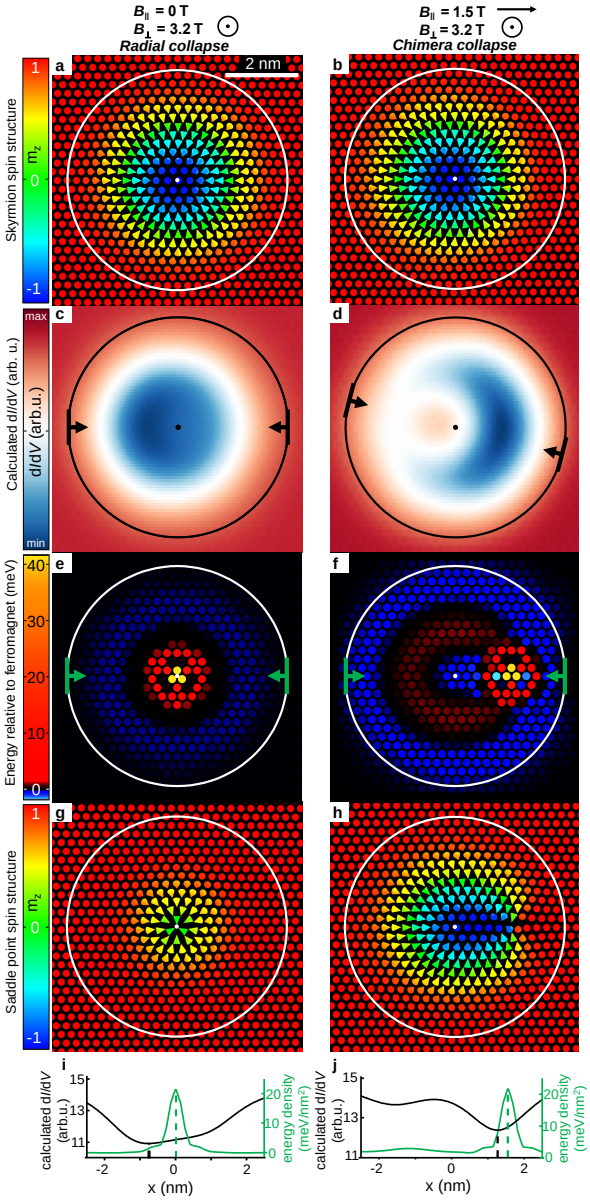

Figure 9.4 | Simulated skyrmions and saddle points of the radial symmetric and chimera collapse in fcc-Pd/Fe/Ir(111) at $B_\perp = 3.2$ T. The radial symmetric collapse **(left)** and the chimera collapse **(right)** are obtained by CI-GNEB with applied $B_\parallel = 0.0$ T and $B_\parallel = 1.5$ T, respectively. **a), b)** The magnetic structures of the initial skyrmion states. **c), d)** The corresponding dI/dV maps, simulated by Florian Muckel. **e), f)** The energy density maps of the saddle points. The colour code of each point denotes the energy of a lattice site relative to the ferromagnetic alignment. The outer circles denote the skyrmion circumference. **g), h)** The magnetic textures of the saddle point states. **i), j)** Line profiles of the dI/dV maps and the maps of energy density along the arrows shown in **(c)-(f)**. Figure published in [XI].

As elaborated in Chap. 8, there are two metastable minimum energy paths (MEPs) from the skyrmion to the ferromagnetic state that the GNEB calculation can relax into: The radial symmetric and the chimera collapse mechanism. In principle, there is also the possibility of an escape mechanism in which the skyrmion moves over the edge of the sample [90], but this mechanism is suppressed in the simulations by periodic boundary conditions.

Experimentally, the escape mechanism is believed to not play a significant role due to the facts, that the maps of transition rates do not exhibit features depending on the distance to the nearest edge of the Pd island and that skyrmions with a varying degree of pinning to defects exhibit similar transition maps. For a more detailed discussion see the supplement of Ref. [XI].

While, both, radial and chimera skyrmion collapse can be relaxed with GNEB at $B_{\parallel} = 0$ T, only the chimera collapse mechanism is metastable at $B_{\parallel} = 1.5$ T. The saddle point (SP) magnetic structures of the radial symmetric collapse at $B_{\parallel} = 0$ T and the chimera collapse at $B \parallel = 1.5$ T are displayed in Fig. 9.4 g and h. The corresponding maps of energy densities are shown in Fig. 9.4 e and f, highlighting hot spots of large contributions to the energy barrier. These hot spots denote the magnetic moments that have to be activated the most in order to pass the energy barrier of the corresponding MEP obtained by GNEB.

On the other hand, the map of switching rates denotes in which area the local activation below the STM tip induces the most switching events, i. e. the activation most likely leads to an overcoming of the energy barrier. Hence, the maps of energy densities of the SPs in Fig. 9.4 e and f can be compared to the recorded maps of transition rates in Fig. 9.3 e and f, as they both depict the spacial distribution of the activation energy required for a transition event.

While the maximum of the energy density line profile of the radial collapse in Fig. 9.4 i is close to 0 nm, the maximum of the chimera SP is located approximately at 1.6 nm in Fig. 9.4 j, which is very similar to the line profiles of the measured transition rates in Fig. 9.3 i and j. Based on this excellent agreement between experimental measurement and simulations, it is possible for the first time to identify both the radial symmetric and the chimera collapse mechanism.

In order to rule out, that the asymmetric map of switching rates is only due to a radial collapse mechanism that becomes slightly asymmetric due to the in-plane

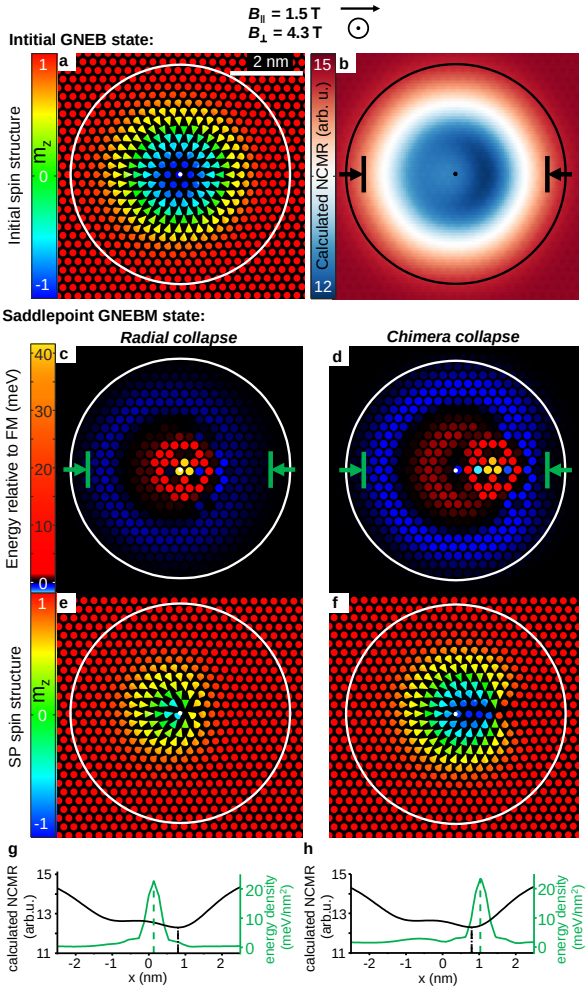

Figure 9.5 | Simulated skyrmions and saddle points of the radial symmetric and chimera collapse in fcc-Pd/Fe/Ir(111) at $B_\perp = 4.3$ T. The radial symmetric collapse **(left)** and the chimera collapse **(right)** are obtained by CI-GNEB with applied $B_\parallel = 1.5$ T. **a)** The magnetic structures of the initial skyrmion state. **b)** The corresponding dI/dV map, simulated by Florian Muckel. **c), d)** The energy density maps of the saddle points states. The colour code of each point denotes the energy of a lattice site relative to the ferromagnetic alignment. The outer circles denote the skyrmion circumference. **e), f)** Magnetic textures of the saddle point states. **g), h)** Line profiles of the dI/dV maps and the maps of energy density along the arrows shown in **(b)-(d)**. Figure published in [XI].

magnetic field, GNEB calculations of skyrmion collapse at $B_\perp = 4.3$ T are performed. Fig. 9.5 a and b displays the magnetic structure and dI/dV signal of the simulated skyrmions at $B_\parallel = 1.5$ T. With the higher out-of-plane magnetic field, the skyrmion size is decreased as compared to the experiment, but both collapse mechanisms can be metastabilised with the in-plane field of $B_\parallel = 1.5$ T.

As it can be seen in Fig. 9.5 e, the SP of the radial collapse becomes slightly asymmetric under in-plane field, but the energy density maximum of the line profile in Fig. 9.5 g is still close to 0 nm. On the other hand, the maximum of the energy density of the chimera SP is again at the skyrmion periphery with a distance of 1 nm (Fig. 9.5 h). This proves that a simple asymmetric version of the radial

collapse cannot explain the measured maps of transition rates and that it is indeed the chimera annihilation mechanism recorded in Fig. 9.3 f-h.

9.4. Skyrmion annihilation over in-plane magnetic field

Here, skyrmion annihilation is systematically investigated as a function of in-plane magnetic field for both the radially symmetric and the chimera-type mechanism. For this purpose both mechanisms are used as initial paths for GNEB computations and successively relaxed for different values of $B_{\parallel}$. The resulting energy barriers over in-plane magnetic field are plotted in Fig. 9.6 for three values of $B_{\perp}$.

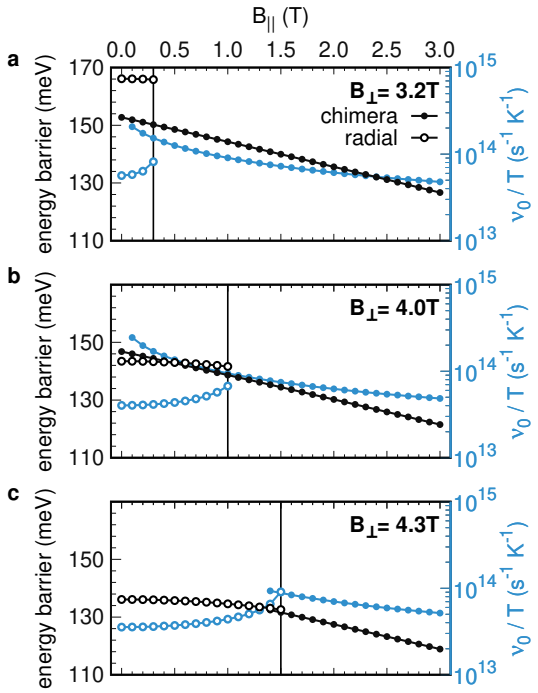

Figure 9.6 | Simulated energy barriers and prefactors of skyrmions annihilation in fcc-Pd/Fe/-Ir(111). For the three out-of-plane magnetic field values of 3.2 T **(a)**, 4.0 T **(b)** and 4.3 T **(c)**, energy barriers (black) and prefactors divided over temperature (light blue) are plotted over the in-plane magnetic field. Open symbols denote barriers and prefactors of the radial symmetric collapse while closed symbols correspond to the chimera-type collapse mechanism. A vertical line marks the limit of appearance of the radial mechanism. The minimum energy paths are calculated by CI-GNEB using the DFT-based atomistic parameters from Tab. 4.1. The prefactors are calculated via transition state theory, modelling all modes except the two skyrmion translation modes in harmonic approximation. Figure published in [XI].

At $B_{\perp} = 3.2$ T in Fig. 9.6 a, the energy barriers of chimera collapse decrease linearly with $B_{\parallel}$ over the entire interval. This can be explained by the magnetic structure of the chimera SP, in which a majority of the in-plane oriented moments is aligned parallel to the in-plane magnetic field. For this reason the SP state gains more energy from the in-plane field than the skyrmion state with more in-plane moments directed

against the field, and therefore the energy barrier decreases with increasing in-plane field.

In contrast, the radial symmetric collapse is found to be metastable only at low in-plane fields up to 0.3 T and with only minor adaptions of the barrier height to the field. These minor adaptions correspond to an increasing asymmetry of the radial SP in which the size of the area parallel to the in-plane field increases while the opposite side decreases, analogue to the adaption of the skyrmion to $B_{\parallel}$.

With increasing out-of-plane fields, the energy barriers of both mechanisms decrease and the radial symmetric collapse becomes more favourable compared to the chimera collapse, which is consistent to the trends observed in Sec. 8.2. The interval in which the radial collapse is metastable increases and at $B_{\perp} = 4.0$ T in Fig. 9.6 b, a crossover between the energy barriers of both mechanisms can be seen. For $B_{\perp} = 4.3$ T, the chimera collapse is metastable only for values of $B_{\parallel} \geq 1.4$ T, which leads to a transition from the radial to the chimera collapse mechanism similar to what has been observed in the experiment.

Note, that the GNEB method has similar problems finding the exact limits to which a MEP is metastable as the spin dynamics has problems finding the limits of metastable states. Close to the limit of a MEP, the disappearance depends on the exact initial path, the time step, the numerical stability and other details of the implementation. Therefore, the magnetic fields that mark the boundaries of the mechanisms found here can only be estimates of the exact limits of the metastable paths.

By diagonalisation of the Hessian matrices, also the eigenvalue spectra of the skyrmion and SP states are investigated. In Fig. 9.7 all eigenvalues up to 2.5 meV are displayed. A small number of eigenvalues corresponding to localised skyrmion modes slightly increases with in-plane field. The magnon bands, on the other hand, decrease with in-plane field because the ferromagnetic alignment in out-of-plane direction becomes less stable and the costs of deformations decrease.

A very similar behaviour is visible for the magnon bands of the SP states. As usual, the negative eigenvalues of the unstable modes are not shown in the spectra of the SPs. The lowest eigenvalue of the radial symmetric collapse is decreasing but due to the small interval of metastability the trends of the radial eigenvalues are hard to determine. The lowest eigenvalues of the chimera SP appear to be rather constant and only slightly increase on the linear scale of Fig. 9.7.

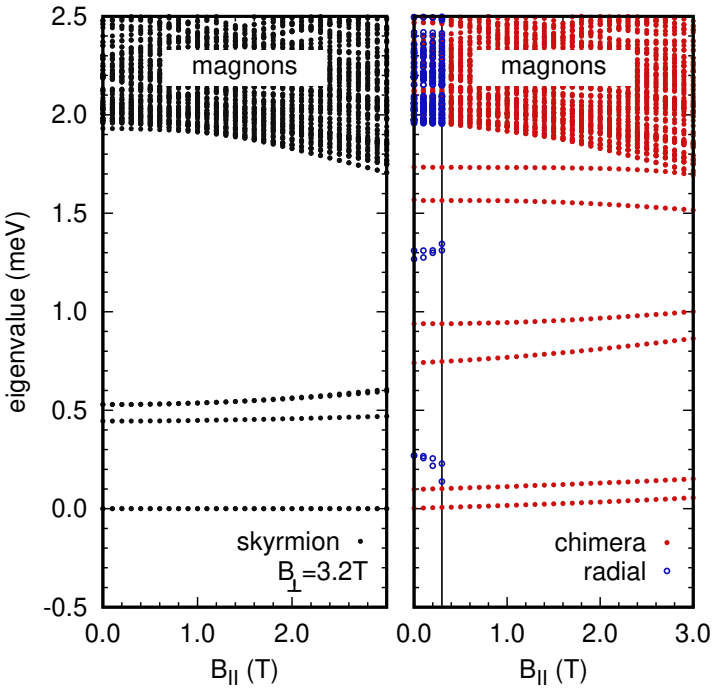

Figure 9.7 | Low-energy eigenvalue spectra of skyrmion collapse over in-plane magnetic field. Eigenvalues of the initial skyrmion state **(left)** and the saddle points of the radial symmetric collapse (blue) and the chimera collapse (red) mechanisms **(right)** are displayed up to 2.5 meV. The eigenvalues are obtained by diagonalisation of the corresponding Hessian matrices in harmonic approximation with an applied out-of-plane field of $B_\perp = 3.2$ T. The minimum energy path of the radial collapse is only found up to $B_\parallel = 0.3$ T which is denoted by a vertical line.

The logarithmic scale of eigenvalues in Fig. 9.8 enables a better visibility of the slope of the second lowest chimera eigenvalue. It corresponds to a rotation of the SP around the Bloch-like point and due to its symmetry is a candidate for a Goldstone mode, as it is discussed in the Sec. 8.4 and 10.4. But with increasing $B_\parallel$, this symmetry is broken and an energy barrier for the rotation of the Bloch-like point around the chimera SP arises. Thus, the Goldstone mode gradually becomes a vibrational mode, allowing for the calculation of the prefactor by harmonic approximation of the rotational chimera mode. This trend can be observed for all out-of-plane fields, even though only a part of the in-plane field interval is visible at $B_\perp = 4.3$ T. The second lowest eigenvalue of the radial SP exhibits an opposite trend and decreases with increasing $B_\parallel$. This mode softening is linked to the transition between the two collapse mechanisms, which is elaborated in more detail in Sec. 10.3.

By modelling the rotation mode of the chimera SP in harmonic approximation, the prefactor of both transition mechanisms can be determined. Fig. 9.6 shows the prefactors for different magnetic fields. For both mechanisms, the prefactor increases in the direction of the crossover between both mechanisms due to the discussed mode softening. Far from the crossover, both mechanisms exhibit a rather similar prefactor

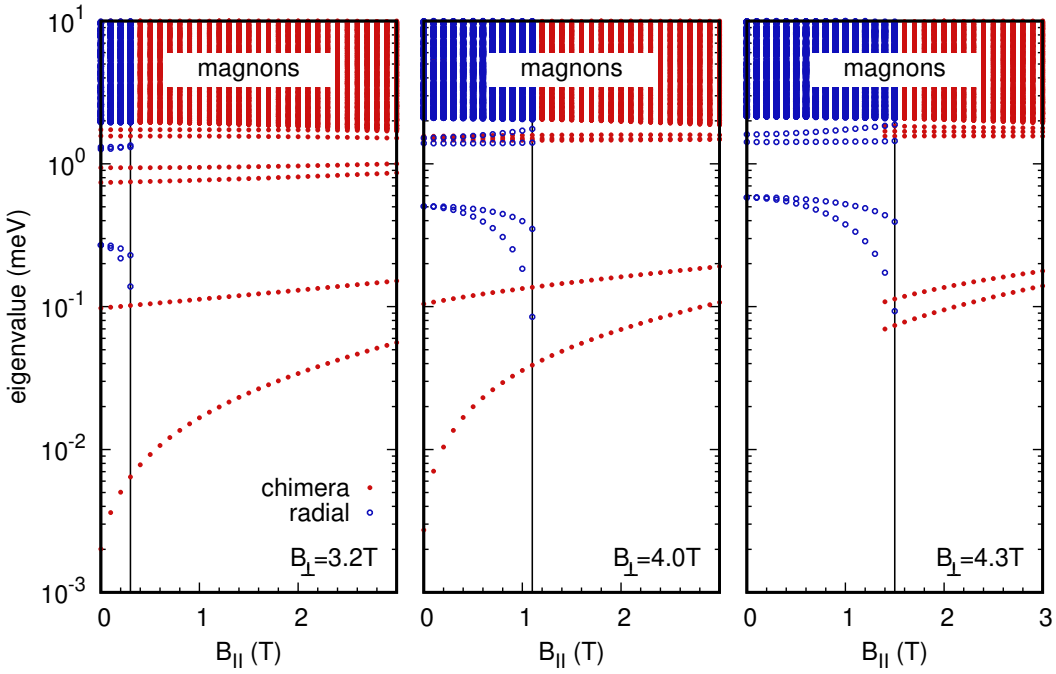

Figure 9.8 | Eigenvalue spectra of the saddle points of skyrmion collapse over in-plane magnetic field with logarithmic scale. All eigenvalues of the chimera (red) and radial (blue) symmetric saddle points are displayed on a logarithmic scale for values up to 10 meV. The eigenvalues are obtained by diagonalisation of the corresponding Hessian matrices in harmonic approximation with applied out-of-plane fields of 3.2 T **(a)**, 4.0 T **(b)** and 4.3 T **(c)**. The corresponding minimum energy paths of the radial and the chimera collapse mechanisms are found to not be metastable over the entire interval of $B_{\parallel}$. The vertical lines denote the largest values of $B_{\parallel}$ at which the radial symmetric collapse appears to be metastable.

on the order of $5 \cdot 10^{13}\mathrm{s}^{-1}\mathrm{K}^{-1}$ for all three out-of-plane field values. As expected, no entropy-size effect occurs with changing $B_{\parallel}$ since the skyrmion size is not affected by in-plane magnetic fields.

Prefactors and energy barriers allow for the calculation of transition rates via Eq. 5.51. In Fig. 9.9, transition rates are displayed for three different temperatures and for different magnetic fields. For both mechanisms the transition rates increase with $B_{\parallel}$ due to decreasing energy barriers. The fairly constant prefactors only slightly affect the trends of the transition rates.

At $B_{\perp} = 3.2$ T, the collapse rate of the chimera mechanism is larger than that of the radial symmetric collapse for all displayed values. This difference decreases with

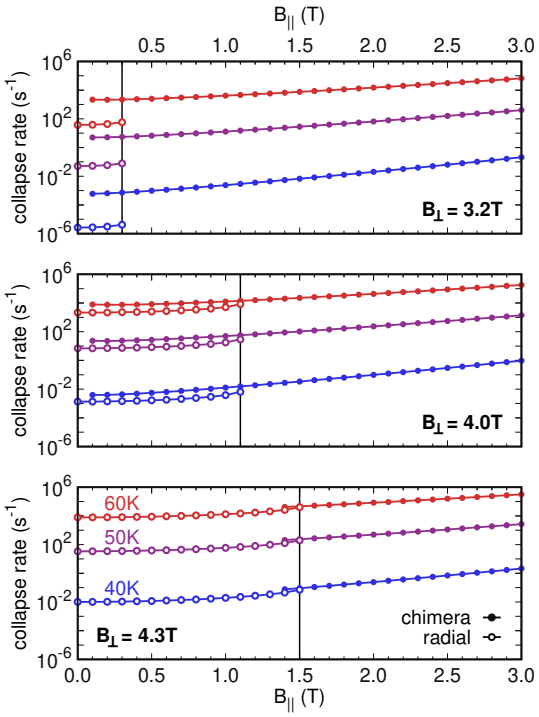

Figure 9.9 | Rates of skyrmion annihilation in fcc-Pd/Fe/Ir(111) over in-plane magnetic field. The rates of radial symmetric (open symbols) and chimera-type collapse (closed symbols) are calculated separately via Eq. 5.55 for three out-of-plane magnetic field values of 3.2 T **(a)**, 4.0 T **(b)** and 4.3 T **(c)**. The corresponding minimum energy paths of the radial and the chimera collapse mechanisms are found to not be metastable over the entire interval of $B_{\parallel}$. The vertical lines denote the largest values of $B_{\parallel}$ at which the radial symmetric collapse appears to be metastable.

$B_{\perp}$ but the skyrmion is still more likely to annihilate via the chimera mechanism at $B_{\perp} = 4.0$ T. For $B_{\perp} = 4.3$ T, however, the chimera collapse is not metastable at low in-plane magnetic fields anymore, and thus, the radial symmetric skyrmion collapse mechanism is preferred in the first half of the magnetic field interval. Naturally, the collapse rates at all fields drastically increase with temperature.

The theoretical results presented here already demonstrate that, both, the radial symmetric and the chimera collapse mechanism occur for fcc-Pd/Fe/Ir(111) and that a transition between them can be induced by, both, out-of-plane and in-plane magnetic fields. Values of the in-plane field found theoretically for the transition are in good quantitative agreement to the fields applied in the experiment, which further supports the interpretation of the experimental data as evidence for radial and chimera-type collapse mechanisms. The out-of-plane magnetic field, on the other hand, is larger in the simulations than in experiment, but still yields similar trends for both. In order to compare the theoretical obtained switching rates directly to the experimental data, however, the time-scale of the single electron process has to be evaluated in more detail.

9.5. Skyrmion creation over in-plane magnetic field

In principle, transitions between metastable states can occur in both directions. Hence, each MEP of skyrmion annihilation found by GNEB also denotes a possible skyrmion creation mechanism. The energy barriers of skyrmion creation over magnetic field are shown in Fig. 9.10 for the radial symmetric and chimera creation mechanisms. Similar to skyrmion annihilation, the energy barriers decrease with $B_{\parallel}$. But in contrast to the annihilation, they increase with $B_{\perp}$ due to the increasing energy difference between the SP and the ferromagnetic state which gains the most energy from $B_{\perp}$.

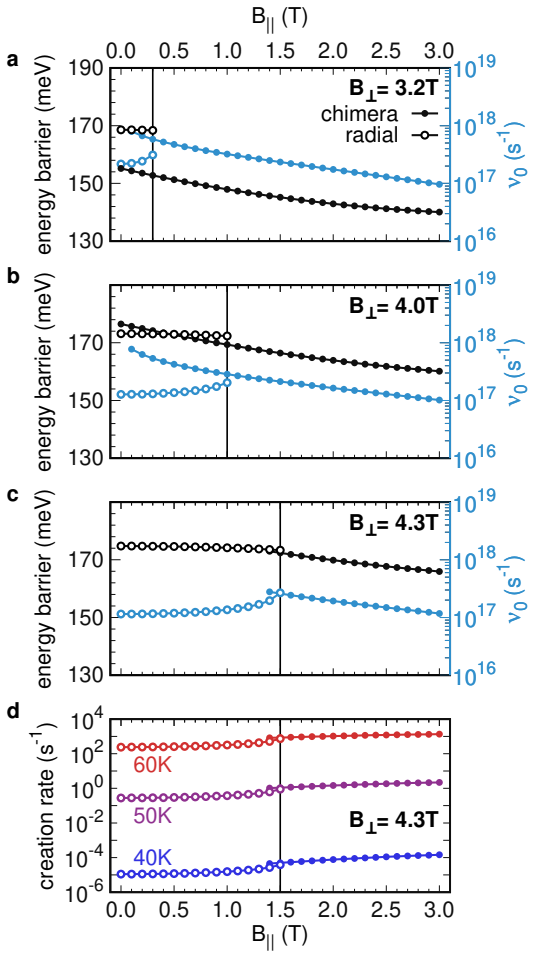

Figure 9.10 | Simulated energy barriers and prefactors of skyrmions creation in fcc-Pd/Fe/-Ir(111). For the three out-of-plane magnetic field values of 3.2 T **(a)**, 4.0 T **(b)** and 4.3 T **(c)**, energy barriers (black) and prefactors (light blue) are plotted over the in-plane magnetic field. Open (closed) symbols denote barriers and prefactors of the skyrmion creation via radial symmetric (chimera) mechanism. A vertical line marks the limit of appearance of the radial mechanism. The minimum energy paths are calculated by CI-GNEB using the DFT-based atomistic parameters from Tab. 4.1. The prefactors are calculated via transition state theory, modelling all modes in harmonic approximation. **d)** The resulting creation rates calculated separately for the radial symmetric and chimera-type creation via Eq. 5.55 at $B_{\perp} = 4.3$ T. Figure published in [XI].

In order to calculate the prefactor, one has to take into account the number of potential SPs leading to the creation of a skyrmion. As discussed further below, the tunnel current yields a thermally activated hot spot below the STM-tip with an estimated size of about 100 atoms. Including two possible SPs per unit cell, this results in about 100 identical SPs that can potentially be activated for a skyrmion creation process. They are considered in the creation rate by the statistical factor of 100. On the contrary, only two identical SPs are considered in the case of skyrmion annihilation.

The prefactors of skyrmion creation rates, displayed in Fig. 9.10, are independent of temperature since all modes of the ferromagnetic (FM) and SP states are modelled in harmonic approximation and thus all factors of the thermal energy cancel out. Similar to skyrmion annihilation, mode softening of low energy modes of the SP states close to the crossover of both mechanisms leads to an increase of the prefactor. With increasing distance to the crossover, however, both mechanisms exhibit a quite similar prefactor of about $10^{17}\mathrm{s}^{-1}$, which is approximately three orders of magnitude larger than the prefactors of skyrmion annihilation.

The trends of energy barriers and prefactors almost cancel out when being combined to the skyrmion creation rates shown in Fig. 9.10 d. For both creation mechanisms, they increase by about one order of magnitude over the magnetic field interval with a slightly larger increase for low temperatures.

9.6. Comparison of measured and simulated transition rates

The skyrmions A and B of another fcc-stacked Pd island, displayed in Fig. 9.11 b, are selected for the systematic measurement of transition rates for different in-plane magnetic field strengths. While the topographic measurement of the area around skyrmion A in Fig. 9.11 a is mainly defect free, several defects are visible at the vicinity of skyrmion B.

As indicated by the linear dependency of the switching rate on the current strength I in Fig. 9.11 c, switching events are initiated by single electron events [XI]. The double logarithmic plots of the collapse and creation rates in Fig. 9.11 d and e show a linear dependence of the rates on the current for all fields and over several orders of magnitudes.

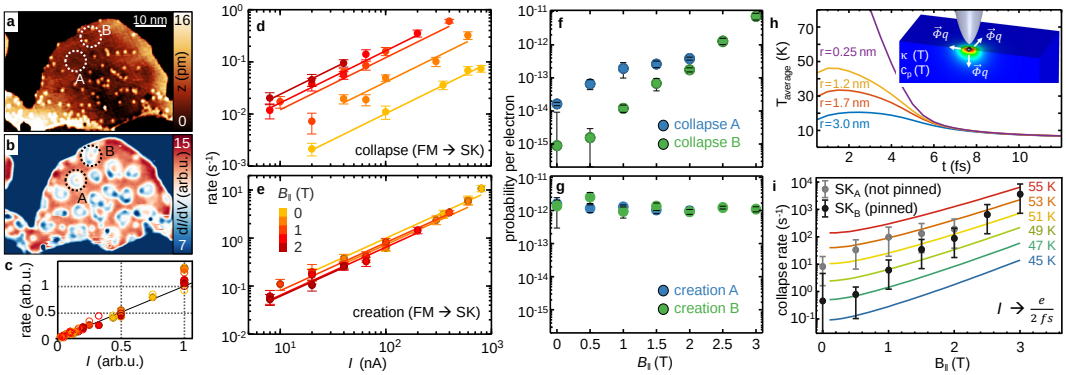

Figure 9.11 | Transition rates of skyrmion creation and collapse in fcc-Pd/Fe/Ir(111) for different magnetic fields. **a)** The STM topography of Pd island on Fe/Ir(111) with marked skyrmions A and B is shown with $B_\perp = 1$ T, $B_\parallel = 0$ T, $V = 610$ mV and $I = 2$ nA. **b)** dI/dV maps simultaneously measured to **(a)**. **c)** Collapse rates over the tunnel current I. The values are scaled such, that they exhibit a similar linear slope $\Delta\nu/\Delta I$ for all measured collapses. **d)**, **e)** The collapse and creation rates are displayed over the tunnel current I for different values of the applied in-plane field which is indicated by the colour code. Straight lines correspond to linear fits to data points with similar fields. From the fits in **(d)** and **(e)**, the collapse and creation probabilities per electron are deduced and shown in **(f)** and **(g)** for both skyrmions A and B separately. **h)** The time-dependent average temperatures of circular sample areas centred below the tip are displayed. The lines are labelled with the corresponding radii of the evaluated areas. The inset of **(h)** shows a sketch of the finite element simulation, in which the heat capacitance, $c_p(T)$, and the heat conductivity, $\kappa(T)$ are taken into account and the heat flow is indicated by $\vec{\Phi}_q$. **i)** The theoretically obtained collapse rates displayed for different temperatures over $B_\parallel$ as coloured lines. The measured collapse probabilities of **(f)** are translated to collapse rates per second by assuming $I = e/(2\text{fs}) = 75$ μA and that the area of 1.2 nm radius is heated continuously to an average temperature of 45 K. With this translation, the collapse rates for both skyrmions A and B are displayed with the corresponding error bars. Figure published in [XI].

This converts into switching probabilities per electron over the in-plane magnetic field as shown in Fig. 9.11 f and g. The rate of skyrmion annihilation increases rapidly with magnetic field by up to five orders of magnitude for skyrmion B and two orders of magnitude of skyrmion A, indicating an influence of the lattice defects on the skyrmion stability. On the other hand, the rate of skyrmion creation remains unchanged over $B_\parallel$ and is very similar for both areas of the Pd island. Hence, the skyrmion creation appears to be less affected by the defect density than the skyrmion annihilation.

Transition state theory is derived only for spacially and temporal evenly distributed thermal energy provided by some kind of heat bath. This assumption gives rise to the Boltzmann distribution on which a large part of the mathematical treatment presented in Sec. 5.3 relies on. On the contrary, the single electron process occurring

in the experiment provides local heating for a limited amount of time. In order to compare the measured transition rates to the results of the simulations, an average temperature is estimated by a simple finite element simulation of the energy transfer during an electron impact event.

As it can be seen in Fig. 9.11 h, the finite-size simulations, performed by Florian Muckel, yield a temperature of about 45 K for an hot spot of about 1.2 nm for a short period of $\Delta t \approx 2$ fs. The area of the skyrmion is heated on average by about 20 K, but also cools down over a few fs. This simulation makes clear, that the thermal activation is limited to a short time interval after the impact of a single electron. The sample quickly cools down before the next electron arrives after the average time interval of $\tau = e/I \geq 150$ fs [XI].

Assuming temperatures close to the estimated 45 K for the hot spot and considering only a time interval of $\Delta t = 2$ fs for each electron process, the measured collapses per activation time can be compared to the simulated skyrmion annihilation rates. According to Eq. 5.30, the simulated contributions of both collapse mechanisms are added up. However, over the entire interval the transition rates of the chimera mechanism are much larger than the rates of the radial collapse and thus dominates the total switching rate.

In Fig. 9.11 i, the switching rates of the skyrmions A and B exhibit similar slopes and values than the theoretically obtained switching rates. The simulated rates are shown for a temperature range between 45 and 55 K with the best agreement for simulations with temperatures around 50 K. This value is surprisingly close to the 45 K of the thermal activation estimated for the experiment considering the simplified finite-element simulation and the local nature of the hot spot.

Additionally, the measured and simulated skyrmion creation rates displayed in Fig. 9.12 coincide well with a theoretical assumed temperature of 50 K. The creation rates of, both, experiment and theory are fairly constant and the influence of defects appears to be smaller on the skyrmion B as in the case of skyrmion annihilation.

The agreement of the calculated transition rates for skyrmion creation and annihilation with the trends and even values of the measured transition rates further underpins the applied theoretical model and the interpretation of two occurring transition processes in the experiment. However, the values of the calculated transition rates have to be interpreted with caution due to the roughly approximated

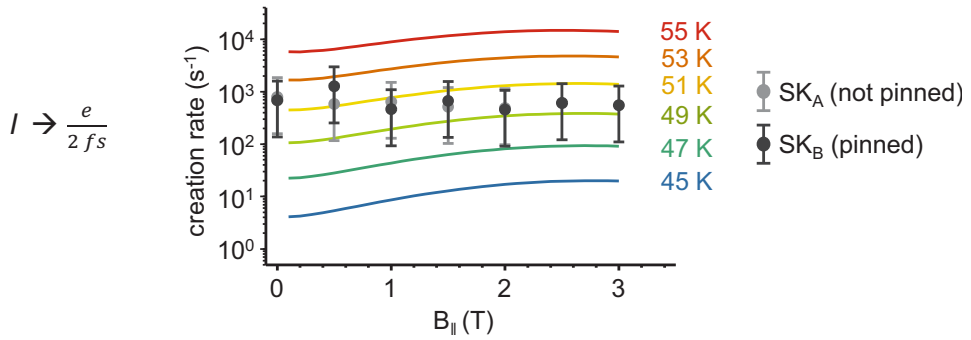

Figure 9.12 | Experimentally and theoretically obtained skyrmion creation rates in fcc-Pd/Fe/Ir(111) over the strength of the in-plane magnetic field. Analogously to the rates in Fig. 9.11 i, the probabilities of skyrmion creation of Fig. 9.11 g are translated to creation rates per second for both skyrmions A and B. Figure published in [XI].

average temperature and other possible effects such as the magnetoelectric effect or spin-transfer torques, which were neglected in the simulations.

Nevertheless, the DFT-based atomistic simulations consistently explain the measured occurrence and transition between the radial and chimera transition mechanisms with external magnetic fields. The direct comparison of the simulated energy density maps of the transition states with the measured transition rate maps does not only provides evidence for both transition mechanisms for the first time. It also confirms that the multiscale approach presented in this thesis is capable of adequately model magnetic transition processes in ultrathin films. A model based on the effective nearest neighbour approximation of exchange interaction, on the other hand, does not reproduce the measured transition rates which can be seen e. g. in Fig. A.10.

10. Results of the mode following method

Up to now, all transition state theory (TST) calculations presented in this thesis have been performed in either harmonic or Goldstone mode approximation of the energy landscapes around the initial and saddle point (SP) states. In order to explore the actual form of these energy landscapes and to go beyond the harmonic approximation, the mode following method has been developed (Sec. 5.4). While the performance of the implemented algorithm has some potential for future optimisation, this novel method already provides promising results for its application, which are presented in this chapter.

First, the energy landscape of the ferromagnetic (FM) state is investigated and compared to the harmonic approximation. Then, the lowest skyrmion eigenmodes are followed and especially the Goldstone approximations of the skyrmion translation modes are evaluated. The mode following is also applied to the lowest eigenmodes of, both, the radial and the chimera SP states, revealing eigenmodes connecting both states. Further, it is investigated for which temperatures the harmonic and Goldstone approximations are valid. For the case of the rotation mode of the chimera SP, it is presented how the integral can be calculated accurately via mode following in the intermediate regime between the harmonic and the Goldstone approximation.

10.1. Magnon eigenmodes

The mode following method is presented on the example of the transition between isolated skyrmions and the FM state in fcc-Pd/Fe/Ir(111) at $B_\perp = 4.0$ T. While the FM state itself only enters the transition rate for the creation of skyrmions, eigenmodes of the FM state, also called magnon modes, can occur in the background of the skyrmion and SP states.

Moreover, magnon modes do not only occur very frequently, they also represent good test cases for the mode following method. Magnon excitations are known to behave as harmonic oscillators for small excitation amplitudes [189], i. e. exhibit parabola shaped energy variations, as long as the contribution of the ferromagnetic exchange interaction is dominating.

The coordinate of the followed eigenmode is labelled q_p and stands for the displacement in the direction of the corresponding eigenvector $\mathbf{q}_p$. Since the sign of the eigenvector is randomised, one direction is arbitrarily assigned to be positive, while the inverted direction is labelled negative.

During an iteration of the mode following method, all magnetic moments are rotated a small step in the direction of the followed eigenvector. Subsequently, the Hessian matrix of the resulting new magnetic state is calculated and from all its eigenvectors, the one with the highest similarity to the previously followed eigenvector is selected as the next eigenvector to follow. This procedure is typically repeated a few thousand times, slowly moving the magnetic structure in the direction of the eigenvector. Simultaneously, occurring magnetic structures and its properties can be evaluated. More details on the algorithm are presented in Sec. 5.4.2.

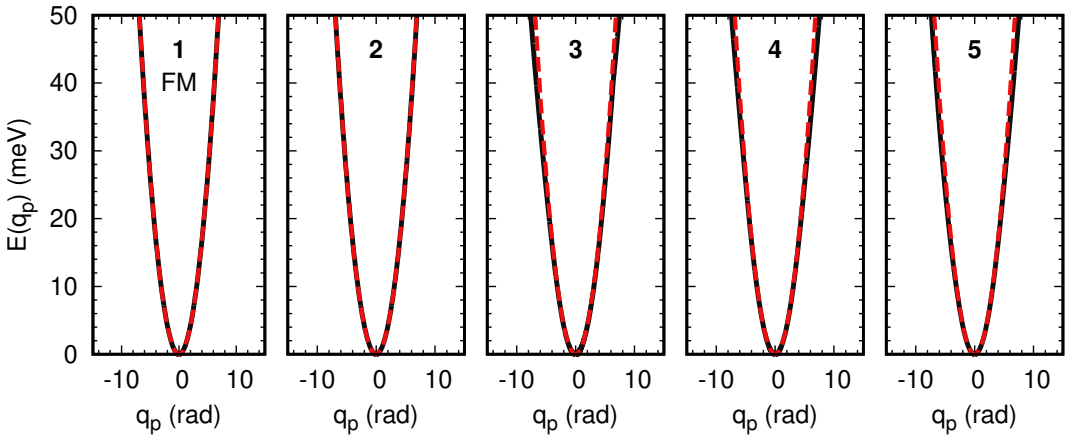

Figure 10.1 | Energy along the lowest five eigenmodes of the FM state calculated via mode following. The energy is displayed relative to the energy of the FM state of fcc-Pd/Fe/Ir(111) at $B_\perp = 4.0$ T. The displacement in the direction of an eigenvector is given by the coordinate q_p, where the negative sign corresponds to the direction of the inverted eigenvector. For comparison, the corresponding energies in harmonic approximation, calculated via Eq. 10.1, are shown as red dotted lines.

In Fig. 10.1, the energies along the first five eigenmodes of the FM state, calculated in positive and negative direction by mode following, are displayed. The energies of all five modes steeply increase in form of a parabola. In harmonic approximation, the energy of a magnetic state expanded along the eigenmode $\mathbf{q}_p$ is calculated analytically via

$$E\left(q_p\right) \approx E_0 + \frac{1}{2} q_p^2 \epsilon_p, \tag{10.1}$$

where ϵ_p is the corresponding eigenvalue of the Hessian matrix as introduced in Sec. 5.3.3. For all five modes, the energies $E\left(q_p\right)$ obtained by mode following excellently agree with the energies calculated in harmonic approximation. The deviations visible for the modes 3-5 are still small for excitation energies up to 50 meV. Since a thermal energy of $k_\mathrm{B}T = 50$ meV corresponds to a temperature of ~ 580 K, these results suggest, that the harmonic approximations for magnon modes performed throughout this work are justified.

10.1.1. Comparison with the harmonic approximation

In addition to the exploration of the energy landscape around magnetic states, the mode following method enables for the direct evaluation of the Boltzmann factor without any approximation of the energy landscape. As shown in Fig. 10.1, the energies along the first FM eigenmodes are well described in harmonic approximation. This makes the FM eigenmodes ideal test cases for the numerical calculation of the integral over the Boltzmann factor, Φ_p, as, both, the numerical determined integral via Eq. 5.77 and the analytically calculated integral in harmonic approximation should result in the same values of Φ_p. The analytical solution of the integral over the Boltzmann factor in harmonic approximation, Φ_p^har, reads

$$\Phi_p^\mathrm{har} = \sqrt{\frac{2\pi}{\beta \epsilon_p}}, \tag{10.2}$$

as introduced in Sec. 5.3.3. Note, that the value of Φ_p^har is proportional to $\sqrt{T}$, due to the increasing occupation of excited states with rising thermal energy.

For three different temperatures, the resulting values of Φ_p^har for the first eigenmode of the FM state are displayed in Fig. 10.2 as constant, dotted lines. The numerically obtained values of the integral, Φ_p^num, are plotted for the same three temperatures and over the maximal displacement considered for the numerical integration.

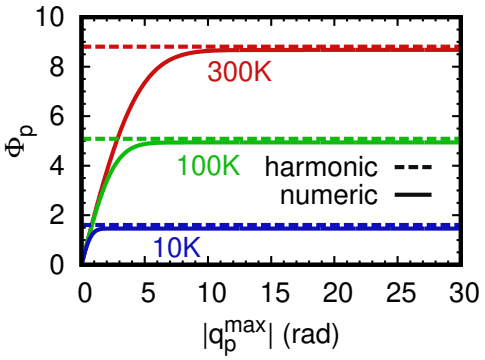

Figure 10.2 | Comparison of the numerically determined value of the integral over the first magnon mode with the harmonic approximation. For the first eigenmode of the FM state at $B_\perp = 4.0$ T, the integral Φ_p is determined numerically by mode following for three different temperatures. The value of the integral is plotted over the maximum displacement, $|q_p^{\max}|$, up to which the contributions in positive and negative direction are summed in the numerical integration. For the same temperatures, the values obtained in harmonic approximation via Eq. 10.2 are shown as dashed lines.

Strictly speaking, the numerical integration has to be performed over the entire valid definition space of q_p. In practice, it occurs, that the values of Φ_p^{num} quickly converge to the reference values of the harmonic approximation in Fig. 10.2, due to the exponential dependency of the Boltzmann factor on the energy. This causes the contributions to the integral to rapidly become negligible for increasing displacements along the eigenmode.

In Fig. 10.2, the values of Φ_p obtained numerically by mode following and analytically by the harmonic approximation nearly coincide and only small deviations are visible. This demonstrates, that the numerical determination of Φ_p by mode following is possible and accurate, which allows for the calculation of transition rates beyond harmonic approximation.

Due to the time-consuming and elaborate simulations necessary to obtain the value of Φ_p^{num}, the mode following is limited to the calculation of the contributions of individual eigenmodes rather than the numerical calculation of the entire spectrum. However, by future optimisations of the presently quite inefficient implementation of the algorithm, more sophisticated calculations should be feasible.

10.2. Skyrmion eigenmodes

The application of the mode following method to the first five eigenmodes of the skyrmion state in fcc-Pd/Fe/Ir(111) at $B_\perp = 4.0$ T yields the energy variations shown in Fig. 10.3. The first two eigenmodes correspond to the skyrmion translation modes, which are discussed in more detail further below.

Following of the third skyrmion eigenmode, the breathing mode, results in the expansions and contractions of the skyrmion illustrated in Fig. 10.4. Although the mode following is applied over a long distance in both directions of the breathing mode, the method's mode tracking has reliably selected the correct eigenvectors and the magnetic structure of the skyrmion appears to have been adequately expanded and contracted.

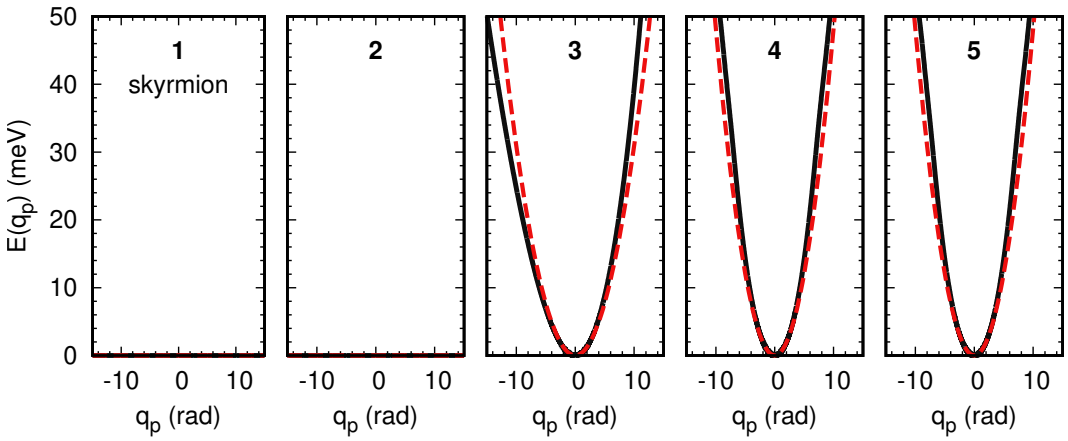

Figure 10.3 | Energy along the lowest five eigenmodes of an isolated skyrmion calculated via mode following. The energy is displayed relative to the energy of an isolated skyrmion in fcc-Pd/Fe/Ir(111) at $B_\perp = 4.0$ T. The displacement in the direction of an eigenvector is given by the coordinate q_p, where the negative sign corresponds to the direction of the inverted eigenvector. For comparison, the corresponding energies in harmonic approximation, calculated via Eq. 10.1, are shown as red dotted lines.

For small excitations, the energy curve of the breathing mode in Fig. 10.3 coincides with the curve of the harmonic approximation. For lager values of $q \approx 10$ rad, however, the excitation energy becomes asymmetric for the expansion (negative q_p) and the contraction (positive q_p). This observation can be explained by the limitations of the contraction movement due to the finite size of the skyrmion, while the movement of the expansion is only limited by the simulation box size. Despite this asymmetric behaviour of the breathing mode, the harmonic approximation appears to be fairly reasonable in the range of temperatures investigated in this work.

The excitations of the next two skyrmion eigenmodes, the four-fold deformation modes, are more symmetric and closer to the curves of the harmonic approximation than in the case of the breathing mode. Considering, that the eigenmodes are sorted

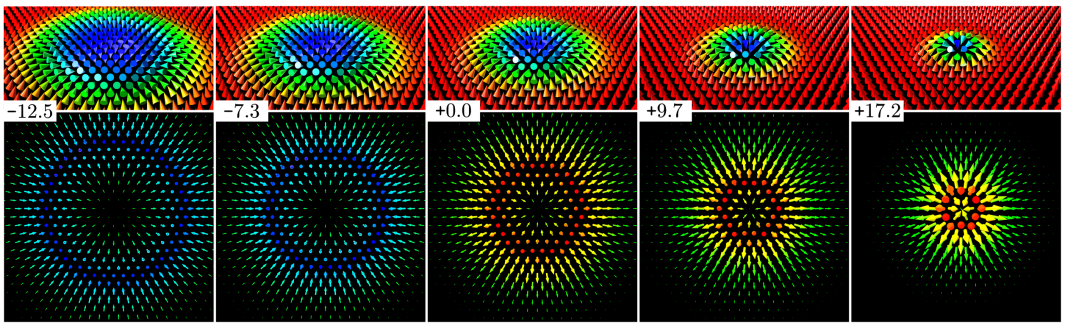

Figure 10.4 | Magnetic structures and eigenvectors obtained by following the third eigenmode of the isolated skyrmion state. The top row shows the magnetic structures of a skyrmion in fcc-Pd/Fe/Ir(111) at $B_\perp = 4.0$ T from a tilted perspective, obtained by mode following for different values of the displacement, q_p. In the corners, the corresponding, rounded values of q_p are displayed. The bottom row shows the respective eigenvectors in a top view. The size of the arrows scales with the size of the individual vectors. The colour codes of both rows correspond to the out-of-plane component of the arrows and cones, respectively.

in increasing order of their eigenvalues, it can be expected that the quality of the harmonic approximation improves for eigenmodes higher in the eigenvalue spectrum.

While the results of this section have been obtained only for a skyrmion in fcc-Pd/-Fe/Ir(111) at $B_\perp = 4.0$ T, they still support the general assumption made throughout this work, as well as in the literature [23, 67, 90, 95, 99, 170], that all skyrmion eigenmodes but the two translational modes can be described sufficiently well in harmonic approximation. Note, however, that skyrmions in other systems may exhibit a more complex energy landscape and, thus, particular modes may deviate from the harmonic approximation. The mode following method is well suited to investigate such eigenmodes and to help answering the question of whether or not they should be described in harmonic approximation.

10.2.1. Energy variation during skyrmion translation

In Fig. 10.3, the energy of the skyrmion seems to be unchanged unter the lateral movement caused by the following of the two skyrmion translation modes. This is not unexpected, since skyrmion translation modes in literature are typically modelled in Goldstone approximation [23, 67, 90, 95, 99, 170].

While the skyrmion energy is exactly conserved in the micromagnetic model of magnetism, the discrete lattice of an atomistic model could lead to an alteration of the energy during translations. Although it is assumed, that these lattice effects are negligible, it is unclear how well this assumption holds when the size of skyrmion becomes as small as a few lattice sites. Here, it is shown how this question can be answered via mode following for the example of the isolated skyrmion in fcc-Pd/Fe/-Ir(111) at $B_\perp = 4.0$ T.

On the much finer energy scale of Fig. 10.5, a slight increase in energy on the order of a few tens of neV can be observed. By comparison with the corresponding magnetic structures, it can be observed, that this increase occurs over a skyrmion displacement of several lattice sites in both directions of $\mathbf{q}_p$. This already indicates, that the energy stems from numerical errors accumulating during the simulations, since in case of an actual lattice effect on the energy of translation, a periodic variation on the energy would be expected.

Furthermore, the energy increase occurs in small, discrete steps and becomes smaller with a smaller step width of the simulation. This confirms, that the visible increase in energy stems indeed from numerical errors and that the energy is conserved during skyrmion translation. This result supports the common description of the skyrmion translation modes in Goldstone approximation and shows, that lattice effects can be neglected for skyrmions of at least the same size as the one of fcc-Pd/Fe/Ir(111) at $B_\perp = 4.0$ T.

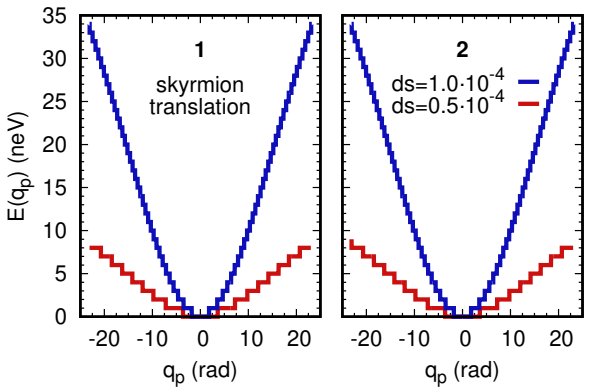

Figure 10.5 | Energy along the first and second skyrmion eigenmodes calculated via mode following. The energy is displayed for two values of the step width, ds, relative to the energy of the skyrmion state of fcc-Pd/Fe/Ir(111) at $B_\perp = 4.0$ T. The displacement in the direction of an eigenvector is given by the coordinate q_p, where the negative sign corresponds to the direction of the inverted eigenvector.

10.2.2. Comparison with the Goldstone mode approximation

Skyrmion translation modes are well-suited as test cases for the numerical calculation via mode following, since an analytic solution of the Goldstone mode volume is available (see Sec. 5.3.4), which allows for a comparison of both methods.

By following a skyrmion translation mode, the skyrmion is moved across the lattice in small steps. The first translational mode corresponds to a movement in the direction of the second nearest neighbour, $\mathbf{T}_1$, as shown in Fig. 10.6 b. Per definition, eigenvectors are perpendicular to each other and therefore the angle between the translation vectors on a surface, $\mathbf{T}_1$ and $\mathbf{T}_2$, must be 90°. Consequently, the second translation mode moves the Skyrmion in the direction of its nearest neighbour, $\mathbf{T}_2$, which is illustrated in Fig. 10.6 c.

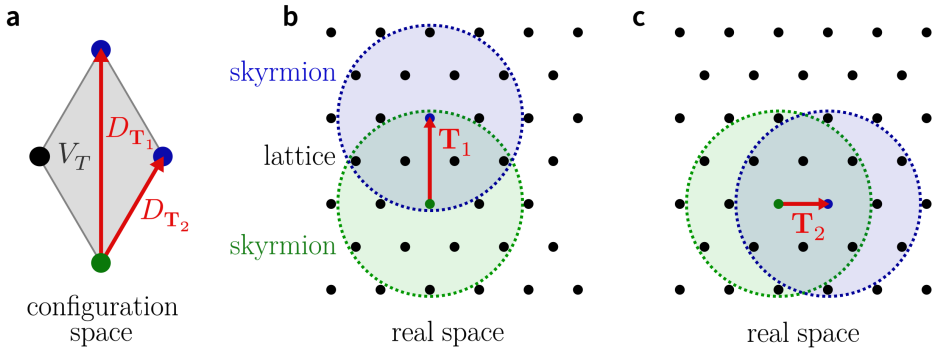

Figure 10.6 | Geometry of the Goldstone mode volume of two surface translational modes. **(a)** The surface area of a rhombus, V_T, spanned by the geodesic distances $D_{\mathbf{T}_1}$ and $D_{\mathbf{T}_2}$ in configuration space. The geodesic distances correspond to the rotational distances of the magnetic configurations during a translation in the directions of $\mathbf{T}_1$ and $\mathbf{T}_2$, respectively. **(b)** Illustration of a skyrmion translation to the lattice site of a second nearest neighbour in the direction of $\mathbf{T}_1$. **(c)** Analogue to **(b)**, the translation of a skyrmion to the lattice site of a nearest neighbour, in the direction of $\mathbf{T}_2$, is shown.

The Goldstone mode volume per unit cell is given by the integration over unity along two perpendicular translation modes in configuration space (see Eq. 5.60). It can be determined directly with the mode following method by evaluating the geodesic distances in configuration space, $D^{\text{geo}}_{\mathbf{T}_1}$ and $D^{\text{geo}}_{\mathbf{T}_2}$, for a single translation by one lattice site in the directions of $\mathbf{T}_1$ and $\mathbf{T}_2$, respectively. Subsequently, the surface area of the unit cell in configuration space, V_T, which is equivalent to the Goldstone mode

volume per unit cell and is shown as a diamond in Fig. 10.6 a, can be calculated with

$$V_T = \frac{D^{\mathrm{geo}}_{\mathbf{T}_1} D^{\mathrm{geo}}_{\mathbf{T}_2}}{2}. \tag{10.3}$$

For the shown example of a skyrmion in fcc-Pd/Fe/Ir(111) at $B_\perp = 4.0$ T, the mode following yields values of $D^{\mathrm{geo}}_{\mathbf{T}_1} \approx 7.61$ rad and $D^{\mathrm{geo}}_{\mathbf{T}_2} \approx 4.39$ rad, which results in a numerically determined Goldstone mode volume per unit cell of

$$V_{\mathrm{T}} \approx 16.70\,(\mathrm{rad})^2\,. \tag{10.4}$$

The analytically determined value, obtained from Eq. 5.60, reads

$$V_0 \approx 16.63\,(\mathrm{rad})^2\,. \tag{10.5}$$

Both values coincide well, which demonstrates, that the Goldstone mode volume can be determined accurately via the mode following method. This is particular interesting for magnetic structures with Goldstone modes for whose volumes no analytical formula is available, as e. g. for the additional rotation mode of antiskyrmions and higher order skyrmions. In fact, the calculation of this mode is the reason why lifetimes of antiskyrmions in fcc-Pd/Fe/Ir(111) have not been predicted yet. However, by applying the mode following method, the calculation of antiskyrmion prefactors is now feasible [XIV].

10.3. Radial saddle point eigenmodes

The application of the mode following method to the first five eigenmodes of the SP state of the radial symmetric skyrmion collapse, yields the energy variations shown in Fig. 10.7. The first eigenmode can be identified by its negative curvature as the unstable mode of the transition. It is oriented perpendicular to the dividing surface and points in the direction of the minimum energy path (MEP).

In Fig. 10.8, the magnetic structures and eigenvectors obtained by mode following are shown along both directions of this mode. One can see, how the magnetic structure of the SP evolves towards the FM state in the negative direction of the eigenmode. In positive direction, the SP expands and turns its core moments downwards, which results in the magnetic structure of a skyrmion. Although the eigenvector evolves

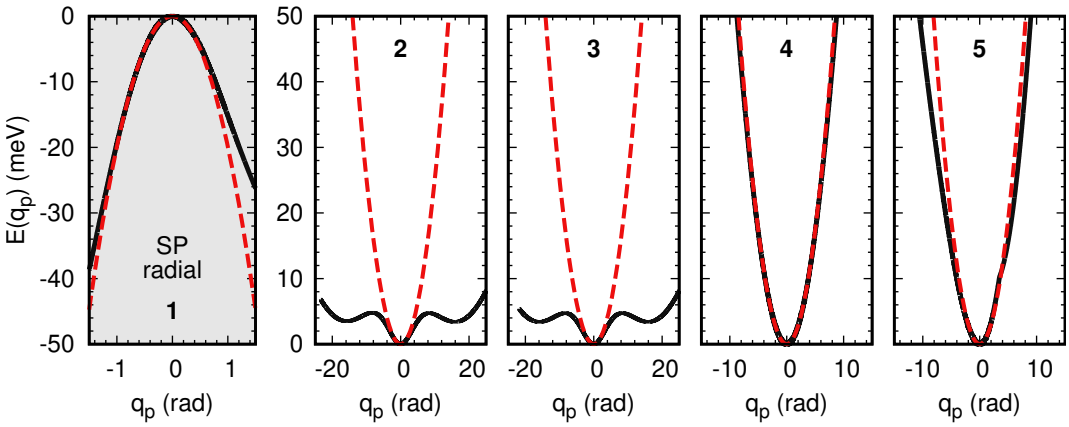

Figure 10.7 | Energy along the lowest five eigenmodes of the saddle point of the radial symmetric skyrmion collapse calculated via mode following. The energy is displayed relative to the energy of the radial saddle point in fcc-Pd/Fe/Ir(111) at $B_\perp = 4.0$ T. The displacement in the direction of an eigenvector is given by the coordinate q_p, where the negative sign corresponds to the direction of the inverted eigenvector. For comparison, the corresponding energies in harmonic approximation, calculated via Eq. 10.1, are shown as red dotted lines.

along the mode following process as well, the mode tracking is able to reliable select the correct eigenvectors to follow the unstable mode for the entire displacement from the skyrmion to the FM state.

The energy curve of the unstable mode is close to the harmonic approximation, whose parabola is opened downwards as well due to the negative eigenvalue of the mode. While the parabola and the numerically obtained curve start to deviate especially in positive direction for increasing values of $|q_p|$, the overall harmonic approximation holds for small excitations.

While the eigenvalue of this mode does not enter the calculation of the prefactor, the parabolic shape of the unstable mode assures, that the placement of the dividing surface on the SP of the MEP indeed minimises the effect of recrossings.

In contrast, the eigenmodes two and three show a more complex behaviour, which will be discussed in more detail further below. Eigenmodes four and five, on the other hand, emerge as typical harmonic oscillators and are well described by the harmonic approximation. For positive displacements along the fifth eigenmode, however, the mode tracking eventually selected a wrong eigenmode which manifests in a subtle kink in the energy curve at $q \approx 3$ rad.

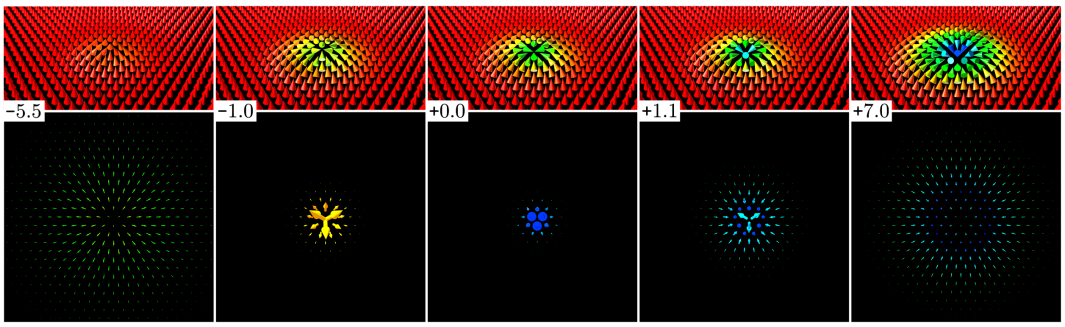

Figure 10.8 | Magnetic structures and eigenvectors obtained by following the first eigenmode of the radial symmetric saddle point state. The top row shows the magnetic structures of the radial saddle point of a skyrmion collapse in fcc-Pd/Fe/Ir(111) at $B_\perp = 4.0$ T from a tilted perspective, obtained by mode following for different values of the displacement, q_p. In the corners, the corresponding, rounded values of q_p are displayed. The bottom row shows the respective eigenvectors in a top view. The size of the arrows scales with the size of the individual vectors. The colour codes of both rows correspond to the out-of-plane component of the arrows and cones, respectively.

10.3.1. Transition between saddle point states

The magnetic structures and the corresponding eigenvectors in positive and negative direction of the second eigenmode are shown in Fig. 10.9. In both directions of $|q_p|$, the three core magnetic moments eventually rotate in out-of-plane direction, such that the in-plane components of two of them become antiparallel. Two other moments next to them align in opposing out-of-plane directions, which in total creates a Bloch-like point. Moreover, one side of the magnetic structure expands while the opposite side contracts, which results in the magnetic structure of the chimera SP state.

While this transition between both SPs occurs for both directions of the second SP mode, the transitions are not equivalent in both directions. The radial SP structure shows a 120° rotation symmetry but no inversion symmetry. A closer look at the intermediate states at $q_p = -6.9$ rad and $q_p = +7.1$ rad in Fig. 10.7 reveals, that the transition either evolves parallel to a crystal axis (negative direction) or in the middle between two of them (positive direction).

The third eigenmode is very similar to the second and also connects the radial and the chimera SP structures, with the sole difference of a 90° rotated transition direction. However, by looking at the corresponding magnetic structures and eigenvectors of

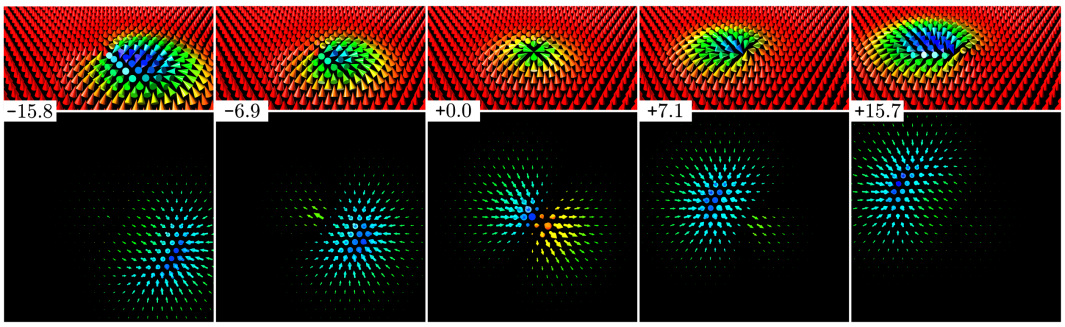

Figure 10.9 | Magnetic structures and eigenvectors obtained by following the second eigenmode of the radial symmetric saddle point state. The top row shows the magnetic structures of the radial saddle point of a skyrmion collapse in fcc-Pd/Fe/Ir(111) at $B_\perp = 4.0$ T from a tilted perspective, obtained by mode following for different values of the displacement, q_p. In the corners, the corresponding, rounded values of q_p are displayed. The bottom row shows the respective eigenvectors in a top view. The size of the arrows scales with the size of the individual vectors. The colour codes of both rows correspond to the out-of-plane component of the arrows and cones, respectively.

Fig. 10.10, one can observe a 120° difference between both directions of q_p. Therefore, the two signs do not correspond to a movement in two inverse directions of the same eigenvector, as it was originally intended for these simulations.

This deviation from the expected behaviour can be straightforwardly explained by the implemented procedure that is used to perform mode following simulations in inverted directions. First, the initial eigenvector with the selected index of the eigenvalue spectrum, which in this case is index 3, is obtained by running a one-step mode following simulation. Subsequently, the components of the eigenvector are inverted and a second mode following simulation is started, which uses the inverted vector as an input. Finally, the mode tracking algorithm of the second simulation decides, which eigenvector of the new simulation resembles the input eigenvector the most. Following this eigenvector is associated with moving in the negative direction of the eigenmode.

While this procedure is working well in other cases, the rotation symmetry of the radial symmetric SP yields three degenerated sets of eigenvectors for the second and third eigenmodes. The eigenvectors are distinguished only by a rotation of a multiple of 120°. By assuming, that two different sets of eigenvectors were used in the simulations for the positive and negative directions, this degeneracy of eigenvectors can explain the unexpected directions of the SP transition shown in Fig. 10.10.

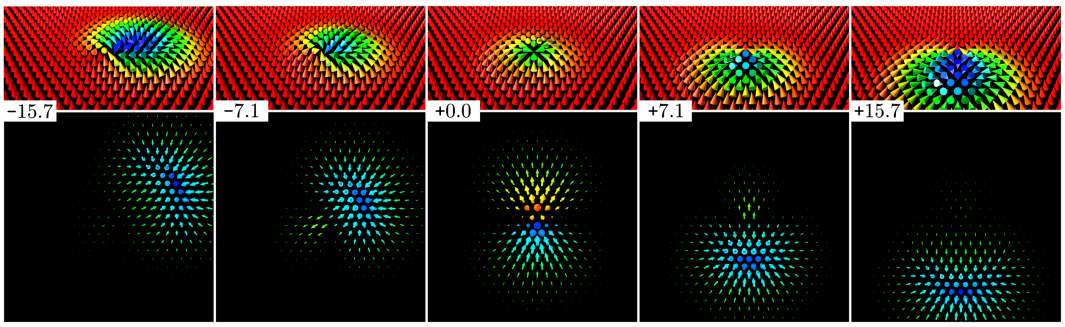

Figure 10.10 | Magnetic structures and eigenvectors obtained by following the third eigenmode of the radial symmetric saddle point state. The top row shows the magnetic structures of the radial saddle point of a skyrmion collapse in fcc-Pd/Fe/Ir(111) at $B_\perp = 4.0$ T from a tilted perspective, obtained by mode following for different values of the displacement, q_p. In the corners, the corresponding, rounded values of q_p are displayed. The bottom row shows the respective eigenvectors in a top view. The size of the arrows scales with the size of the individual vectors. The colour codes of both rows correspond to the out-of-plane component of the arrows and cones, respectively.

The chimera states found along the second and third eigenmodes of the radial SP occur as local energy minima of the energy curves of Fig. 10.7. The four chimera SP states exhibit a similar energy of 3.5 meV with respect to the radial SP, which is in excellent agreement with the difference in energy barrier between the two collapse mechanisms displayed in Fig. 8.3.

Furthermore, the energy curves of the second and third eigenmodes in Fig. 10.11 show, that the local energy minima of the chimera SPs are very shallow, which is consistent with the observation, that the chimera SP only appears for magnetic fields up to $B_\perp = 4.15$ T (see Fig. 8.3).

The energy barriers separating both SP states, which can be extracted from the energy curves in Fig. 10.11, do not necessarily correspond to the energy barriers of a MEP between these two states. However, one can interpret these energy barriers as an upper limit for the real barriers. Thus, it can be speculated, that the disappearance of the chimera transition for fields higher than $B_\perp = 4.15$ T corresponds to a disappearing energy barrier between the two states, which causes the geodesic nudged elastic band (GNEB) calculation to relax an initial chimera transition into a radial symmetric collapse mechanism.

Moreover, the harmonic approximations of the modes two and three only agree with the energy curves obtained by mode following for low excitation energies of a few

meV. For larger energies, however, the harmonic approximation does not hold and requires a more sophisticated treatment to determine the contributions of the states along these modes. This demonstrates a more general challenge for the accurate calculation of the prefactor.

As discussed earlier in this chapter, skyrmion, magnon and the other SP eigenmodes are modelled in either harmonic or Goldstone mode approximation with sufficient accuracy. However, when the energy difference between two states such as the two SP states vanishes, the intermediate energy landscape can become exceptionally flat, as it is the case for the second and third radial SP modes discussed here.

Such a flat energy landscape is typically accompanied by a decrease of the corresponding eigenvalues, i. e. mode softening, as it is observed for the chimera and the radial symmetric collapse mechanisms. For example, in Fig. 8.8, the chimera collapse is only metastable up to $B_\perp \approx 4.15$ T. The closer the magnetic field is to this point, the more the corresponding eigenvalue of the spectrum decreases (see e. g.. Fig. 8.8) and the resulting prefactor diverges. Such an asymptotic behaviour of the prefactor is typical for a transition between two metastable or SP states.

As the quality of the harmonic approximation rapidly decreases in the vicinity of such a transition point, the prefactors around these points are difficult to determine. The application of the mode following method in order to numerically calculate the contributions of these modes seems promising, but requires further development.

10.4. Chimera saddle point eigenmodes

For the SP of the chimera collapse mechanism, the energy variations obtained via mode following are displayed in Fig. 10.11. Again, the first mode has a negative curvature as it corresponds to the unstable mode of the transition. Similar to the case of the radial symmetric SP, the energy curve is well described by the parabola of the harmonic approximation for small displacements.

Displacements along the second eigenmode, on the other hand, yield a constant energy and thus, cannot be described in harmonic approximation. This mode corresponds to a rotation of the chimera SP and is discussed in Sec. 10.4.1 in more detail.

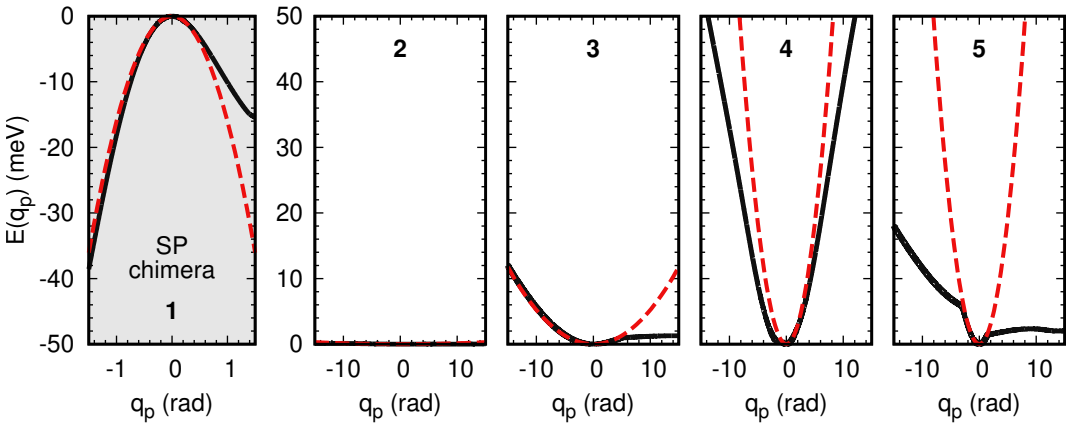

Figure 10.11 | Energy along the lowest five eigenmodes of the saddle point of the chimera skyrmion collapse mechanism calculated via mode following. The energy is displayed relative to the energy of the chimera saddle point in fcc-Pd/Fe/Ir(111) at $B_\perp = 4.0$ T. The displacement in the direction of an eigenvector is given by the coordinate q_p, where the negative sign corresponds to the direction of the inverted eigenvector. For comparison, the corresponding energies in harmonic approximation, calculated via Eq. 10.1, are shown as red dotted lines.

Similar to the second and third eigenmode of the radial symmetric SP, the third mode of the chimera SP seems to transform the magnetic structure towards the radial SP state. The results of the short interval of successful mode following are shown in Fig. 10.12. For this transition, however, no reliable mode following simulation has been obtained for the duration of a full transformation, as the mode tracking routine starts to follow a rotation mode around $q_p \approx 4$ rad, visible as a kink in the energy curve of Fig. 10.11.

In contrast to the two degenerated eigenvectors (2,3) found for the radial SP, only the third eigenmode of the chimera SP connects the chimera with the radial symmetric transition mechanism. This can be explained by the lower symmetry of the chimera SP compared to the radial symmetric SP, which allows for less degenerate displacements towards the radial SP.

The fourth and fifth eigenmodes again cause problems with the mode tracking algorithm which follows other eigenmodes early on and therefore does not provide solid information about the energy landscape of the eigenmodes that were intended to be followed. One can speculate, that the mode tracking is difficult for more complex magnetic structures such as the chimera SP state, which yield more complex and less distinct eigenvectors. Nevertheless, the energy curves obtained in the small interval

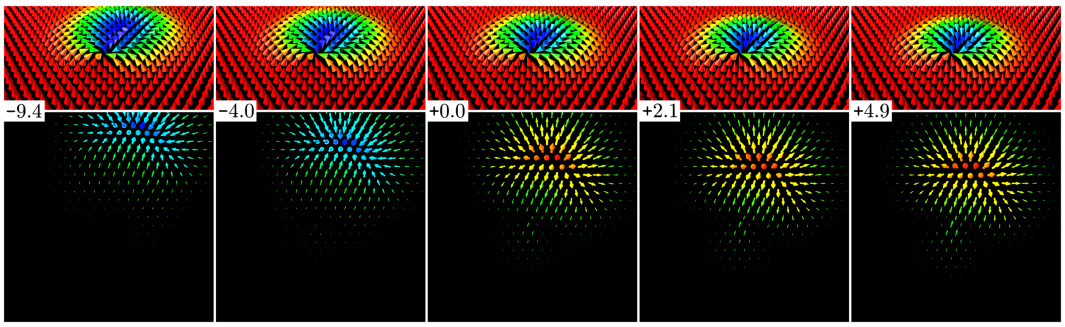

Figure 10.12 | Magnetic structures and eigenvectors obtained by following the third eigenmode of the chimera saddle point state. The top row shows the magnetic structures of the chimera saddle point of a skyrmion collapse in fcc-Pd/Fe/Ir(111) at $B_\perp = 4.0\,\mathrm{T}$ from a tilted perspective, obtained by mode following for different values of the displacement, q_p. In the corners, the corresponding, rounded values of q_p are displayed. The bottom row shows the respective eigenvectors in a top view. The size of the arrows scales with the size of the individual vectors. The colour codes of both rows correspond to the out-of-plane component of the arrows and cones, respectively.

of successful mode following close to the chimera SP state suggest, that all chimera eigenmodes but the second and third can be described in harmonic approximation.

10.4.1. Rotation of the chimera saddle point state

Performing a long mode following simulation of the second eigenmode of the chimera SP state in both directions yields the small energy variation displayed in Fig. 10.13. The energy is periodic under displacement along q_p, but has a more complex form than a simple sine or cosine function.

In addition to the periodic behaviour, a slight energy increase occurs with rising values of $|q_p|$, visible at the energy minima in Fig. 10.13, which increasingly rise above the zero line. This is most likely due to an accumulation of numerical errors during the exceptionally long simulation.

The displacement in positive and negative directions of the second eigenmode equals a clockwise and counterclockwise rotation of the chimera SP around the Bloch-like point, respectively. This is demonstrated in Fig. 10.14, in which the corresponding magnetic structures and eigenvectors are displayed for selected values of q_p.

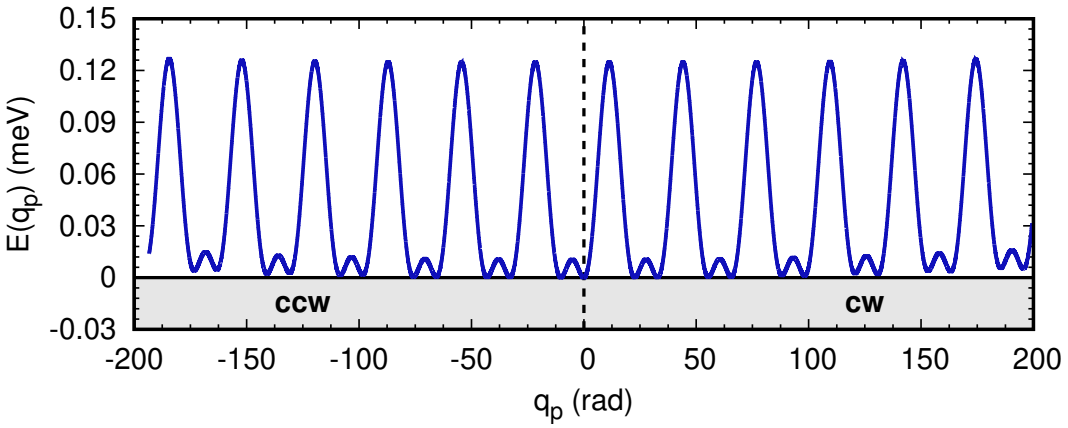

Figure 10.13 | Energy along the second eigenmode of the chimera saddle point state calculated via mode following. The energy is displayed relative to the energy of the chimera saddle point state of fcc-Pd/Fe/-Ir(111) at $B_\perp = 4.0$ T. The displacement in the direction of an eigenvector is given by the coordinate q_p, where the positive and negative signs correspond to the clockwise and counterclockwise rotation of the chimera saddle point state, respectively.

At the energy minima, the central line of the magnetic structure of the chimera SP state points in the direction of a next nearest neighbour. This magnetic structure has a 6-fold rotation symmetry and therefore, occurs two times during a rotation of 120°, which corresponds to one complete period of the numerically obtained energy over q_p.

The local energy maxima of the rotation occur, when the central line of the chimera SP state points towards a second nearest neighbour. In contrast to the energy minima, the maxima are of different magnitude which stems from opposite rotational senses of the magnetic moments at the Bloch-like point. In Fig. 10.14 a, the two moments with a 120° angle at the end of the central line are pointing downwards at $q_p = 11.0$ rad, while a similar magnetic structure at $q_p = 28.0$ rad occurs with the corresponding moments pointing upwards. This results in opposite contributions of the Dzyaloshinskii-Moriya interaction (DMI), lifting the degeneracy between these states.

The application of the mode following method to the second chimera SP eigenmode has made it possible to understand the character of this mode, which would otherwise have remained hidden. In addition, the magnitude of the energy variation could be determined to be 0.12 meV, allowing it to be calculated for temperatures beyond a few K using a Goldstone approximation.

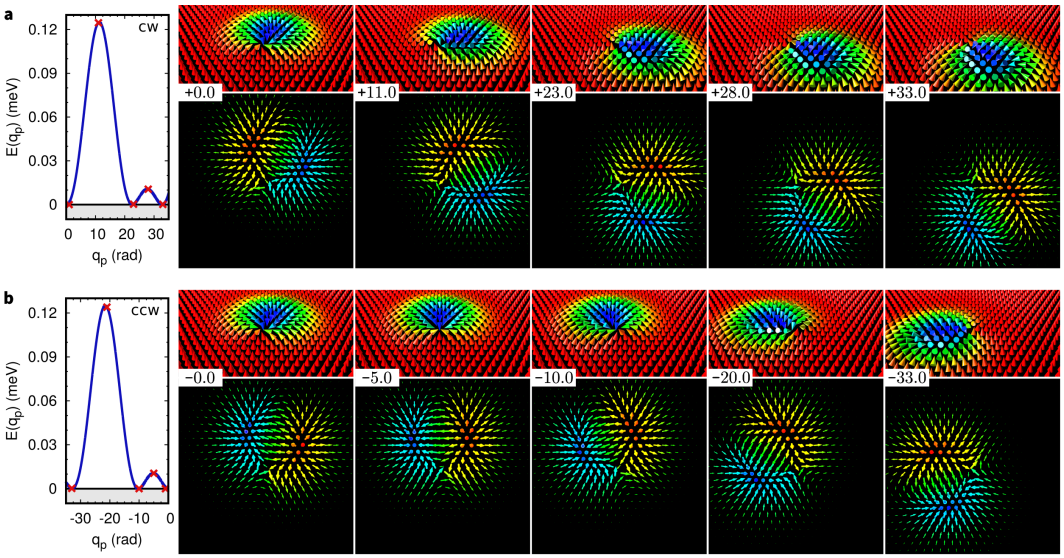

Figure 10.14 | Magnetic structures and eigenvectors by following the second eigenmode of the chimera saddle point state in clockwise and counterclockwise direction. a) The top row of **(a)** shows the magnetic structures of the chimera saddle point state in fcc-Pd/Fe/Ir(111) at $B_\perp = 4.0$ T from a tilted perspective, obtained by mode following for different values of the displacement, q_p. On the left, the dispersion of the energy relative to the saddle point energy is displayed over q_p. The points marked by red crosses correspond to the shown magnetic structures whose values of q_p are displayed in the corners. The bottom row of **(a)** shows the respective eigenvectors in a top view. The size of the arrows scales with the size of the individual vectors. The colour codes of both rows correspond to the out-of-plane component of the arrows and cones, respectively. **b)** Same as in **(a)**, but for counterclockwise rotation.

By applying the mode following to the rotation eigenmode of chimera SP state, the prefactor of the chimera transition can be determined. In Fig. 10.15, the prefactors of both the radial symmetric and the chimera transition mechanism are shown for an applied field of $B_\perp = 4.0$ T and as a function of temperature. The chimera transition has an increased prefactor due to a larger number of low energy eigenmodes at the SP state and the larger number of positions to create a Bloch-like point, which manifests itself in the additional Goldstone eigenmode treated with mode following. In the low temperature range up to 50 K, the difference in the prefactor is about one order of magnitude.

Additionally, the prefactor of the chimera mechanism has a smaller slope than the radial collapse due to an unequal number of Goldstone modes. In case of the radial collapse, the two translation eigenmodes of the initial skyrmion state lead to an explicit temperature dependence of the prefactor proportional to T.

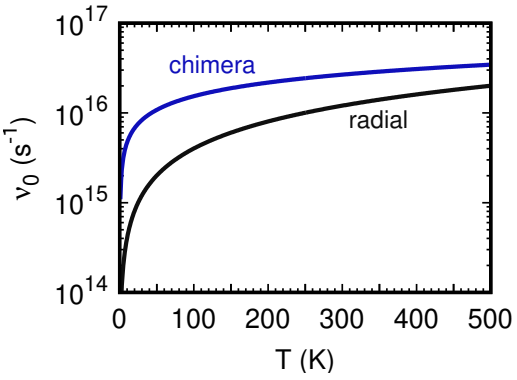

Figure 10.15 | The prefactors of skyrmion annihilation via the radial symmetric and chimera transition mechanism for different temperatures. The prefactors of skyrmion annihilation in fcc-Pd/Fe/Ir(111) at $B_\perp = 4.0$ T and without in-plane magnetic field have been calculated via transition state theory. For the chimera transition mechanism, the entropy contribution of the second saddle point mode has been determined numerically via mode following. Note, that the prefactor of the radial symmetric collapse has been multiplied with the usual factor of two for two saddle points per unit cell.

For the chimera transition, on the other hand, one of these skyrmion Goldstone modes is counterbalanced by the additional Goldstone mode of the chimera SP, yielding a temperature dependence proportional to $\sqrt{T}$. Note that the prefactors of Fig. 10.15 are shown on a logarithmic scale, which makes the different dependencies on temperature less obvious.

10.4.2. The intermediate regime

While the second chimera SP mode can be modelled as a Goldstone mode for most temperatures, the situation gradually changes with increasing in-plane magnetic field, $B_\parallel$. In Fig. 10.16, the energy variation along q_p is displayed for three different values of $B_\parallel$. For comparison, a section of the data already presented in Fig. 10.13 is shown on a different scale in Fig. 10.16 a. The small fluctuations of the energy are solely due to the discrete lattice.

With increasing $B_\parallel$, however, the alignment of the whole chimera SP structure to the in-plane field is increasingly relevant, and thus, the 6-fold rotational symmetry of the chimera SP state is lifted. As displayed in Fig. 10.16 b, an alignment opposite to a field of $B_\parallel = 0.1$ T already results in energy costs of about 1.7 meV, which is more than an order of magnitude larger than the lattice effects evaluated in the previous section. However, the cosine shape of the in-plane Zeeman contribution is noticeably deformed by the lattice effects.

For $B_\parallel = 0.2$ T, the in-plane Zeeman contribution doubles and the energy increasingly resembles the absolute value of a cosine function in both directions. Each period of

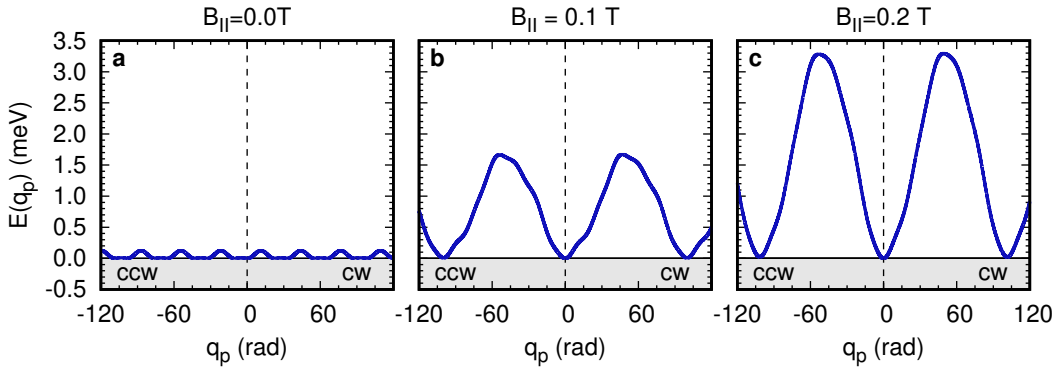

Figure 10.16 | Energy along the second eigenmode of the chimera saddle point state with varying strength of in-plane magnetic field. The energy is displayed relative to the energy of the chimera saddle point state of fcc-Pd/Fe/Ir(111) at $B_\perp = 4.0$ T. Additionally, different values of $B_\parallel$ are applied. The displacement in the direction of an eigenvector is given by the coordinate q_p, where the positive and negative signs correspond to the clockwise and counterclockwise rotation of the chimera saddle point state, respectively.

the energy corresponds to a full rotation of the chimera SP state. At low energies the system is not able to escape the local energy minima, and the second eigenmode corresponds to an oscillation of the orientation of the chimera state around its equilibrium orientation.

These results already show that the in-plane magnetic field can induce a transition from a Goldstone mode to a harmonic vibration mode for the rotational mode. Of course the decision for an adequate model for this mode depends on the temperature. For this reason Fig. 10.17 shows the values of the integral Φ_p along this mode over temperature, obtained by the two approximations and by the numerical mode following method.

In Goldstone approximation, the value of the integral is temperature independent and forms a constant line in Fig. 10.17. Its value is evaluated via the displacement in configuration space over one complete rotation of the magnetic structure, numerically determined by mode following. With a value of ~ 100 rad, it is much larger than the Goldstone mode volume per unit cell of the skyrmion translation presented in Eq. 10.4 and Eq. 10.5.

In contrast, the value of the integral in harmonic approximation is calculated via Eq. 10.2. Starting from zero, it increases with $\sqrt{T}$ up to ~ 160 rad for a temperature of 500 K, crossing the Goldstone mode volume at ~ 200 K. This behaviour cannot be

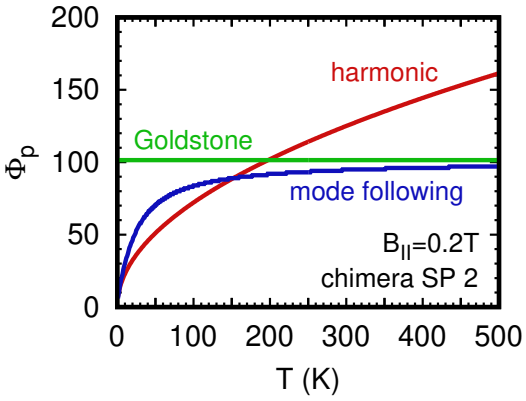

Figure 10.17 | Value of the integral over the second eigenmode of the chimera saddle point state obtained by different methods. The integral Φ_p of the chimera saddle point state in fcc-Pd/Fe/Ir(111) at $B_\perp = 4.0$ T and $B_\parallel = 0.2$ T is obtained in Goldstone approximation (green line), harmonic approximation (red line) and numerically via mode following (blue line) for different temperatures. The constant value of the Goldstone volume is determined by mode following as the geodesic distance of a full rotation of the chimera saddle point state. The value of the harmonic approximation is obtained via Eq. 10.1.

physically sound, since the Goldstone approximation assumes a Boltzmann-factor of unity and integrates of all valid values of q_p. Thus it forms an upper limit to the value of Φ_p.

While it is clear, that the harmonic approximation is suited best for low temperatures and that the Goldstone approximation is the upper limit for high temperatures, there is an intermediate regime in which none of the two approximation can be applied properly. By applying the mode following method and numerically calculate the value of Φ_p, this regime can now be investigated.

For very low temperatures, the numerically obtained value coincides with the value of the harmonic approximation. In this regime, the second eigenmode of the chimera SP state is a vibration mode, in which the orientation of the central line oscillates around the direction of $B_\parallel$. For high temperatures, the numerical result converges to the Goldstone mode volume, which is consistent with the expectation of small energy variations becoming increasingly negligible with rising temperatures.

At intermediate temperatures of around 10 to 200 K, which coincide with the temperature range investigated throughout this thesis, the numerical result noticeably deviates from, both, the harmonic and the Goldstone mode approximation. At low temperatures, it increases faster than the harmonic approximation which underestimates the occupation probability away from the expansion point, the initial chimera SP state. The resulting value is in between both approximations, until it crosses the value of the harmonic approximation which now increasingly overestimates the volume of the integration.

For the investigated example of an isolated skyrmion in fcc-Pd/Fe/Ir(111) at $B_\perp = 4.0$ T with an additional in-plane magnetic field of $B_\parallel = 0.2$ T, the deviation between the numerical result and the harmonic approximation of about a factor of two, depending on the assumed temperature. While this only slightly affects the skyrmion collapse rates presented in Chap. 9, this result demonstrates that going beyond the harmonic approximation is necessary for particular eigenmodes.

The occurrence of intermediate modes increases with the complexity of the energy landscapes, e. g. due to exchange frustration, higher order exchange interactions and multilayer exchange coupling. In this chapter it has been demonstrated, that the application of the mode following method is a promising solution to the presented issues and that a numerical calculation of eigenmodes beyond harmonic approximation is feasible.

11. Conclusion

In this thesis a detailed understanding of transition processes of magnetic skyrmions and the effects involved could be obtained. The magnetism of ultrathin film systems is described by a theoretical multiscale approach consisting of magnetic interaction parameters obtained by density functional theory (DFT) calculations applied to atomistic spin simulations. The investigations presented in this work have been performed for skyrmions in the well-established model system Pd/Fe/Ir(111) which allows a clear distinction of the examined effects.

It has been demonstrated that an effective nearest neighbour approximation of exchange interaction, as it is typically assumed in micromagnetic models, cannot adequately describe skyrmion transition processes in ultrathin transition metal films due to the inherent long-range exchange interaction in itinerant magnets. While such a model correctly depicts properties of skyrmions in equilibrium configuration, it fails to determine the energies of highly excited states that occur during skyrmion creation and annihilation.

In the applied multiscale approach, the effect of exchange frustration is captured by fitting the parameters of an extended Heisenberg model to spin spiral dispersions obtained by DFT. Subsequent geodesic nudged elastic band (GNEB) method calculations yield the minimum energy paths (MEPs) and energy barriers of the radial symmetric skyrmion annihilation process. A comparison of different models of exchange interaction reveals an enhancement of the energy barrier by about a factor of two due to exchange frustration, which has a decisive effect on skyrmion stability. A similar effect has been found for antiskyrmions, which could only be metastabilised in the presence of exchange frustration.

However, the results of this work also show that, contrary to common belief, the energy barrier alone is not a sufficient criterion for the stability of magnetic skyrmions. By applying transition state theory (TST) in harmonic approximation, the prefactor

of the Arrhenius-law describing average lifetimes of metastable skyrmions in Pd/Fe/-Ir(111) and Pd/Fe/Rh(111) have been calculated. Large entropic effects have been found to vary skyrmion lifetimes in hcp-Pd/Fe/Ir(111) by seven orders of magnitude with the strength of the external magnetic field, even exceeding the effect of the energy barrier.

The origin of this effect could be traced back to a small number of low-energy skyrmion eigenmodes which strongly depend on the skyrmion size and thus the external magnetic field. These skyrmion eigenmodes also depend on the system parameters, which opens a novel route towards room temperature of sub-10 nm skyrmions beyond the usual optimisation of the energy barrier, which is further elaborated in Ref. [XII]. With the presented methods, the lifetimes of metastable skyrmions in Pd/Fe/Ir(111) and Pd/Fe/Rh(111) [II] are predicted over a wide range of external magnetic fields and temperatures.

In the course of this study, the chimera mechanism of skyrmion creation and annihilation has been discovered and predicted to occur in exchange frustrated ultrathin films [VII]. Details of this novel transition mechanism and its dependence on system parameters and the external magnetic field were discussed in comparison to the radial symmetric collapse mechanism.

In a cooperation with the group of Prof. Markus Morgenstern, first experimental evidence for both the radial symmetric and the chimera skyrmion collapse was found. By comparing the measured transition rate maps with the energy density maps of the transition state obtained by the theoretical multiscale approach, both mechanisms could be identified.

In addition, both experimentally and theoretically, a transition from the radial symmetric to the chimera skyrmion collapse mechanism with increasing in-plane magnetic field was observed. Finally, the ability of the multiscale approach to calculate the average skyrmion lifetime using TST was demonstrated by a sound agreement between measured and calculated transition rates.

However, the quality of the harmonic and Goldstone mode approximations typically used in TST to calculate the prefactor of transition processes is generally unknown, and they even fail for some cases such as antiskyrmion collapse or transitions via the chimera mechanism. As a solution to these problems, the mode following method was developed in this thesis. It allows for the numerical determination of the energy

along individual eigenmodes and their contribution to the prefactor without the application of further approximations. This also provides access to an intermediate temperature regime in which prefactors could not be calculated previously. With this method, the prefactor of the chimera transition mechanism could be calculated, showing an increased entropy of the saddle point (SP) state in comparison to the radial symmetric collapse mechanism due to an additional rotational symmetry.

The detailed analysis of skyrmion transition processes and the tools provided in this thesis can be used to find new skyrmion-hosting materials and mechanisms to improve skyrmion stability. The entropic stabilisation of skyrmions appears as a promising method to overcome the limited thermal stability of sub-10 nm skyrmions [XII, 23]. Furthermore, the multiscale approach can be applied in order to study magnetic multilayer systems [XV, 23, 190] or skyrmion-hosting antiferromagnetic materials [170].

The improvements of the magnetic model are not restricted to the adequate description of exchange frustration discussed in this thesis. Recently, it could be shown that higher-order exchange interactions (HOIs) can play a decisive role for the stabilisation of magnetic skyrmions as they especially affect the energy of excited SP states [X]. The usage of non-chiral interactions such as exchange frustration and HOIs may also be a route towards metastable antiskyrmions coexisting with skyrmions in ultrathin films [VII, XIV].

The mode following method is a promising tool for the evaluation of approximations used in classical TST in general. Especially the increasing complexity of energy landscapes and magnetic states encountered in skyrmion research demands for the accurate description of low-energy eigenmodes that becomes feasible by the mode following method.

A. Appendix

A.1. Computational details

All simulations presented in this work have been performed with the Kieler atomistic spin simulations code. The hexagonal atomic lattices of Pd/Fe/Ir(111) and Pd/Fe/-Rh(111) are spanned by two lattice vectors with a 120° angle, resulting in a diamond shaped simulation box. Most calculations have been performed in simulation boxes consisting of 70×70 magnetic moments along the lattice vectors with the following exceptions: In Chap. 6, 100×100 magnetic moments have been assumed, while the calculations presented in Chap. 10 used a simulation box of 50×50 magnetic moments. In addition, periodic boundary conditions were applied for all simulations, which lead to magnetic moments interacting with each other beyond the edges of the simulation box suppressing edge effects.

A.1.1. Spin dynamics simulations

For all spin dynamics simulations, the Landau-Lifshitz equation has been solved numerically via the semi-implicit solver B (SIB) of Mentink *et al.* [129] without considered temperature effects. Since in this thesis spin dynamics simulations were only used for the energetic relaxation of magnetic structures and no time resolution of the dynamics was investigated, a damping parameter of $\lambda = 0.1$ and a time step of $\Delta t = 0.1$ fs was chosen for most simulations. For the energetic relaxation, 10^6 time steps were usually carried out.

In Chap. 10, damping parameters of $\lambda \in [0.5, 1.0]$ were used for a fast relaxation. In Chap. 6, different values of $\lambda \in [0.05, 0.5]$ and $\Delta t \in [0.05, 0.1]$ have been applied for simulations carried out over $10^6 - 5 \cdot 10^6$ time steps. For the simulations presented

in Fig. 8.6 and 8.7, the energetic relaxation has been performed only with a vpo minimisation algorithm and no spin dynamics simulations have been performed.

For most spin dynamics simulations, pre-relaxed magnetic structures from other simulations have been used as initial magnetic structure. When the energy barriers between metastable states become too small, however, the relaxation of a metastable state such as isolated skyrmions in the FM phase has to be carried out more carefully. This issue occurs e. g. for the relaxation of isolated skyrmion whose energies are presented in Fig. 6.4, where they are relaxed over a large interval of a control parameter. In order to prevent magnetic structures from collapsing due to numerical errors, the control parameter can be varied successively in small steps with intermediate relaxation of the magnetic structures.

A.1.2. GNEB simulations

Prior to each GNEB or CI-GNEB calculation, the initial and final state of the path is energetically relaxed further by a build-in vpo method. Subsequently, either the geodesic path between both states is created as initial state, or a predefined initial path is provided as an input for the simulation. Each path presented in this work consists of 30 images. Since the algorithm follows the path into a local energy minimum, the choice of the initial path can affect the result of the calculation. In order to prevent the relaxation to be stuck in perfectly symmetric but unstable states due to the choice of the initial path, small random fluctuations on the order of $10^{-3} - 10^{-4}$ of the components of the normed magnetic moments are applied in some cases to the images of the initial path.

Typically, a simulation has been considered converged when the largest force of a lattice site is smaller than 10^{-6} or 10^{-8} eV/rad for GNEB and CI-GNEB calculations, respectively. For the simulations of Chap. 6, a converge criterion of 10^{-8} has been applied for both GNEB and CI-GNEB, while in Chap. 7, a value of 10^{-5} has been used for the GNEB.

The GNEB and CI-GNEB calculations can either be performed independently from each other or the CI-GNEB can be carried out directly after the GNEB calculation. All results from minimum energy path calculations presented in this work are performed first with the GNEB method and subsequent with CI-GNEB, except

the calculations presented in Fig. 5.8, which show the geodesic path and the path obtained by GNEB only.

Similar to the successive relaxation of magnetic states in spin dynamics simulations, minimum energy paths of previous GNEB or CI-GNEB calculations can be used as initial paths for the next interval of a varied control parameter. This procedure has been used in order to obtain relaxed minimum energy paths of both the radial symmetric and the chimera skyrmion collapse simultaneously for the same external magnetic fields.

In most GNEB and CI-GNEB calculations, a hybrid measure of distance has been applied with the spring constants of $\kappa_{\text{geo}} = 10^{-4}$ and $\kappa_{\text{en}} = 1.0$. For numerical stability, the total spring force has also been multiplied by an additional spring constant of $\kappa = 10^{-2}$. The calculations of Chap. 6 and 7 used a geodesic measure of distance with the overall spring constant of $\kappa = 0.5$. In Fig. 5.9, different measures of distance have been used as described in the caption.

A.1.3. TST simulations

For all transition state theory calculations of skyrmion annihilation performed in this work, the lowest two skyrmion eigenmodes have been treated as translational modes in Goldstone mode approximation. Any other eigenmode is treated in harmonic approximation, unless something else is explicitly stated.

A.1.4. Mode following simulations

In order to run mode following calculations in both directions of an eigenmode, first the eigenvector of the eigenmode is determined by an initial diagonalisation of the Hessian matrix. Then two mode following calculations are performed, one of which uses the eigenvector previously determined as input for the mode tracker. For the other calculation, each 3D component of the input eigenvector is inverted, effectively ensuring that the mode tracker follows the eigenmode in the opposite direction.

A.2. Definition of functions

The function $\arctan 2(x, y)$ is defined as [94]

$$\arctan 2(x,y) = \begin{cases} \arctan \frac{y}{x}, & \text{if } x > 0 \\ \arctan \frac{y}{x} + \pi, & \text{if } y \geq 0, x < 0 \\ \arctan \frac{y}{x} - \pi, & \text{if } y < 0, x < 0 \\ \frac{+\pi}{2}, & \text{if } y > 0, x = 0 \\ \frac{-\pi}{2}, & \text{if } y < 0, x = 0 \\ \text{undefined}, & \text{if } y = 0, x = 0 \end{cases} \tag{A.1}$$

A.3. Used Software

The simulations were performed with the Kieler atomistic spin simulation code, which is implemented with Fortran. Data analysis, automation and general scripting were mainly done with Python and the Unix shell Bash. Figures, data plots and tables were mainly created with Gnuplot, Povray, Inkscape and Latex.

A.4. The Pd/Fe/Rh(111) systems

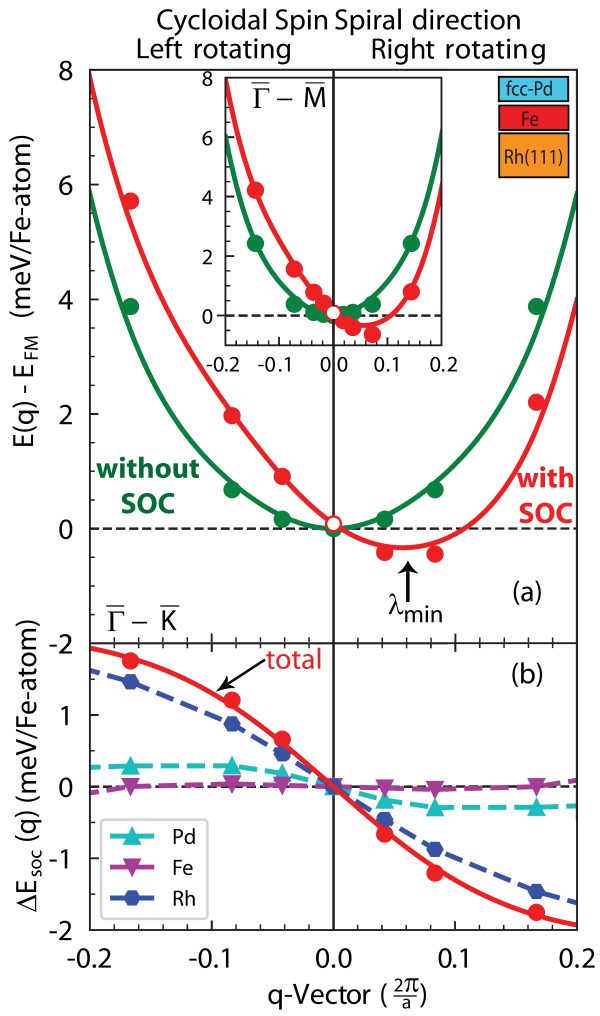

Figure A.1 | Spin spiral dispersion curve of fcc-Pd/Fe/Rh(111). a) The red and green points show the energy of spin spirals calculated with DFT as a function of $\mathbf{q}$ with and without spin-orbit coupling (SOC), respectively. For both rotational senses, the $\mathbf{q}$ vectors are chosen along the $\overline{\Gamma}\overline{\mathrm{K}}$ direction, while the inset shows the dispersion along the $\overline{\Gamma}\overline{\mathrm{M}}$ direction. The $\overline{\Gamma}$ and $\overline{\mathrm{K}}$ points correspond to the FM and Néel state, respectively. Energies are displayed relative to the FM state without SOC. **b)** The SOC energy contributions of the individual Pd, Fe and top Rh layers are shown relative to the energy of the $\overline{\Gamma}$ point in $\overline{\Gamma}\overline{\mathrm{K}}$ direction. Figure published in [II].

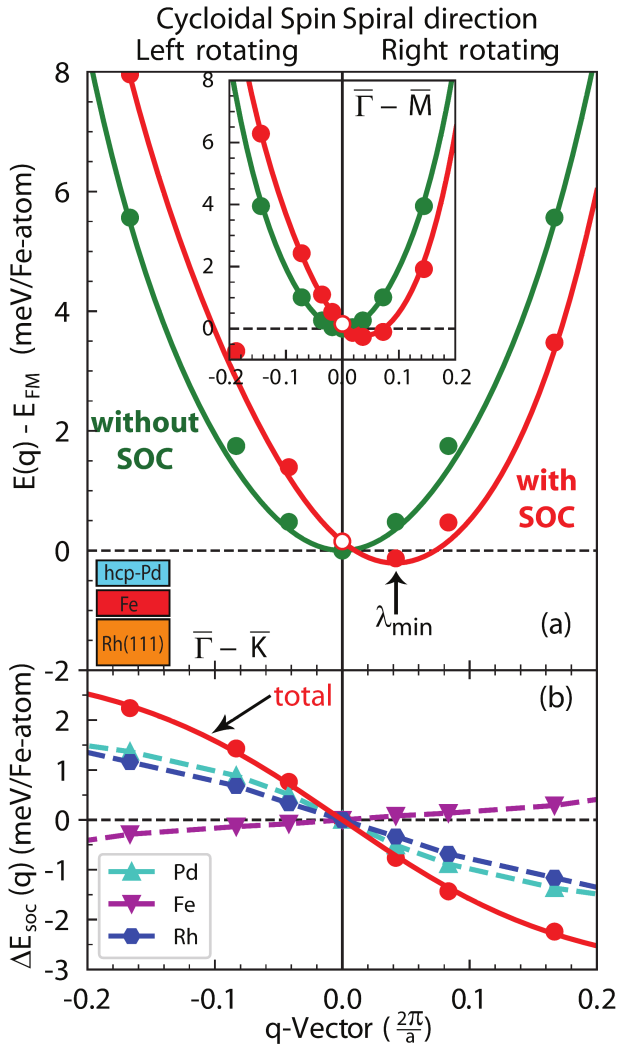

Figure A.2 | Spin spiral dispersion curve of hcp-Pd/Fe/Rh(111). a) The red and green points show the energy of spin spirals calculated with DFT as a function of $\mathbf{q}$ with and without spin-orbit coupling (SOC), respectively. For both rotational senses, the $\mathbf{q}$ vectors are chosen along the $\overline{\Gamma}\overline{\mathrm{K}}$ direction, while the inset shows the dispersion along the $\overline{\Gamma}\overline{\mathrm{M}}$ direction. The $\overline{\Gamma}$ and $\overline{\mathrm{K}}$ points correspond to the FM and Néel state, respectively. Energies are displayed relative to the FM state without SOC. **b)** The SOC energy contributions of the individual Pd, Fe and top Rh layers are shown relative to the energy of the $\overline{\Gamma}$ point in $\overline{\Gamma}\overline{\mathrm{K}}$ direction. Figure published in [II].

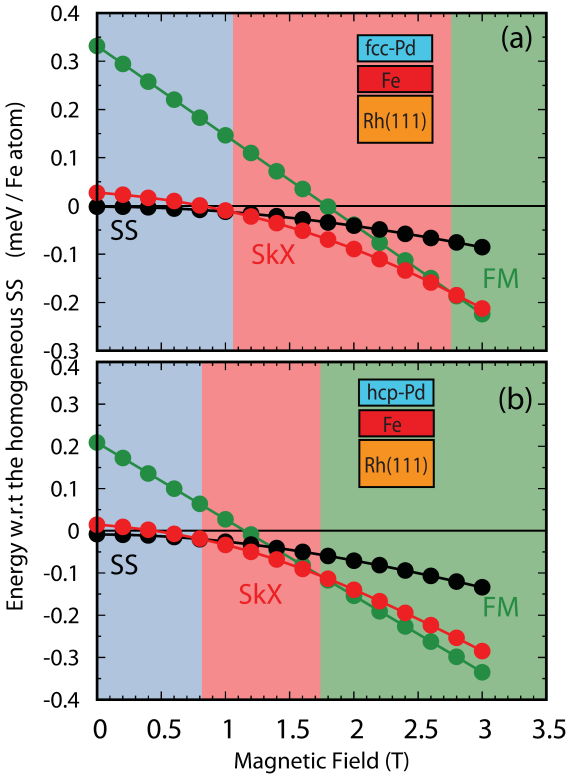

Figure A.3 | Zero temperature stability diagrams of Pd/Fe/Rh(111). The diagrams show the magnetic field dependent energy of magnetic states for Pd/Fe/Rh(111) with a fcc (**a**) and hcp (**b**) stacked Pd layer. The energies of the FM state (FM, green), relaxed spin spirals (SS, black) and skyrmion lattice state (SkX, red) are displayed relative to the energy of the homogeneous spin spiral (black line). Background colours indicate the ground state of the SS (blue), SkX (red) and FM state (green). Figure published in [II].

A.5. Skyrmion and antiskyrmion collapses

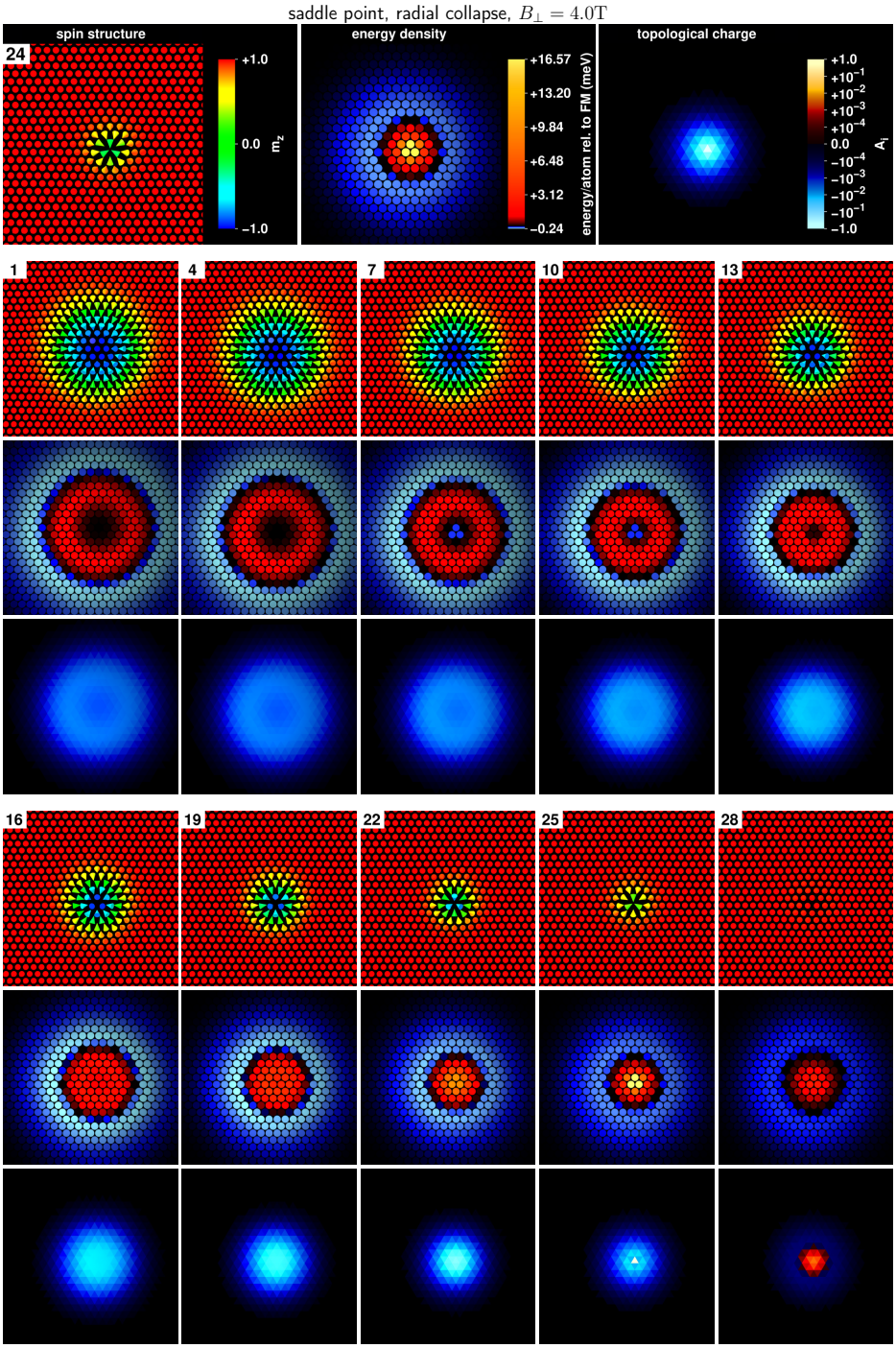

Figure A.4 | Sequence of the radial symmetric skyrmion collapse in fcc-Pd/Fe/Ir(111) calculated with J_{eff} parameters at $B = 4.0\,\mathrm{T}$. The magnetic structure, energy density map relative to the FM state, topological charge density map of the saddle point image and the corresponding colour codes are displayed at the top. The topological charge density is calculated per triangle of adjacent magnetic moments. Below, the same information is shown for every third image of the MEP whose indices are shown in the upper left corner.

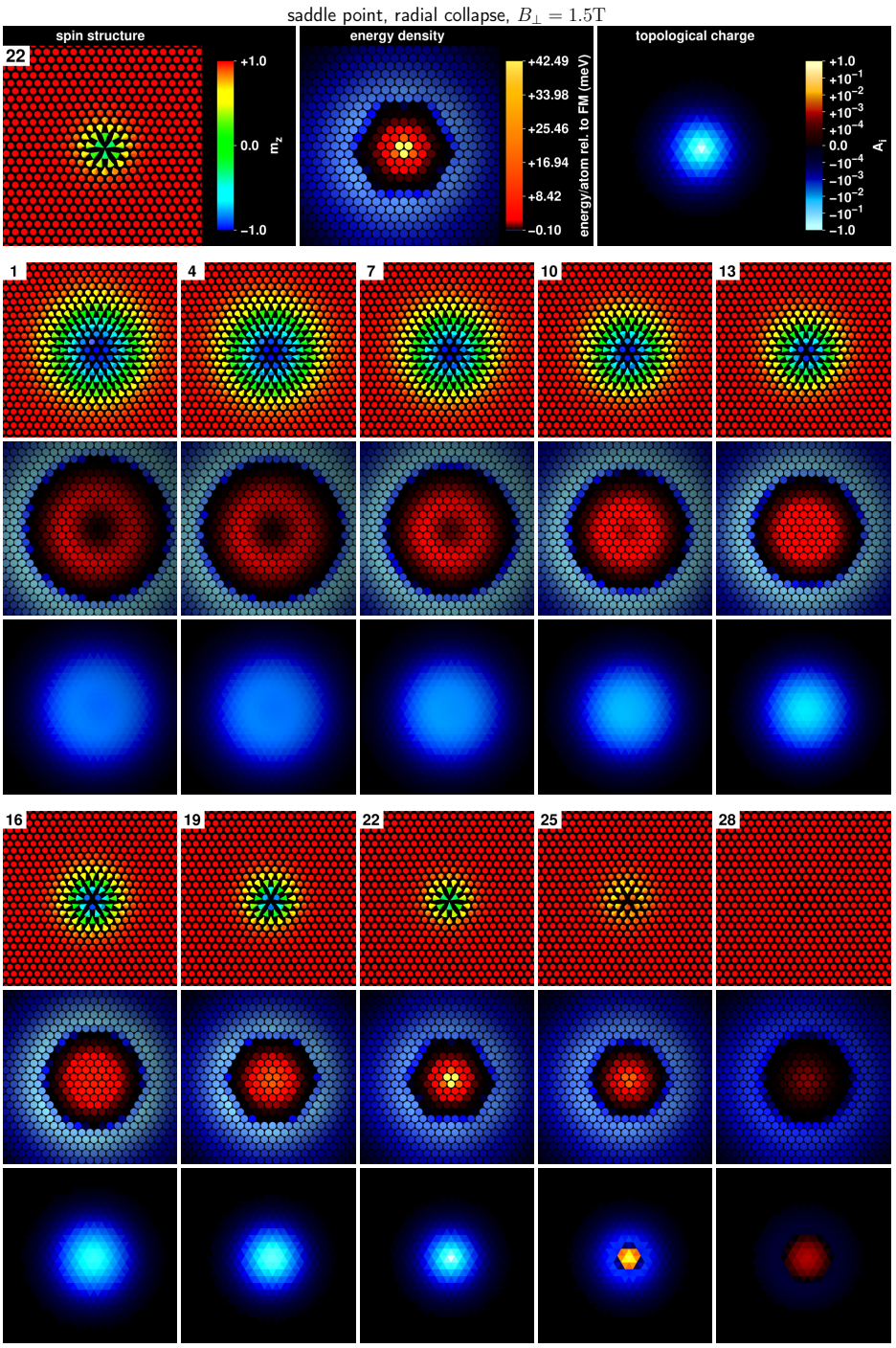

Figure A.5 | Sequence of the radial symmetric skyrmion collapse in hcp-Pd/Fe/Ir(111) calculated with J_{DFT} parameters at $B = 1.5\,\mathrm{T}$. The magnetic structure, energy density map relative to the FM state, topological charge density map of the saddle point image and the corresponding colour codes are displayed at the top. The topological charge density is calculated per triangle of adjacent magnetic moments. Below, the same information is shown for every third image of the MEP whose indices are shown in the upper left corner.

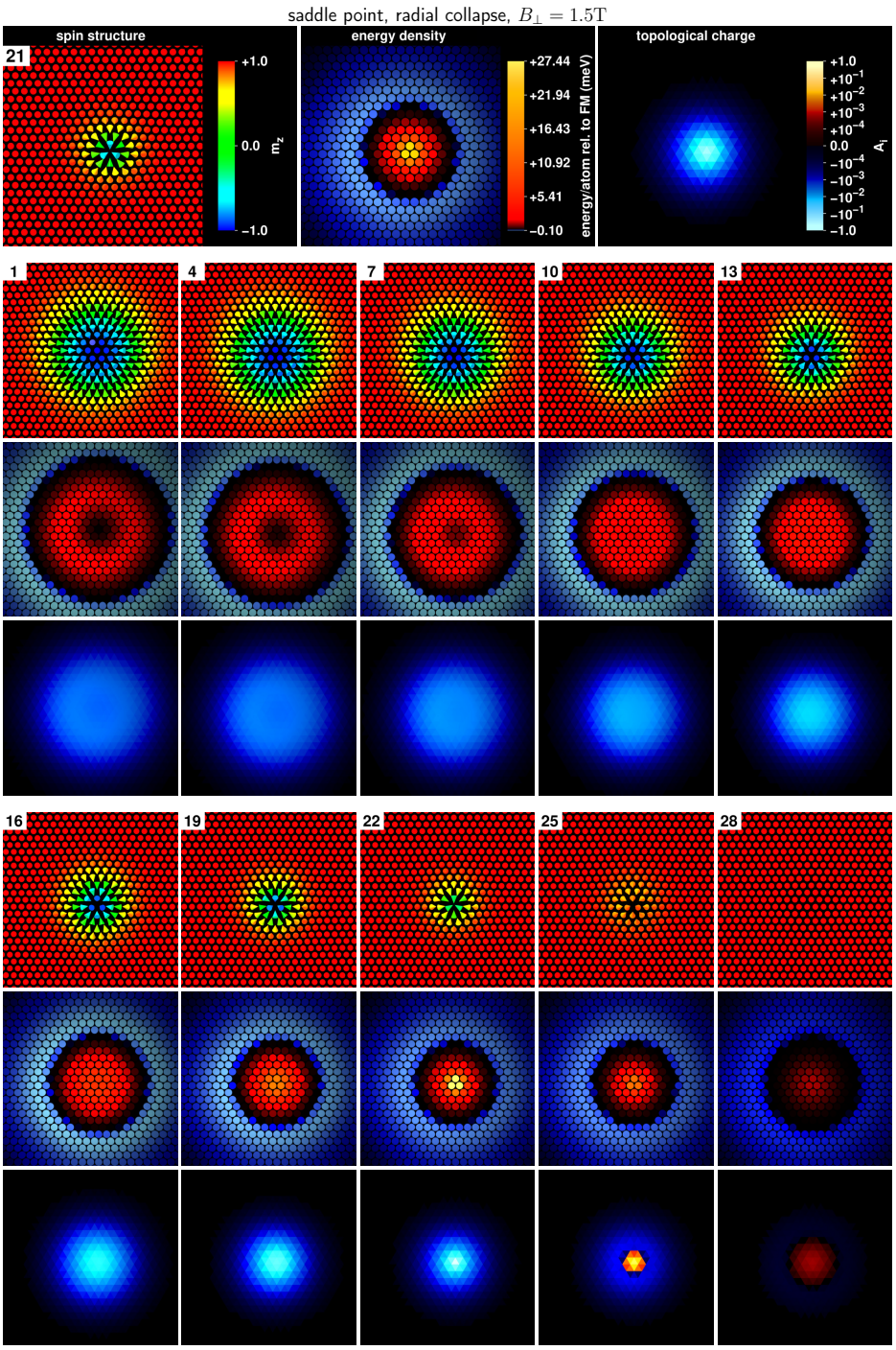

Figure A.6 | Sequence of the radial symmetric skyrmion collapse in hcp-Pd/Fe/Ir(111) calculated with J_{eff} parameters at $B = 1.5\,\mathrm{T}$. The magnetic structure, energy density map relative to the FM state, topological charge density map of the saddle point image and the corresponding colour codes are displayed at the top. The topological charge density is calculated per triangle of adjacent magnetic moments. Below, the same information is shown for every third image of the MEP whose indices are shown in the upper left corner.

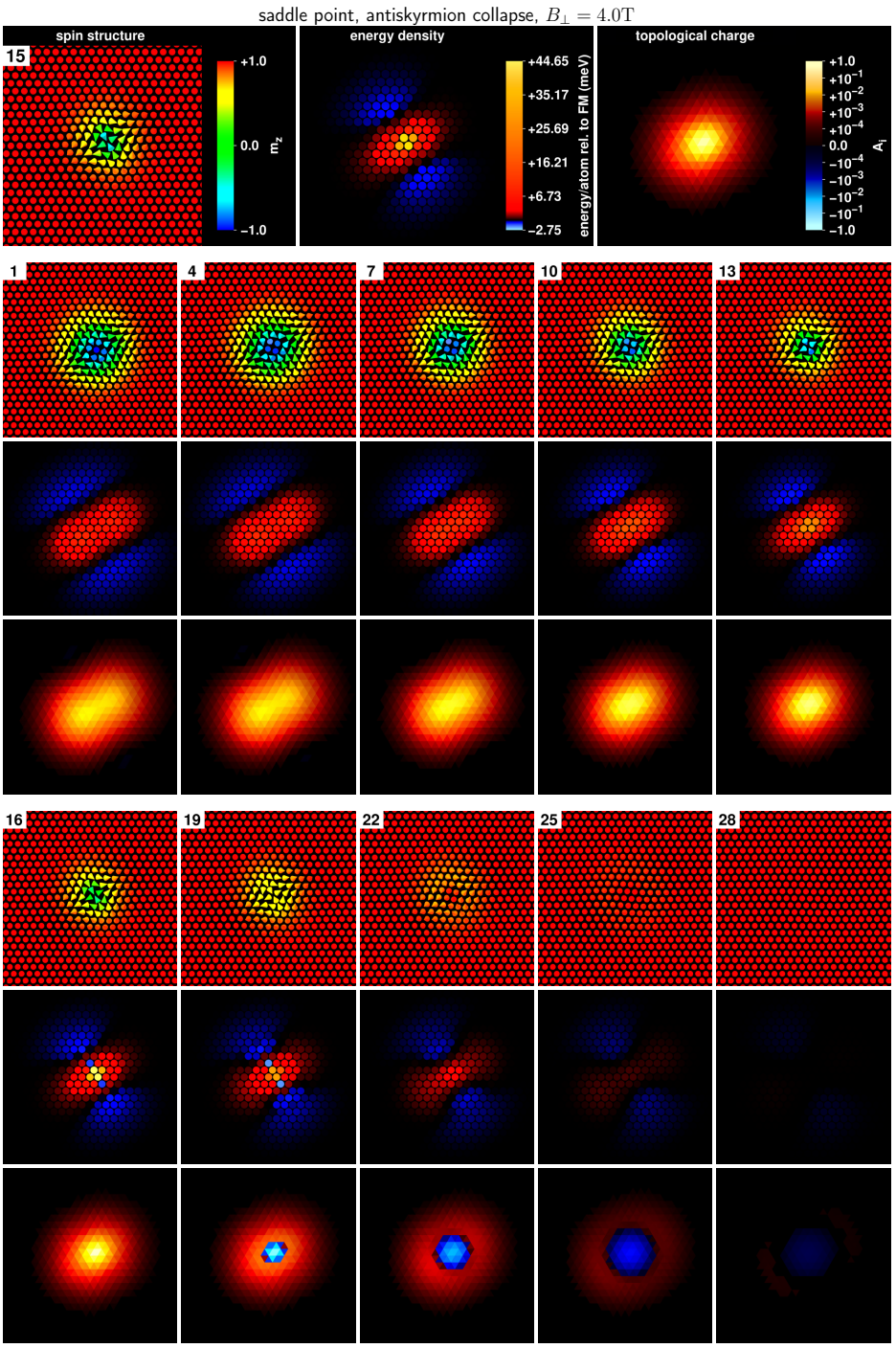

Figure A.7 | Sequence of the antiskyrmion collapse in fcc-Pd/Fe/Ir(111) calculated with J_{DFT} parameters at $B = 4.0\ \mathrm{T}$. The magnetic structure, energy density map relative to the FM state, topological charge density map of the saddle point image and the corresponding colour codes are displayed at the top. The topological charge density is calculated per triangle of adjacent magnetic moments. Below, the same information is shown for every third image of the MEP whose indices are shown in the upper left corner.

A.6. Eigenvectors of radial skyrmion collapse in Pd/Fe/Ir(111)

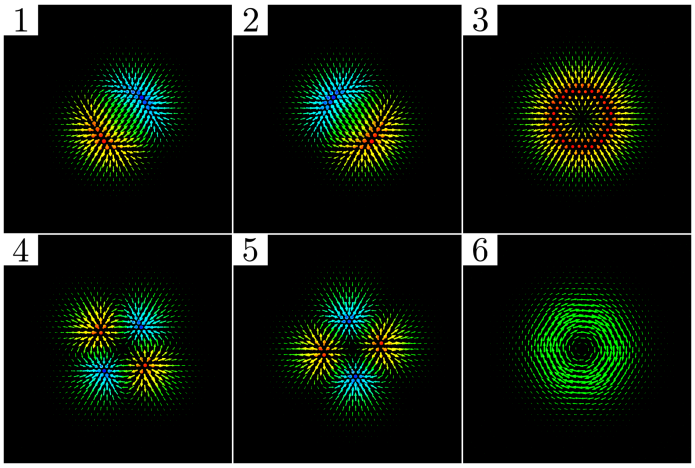

Figure A.8 | First six skyrmion eigenvectors for fcc-Pd/Fe/Ir(111) at $B = 3.8$ T. A zoom of the eigenvectors consisting of one $3D$ vector per lattice site is shown with the isolated skyrmion at its centre. The size of the arrows scales with the norm of the vector, while the colour code denotes its orientation. The eigenvectors correspond to the following localised skyrmion modes: **1,2**: translation; **3**: breathing; **4,5**: 4-fold deformation; **6**: rotation.

.

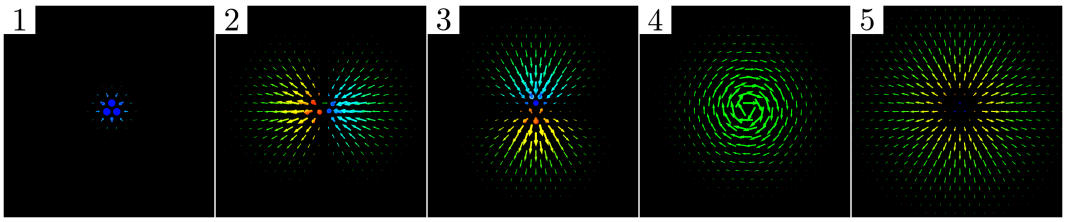

Figure A.9 | First five eigenvectors of the saddle point of radial symmetric skyrmion collapse in fcc-Pd/-Fe/Ir(111) at $B = 3.8$ T. A zoom of the eigenvectors consisting of one $3D$ vector per lattice site is shown with the saddle point structure at its centre. The size of the arrows scales with the norm of the vector, while the colour code denotes its orientation. The first eigenvector corresponds to the unstable mode and its vector components have been scaled down compared to the other four displayed eigenvectors. The other eigenvectors correspond to: **2,3**: transition to the chimera saddle point state; **4**: rotation; **5**: expansion.

.

A.7. Rates of skyrmion transitions with effective parameters

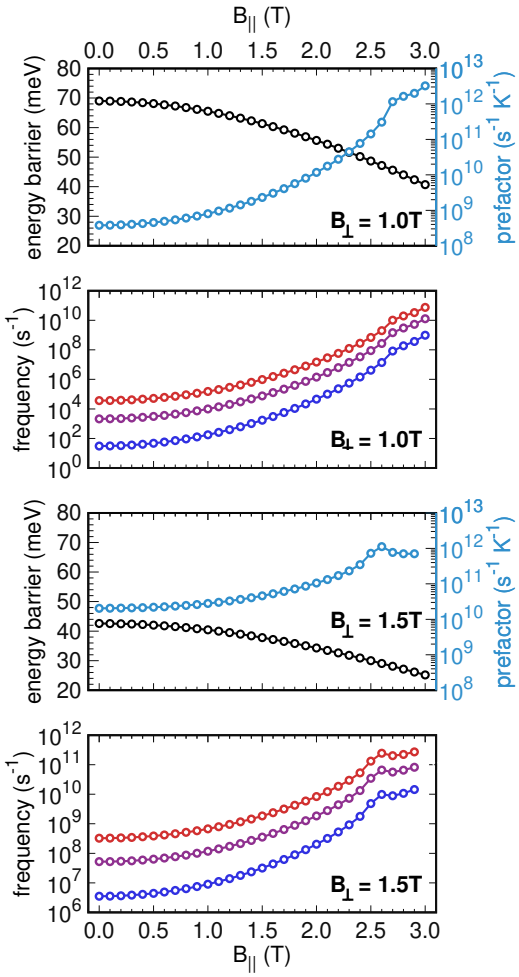

Figure A.10 | Rates of skyrmion annihilation in Pd/Fe/Ir(111) calculated over in-plane magnetic field. The transition rates are calculated at $B = 1.0\,\mathrm{T}$ and $B_\perp = 1.5\,\mathrm{T}$ with the interaction parameters obtained by Romming *et al.* [81] by fitting micromagnetic parameters to the experimental results. The rates are calculated for temperatures of $T = 40$ K (blue), $T = 50$ K (purple) and $T = 60$ K (red).

References

1. C. H. Back, V. Cros, H. Ebert, K. Everschor-Sitte, A. Fert, M. Garst, T. Ma, S. Mankovsky, T. Monchesky, M. V. Mostovoy, N. Nagaosa, S. S. P. Parkin, C. Pfleiderer, N. Reyren, A. Rosch, Y. Taguchi, Y. Tokura, K. von Bergmann & J. Zang, *The 2020 skyrmionics roadmap,* Journal of Physics D: Applied Physics **53,** 363001 (2020).

2. R. Wiesendanger, *Nanoscale magnetic skyrmions in metallic films and multilayers: a new twist for spintronics,* Nature Reviews Materials **1,** 1–11 (2016).

3. A. Fert, N. Reyren & V. Cros, *Magnetic skyrmions: advances in physics and potential applications,* Nature Reviews Materials **2,** 1–15 (2017).

4. G. Finocchio, F. Büttner, R. Tomasello, M. Carpentieri & M. Kläui, *Magnetic skyrmions: from fundamental to applications,* Journal of Physics D: Applied Physics **49,** 423001 (2016).

5. T. H. R. Skyrme, *A unified field theory of mesons and baryons,* Nuclear Physics **31,** 556–569 (1962).

6. A. N. Bogdanov & D. A. Yablonskii, *Thermodynamically stable "vortices" in magnetically ordered crystals. The mixed state of magnets,* Zh. Eksp. Teor. Fiz **95,** 178 (1989).

7. A. Bogdanov & A. Hubert, *Thermodynamically stable magnetic vortex states in magnetic crystals,* Journal of Magnetism and Magnetic Materials **138,** 255–269 (1994).

8. W. Heisenberg, *Zur Theorie des Ferromagnetismus,* Zeitschrift für Physik **49,** 619–636 (1928).

9. P. Bruno, *Tight-binding approach to the orbital magnetic moment and magnetocrystalline anisotropy of transition-metal monolayers,* Physical Review B **39,** 865 (1989).

10. I. Dzyaloshinsky, *A thermodynamic theory of "weak" ferromagnetism of antiferromagnetics,* Journal of Physics and Chemistry of Solids **4,** 241–255 (1958).

11. T. Moriya, *Anisotropic superexchange interaction and weak ferromagnetism,* Physical Review **120,** 91 (1960).

12. A. Fert & P. M. Levy, *Role of anisotropic exchange interactions in determining the properties of spin-glasses,* Physical Review Letters **44,** 1538 (1980).

13. M. Heide, G. Bihlmayer & S. Blügel, *Dzyaloshinskii-Moriya interaction accounting for the orientation of magnetic domains in ultrathin films: Fe/W (110),* Physical Review B **78,** 140403 (2008).

14. M. Bode, M. Heide, K. von Bergmann, P. Ferriani, S. Heinze, G. Bihlmayer, A. Kubetzka, O. Pietzsch, S. Blügel & R. Wiesendanger, *Chiral magnetic order at surfaces driven by inversion asymmetry,* Nature **447,** 190 (2007).

15. *The Nobel Prize in Physics 2016,* `https://www.nobelprize.org/prizes/physics/2016/press-release/`.

16. A. Abanov & V. L. Pokrovsky, *Skyrmion in a real magnetic film,* Physical Review B **58,** R8889–R8892 (14 1998).

17. S. Mühlbauer, B. Binz, F. Jonietz, C. Pfleiderer, A. Rosch, A. Neubauer, R. Georgii & P. Böni, *Skyrmion lattice in a chiral magnet,* Science **323,** 915–919 (2009).

18. K. Karube, J. S. White, D. Morikawa, M. Bartkowiak, A. Kikkawa, Y. Tokunaga, T. Arima, H. M. Rønnow, Y. Tokura & Y. Taguchi, *Skyrmion formation in a bulk chiral magnet at zero magnetic field and above room temperature,* Physical Review Materials **1,** 074405 (2017).

19. X. Z. Yu, Y. Onose, N. Kanazawa, J. H. Park, J. H. Han, Y. Matsui, N. Nagaosa & Y. Tokura, *Real-space observation of a two-dimensional skyrmion crystal,* Nature **465,** 901–904 (2010).

20. N. Romming, C. Hanneken, M. Menzel, J. E. Bickel, B. Wolter, K. von Bergmann, A. Kubetzka & R. Wiesendanger, *Writing and deleting single magnetic skyrmions,* Science **341,** 636–639 (2013).

21. S. Heinze, K. von Bergmann, M. Menzel, J. Brede, A. Kubetzka, R. Wiesendanger, G. Bihlmayer & S. Blügel, *Spontaneous atomic-scale magnetic skyrmion lattice in two dimensions,* Nature Physics **7,** 713 (2011).

22. J. Grenz, A. Köhler, A. Schwarz & R. Wiesendanger, *Probing the Nano-Skyrmion Lattice on Fe/Ir (111) with Magnetic Exchange Force Microscopy,* Physical Review Letters **119,** 047205 (2017).

23. M. Hoffmann, G. P. Müller & S. Blügel, *Atomistic Perspective of Long Lifetimes of Small Skyrmions at Room Temperature,* Physical Review Letters **124,** 247201 (24 2020).

24. B. Dupé, M. Hoffmann, C. Paillard & S. Heinze, *Tailoring magnetic skyrmions in ultra-thin transition metal films,* Nature Communications **5,** 4030 (2014).

25. A. K. Nandy, N. S. Kiselev & S. Blügel, *Interlayer Exchange Coupling: A General Scheme Turning Chiral Magnets into Magnetic Multilayers Carrying Atomic-Scale Skyrmions,* Physical Review Letters **116,** 177202 (17 2016).

26. A. Belabbes, G. Bihlmayer, F. Bechstedt, S. Blügel & A. Manchon, *Hund's Rule-Driven Dzyaloshinskii-Moriya Interaction at* $3d$*—*$5d$ *Interfaces,* Physical Review Letters **117,** 247202 (24 2016).

27. P.-J. Hsu, A. Kubetzka, A. Finco, N. Romming, K. von Bergmann & R. Wiesendanger, *Electric-field-driven switching of individual magnetic skyrmions,* Nature Nanotechnology **12,** 123–126 (2017).

28. J. Sassmannshausen, A. Kubetzka, P.-J. Hsu, K. von Bergmann & R. Wiesendanger, *Pb-induced skyrmions in a double layer of Fe on Ir(111),* Physical Review B **98,** 144443 (14 2018).

29. S. Meyer, M. Schmitt, M. Vogt, M. Bode & S. Heinze, *Dead magnetic layers at the interface: Moment quenching through hybridization and frustration,* Physical Review Research **2,** 012075 (1 2020).

30. B. Hardrat, A. Al-Zubi, P. Ferriani, S. Blügel, G. Bihlmayer & S. Heinze, *Complex magnetism of iron monolayers on hexagonal transition metal surfaces from first principles,* Physical Review B **79,** 094411 (9 2009).

31. P. Ferriani, I. Turek, S. Heinze, G. Bihlmayer & S. Blügel, *Magnetic Phase Control in Monolayer Films by Substrate Tuning,* Physical Review Letters **99,** 187203 (18 2007).

32. S. Meyer, B. Dupé, P. Ferriani & S. Heinze, *Dzyaloshinskii-Moriya interaction at an antiferromagnetic interface: First-principles study of Fe/Ir bilayers on Rh(001),* Physical Review B **96,** 094408 (9 2017).

33. B. Zimmermann, W. Legrand, D. Maccariello, N. Reyren, V. Cros, S. Blügel & A. Fert, *Dzyaloshinskii-Moriya interaction at disordered interfaces from ab initio theory: Robustness against intermixing and tunability through dusting,* Applied Physics Letters **113,** 232403 (2018).

34. M. Hervé, B. Dupé, R. Lopes, M. Böttcher, M. D. Martins, T. Balashov, L. Gerhard, J. Sinova & W. Wulfhekel, *Stabilizing spin spirals and isolated skyrmions at low magnetic field exploiting vanishing magnetic anisotropy,* Nature Communications **9,** 1–8 (2018).

35. S. Woo, K. Litzius, B. Krüger, M.-Y. Im, L. Caretta, K. Richter, M. Mann, A. Krone, R. M. Reeve, M. Weigand, P. Agrawal, I. Lemesh, M.-A. Mawass, P. Fischer, M. Kläui & G. S. D. Beach, *Observation of room-temperature magnetic skyrmions and their current-driven dynamics in ultrathin metallic ferromagnets,* Nature Materials **15,** 501–506 (2016).

36. O. Boulle, J. Vogel, H. Yang, S. Pizzini, D. de Souza Chaves, A. Locatelli, T. O. Menteş, A. Sala, L. D. Buda-Prejbeanu, O. Klein, M. Belmeguenai, Y. Roussigné, A. Stashkevich, S. M. Chérif, L. Aballe, M. Foerster, M. Chshiev, S. Auffret, I. M. Miron & G. Gaudin, *Room-temperature chiral magnetic skyrmions in ultrathin magnetic nanostructures,* Nature Nanotechnology **11,** 449 (2016).

37. C. Moreau-Luchaire, C. Moutafis, N. Reyren, J. Sampaio, C. A. F. Vaz, N. Van Horne, K. Bouzehouane, K. Garcia, C. Deranlot, P. Warnicke, P. Wohlhüter, J.-M. George, M. Weigand, J. Raabe, V. Cros & A. Fert, *Additive interfacial chiral interaction in multilayers for stabilization of small individual skyrmions at room temperature,* Nature Nanotechnology **11,** 444–448 (2016).

38. A. Soumyanarayanan, M. Raju, A. L. G. Oyarce, A. K. C. Tan, M.-Y. Im, A. P. Petrović, P. Ho, K. H. Khoo, M. Tran, C. K. Gan, F. Ernult & P. C., *Tunable room-temperature magnetic skyrmions in Ir/Fe/Co/Pt multilayers,* Nature Materials **16,** 898–904 (2017).

39. A. K. Nayak, V. Kumar, T. Ma, P. Werner, E. Pippel, R. Sahoo, F. Damay, U. K. Rößler, C. Felser & S. S. P. Parkin, *Magnetic antiskyrmions above room temperature in tetragonal Heusler materials,* Nature **548,** 561–566 (2017).

40. L. Peng, R. Takagi, W. Koshibae, K. Shibata, K. Nakajima, T.-h. Arima, N. Nagaosa, S. Seki, X. Yu & Y. Tokura, *Controlled transformation of skyrmions and antiskyrmions in a non-centrosymmetric magnet,* Nature Nanotechnology **15,** 181–186 (2020).

41. B. Dupé, C. N. Kruse, T. Dornheim & S. Heinze, *How to reveal metastable skyrmionic spin structures by spin-polarized scanning tunneling microscopy,* New Journal of Physics **18,** 055015 (2016).

42. L. Rózsa, K. Palotás, A. Deák, E. Simon, R. Yanes, L. Udvardi, L. Szunyogh & U. Nowak, *Formation and stability of metastable skyrmionic spin structures*

with various topologies in an ultrathin film, Physical Review B **95,** 094423 (2017).

43. W. Legrand, D. Maccariello, F. Ajejas, S. Collin, A. Vecchiola, K. Bouzehouane, N. Reyren, V. Cros & A. Fert, *Room-temperature stabilization of antiferromagnetic skyrmions in synthetic antiferromagnets,* Nature Materials **19,** 34–42 (2020).

44. S. Woo, K. M. Song, X. Zhang, M. Ezawa, Y. Zhou, X. Liu, M. Weigand, S. Finizio, J. Raabe, M.-C. Park, K.-Y. Lee, J. W. Choi, B.-C. Min, H. C. Koo & J. Chang, *Deterministic creation and deletion of a single magnetic skyrmion observed by direct time-resolved X-ray microscopy,* Nature Electronics **1,** 288–296 (2018).

45. L. Caretta, M. Mann, F. Büttner, K. Ueda, B. Pfau, C. M. Günther, P. Hessing, A. Churikova, C. Klose, M. Schneider, D. Engel, C. Marcus, D. Bono, K. Bagschik, S. Eisebitt & G. S. D. Beach, *Fast current-driven domain walls and small skyrmions in a compensated ferrimagnet,* Nature Nanotechnology **13,** 1154–1160 (2018).

46. J. Iwasaki, M. Mochizuki & N. Nagaosa, *Universal current-velocity relation of skyrmion motion in chiral magnets,* Nature Communications **4,** 1–8 (2013).

47. J. Sampaio, V. Cros, S. Rohart, A. Thiaville & A. Fert, *Nucleation, stability and current-induced motion of isolated magnetic skyrmions in nanostructures,* Nature Nanotechnology **8,** 839–844 (2013).

48. N. Nagaosa & Y. Tokura, *Topological properties and dynamics of magnetic skyrmions,* Nature Nanotechnology **8,** 899–911 (2013).

49. R. Tomasello, E. Martinez, R. Zivieri, L. Torres, M. Carpentieri & G. Finocchio, *A strategy for the design of skyrmion racetrack memories,* Scientific Reports **4,** 6784 (2014).

50. P. M. Buhl, F. Freimuth, S. Blügel & Y. Mokrousov, *Topological spin Hall effect in antiferromagnetic skyrmions,* Physica Status Solidi (RRL)–Rapid Research Letters **11,** 1700007 (2017).

51. S. Woo, K. M. Song, H.-S. Han, M.-S. Jung, M.-Y. Im, K.-S. Lee, K. S. Song, P. Fischer, J.-I. Hong, J. W. Choi, B.-C. Min, H. C. Koo & J. Chang, *Spin-orbit torque-driven skyrmion dynamics revealed by time-resolved X-ray microscopy,* Nature Communications **8,** 1–8 (2017).

52. F. Büttner, I. Lemesh, M. Schneider, B. Pfau, C. M. Günther, P. Hessing, J. Geilhufe, L. Caretta, D. Engel, B. Krüger, J. Viefhaus, S. Eisebitt & G. S. D.

Beach, *Field-free deterministic ultrafast creation of magnetic skyrmions by spin–orbit torques,* Nature Nanotechnology **12,** 1040–1044 (2017).

53. W. Jiang, P. Upadhyaya, W. Zhang, G. Yu, M. B. Jungfleisch, F. Y. Fradin, J. E. Pearson, Y. Tserkovnyak, K. L. Wang, O. Heinonen, S. G. E. te Velthuis & A. Hoffmann, *Blowing magnetic skyrmion bubbles,* Science **349,** 283–286 (2015).

54. W. Legrand, D. Maccariello, N. Reyren, K. Garcia, C. Moutafis, C. Moreau-Luchaire, S. Collin, K. Bouzehouane, V. Cros & A. Fert, *Room-temperature current-induced generation and motion of sub-100 nm skyrmions,* Nano Letters **17,** 2703–2712 (2017).

55. X. Zhang, M. Ezawa & Y. Zhou, *Magnetic skyrmion logic gates: conversion, duplication and merging of skyrmions,* Scientific Reports **5,** 1–8 (2015).

56. D. Pinna, F. Abreu Araujo, J.-V. Kim, V. Cros, D. Querlioz, P. Bessiere, J. Droulez & J. Grollier, *Skyrmion Gas Manipulation for Probabilistic Computing,* Physical Review Applied **9,** 064018 (6 2018).

57. J. Zázvorka, F. Jakobs, D. Heinze, N. Keil, S. Kromin, S. Jaiswal, K. Litzius, G. Jakob, P. Virnau, D. Pinna, K. Everschor-Sitte, L. Rózsa, A. Donges, U. Nowak & M. Kläui, *Thermal skyrmion diffusion used in a reshuffler device,* Nature Nanotechnology **14,** 658–661 (2019).

58. M.-C. Chen, A. Sengupta & K. Roy, *Magnetic skyrmion as a spintronic deep learning spiking neuron processor,* IEEE Transactions on Magnetics **54,** 1–7 (2018).

59. S. S. P. Parkin, *Shiftable magnetic shift register and method of using the same,* US Patent 6,834,005, 2004.

60. S. Parkin & S.-H. Yang, *Memory on the racetrack,* Nature Nanotechnology **10,** 195–198 (2015).

61. B. Göbel, A. F. Schäffer, J. Berakdar, I. Mertig & S. S. P. Parkin, *Electrical writing, deleting, reading, and moving of magnetic skyrmioniums in a racetrack device,* Scientific Reports **9,** 1–9 (2019).

62. K. von Bergmann & A. Kubetzka, *Knoten in der Magnetisierung,* Physik in unserer Zeit **48,** 118–123 (2017).

63. B. Göbel, A. Mook, J. Henk & I. Mertig, *Overcoming the speed limit in skyrmion racetrack devices by suppressing the skyrmion Hall effect,* Physical Review B **99,** 020405 (2019).

64. W. Jiang, X. Zhang, G. Yu, W. Zhang, X. Wang, M. B. Jungfleisch, J. E. Pearson, X. Cheng, O. Heinonen, K. L. Wang, Y. Zhou, A. Hoffmann & S. G. E. te Velthuis, *Direct observation of the skyrmion Hall effect,* Nature Physics **13,** 162–169 (2017).

65. A. O. Leonov & M. Mostovoy, *Multiply periodic states and isolated skyrmions in an anisotropic frustrated magnet,* Nature Communications **6,** 1–8 (2015).

66. J. Wild, T. N. G. Meier, S. Pöllath, M. Kronseder, A. Bauer, A. Chacon, M. Halder, M. Schowalter, A. Rosenauer, J. Zweck, J. Müller, A. Rosch, C. Pfleiderer & C. H. Back, *Entropy-limited topological protection of skyrmions,* Science Advances **3,** e1701704 (2017).

67. L. Desplat, D. Suess, J.-V. Kim & R. L. Stamps, *Thermal stability of metastable magnetic skyrmions: Entropic narrowing and significance of internal eigenmodes,* Physical Review B **98,** 134407 (2018).

68. G. P. Müller, M. Hoffmann, C. Dißelkamp, D. Schürhoff, S. Mavros, M. Sallermann, N. S. Kiselev, H. Jónsson & S. Blügel, *Spirit: Multifunctional framework for atomistic spin simulations,* Physical Review B **99,** 224414 (2019).

69. O. Eriksson, A. Bergman, L. Bergqvist & J. Hellsvik, *Atomistic spin dynamics: Foundations and applications* (Oxford University Press, 2017).

70. P. Hohenberg & W. Kohn, *Inhomogeneous Electron Gas,* Physical Review **136,** B864–B871 (3B 1964).

71. W. Kohn & L. J. Sham, *Self-Consistent Equations Including Exchange and Correlation Effects,* Physical Review **140,** A1133–A1138 (4A 1965).

72. M. Bode, S. Heinze, A. Kubetzka, O. Pietzsch, X. Nie, G. Bihlmayer, S. Blügel & R. Wiesendanger, *Magnetization-Direction-Dependent Local Electronic Structure Probed by Scanning Tunneling Spectroscopy,* Physical Review Letters **89,** 237205 (23 2002).

73. P. Kurz, F. Förster, L. Nordström, G. Bihlmayer & S. Blügel, *Ab initio treatment of noncollinear magnets with the full-potential linearized augmented plane wave method,* Physical Review B **69,** 024415 (2 2004).

74. M. C. Ambrose & R. L. Stamps, *Melting of hexagonal skyrmion states in chiral magnets,* New Journal of Physics **15,** 053003 (2013).

75. S. Buhrandt & L. Fritz, *Skyrmion lattice phase in three-dimensional chiral magnets from Monte Carlo simulations,* Physical Review B **88,** 195137 (19 2013).

76. R. L. Silva, L. D. Secchin, W. A. Moura-Melo, A. R. Pereira & R. L. Stamps, *Emergence of skyrmion lattices and bimerons in chiral magnetic thin films with nonmagnetic impurities,* Physical Review B **89,** 054434 (5 2014).

77. J. Hagemeister, N. Romming, K. von Bergmann, E. Y. Vedmedenko & R. Wiesendanger, *Stability of single skyrmionic bits,* Nature Communications **6,** 8455 (2015).

78. L. Rózsa, E. Simon, K. Palotás, L. Udvardi & L. Szunyogh, *Complex magnetic phase diagram and skyrmion lifetime in an ultrathin film from atomistic simulations,* Physical Review B **93,** 024417 (2016).

79. L. Cai, E. M. Chudnovsky & D. A. Garanin, *Collapse of skyrmions in two-dimensional ferromagnets and antiferromagnets,* Physical Review B **86,** 024429 (2012).

80. E. Simon, K. Palotás, L. Rózsa, L. Udvardi & L. Szunyogh, *Formation of magnetic skyrmions with tunable properties in PdFe bilayer deposited on Ir (111),* Physical Review B **90,** 094410 (2014).

81. N. Romming, A. Kubetzka, C. Hanneken, K. von Bergmann & R. Wiesendanger, *Field-dependent size and shape of single magnetic skyrmions,* Physical Review Letters **114,** 177203 (2015).

82. B. Dupé, G. Bihlmayer, M. Böttcher, S. Blügel & S. Heinze, *Engineering skyrmions in transition-metal multilayers for spintronics,* Nature Communications **7,** 11779 (2016).

83. A. Fert, V. Cros & J. Sampaio, *Skyrmions on the track,* Nature Nanotechnology **8,** 152–156 (2013).

84. M. Garst, J. Waizner & D. Grundler, *Collective spin excitations of helices and magnetic skyrmions: review and perspectives of magnonics in non-centrosymmetric magnets,* Journal of Physics D: Applied Physics **50,** 293002 (2017).

85. K. Everschor-Sitte, M. Sitte, T. Valet, A. Abanov & J. Sinova, *Skyrmion production on demand by homogeneous DC currents,* New Journal of Physics **19,** 092001 (2017).

86. S. Rohart, J. Miltat & A. Thiaville, *Path to collapse for an isolated Néel skyrmion,* Physical Review B **93,** 214412 (2016).

87. K. Hukushima & K. Nemoto, *Exchange Monte Carlo method and application to spin glass simulations,* Journal of the Physical Society of Japan **65,** 1604–1608 (1996).

88. R. H. Swendsen & J.-S. Wang, *Replica Monte Carlo Simulation of Spin-Glasses,* Physical Review Letters **57,** 2607–2609 (21 1986).

89. L. Desplat, C. Vogler, J.-V. Kim, R. L. Stamps & D. Suess, *Path sampling for lifetimes of metastable magnetic skyrmions and direct comparison with Kramers' method,* Physical Review B **101,** 060403 (2020).

90. P. F. Bessarab, G. P. Müller, I. S. Lobanov, F. N. Rybakov, N. S. Kiselev, H. Jónsson, V. M. Uzdin, S. Blügel, L. Bergqvist & A. Delin, *Lifetime of racetrack skyrmions,* Scientific Reports **8,** 3433 (2018).

91. P. F. Bessarab, *Theoretical description of stability and transitions between magnetic states,* PhD thesis, University of Iceland, 2013.

92. G. Fiedler, J. Fidler, J. Lee, T. Schrefl, R. L. Stamps, H. B. Braun & D. Suess, *Direct calculation of the attempt frequency of magnetic structures using the finite element method,* Journal of Applied Physics **111,** 093917 (2012).

93. P. F. Bessarab, V. M. Uzdin & H. Jónsson, *Harmonic transition-state theory of thermal spin transitions,* Physical Review B **85,** 184409 (2012).

94. P. F. Bessarab, V. M. Uzdin & H. Jónsson, *Method for finding mechanism and activation energy of magnetic transitions, applied to skyrmion and antivortex annihilation,* Computer Physics Communications **196,** 335–347 (2015).

95. I. S. Lobanov, H. Jónsson & V. M. Uzdin, *Mechanism and activation energy of magnetic skyrmion annihilation obtained from minimum energy path calculations,* Physical Review B **94,** 174418 (2016).

96. F. Büttner, I. Lemesh & G. S. D. Beach, *Theory of isolated magnetic skyrmions: From fundamentals to room temperature applications,* Scientific Reports **8,** 1–12 (2018).

97. M. Böttcher, S. Heinze, S. Egorov, J. Sinova & B. Dupé, *B–T phase diagram of Pd/Fe/Ir (111) computed with parallel tempering Monte Carlo,* New Journal of Physics **20,** 103014 (2018).

98. P. Lindner, L. Bargsten, S. Kovarik, J. Friedlein, J. Harm, S. Krause & R. Wiesendanger, *Temperature and magnetic field dependent behavior of atomic-*

scale skyrmions in Pd/Fe/Ir(111) nanoislands, Physical Review B **101,** 214445 (21 2020).

99. L. Desplat, J.-V. Kim & R. L. Stamps, *Paths to annihilation of first-and second-order (anti) skyrmions via (anti) meron nucleation on the frustrated square lattice,* Physical Review B **99,** 174409 (2019).

100. W. Nolting & A. Ramakanth, *Quantum theory of magnetism* (Springer-Verlang, 2009).

101. S. Blügel, *Electronic oxides - correlation phenomena, exotic phases and novel functionalities, Chapter: Exchange interactions* (Lecture Notes of the 41st Spring School 2010 - Schriften des Forschungszentrums Jülich, Reihe Schlüsseltechnologien / Key Technologies, 2010).

102. S. Blügel, *Strong ferromagnetism of 3d-metal overlayers on Pd (001),* EPL (Europhysics Letters) **7,** 743 (1988).

103. A. D. McNaught, A. Wilkinson, I. U. of Pure & A. Chemistry, *Compendium of Chemical Terminology, 2nd ed. (the "Gold Book"),* 0-9678550-9-8, `https://doi.org/10.1351/goldbook` (Blackwell Scientific Publications, Oxford (1997). Online version (2019-) created by S. J. Chalk, 1997).

104. P. Kurz, *Non-Collinear magnetism at surfaces and in ultrathin films,* PhD thesis, Rheinisch-Westfälische technische Hochschule Aachen, 2000.

105. P. Weiss, *L'hypothèse du champ moléculaire et la propriété ferromagnétique,* Journal de Physique Théorique et Appliquée **6,** 661–690 (1907).

106. W. Heitler & F. London, *Wechselwirkung neutraler Atome und homöopolare Bindung nach der Quantenmechanik,* Zeitschrift für Physik **44,** 455–472 (1927).

107. N. S. Kiselev, B. Zimmermann & J. Chico, *Topological Matter - Topological Insulators, Skyrmions and Majoranas, Chapter: Atomistic and micromagnetic models of magnetism* (Lecture Notes of the 41st Spring School 2010 - Schriften des Forschungszentrums Jülich, Reihe Schlüsseltechnologien / Key Technologies, 2017).

108. M. Hoffmann & S. Blügel, *Systematic derivation of realistic spin models for beyond-Heisenberg solids,* Physical Review B **101,** 024418 (2020).

109. M. A. Ruderman & C. Kittel, *Indirect exchange coupling of nuclear magnetic moments by conduction electrons,* Physical Review **96,** 99 (1954).

110. T. Kasuya, *A theory of metallic ferro-and antiferromagnetism on Zener's model,* Progress of theoretical physics **16,** 45–57 (1956).

111. K. Yosida, *Magnetic properties of Cu-Mn alloys,* Physical Review **106,** 893 (1957).

112. F. Meier, L. Zhou, J. Wiebe & R. Wiesendanger, *Revealing magnetic interactions from single-atom magnetization curves,* Science **320,** 82–86 (2008).

113. D. Smith, *New mechanisms for magnetic anisotropy in localised s-state moment materials,* Journal of Magnetism and Magnetic Materials **1,** 214–225 (1976).

114. J. Spethmann, S. Meyer, K. von Bergmann, R. Wiesendanger, S. Heinze & A. Kubetzka, *Discovery of Magnetic Single- and Triple-***q** *States in* Mn/Re(0001)*,* Physical Review Letters **124,** 227203 (22 2020).

115. S. Brinker, M. dos Santos Dias & S. Lounis, *The chiral biquadratic pair interaction,* New Journal of Physics **21,** 083015 (2019).

116. S. Mankovsky, S. Polesya & H. Ebert, *Extension of the standard Heisenberg Hamiltonian to multispin exchange interactions,* Physical Review B **101,** 174401 (2020).

117. D. V. Berkov, K. Ramstöcck & A. Hubert, *Solving micromagnetic problems. Towards an optimal numerical method,* Physica Status Solidi (a) **137,** 207–225 (1993).

118. D. Hinzke & U. Nowak, *Magnetization switching in nanowires: Monte Carlo study with fast Fourier transformation for dipolar fields,* Journal of Magnetism and Magnetic Materials **221,** 365–372 (2000).

119. A. Kubetzka, O. Pietzsch, M. Bode & R. Wiesendanger, *Spin-polarized scanning tunneling microscopy study of 360 walls in an external magnetic field,* Physical Review B **67,** 020401 (2003).

120. H.-B. Braun, *Fluctuations and instabilities of ferromagnetic domain-wall pairs in an external magnetic field,* Physical Review B **50,** 16485 (1994).

121. B. Lilley, *LXXI. Energies and widths of domain boundaries in ferromagnetics,* The London, Edinburgh, and Dublin Philosophical Magazine and Journal of Science **41,** 792–813 (1950).

122. R. Skomski, Z. Li, R. Zhang, R. D. Kirby, A. Enders, D. Schmidt, T. Hofmann, E. Schubert & D. J. Sellmyer, *Nanomagnetic skyrmions,* Journal of Applied Physics **111,** 07E116 (2012).

123. B. Berg & M. Lüscher, *Definition and statistical distributions of a topological number in the lattice O (3) σ-model,* Nuclear Physics B **190,** 412–424 (1981).

124. B. Heil, A. Rosch & J. Masell, *Universality of annihilation barriers of large magnetic skyrmions in chiral and frustrated magnets,* Physical Review B **100,** 134424 (2019).

125. D. M. Crum, M. Bouhassoune, J. Bouaziz, B. Schweflinghaus, S. Blügel & S. Lounis, *Perpendicular reading of single confined magnetic skyrmions,* Nature Communications **6,** 1–8 (2015).

126. S. Blügel, *Topological Matter - Topological Insulators, Skyrmions and Majoranas, Chaper: Non-collinear magnetism in density functional theory* (Lecture Notes of the 41st Spring School 2010 - Schriften des Forschungszentrums Jülich, Reihe Schlüsseltechnologien / Key Technologies, 2017).

127. M. Heide, G. Bihlmayer & S. Blügel, *Describing Dzyaloshinskii–Moriya spirals from first principles,* Physica B: Condensed Matter **404,** 2678–2683 (2009).

128. S. Meyer, *Complex spin structures in frustrated ultrathin films,* PhD thesis, Christian-Albrechts-Universität zu Kiel, 2020.

129. J. H. Mentink, M. V. Tretyakov, A. Fasolino, M. I. Katsnelson & T. Rasing, *Stable and fast semi-implicit integration of the stochastic Landau–Lifshitz equation,* Journal of Physics: Condensed Matter **22,** 176001 (2010).

130. L. Landau & E. Lifshitz, *3 - On the theory of the dispersion of magnetic permeability in ferromagnetic bodies* (ed Pitaevski, L. P.) Reprinted from Physikalische Zeitschrift der Sowjetunion 8, Part 2, 153, 1935. Amsterdam, 1992.

131. R. Wieser, *Description of a dissipative quantum spin dynamics with a Landau-Lifshitz/Gilbert like damping and complete derivation of the classical Landau-Lifshitz equation,* The European Physical Journal B **88,** 77 (2015).

132. R. Kikuchi, *On the minimum of magnetization reversal time,* Journal of Applied Physics **27,** 1352–1357 (1956).

133. T. L. Gilbert, *A phenomenological theory of damping in ferromagnetic materials,* IEEE Transactions on Magnetics **40,** 3443–3449 (2004).

134. W. F. Brown Jr, *Thermal fluctuations of a single-domain particle,* Physical Review **130,** 1677 (1963).

135. J. C. Slonczewski *et al., Current-driven excitation of magnetic multilayers,* Journal of Magnetism and Magnetic Materials **159,** L1 (1996).

136. G. D. Fuchs, J. C. Sankey, V. S. Pribiag, L. Qian, P. M. Braganca, A. G. F. Garcia, E. M. Ryan, Z.-P. Li, O. Ozatay, D. C. Ralph & R. A. Buhrman, *Spin-*

torque ferromagnetic resonance measurements of damping in nanomagnets, Applied Physics Letters **91,** 062507 (2007).

137. Y. Tserkovnyak, A. Brataas & G. E. Bauer, *Enhanced Gilbert damping in thin ferromagnetic films,* Physical Review Letters **88,** 117601 (2002).

138. S. Mizukami, Y. Ando & T. Miyazaki, *Effect of spin diffusion on Gilbert damping for a very thin permalloy layer in Cu/permalloy/Cu/Pt films,* Physical Review B **66,** 104413 (2002).

139. M. Oogane, T. Wakitani, S. Yakata, R. Yilgin, Y. Ando, A. Sakuma & T. Miyazaki, *Magnetic damping in ferromagnetic thin films,* Japanese Journal of Applied Physics **45,** 3889 (2006).

140. M. A. W. Schoen, J. Lucassen, H. T. Nembach, B. Koopmans, T. J. Silva, C. H. Back & J. M. Shaw, *Magnetic properties in ultrathin 3 d transition-metal binary alloys. II. Experimental verification of quantitative theories of damping and spin pumping,* Physical Review B **95,** 134411 (2017).

141. S. Mankovsky, D. Ködderitzsch, G. Woltersdorf & H. Ebert, *First-principles calculation of the Gilbert damping parameter via the linear response formalism with application to magnetic transition metals and alloys,* Physical Review B **87,** 014430 (2013).

142. H. Ebert, S. Mankovsky, D. Ködderitzsch & P. J. Kelly, *Ab initio calculation of the Gilbert damping parameter via the linear response formalism,* Physical Review Letters **107,** 066603 (2011).

143. J. Kuneš & V. Kamberskỳ, *First-principles investigation of the damping of fast magnetization precession in ferromagnetic 3 d metals,* Physical Review B **65,** 212411 (2002).

144. L. Rózsa, J. Hagemeister, E. Y. Vedmedenko & R. Wiesendanger, *Effective damping enhancement in noncollinear spin structures,* Physical Review B **98,** 100404 (10 2018).

145. W. H. Press, S. A. Teukolsky, B. P. Flannery & W. T. Vetterling, *Numerical recipes in Fortran 77: volume 1, volume 1 of Fortran numerical recipes: the art of scientific computing* (Cambridge University Press, 1992).

146. P. Muller, *Glossary of terms used in physical organic chemistry (IUPAC Recommendations 1994),* Pure and Applied Chemistry **66,** 1077–1184 (1994).

147. E. Wigner, *The transition state method,* Transactions of the Faraday Society **34,** 29–41 (1938).

148. G. Henkelman, B. P. Uberuaga & H. Jónsson, *A climbing image nudged elastic band method for finding saddle points and minimum energy paths,* The Journal of Chemical Physics **113,** 9901–9904 (2000).

149. G. Henkelman & H. Jónsson, *Improved tangent estimate in the nudged elastic band method for finding minimum energy paths and saddle points,* The Journal of Chemical Physics **113,** 9978–9985 (2000).

150. O. Rodrigues, *Des lois géométriques qui régissent les déplacements d'un système solide dans l'espace: et de la variation des cordonnées provenant de ces déplacements considérés indépendamment des causes qui peuvent les produire,* Journal de mathématiques pures et appliquées 1re série **5,** 380–440 (1840).

151. T. Vincenty, *Direct and inverse solutions of geodesics on the ellipsoid with application of nested equations,* Survey Review **23,** 88–93 (1975).

152. M. G. Evans & M. Polanyi, *Some applications of the transition state method to the calculation of reaction velocities, especially in solution,* Transactions of the Faraday Society **31,** 875–894 (1935).

153. H. Eyring, *The activated complex in chemical reactions,* The Journal of Chemical Physics **3,** 107–115 (1935).

154. H. Eyring & M. Polanyi, *Über einfache Gasreaktionen,* Zeitschrift für Physikalische Chemie, Abteilung B **12,** 279–311 (1931).

155. H. Pelzer & W. E., *Über die Geschwindigkeitskonstante von Austauschreaktionen.* Zeitschrift für Physikalische Chemie **15B,** 445–471 (1932).

156. K. J. Laidler & M. C. King, *Development of transition-state theory,* The Journal of Physical Chemistry **87,** 2657–2664 (1983).

157. D. G. Truhlar, W. L. Hase & J. T. Hynes, *Current status of transition-state theory,* The Journal of Physical Chemistry **87,** 2664–2682 (1983).

158. D. G. Truhlar, B. C. Garrett & S. J. Klippenstein, *Current status of transition-state theory,* The Journal of Physical Chemistry **100,** 12771–12800 (1996).

159. P. F. Bessarab, V. M. Uzdin & H. Jónsson, *Potential energy surfaces and rates of spin transitions,* Zeitschrift für Physikalische Chemie **227,** 1543–1557 (2013).

160. P. F. Bessarab, V. M. Uzdin & H. Jónsson, *Size and shape dependence of thermal spin transitions in nanoislands,* Physical Review Letters **110,** 020604 (2013).

161. G. H. Vineyard, *Frequency factors and isotope effects in solid state rate processes,* Journal of Physics and Chemistry of Solids **3,** 121–127 (1957).

162. W. H. Miller, *Importance of nonseparability in quantum mechanical transition-state theory,* Accounts of Chemical Research **9,** 306–312 (1976).

163. T. Fließbach, *Statistische Physik* (Springer, 1993).

164. G. P. Müller, *Advanced methods for atomic scale spin simulations and application to localized magnetic states,* PhD thesis, Forschungszentrum Jülich GmbH, Peter Grünberg Institut (PGI), 2019.

165. G. P. Müller, P. F. Bessarab, S. M. Vlasov, F. Lux, N. S. Kiselev, S. Blügel, V. M. Uzdin & H. Jónsson, *Duplication, collapse, and escape of magnetic skyrmions revealed using a systematic saddle point search method,* Physical Review Letters **121,** 197202 (2018).

166. J. S. Langer, *Statistical theory of the decay of metastable states,* Annals of Physics **54,** 258–275 (1969).

167. J. Goldstone, *Field theories with «Superconductor» solutions,* Il Nuovo Cimento (1955-1965) **19,** 154–164 (1961).

168. S. Hoinka, P. Dyke, M. G. Lingham, J. J. Kinnunen, G. M. Bruun & C. J. Vale, *Goldstone mode and pair-breaking excitations in atomic Fermi superfluids,* Nature Physics **13,** 943–946 (2017).

169. H.-B. Braun, *Statistical mechanics of nonuniform magnetization reversal,* Physical Review B **50,** 16501 (1994).

170. M. N. Potkina, I. S. Lobanov, H. Jónsson & V. M. Uzdin, *Skyrmions in antiferromagnets: Thermal stability and the effect of external field and impurities,* Journal of Applied Physics **127,** 213906 (2020).

171. L. H. Sprowl, C. T. Campbell & L. Arnadottir, *Hindered translator and hindered rotor models for adsorbates: Partition functions and entropies,* The Journal of Physical Chemistry C **120,** 9719–9731, `https://pubs.acs.org/doi/full/10.1021/acs.jpcc.5b11616` (2016).

172. X. Zhang, Y. Zhou & M. Ezawa, *Antiferromagnetic skyrmion: stability, creation and manipulation,* Scientific Reports **6,** 24795 (2016).

173. J. Müller, A. Rosch & M. Garst, *Edge instabilities and skyrmion creation in magnetic layers,* New Journal of Physics **18,** 065006 (2016).

174. P. F. Bessarab, *Comment on "Path to collapse for an isolated Néel skyrmion",* Physical Review B **95,** 136401 (2017).

175. S. Rohart, J. Miltat & A. Thiaville, *Reply to "Comment on 'Path to collapse for an isolated Néel skyrmion'",* Physical Review B **95,** 136402 (2017).

176. D. Cortés-Ortuño, N. Romming, M. Beg, K. von Bergmann, A. Kubetzka, O. Hovorka, H. Fangohr & R. Wiesendanger, *Nanoscale magnetic skyrmions and target states in confined geometries,* Physical Review B **99,** 214408 (2019).

177. T. Hartmann, *Skyrmionen in hcp-Pd/Fe/Ir(111),* Bachelors Thesis, Christian-Albrechts-Universität zu Kiel, 2018.

178. A. O. Leonov, T. L. Monchesky, N. Romming, A. Kubetzka, A. N. Bogdanov & R. Wiesendanger, *The properties of isolated chiral skyrmions in thin magnetic films,* New Journal of Physics **18,** 065003 (2016).

179. D. Cortés-Ortuño, W. Wang, M. Beg, R. A. Pepper, M.-A. Bisotti, R. Carey, M. Vousden, T. Kluyver, O. Hovorka & H. Fangohr, *Thermal stability and topological protection of skyrmions in nanotracks,* Scientific Reports **7,** 1–13 (2017).

180. D. Stosic, J. Mulkers, B. Van Waeyenberge, T. B. Ludermir & M. V. Milošević, *Paths to collapse for isolated skyrmions in few-monolayer ferromagnetic films,* Physical Review B **95,** 214418 (2017).

181. V. M. Uzdin, M. N. Potkina, I. S. Lobanov, P. F. Bessarab & H. Jónsson, *The effect of confinement and defects on the thermal stability of skyrmions,* Physica B: Condensed Matter **549,** 6–9 (2018).

182. J. Hagemeister, A. Siemens, L. Rózsa, E. Y. Vedmedenko & R. Wiesendanger, *Controlled creation and stability of k π skyrmions on a discrete lattice,* Physical Review B **97,** 174436 (2018).

183. M. Bode, *Spin-polarized scanning tunnelling microscopy,* Reports on Progress in Physics **66,** 523 (2003).

184. C. Hanneken, F. Otte, A. Kubetzka, B. Dupé, N. Romming, K. von Bergmann, R. Wiesendanger & S. Heinze, *Electrical detection of magnetic skyrmions by tunnelling non-collinear magnetoresistance,* Nature Nanotechnology **10,** 1039 (2015).

185. A. Kubetzka, C. Hanneken, R. Wiesendanger & K. von Bergmann, *Impact of the skyrmion spin texture on magnetoresistance,* Physical Review B **95,** 104433 (2017).

186. M. Goerzen, *Atomistische Simulationen des Einflusses elektrischer Felder auf die Erzeugung und Vernichtung magnetischer Skyrmionen,* Master thesis, Christian-Albrechts-Universität zu Kiel, 2019.

187. M. Hoffmann, *Ab initio Studie komplexer magnetischer Strukturen an Oberflächen: Einfluss atomarer Adlagen und elektrischer Felder,* Master thesis, Christian-Albrechts-Universität zu Kiel, 2013.

188. L. Schmidt, J. Hagemeister, P.-J. Hsu, A. Kubetzka, K. von Bergmann & R. Wiesendanger, *Symmetry breaking in spin spirals and skyrmions by in-plane and canted magnetic fields,* New Journal of Physics **18,** 075007 (2016).

189. J. Van Kranendonk & J. H. Van Vleck, *Spin waves,* Reviews of Modern Physics **30,** 1 (1958).

190. H. Schrautzer, *Atomistische Spindynamiksimulationen für magnetische Multilagensysteme mit Dzyaloshinskii-Moriya-Wechselwirkung: Implementierung und Anwendung,* Master thesis, Christian-Albrechts-Universität zu Kiel, 2020.

Acknowledgements

I am very grateful for all the support I have received over the past years. While this thesis would not have been possible without the help of many people, my special thanks goes to:

- Prof. Stefan Heinze for the opportunity to work in his group, the many conferences I had the chance to visit and the excellent supervision he provided with a contagious fascination about physics. Not only did I learn about many aspects of scientific work, but also about the value of team work in a friendly, cooperative and productive environment.

- Pavel Bessarab for introducing me to the field of transition state theory, welcoming me to Reykjavík for research visits on several occasions, proofreading and a close collaboration throughout the past years.

- Prof. Markus Morgenstern and his group from the RWTH Aachen university, in particular Florian Muckel, for the pleasant and productive collaboration and discussions.

- Bertrand Dupé, who taught me many things about scientific computing and gave me valuable criticism at the early stages of my work.

- The FET-Open project MAGicSky, coordinated by Vincent Cros and the CNRS, which allowed me to interact with many scientists of my field and attend several interesting conferences.

- Sebastian Meyer with whom I have worked side by side over the years and spent a great time during many conferences. Our numerous discussions about physics and all the rest have been very valuable.

- Moritz Goerzen for proofreading and the good times working together.

- Patrick Ludwig, who has always made sure that I have efficient and functioning work equipment.
- Gideon Müller for the discussions we had on many conferences.
- All the other members of the group for the open atmosphere and numerous discussions: Hendrik Schrautzer, Thaddäus Hartmann, Soumyajyoti Haldar, Anastasiia Varentcova, Souvik Paul, Marie Böttcher, Nanning Petersen, Henning Pralow, Grzegorz Kwiatkowski, Tim Drevelow, Lydia Stühmer-Hermann, Felix Nickel, Mara Gutzeit and Mohammad Badarneh. Office would have been different without all of you.
- My parents Jörg and Kerstin von Malottki, my sister Carina von Malottki and my girlfriend Anna Carina Lange for all the support throughout my life.

Eidesstattliche Erklärung

Hiermit versichere ich an Eides statt, dass die vorliegende Dissertation – abgesehen von der Beratung durch meinen wissenschaftlichen Lehrer und der Verwendung der angegebenen Hilfsmittel – nach Inhalt und Form meine eigene ist. Sie hat weder ganz noch teilweise an einer Stelle im Rahmen eines Prüfungsverfahrens vorgelegen. Die hier vorgestellten Ergebnisse sind in Teilen bereits in wissenschaftlichen Fachzeitschriften veröffentlicht worden. Eine ausführliche Publikationsliste befindet sich am Beginn dieser Arbeit. Diese Arbeit ist unter Einhaltung der Regeln guter wissenschaftlicher Praxis der Deutschen Forschungsgemeinschaft entstanden. Es wurde kein akademischer Grad entzogen.

Ort, Datum	Unterzeichner